SMALL PUNCH TESTING
OF ADVANCED
METAL MATRIX COMPOSITES

A dissertation submitted in fulfilment
of the requirements for
the degree of
Doctor of Philosophy

By
Jonathan Chung Kit Mak
BSc (Honours) in Nanotechnology

Department of Physics and Advanced Materials
Faculty of Science
University of Technology, Sydney
June, 2011

For my loving parents
Mak Shu Kai and Mak Cheuk Ping

I know that the molecules in my body are traceable, to phenomenon in the cosmos, and it's out of 15 pounds of grey-matter that figured this out! The kingship with the cosmos that resinates deeply with new age thinking... But I'm not apologetic about that, it's what we find, if whatever we find resinates with whomever. Go ahead take it!

I want somebody to put electrodes on my head, and when I reflect on, our kingship with the cosmos, when I do the calculations that shows, that a 15 tonne meteorite that we have in the Rose Centre for Earth and Space, it's an iron meteorite, when I do the calculations that shows, that if you take all the iron from the haemoglobin of the people in Tri-State Area of New York City. You can recover that much iron out of their blood and realise that the iron from that meteorite and iron from your blood has

Common origin! In the core of a star!

Tell me what part of my brain is lighting up because that excites me. That makes me want to grab people in the street and say "have you heard this"??

It's quite literally true that we are stardust… In the highest exalted way that one can use that phrase.

When it was announced that we were going to cancel the Hubble Telescope the greatest outcry to not do that was not the Astrophysicist, it wasn't from within NASA, it was the public. It was all over the op-ed pages and the talk shows. The public took ownership of the Hubble Space Telescope because the Universe was coming into their bedroom, into their living room and onto their computer. They were participants on the frontiers of discovery. And as far as I can tell, if you let them know, that we're not just something in the Universe, but in fact, given the Chemistry of it all and the Nuclear Physics of it all. Not only are we in the Universe, the Universe is in us…

And, I don't know, any deeper spiritual feeling, than what that brings upon me.

Neil deGrasse Tyson
Beyond Belief Conference, 2006

ABSTRACT

This Doctoral thesis investigates the use of the small punch test (SPT) as a means for assessing yield strength and fracture toughness from alloys and metal matrix composites (MMCs). Metal matrix composites have been implemented in many high performance applications due to their high strength to weight ratio, however, low fracture toughness and ductility remain a concern for these materials. Therefore, techniques for conventional mechanical tests including tensile and fracture toughness tests have been utilised to assess the mechanical performance for these materials, however, more often than not, situations will arise where there are limited volumes of material for testing, this is especially true in the case of MMCs. Thus, there is great demand for mechanical tests that are capable of assessing small samples. The small punch test (SPT) is proposed as a suitable small specimen mechanical test technique that is capable to meet this challenge. This research examines the SPT on MMCs and the effect of ceramic reinforcement content on yield strength and fracture toughness. To achieve this small punch, tensile and fracture toughness tests are performed on as-received 7A04-T6 aluminium and TC4 titanium alloy and related MMCs. In particular, small punch values such as the small punch elastic-plastic load, P_y, equivalent fracture strain, ε_{qF}, and small punch energy, E_{SP}, are correlated against conventional tensile yield strength, σ_{YS}, and plane-strain fracture toughness, J_{1c}, values. Furthermore, empirical, analytical and numerical solutions are assessed. A polynomial relationship is found to correspond well with J_{1c}-ε_{qF} relationship for both elastic and elastic-plastic materials. This research further investigates and develops the application of the SPT which may lead to an inexpensive straightforward multi-mechanical non-destructive test technique for advanced alloys and MMCs.

CERTIFICATE OF AUTHORSHIP

I certify that the work on this thesis has not previously been submitted for a degree nor has it been submitted in part of the requirements for a degree except when fully acknowledged within the text.

I also certify that the thesis has been written by me. Any help that I have received in my research work and the preparation of the thesis itself has been acknowledged. In addition, I certify that all information sources and literature used are acknowledged within this thesis.

Candidature's Signature

Dated: 30-June-2011

ACKNOWLEDGEMENTS

I would like to begin by expressing my deepest appreciation to all whom have contributed their precious time, knowledge and support towards the completion of my Doctoral thesis.

For the University of Technology, Sydney, I wish to sincerely thank my final year supervisors Dr Greg Heness and Dr Richard Wuhrer for their guidance, encouragement and support throughout my research. In addition, I wish to thank my former supervisor Dr Wing Yui Yeung for providing me with the opportunity to conduct a challenging and engaging project. I also wish to thank fellow researchers Mr Tim Lucy and Mr Sam Humphries for their insightful comments and assistance from our weekly materials research meetings. Finally, I wish to mention Dr Norman Booth and Mr Greg Delsanto whom were gracious enough to provide their technical expertise and skills toward the completion of this degree. I would also like to extend a warm thanks to Prof. Zhang Di from Shanghai Jiao Tong University (SJTU) for allowing me the opportunity to conduct overseas research at the State Key Laboratory of Metal Matrix Composites. I would also like to thank Dr Qin JiNing for providing supervisory support. In addition, I wish to thank Dr Lu Weiji and Dr Ouyang Quibo whom provided the necessary materials for this research. I wish to express my thanks to Dr Tao Wei from the Australian Nuclear Science Technology Organisation (ANSTO) for support in mechanical testing and finite element analysis. I would also like to extend my thanks to Mr Darren Attard, Mr Graham Smith, Dr Massey De Los Reyes, Dr Mark Callaghan and Mr Tim Palmer for making my time at ANSTO memorable. I would also like to thank Mr Ken Moran and Mr Peter Davey from Moran Scientific for providing insight into the world of scanning electron microscopy with a few good burning jokes along the way.

Finally, I wish to express how grateful I am to my family and friends for their love, encouragement and support. And especially to my sister Mrs Lisa S. Lynch, who helped with much needed last minute editing!

I thank you all!

TABLE OF CONTENTS

ABSTRACT .... **I**

CERTIFICATE OF AUTHORSHIP .... **II**

ACKNOWLEDGEMENTS .... **III**

TABLE OF CONTENTS .... **IV**

LIST OF FIGURES .... **IX**

LIST OF TABLES .... **XVI**

LIST OF SYMBOLS .... **XVIII**

CHAPTER ONE INTRODUCTION **1**

1.1 Background 2

1.2 Significance of this research 3

1.3 Research objectives 4

1.4 Statement of main findings 5

1.5 Publications arising from this research 6

1.6 Awards arising from this research 7

CHAPTER TWO METAL MATRIX COMPOSITES **8**

2.1 Introduction 9

2.2 A brief history 10

2.3 The current market 11

2.4 Applications 13
  2.4.1 Ground transport 13
  2.4.2 Thermal management 14
  2.4.3 Aerospace 16

2.5 Processing routes 17
  2.5.1 Stir-cast process 18
  2.5.2 Vacuum arc remelting process 19

2.6 Concluding remarks 20

CHAPTER THREE MECHANICAL BEHAVIOUR 21

3.1 Introduction 22

3.2 Strength 22

3.3 Fracture toughness 24

3.4 Failure and fracture mechanism 25

3.5 Concluding remarks 29

CHAPTER FOUR FRACTURE TOUGHNESS TEST 30

4.1 Introduction 31

4.2 Standard fracture toughness test 33
  4.2.1 Single-edge bend test 33
  4.2.2 Compact tension test 35
  4.2.3 Chevron-notched short rod or bar tests 36

4.3 Non-standard fracture toughness test 41
  4.3.1 Circumferential notch tension test 41

4.4 Concluding remarks 44

CHAPTER FIVE THE SMALL PUNCH TEST 45

5.1 Introduction 46

5.2 Defining the small punch test 47

5.3 Determination of the small punch elastic-plastic load, P_y 53

5.4 Determination of the small punch energy, E_{SP} 54

5.5 Determination of the small punch equivalent fracture strain, ε_{qF} 54

5.6 An analytical method for the determination of small punch maximum bend yield strength, σ_y 56

5.7 An empirical method for the determination of plane-strain fracture toughness, K_{1c} and J_{1c} 60

5.8 Finite element methods for the small punch test 66

5.9 Neural networks for the small punch test 70

5.10 Concluding remarks 71

CHAPTER SIX EXPERIMENTAL METHOD 72

6.1 Introduction 73

6.2 Research materials 73
  6.2.1 Aluminium materials 74
  6.2.2 Titanium materials 75

6.3 Specimen orientation system 76

6.4 Metallographic procedure 77

6.5 Microstructural examination 79

6.6 Compositional analysis 80
  6.6.1 Aluminium materials 80
  6.6.2 Titanium materials 80

6.7 Quantitative x-ray mapping 81

6.8 Tensile testing 81
  6.8.1 Flat tensile test specimens 81

6.9 Fracture toughness testing 85
  6.9.1 Single-edge bend testing 85
  6.9.2 Circumferential notch tension testing 87
  6.9.3 Small punch testing 91

6.10 Finite elemental analysis of small punch test 94

6.11 Concluding remarks 95

CHAPTER SEVEN RESULTS AND DISCUSSION 96

7.1 Introduction 97

7.2 Aluminium results 97
  7.2.1 The microstructure 97
  7.2.2 The tensile test 103
  7.2.3 The single-edge bend test 105
  7.2.4 The circumferential notch tension test 112
  7.2.5 Small punch test 122
  7.2.6 Finite element analysis 129

7.3 Titanium results 132
  7.3.1 The microstructure 132
  7.3.2 The tensile test 137
  7.3.3 The circumferential notch tension test 139
  7.3.4 Small punch test 142
  7.3.5 Finite element analysis 150

7.4 Concluding remarks 153

CHAPTER EIGHT SMALL PUNCH TEST CORRELATIONS 154

8.1 Introduction 155

8.2 Empirical correlations between the small punch and mechanical values 159

8.2.1 Correlating yield strength, σ_{YS}, and small punch elastic-plastic load, P_y 159

8.2.2 Correlating plane-strain fracture toughness, J_{1c} and small punch equivalent fracture strain, ε_{qF} 166

8.2.3 Correlating plane-strain fracture toughness, J_{1c}, with the small punch energy, E_{SP} 170

8.3 An analytical approach for the determination of the small punch maximum bend strength, σ_y 174

8.4 A literature survey of the plane-strain fracture toughness, J_{1c}, and small punch equivalent fracture strain, ε_{qF} 181

8.5 A potential small punch analytical solution to derive the plane-strain fracture toughness, J_{1c} 184

8.6 Concluding remarks 185

CHAPTER NINE CONCLUSIONS 187

9.1 Conclusions regarding the small punch test 188

CHAPTER TEN FUTURE WORK 191

REFERENCES 193

APPENDIX I 206

LIST OF FIGURES

Figure 1–1. Article publication history for the small punch test, data from SciFinder.....2

Figure 2–1. Metal matrix composites for the transport industry (a) engine block (b) piston lining and (c) piston head [34]. 14

Figure 2–2. Materials for thermal management. Optimum materials for electronic packaging and thermal management are located within the shaded band [34]..............15

Figure 2–3. Metal matrix composites for thermal management and electronic packaging, MMCC Inc. [40]. 16

Figure 2–4. Metal matrix composites for the aerospace (a) F-16 fighter aircraft ventral fins (b) F-16 fighter fuselage doors and (c) Hubble space telescope high gain antennae wave guide boom [28, 34]..........17

Figure 2–5. The stir-cast processing route for metal matrix composites [28]. 19

Figure 2–6. Non-consumable vacuum arc remelting furnace (a) diagram and (b) furnace employed at the State Key Laboratory of Metal Matrix Composites. 20

Figure 3–1. Tensile behaviour for Al-Cu-Mg 2080/SiC$_p$-T8 metal matrix composites with increasing reinforcement content [28, 50]. 23

Figure 3–2. The fracture toughness for several particulate reinforced metal matrix composite with increasing reinforcement content [28, 63]. 24

Figure 4–1. The effect of specimen thickness on fracture toughness [76]......................31

Figure 4–2. American Society for Testing and Materials single-edge bend test specimen [77]. 33

Figure 4–3. American Society for Testing and Materials compact tension test specimen [77]. 36

Figure 4–4. American Society for Testing and Materials chevron-notched (a) short rod and (b) short bar specimens [78]. 37

Figure 4–5. A comparison of the (a) compact tension and (b) chevron-notched short rod specimen [83]. 40

Figure 4–6. The circumferential notch tensile test configuration [95]...........................41

Figure 4–7. A comparison of the circumferential notch tension and the standard compact tension specimens test size [95]..........43

Figure 5–1. The Massachusetts Institute of Technology small punch test [98]..............46

Figure 5–2. A schematic representation of the small punch test configuration. 48

Figure 5–3. Small punch disk-shaped specimens cut from a cylindrical sample...........50

Figure 5–4. Small punch test load-displacement curve [149]..52

Figure 5–5. The *offset* method and *2 tangent* method for the determination of elastic-plastic load, P_y [152]..53

Figure 5–6. A flat circular plate with constant thickness [156]. Where P_y is the small punch elastic-plastic load, r_o is the radius of the spherical punch and R_l is the radius of the lower die bore...56

Figure 5–7. Method for the determination of the elastic deformation energy, EDE and the elastic displacement, D_e [152]...60

Figure 5–8. The theoretical plane strain fracture toughness J_{1c} and equivalent fracture strain relationship proposed by Bayoumi and Bassim [26]. 61

Figure 5–9. Infinite sharp notched plate-shaped small punch test subjected to uniform bending. Where M_o is the bending moment applied around the boundaries of an infinite plate...63

Figure 5–10. Procedure for estimating the fracture toughness by evaluating the local strain energy density from small punch test load-displacement curve [148]..................68

Figure 5–11. Parameters that govern each region of the small punch test load-displacement curve for structural steels [149]. 69

Figure 5–12. Neural network procedure to determine small punch test mechanical parameters [139]...71

Figure 6–1. The as-received materials consist of (a) 7A04-T6, (b) 7A04/SiC/7.5p-T6, (c) 7A04/SiC/10p-T6, (d) TC4, (e) TC4/TiB, TiC/2.5w, 2.5p and (f) TC4/TiB, TiC/5w, 5p...73

Figure 6–2. The as-machined mechanical test specimen orientation for the (a) SPT specimen, (b) tensile test specimen and (c) circumferential notch tension test specimen. Where L is the direction of the principle grain flow, T is the direction of least deformation and S is the third orthogonal direction. 76

Figure 6–3. the formation of spot dimples or comet-like dimple on the surface of TC4 alloy after 1μm diamond polishing. 78

Figure 6–4. Australian Standard tensile specimen [153] (a) specimen configuration and (b) machined specimen. Where a represents the thickness, L_c is the parallel length, b is the parallel lengths and L_t is the total length of the test piece. 82

Figure 6–5. The tensile test setup with a flat tensile specimen clamped between two pairs of tension wedge grips. An extensometer is attached to the tensile specimen for strain measurement. The load capacity of the wedge grips are 100kN. 84

Figure 6–6. (a) single-edge bend fracture toughness test specimen and (b) straight-through notch. 85

Figure 6–7. The high speed fatigue precracker. 86

Figure 6–8. The circumferential notched tension test (a) specimen configuration and (b) machined specimen. 87

Figure 6–9. Rotational-bend fatigue machine, to induce a precrack in the circumferential notch tension test specimen. 88

Figure 6–10. Circumferential notch tension test (a) specimen held by split-collet grips. 90

Figure 6–11. The small punch test specimen configuration. 91

Figure 6–12. The small punch test configuration (a) schematic diagram (b) experimental setup at the University of Technology, Sydney. 93

Figure 6–13. The finite element model of the small punch test configuration. 94

Figure 7–1. Backscatter electron micrographs for the as-received (a, b, c) 7A04-T6 aluminium alloy, (d, e, f) 7A04/SiC/7.5p-T6 aluminium MMC and (g, h, i) 7A04/SiC/10p-T6 aluminium MMC. 98

Figure 7–2. Backscatter electron micrographs for the as-received (a, b, c) 7A04-T6 aluminium alloy, (d, e, f) 7A04/SiC/7.5p-T6 aluminium MMC and (g, h, i) 7A04/SiC/10p-T6 aluminium MMC. 99

Figure 7–3. Pseudo colour quantitative x-ray mapping for the as-received (a) 7A04-T6 aluminium alloy, (b) 7A04/SiC/7.5-T6 aluminium MMC and (c) 7A04/SiC/10-T6 aluminium MMC. The mapping parameters included 6000cps, 20kV and 512x512 pixels resolution. 102

Figure 7–4. Engineering stress-strain behaviour for 7A04-T6 aluminium alloy, 7A04/SiC/7.5p-T6 aluminium MMCs and 7A04/SiC/10p-T6 aluminium MMCs. 103

Figure 7–5. Single-edge bend test specimen in a three point bending configuration. 105

Figure 7–6. Fracture toughness load-displacement curve for 7A04-T6 aluminium alloy. 108

Figure 7–7. Fracture toughness load-displacement curve for 7A04-T6 aluminium alloy. 108

Figure 7–8. Fracture toughness load-displacement curve for 7A04-T6 aluminium alloy. 109

Figure 7–9. Secondary electron image of the aluminium MMCs fracture surface at the crack tip. The shallow crack length is approximately 200µm as indicated in the micrograph. 110

Figure 7–10. Backscatter secondary electron image of the aluminium MMCs fracture surface. 110

Figure 7–11. Circumferential notch tension precrack fracture surface for 7A04-T6 alloys. The top and bottom fractographs for each column are the matching fracture halves for each specimen. The letters A, B and C are used in this section to designate the test specimens. 112

Figure 7–12. Circumferential notch tension load curves for the 7A04-T6 aluminium materials. The letters A, B and C are used in this section to designate the test specimens. 113

Figure 7–13. Circumferential notch tension precrack fracture surface for the 7A04/SiC/7.5p-T6 aluminium materials. The top and bottom fractographs for each column are the matching fracture halves for each specimen. The letters A, B and C are used in this section to designate the test specimens. 115

Figure 7–14. Side view of the circumferential notch tension precrack fracture surface for the 7A04/SiC/7.5p-T6 aluminium materials. The letters A, B and C are used in this section to designate the test specimens. 115

Figure 7–15. Circumferential notch tension load curves for the 7A04/SiC/7.5p-T6 aluminium materials. The letters A, B and C are used in this section to designate the test specimens. 116

Figure 7–16. Circumferential notch tension precrack fracture surface for 7A04 /SiC/10p-T6 MMCs. The top and bottom fractographs for each column are the matching fracture halves for each specimen. The letters A, B and C are used in this section to designate the test specimens 117

Figure 7–17. Side view of the circumferential notch tension precrack fracture surface for the 7A04/SiC/10p-T6 aluminium materials. The letters A, B and C are used in this section to designate the test specimens. 117

Figure 7–18. Circumferential notch tension load curves for 7A04/SiC/10p-T6 aluminium materials. The letters A, B and C are used in this section to designate the test specimens. 118

Figure 7–19. The 7A04-T6 aluminium alloy fracture surface exhibiting a common flaw. 121

Figure 7–20. Typical small punch test load-displacement curves for 7A04-T6 aluminium alloy. 123

Figure 7–21. Typical small punch test load-displacement curves for 7A04-T6/SiC/7.5p-T6 aluminium MMC. 123

Figure 7–22. Typical small punch test load-displacement curves for 7A04-T6/SiC/10p-T6 aluminium MMC. 124

Figure 7–23. Averaged small punch test load-displacement curves for 7A04-T6 aluminium alloy, 7A04/SiC/7.5p-T6 aluminium MMC and 7A04/SiC/10p-T6 aluminium MMC. The dots indicate the observed load at crack initiation. 124

Figure 7–24. Micrographs illustrating the small punch test crack profile for (a) 7A04-T6, (b) 7A04/SiC/7.5p-T6 and (c) 7A04/SiC/10p-T6 aluminium materials. 127

Figure 7–25. Backscatter electron micrograph illustrating the cross-section of the small punch test crack profile for (a) 7A04-T6, (b) 7A04/SiC/7.5p-T6 and (c) 7A04/SiC/10p-T6 aluminium materials. 128

Figure 7–26. Finite element prediction of the small punch load-displacement curve for aluminium materials. 129

Figure 7–27. Crack initiation and propagation behaviour for 7A04/SiC/7.5p-T6 aluminium MMC with increasing loads. 130

Figure 7–28. Crack initiation and propagation behaviour for 7A04/SiC/10p-T6 aluminium MMC with increasing loads. 130

Figure 7–29. Finite element prediction of the small punch load-displacement curve for aluminium materials up to 200N. 131

Figure 7–30. Backscatter secondary electron micrographs for the as-received (a, b, c) TC4 titanium alloy, (d, e, f) TC4/TiB, TiC/2.5w, 2.5p titanium MMC and (g, h, i) TC4/TiB, TiC/5w, 5p titanium MMC. 133

Figure 7–31. Backscatter secondary electron micrographs for the as-received (a, b, c) TC4 titanium alloy, (d, e, f) TC4/TiB, TiC/2.5w, 2.5p titanium MMC and (g, h, i) TC4/TiB, TiC/5w, 5p titanium MMC. 134

Figure 7–32. Pseudo coloured Quantitative x-ray mapping for as-received (a) TC4 titanium alloy (b) TC4/TiB, TiC/2.5w, 2.5p titanium MMC and (c) TC4/TiB, TiC/5w, 5p titanium MMC. The image size is set to 512x512 pixels, 16kV acceleration voltage. All Quantitative x-ray mapping is weighted averaged. 136
Figure 7–33. Engineering stress-strain behaviour for TC4 titanium alloy, TC4/TiB, TiC/2.5w, 2.5p titanium MMC and TC4/TiB, TiC/5w, 5p titanium MMC. 137
Figure 7–34. Circumferential notch tension test fracture surface for the (a) TC4, (b) TC4/TiB, TiC/2.5w, 2.5p and (c) TC4/TiB, TiC/5w, 5p. The top and bottom fractographs for each column are the matching fracture halves for each specimen. 140
Figure 7–35. Circumferential notch tension load curves for titanium materials. 141
Figure 7–36. Typical small punch test load-displacement curves for TC4 titanium alloy. 142
Figure 7–37. Typical small punch test load-displacement curves for TC4/TiB, TiC/2.5w, 2.5p titanium MMC. 143
Figure 7–38. Typical small punch test load-displacement curves for TC4/TiB, TiC/5w, 5p titanium MMC. 143
Figure 7–39. Averaged small punch test load-displacement curves for TC4 titanium alloy, TC4/TiB, TiC/2.5W, 2.5p titanium MMC and TC4/TiB, TiC/5W, 5p titanium MMC. The dots indicate the observed load at crack initiation. 144
Figure 7–40. Shear punch load-displacement curve for various materials including MMCs [202, 203]. 145
Figure 7–41. Fractographs showing the cracking profile of (a) TC4 titanium alloy, (b) TC4/TiB, TiC/2.5w, 2.5p titanium MMC, (c) TC4/TiB, TiC/5w, 5p titanium MMC at increasing magnifications. 148
Figure 7–42. Side view of the small punch test crack profile for (a) TC4 titanium alloy, (b) TC4/TiB, TiC/2.5w, 2.5p titanium MMC and (c) TC4/TiB, TiC/5w, 5p titanium MMC. 149
Figure 7–43. Finite element prediction of the small punch load-displacement curves for titanium materials. 150
Figure 7–44. Crack initiation and propagation behaviour for TC4/TiB, TiC/2.5w, 2.5p titanium MMC with increasing loads. 151
Figure 7–45. Crack initiation and propagation behaviour for TC4/TiB, TiC/2.w, 2.5p titanium MMC with increasing loads. 151

Figure 7–46. Finite element prediction of the small punch load-displacement curve for titanium materials up to 300N. 152

Figure 8–1. A qualitative comparison of the methods for deriving small punch elastic-plastic load, P_y. 159

Figure 8–2. Correlation of the yield strength, σ_{YS}, and the small punch elastic-plastic load, P_y, for aluminium materials. 162

Figure 8–3. Correlation of the yield strength, σ_{YS}, and the small punch elastic-plastic load, P_y, for titanium materials. 163

Figure 8–4. Correlation of the yield strength, σ_{YS}, and the small punch elastic-plastic load, P_y, for both aluminium and titanium materials. 164

Figure 8–5. A correlation of the plane-strain fracture toughness, J_{1c}, and equivalent fracture strain, ε_{qF}, for aluminium materials. 167

Figure 8–6. A correlation of the plane-strain fracture toughness, J_{1c}, and equivalent fracture strain, ε_{qF}, for titanium materials. 168

Figure 8–7. A correlation of the plane-strain fracture toughness, J_{1c}, and equivalent fracture strain, ε_{qF}, for both aluminium and titanium materials. 168

Figure 8–8. A correlation of normalised plane-strain fracture toughness/yield strength, K_{1c}/σ_{YS}, and equivalent fracture strain, ε_{qF}, relationship for both aluminium and titanium materials. 169

Figure 8–9. A qualitative comparison of the methods for deriving small punch energy, E_{SP}. Where (a) is the energy up to crack initiation, (b) is the total small punch energy and (c) is the energy after crack initiation. 170

Figure 8–10. A correlation of the plane-strain fracture toughness, J_{1c}, and total small punch energy, E_{SP}. 172

Figure 8–11. A geometric method for determining the small punch equivalent contact radius, r′. 174

Figure 8–12. Analytical solutions for solving the small punch maximum bend strength, σ_y. 177

Figure 8–13. A correlation of the tensile yield strength, σ_{YS}, plotted against small punch maximum bend strength, σ_y. 179

Figure 8–14. A global overview of the relationship between plane-strain fracture toughness, J_{Ic}, and the 182

LIST OF TABLES

Table 2-1. Classification system for reinforcements. 10
Table 2-2. The current market and applications for metal matrix composites. 12
Table 2-3. Processing routes for metal matrix composites. 18
Table 4-1. Stress intensity factors relevant to the chevron-notched short rod and bar fracture toughness test. 38
Table 5-1. Small punch test specimen and die configurations. 49
Table 5-2. Reported yield strength correlation coefficients for the small punch test. 58
Table 6-1. The nomenclature for the aluminium research material. 74
Table 6-2. The nomenclature for the titanium research materials. 75
Table 6-3. The chemical composition (wt.%) for the 7A04-T6 base alloy. 80
Table 6-4. The chemical composition (wt.%) for the TC4 base alloy. 80
Table 6-5. Accutom-50 cut-off saw parameters for aluminium based materials. 91
Table 7-1. The particle size and volume percent of SiC_p for aluminium metal matrix composites. 101
Table 7-2. Tensile mechanical properties for 7A04-T6 aluminium alloy, 7A04/SiC/7.5p-T6 aluminium MMC and 7A04/SiC/10p-T6 aluminium MMC. 104
Table 7-3. The 7A04-T6 aluminium base alloy single-edge bend loads, validity requirements and fracture toughness values. The 0.2% off-set yield strength, σ_{YS}, for the 7A04-T6 aluminium base alloy is 462MPa. 107
Table 7-4. Circumferential notch tension plane-strain fracture toughness, K_{1c}, values for the 7A04-T6 aluminium materials. The letters A, B and C are used in this section to designate the test specimens. 114
Table 7-5. Circumferential notch tension plane-strain fracture toughness, K_{1c} values for the 7A04/SiC/7.5p-T6 aluminium materials. The letters A, B and C are used in this section to designate the test specimens. 116
Table 7-6. Circumferential notch tension plane-strain fracture toughness, K_{1c} values for the 7A04/SiC/10p-T6 aluminium materials. The letters A, B and C are used in this section to designate the test specimens. 118
Table 7-7. Summary of the valid circumferential notched tension test fracture toughness specimens. 120
Table 7-8. Circumferential notched tension fracture toughness results. 120

Table 7-9. Compositional analysis of 7A04-T6 aluminium alloy................................121
Table 7-10. Small punch test properties for the as-received aluminium based materials. 125
Table 7-11. The statistical difference between two small punch energy, E_{SP}, 7A04-T6 aluminium MMCs. 126
Table 7-12. The particle size and volume percent for titanium MMCS. 135
Table 7-13. Tensile properties for TC4 titanium alloy, TC4/TiB, TiC/2.5w, 2.5p TC4/TiB, TiC/5w, 5p MMC. 138
Table 7-14. Circumferential notch tension plane-strain fracture toughness, K_{1c} values for the titanium materials. 141
Table 7-15. Small punch test properties for the as-received titanium materials...........146
Table 7-16. The statistical difference between two small punch energy, E_{SP}, TC4 titanium MMCs. 147
Table 8-1. Summary of the small punch test P_y, ε_{qF} and E_{SP} values for aluminium and titanium materials. 156
Table 8-2. Summary of conventional mechanical properties σ_{YS}, K_{1c} and J_{1c}, values for aluminium and titanium materials. 157
Table 8-3. Comparison of small punch and conventional mechanical properties. 158
Table 8-4. Correlation coefficients, α, for the aluminium and titanium materials........164
Table 8-5. Calculated small punch energies. 171

LIST OF SYMBOLS

Symbol	Unit	Description
r_o	mm	Small punch ball radius
R_u	mm	Small punch hole radius of the upper die
R_l	mm	Small punch hole radius of the lower die
r^*	mm	Small punch chamfer edge
d_o	mm	Small punch specimen diameter
t_o	mm	Small punch specimen thickness
t_f	mm	Small punch minimum thickness at fracture
r'	mm	Small punch equivalent contact radius
δ^*	mm	Small punch displacement at fracture
δ_y	mm	Small punch elastic-plastic displacement
P_y	N	Small punch elastic-plastic load
P_i	N	Small punch load at crack initiation
P_{max}	N	Small punch maximum load
E_{SP}	J	Small punch fracture energy
ε_{qF}	-	Small punch equivalent fracture strain
σ_y	MPa	Small punch maximum bend strength
α	-	Small punch correlation coefficient
σ_{YS}	MPa	Yield strength
σ_{UTS}	MPa	Ultimate tensile strength
E	GPa	Elastic modulus
ν	-	Poisson’s ratio
J_{1c}	kJ/m^2	Ductile plane-strain fracture toughness
K_{1c}	$MPa\sqrt{m}$	Brittle plane-strain fracture toughness
n	-	Strain hardening exponent

CHAPTER ONE

INTRODUCTION

1.1 Background

The general trend towards ever smaller mechanical test specimens has lead researchers to invest a great deal of time and effort in the study of small specimen mechanical test techniques. Once such candidate that has still retained the interest of researcher is the small punch test (SPT). The SPT is an innovative small specimen test technique that has been around for the past 30 years as a way of assessing mechanical behaviour and lifetime predictions for embrittled neutron irradiated engineering materials [1, 2], including strength, fracture toughness and creep based assessment. In recent years the application of the SPT has extended beyond testing nuclear materials to a variety of biomaterials [3-6], layered composites [7], welds [7-10], materials that has experienced hydrogen embrittlement [11, 12] or even possibly fusion based materials [13-17]. In spite of this, clear consensus on the SPT methodologies, procedures and analysis techniques have yet to be universally established. Therefore, further research is needed in order to overcome this problem. Interest in the application of the SPT has continued to grow steadily as can be seen in Figure 1–1.

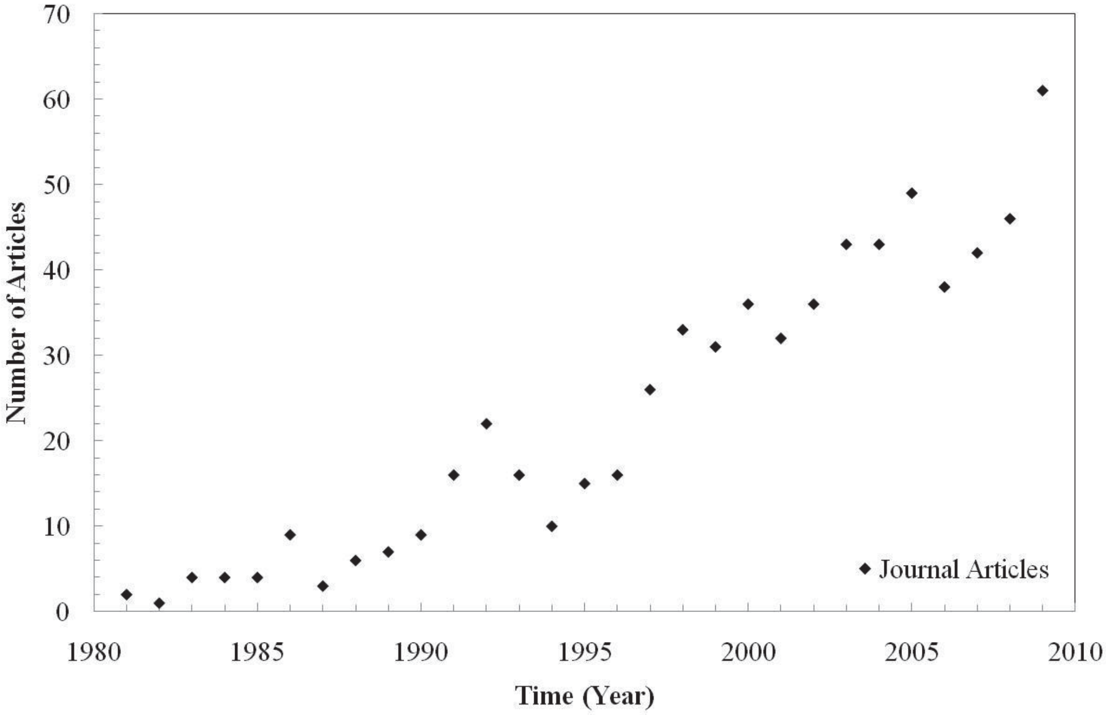

Figure 1–1. Article publication history for the small punch test, data from SciFinder.

1.2 Significance of this research

It is the goal of this research to extend the application of the SPT towards assessing mechanical properties, in particular deriving both strength and fracture toughness properties from alloys and advanced Metal Matrix Composite (MMC) [18-25] and to establish basic SPT methodologies, procedures and analysis techniques. This research can in future lead to an established multi-purpose multi-mechanical test method that is capable of determining meaningful mechanical properties from small amounts of materials. In this research, the strength and fracture toughness of advanced MMCs with varying reinforcement content shall be investigated. Furthermore, this is the first case where SPT is specifically implemented on MMCs. Metal matrix composites are predominantly more expensive to fabricate than alloys owing to the extra step of adding reinforcement content. Thus, only few or limited amounts are generally available for mechanical test and research purposes. Standard tests often require large specimen sizes. Therefore, it becomes impractical to conduct conventional tensile and fracture toughness tests with only small quantities of materials. The importance of this research is outlined as follows.

- Assessing the strength and fracture toughness of MMCs via small specimen test when insufficient volumes of materials for fracture toughness testing are unavailable.
- To develop a multi-purpose multi-mechanical non-destructive test.

This research is part of collaboration between the University of Technology, Sydney (UTS) and the State Key Laboratory of Metal Matrix Composites (SKLMMC) Shanghai Jiao Tong University (SJTU) of P. R. China which is formed in 2007. The aim is to further develop the understanding of the SPT specifically towards testing MMCs which in the past has been limited to alloys. The SKLMMC provided the necessary MMCs for the research including theory behind processing of MMCs. The materials were brought back to Australia. Microscopy and microanalysis is conducted at the Microstructural Analysis Unit (MAU), mechanical testing is performed at UTS Mechanical Testing Facility and the SPT and finite element analysis (FEA) were conducted at the Australian Nuclear Science and Technology Organisation (ANSTO).

1.3 Research objectives

- Conduct an extensive review of the history, microstructure, properties, processing and applications of MMCs. Including a study on the strength and fracture mechanisms of MMCs.

- Research standard to non-standard conventional fracture toughness testing techniques. Perform an extensive review of SPT methodologies, procedures and analysis techniques.

- Conduct scanning electron microscopy on advanced alloys and MMCs microstructure before and after mechanical testing. Characterise the microstructure of alloys and MMCs. In addition, assess the reinforcement effect on the fracture behaviour.

- Perform mechanical testing on advanced alloys and MMCs. Including SPT, single-edge bend test, circumferential notch tension tests and tensile tests. Characterise the mechanical behaviour of alloys and MMCs.

- Assess the SPT through finite element method. Correlate the experimental SPT results with the theoretical SPT finite element results. In addition, characterise the stress distribution for the SPT specimens. Interpret the numerical findings.

- Correlate the small punch elastic-plastic load, P_y, small punch equivalent fracture strain, ε_{qF}, and small punch energy, E_{SP}, values against conventional mechanical properties such as the yield strength, σ_{YS}, and plane-strain fracture toughness, K_{1c} and J_{1c}, values. Evaluate empirical, analytical and numerical solutions.

- Evaluate the SPT role as a multi-mechanical non-destructive test technique for advanced alloys and MMCs.

1.4 Statement of main findings

- Fractography revealed alloys exhibited circumferential complex crack profile indicative of ductile materials, whilst MMCs exhibited multi-crack profile which is a consequence of the reinforcement content. Scanning electron microscopy confirmed the early onset of crack initiation.

- Empirical correlation of the small punch elastic-plastic load, P_y, and tensile yield strength, σ_{YS}, values demonstrated a linear relationship. Good correlations are found. Furthermore, this research found previous methods tended to overestimate the small punch elastic-plastic load, P_y. This leads to a new technique for determining the elastic-plastic load, P_y which is described as the *small punch point of nonlinearity*.

- An analytical solution for determining yield strength, σ_{YS}, is proposed providing good results. In particular, the small punch elastic-plastic load, P_y, and corresponding small punch elastic-plastic displacement, δ_y, value are utilised. Furthermore, a new method for determining the small punch equivalent contact radius, r', is introduced.

- The small punch fracture energy, E_{SP}, is compared against the plane-strain fracture toughness, J_{1c} and K_{1c} values. It is found that in general the alloys exhibited higher energies when compared to MMCs. This corresponds with alloys that have a higher plane-strain fracture toughness when compared to MMCs.

- This research found excellent empirical relationship of the small punch equivalent fracture strain, ε_{qF}, and the plane-strain fracture toughness, J_{1c} and K_{1c} as proposed by Bayoumi and Bassim [26, 27]. In particular, MMCs are demonstrated to belong in the non-linear regime. This finding is compared against literature values to provide a global overview of this empirical relationship.

1.5 Publications arising from this research

Mak, J., Wuhrer, R., Humphries, S., Yeung, W.Y., Wei, T., Qin, J.N., Lu, W.J., and Zhang, D., 2010, 'Small Punch Test of LC4/SiCp Metal Matrix Composites', *Advanced Materials Research*, Vol. 123-125, pp. 439-442.

Zhu, C.C., Mak, J., Wing, Y.Y., Qin, J.N., Lu, W.J., and Zhang, D., 2010, 'Finite Element Analysis of Small Punch Test for Ti Matrix Composites', *机械工程材料*, Vol. 34, no. 4, pp. 87-91.

Mak, J., Wing, Yeung, W. Y., Wuhrer, R. and Zhang, D., 2010, 'Circumferential Notch Testing of Metal Matrix Composites', *Proceedings of the 7th Pacific Rim International Conference on Advanced Material and Processing*, Cairns, Queensland, Australia (Abstract).

Mak, J., Lucey, T., Wuhrer, R., Booth, N., Humphries, S., Heness, G., Yeung, W. Y., Lu, W., Ouyang, O., Qin, J. and Zhang, D., 2010, 'Research on Titanium Metal Matrix Composites at the University of Technology, Sydney', Materials Australia, Melbourne, Victoria, Australia.

Mak, J., Wuhrer, R., Heness, G., Yeung, W. Y., Callaghan, M., Wei, T., Qin, J., Lu, W. and Zhang, Di. 2008, 'Small Punch Test of Advanced In-Situ Synthesized Titanium Metal Matrix Composites', *Advanced Materials Research*, Vol. 47-50, pp. 738-741.

Mak, J., Wuhrer, R., Heness, G., Yeung, W. Y., Qin, J., Lu, W. and Zhang, Di., 2008, 'Microstructural Analysis of Ti-6Al-4V alloy and 10 Vol. % (TiB + TiC)/Ti-6Al-4V Metal Matrix Composites', *Advanced Materials Research*, Vol. 32, pp. 115-118.

Mak, J., Wuhrer, R., Zhang, D., Yeung, W. Y., and Moran, K., 2008, 'Characterization of Advance Titanium Metal Matrix Composites through Quantitative X-Ray Mapping', *Proceedings of the ACMM-20 & IUMAS-IV*, ed. Griffin, B. J., 10-15 February 2008, Perth, WA pp. 426-428.

1.6 Awards arising from this research

University of Technology, Sydney Doctoral (UTSD) Scholarship 2007 to 2010
“From the University Graduate School, University of Technology, Sydney”

Postgraduate Research Student Conference Fund 2010
“From the Faculty of Science, University of Technology, Sydney”

ACMM-20 and IUMAS-4 Student Award 2008
“From the microscopy and microanalysis society”

Frontiers of Materials Science Student Award 2008
“From the Faculty of Built Environment and Engineering, Queensland University of Technology, Brisbane, Australia”

Postgraduate Research Student Conference Fund 2008
“From the Faculty of Science, University of Technology, Sydney”

Australian Institute of Nuclear Science and Engineering (AINSE) Postgraduate Research Award 2008
“From the Australian Institute of Nuclear Science and Engineering”

Vice Chancellor’s Postgraduate Research Student Conference Fund 2007
“From the University Graduate School, University of Technology, Sydney”

CHAPTER TWO

Metal Matrix Composites

2.1 Introduction

Metal Matrix Composites (MMCs) are considered as a composite consisting of either particulate, whisker, fiber or structural reinforcements within a continuous metal matrix [21, 28]. In accordance with the *principle of combined action* the combination of these phases produce a new material with desirable properties that are distinct from either phase [29].

In general, the primary role of the metal matrix is to hold the reinforcement in place whilst the reinforcement provides stiffness and strength which is a consequence of its load sharing strengthening mechanism [28]. Furthermore, load sharing mechanisms are further supported by finite element method studies [30]. Moreover, it can be concluded that the monotonic strength and stiffness of MMCs are higher when compared to its unreinforced counterpart.

The properties of MMCs depend upon the interaction between the metal matrix and reinforcement. Furthermore, the properties of the composite are influenced by the concentration, size, shape, distribution [31] and orientation of the reinforcement. The prime motivation for the development of MMCs is the high stiffness and strength properties that can be attained.

Other notable properties of MMCs include high wear [32], creep and fatigue resistance as well as tailored thermal and electrical properties. The thermal properties of an MMC are a consequence of the ceramic reinforcements low coefficient of thermal expansion (CTE) and high melting temperature whilst the electrical properties are due to the conductive nature of the of metal matrix. Although MMCs possess many significant advantages over their alloying counterparts, challenges remain in improving the low fracture toughness, ductility and machinability of these materials.

Metals that have been utilised in the past as the metal matrix include aluminium, titanium, magnesium, copper, nickel, lead, zinc and iron whilst ceramic reinforcements include nitrides, carbides and oxides. The reinforcement phase can either be particulate, whisker, fiber or structural based as presented in Table 2-1.

Table 2-1. Classification system for reinforcements.

Reinforcement	Subscript	Aspect ratio	Sub-classification
Particulate	p	1	Equiaxed
Whisker	w	20 - 100	Discontinuous
Fiber	f	> 100	Discontinuous or continuous
Structural	s	N/A	Laminates or sandwich panels

The nomenclature system used to describe the MMCs is based on the “Nomenclature System for Aluminium Metal Matrix Composites Materials” as presented in Table 6-1and Table 6-2.

2.2 A brief history

The first significant developments of MMCs occurred during the late 1950s. The goal is to improve the structural integrity of components whilst maintaining good mechanical properties at high operational temperatures [33]. During this time progress had been made on the development of high strength boron and silicon carbide monofilament fiber reinforcements. Early development of monofilament fibres were hampered by expensive manufacturing cost and by marginal reproducibility, however, important applications were established for the aerospace industry including 243 structural support components for NASA’s Space Shuttle Orbiter [34]. Progress on MMCs continued until the 1969 recession.

Renewed interests on MMCs occurred during the late 1970s when discontinuously reinforced MMCs employing silicon carbide whiskers were developed. The expense and fracture damage to the whiskers reinforcement during the consolidation process quickly lead to the concept of particulate reinforcements in the early 1980s which proved to be less costly and less problematic to produce [34].

Further developments continued throughout the 1980s with significant advancements in the processing, design, manufacturing scale-up and certification for fiber, whisker and particulate reinforced MMCs. Applications were established for aluminium, copper, magnesium, titanium and iron MMCs for thermal management, automotive and aerospace applications. In addition, monofilament reinforced titanium MMCs were developed for high temperature aeronautical systems including performance airframes and critical rotating components for advanced gas turbine engines.

Research on MMCs peaked during the 1990s when significant investments were provided by the US Air Force. The funding produced several landmark military and commercial aerospace applications including discontinuously reinforced aluminium and titanium MMCs [33].

The current research has changed significantly since the 1990s with the introduction of a plethora of new MMCs rivalling the more traditional aluminium and titanium MMCs. These new MMCs include copper MMCs, layered composites, high conductivity composites, nano-scale composites, micro-molecular metals and bio-derived composites [21].

2.3 The current market

The market uptake for MMCs has steadily grown over the past 50 years. The world market for MMCs is projected to reach 5.9 x 10^6kg by 2013 based on a compound annular growth rate [35]. The current market for MMCs can be summarised into ground transport, thermal management, electronic, aerospace, industrial and commercial components as shown in Table 2-2, where the largest proportion of the MMC market belongs to ground transport and thermal management.

Table 2-2. The current market and applications for metal matrix composites.

Market	**Applications**
Ground transport **[25, 28, 34, 36, 37]**	Drive shafts, engine blocks cylinders, piston head, piston liners, disk brakes, cylindrical push rods, rail brake components, brake callipers, brake rotors, brake drums, pump housing, gears, brackets, piston rings, compressors, combustion bowl, connecting rod, prop-shaft, aluminium MMC snow tire studs and titanium MMC automotive intake and exhaust valves.
Thermal management **[34, 38]**	Electronic packaging, space components, solar battery array and computer disk drives.
Aerospace **[25, 39-41]**	Hollow long screws, crossbeams, nuts, connectors, fan exit guide vanes, turbine engines, high-mach airframes, ventral fins, access panels, struts, tie rods, fittings, structural airframes, motor shell, wing slate tracks, bulk heads, doors, landing gear, propeller skids, propeller runners, wheels, bolts, compressor blades, turbine blades and speed brakes.
Industrial **[34]**	Conductor cables, superconducting magnets, cutting tools, drills, spent nuclear fuel containment and robotics.
Sport **[34]**	Climbing gear, hang gliding frame, mountain bike frames and golf club heads.

2.4 Applications

2.4.1 *Ground transport*

Ground transport (automotive and rail) accounts for almost 55% of the total MMC world market volume (4.4 million kilograms) in 2008 [35, 42]. Particulate reinforced aluminium MMCs are the most prevalent form of MMC employed in the ground transport industry. These aluminium MMCs are incorporated in the ground transport industry in order to displace traditional cast iron and steel components. The selection process for aluminium MMCs depends whether the weight savings can justify the economic cost and not simply on weight reduction. Metal matrix composites are now well established in the transport industry.

Many applications have been developed for the ground transport industry. Squeeze cast piston heads were developed by Toyota Motor Corporation in 1983 [33, 34]. Up to 100,000 high quality components per month can be manufactured inexpensively from the squeeze cast process. Aluminium MMC piston heads are developed with improved wear resistance for longer operating life. In addition, the piston heads exhibited lower thermal conductivity properties allowing for more combustion energy to undergo work. Furthermore, the piston head exhibited lower coefficient of thermal expansion (CTE) leading to increased pressure capability. The trend continues with Mazda Ford Motor Company implementing a low pressure die casting for selectively reinforced pistons in 1998.

Since 1990 the Honda Motor Company developed squeeze cast piston cylinder liners for their Honda engines. The novel manufacturing process involved simultaneous casting of both the engine block and the cylinder liner via preform infiltration process. The cylinder liners exhibited increased wear resistance which allowed for reduced cylinder wall liner thickness leading to increased engine displacement. The result is an engine that can produce more horse power than conventional engines with similar size and weight. Furthermore, the thermal conductivity for MMCs are higher compared to cast iron liners, this allows the engine to work at higher operational temperatures thereby increasing the engine's life.

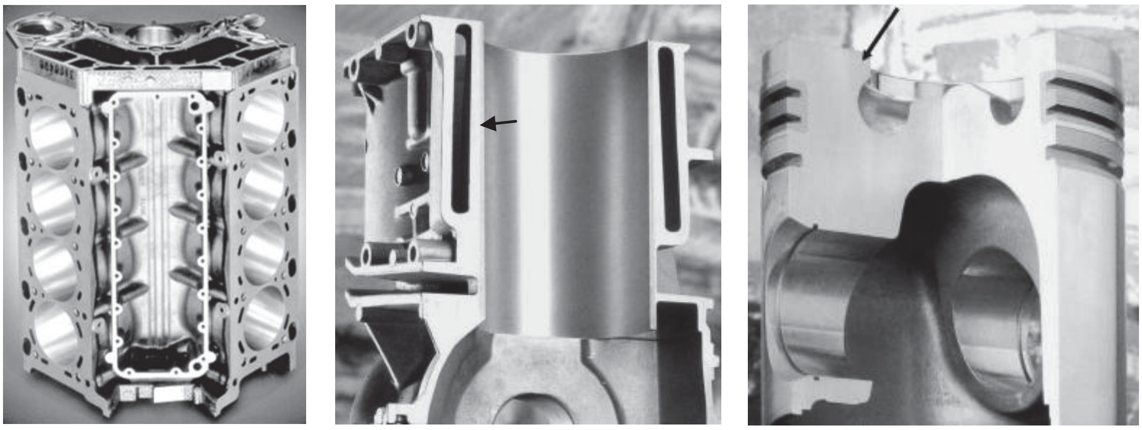

(a) (b) (c)

Figure 2–1. Metal matrix composites for the transport industry (a) engine block (b) piston lining and (c) piston head [34].

The aluminium MMC driveshaft is first developed by General Motor Company in 1996. The application of MMCs driveshaft led to greater specific stiffness and rotational stability of the component. In addition, major weight savings were accomplished. Longer driveshaft for a given diameter can then be developed. In addition, driveshafts can be implemented for larger vehicles such as trucks and buses. The Ford Motor Company implemented the aluminium MMC driveshaft for its Ford Crown Victoria Police Interceptor (1999 to 2005) allowing for safer operating speeds at over 241km/h [33].

2.4.2 *Thermal management*

Thermal management is the second largest market share accounting for almost 34% of the total MMC world market volume in 2008 [35]. Metal matrix composites are employed to manage the electronic components heat dissipation thereby improving reliability of the component and to prevent failure [38]. Applications include power semiconductor devices, substrates for computers processor chips, heat sinks and packaging for microwave devices used in telecommunication [34]. A range of materials exhibiting good coefficient of expansion (CTE) is plotted against the specific thermal conductivity (λ/ρ) as presented in Figure 2–2. The specific thermal conductivity is obtained by dividing the thermal conductivity, λ, with the density, ρ, of the material.

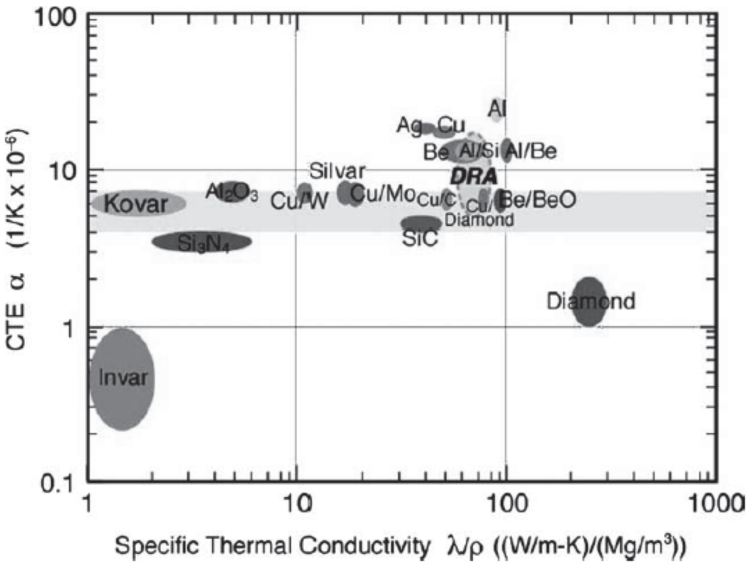

Figure 2–2. Materials for thermal management. Optimum materials for electronic packaging and thermal management are located within the shaded band [34].

Thermal management materials that possess high specific thermal conductivity are preferred. In addition, a CTE between 4 to 7 x 10^{-6}/K similar to semiconductor and ceramic based materials are necessary to minimise thermal stress.

Materials that have been used in the past include Kovar, Cu/Mo MMCs, Cu/W MMCs, Cu/diamond MMCs, Be/BeO MMCs and Al MMCs [25, 28, 33]. At present the predominant material for thermal management are 55 to 70 vol. % SiC particulate reinforced aluminium MMCs. Be/BeO possess slightly higher specific thermal conductivity than aluminium MMCs, however, the toxicity of beryllium and cost prevents further use. Aluminium MMCs reinforced with SiC particulates are the material of choice as it exhibits excellent thermal conductive properties whilst providing acceptable CTE values at minimal cost.

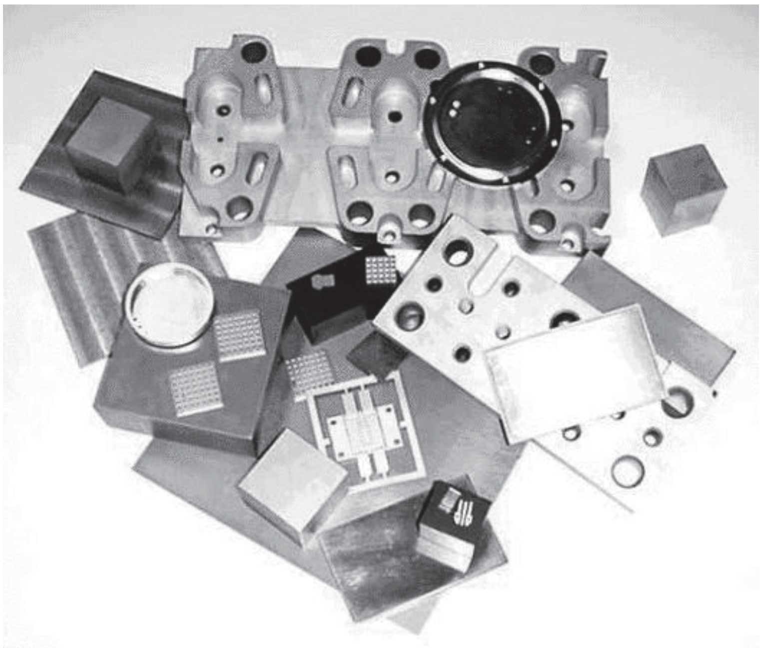

Figure 2–3. Metal matrix composites for thermal management and electronic packaging, MMCC Inc. [40].

2.4.3 *Aerospace*

Metal matrix composites were developed for the aerospace industry to meet the demands for high performance high temperature military (fighter aircraft and missile guidance systems) and aerospace (satellite and space vehicles) programs. The aerospace space industry is the third largest market accounting for only 1% of the total MMC world market volume in 2008.

Several successful aluminium MMC applications emerged from the US Defence Advance Tactical Fighter Program during the 1990s. The F-16 fighter aircraft employs ventral fins as stabilisers during high angle ascent and high speed manoeuvres as presented in Figure 2–4 (a). The original design of the ventral fins utilising an unreinforced honey comb aluminium alloy experienced instability issues and a high incidence of failure. This led to the parts replacement with aluminium MMCs. The aluminium MMCs higher specific strength and stiffness greatly improved stability leading to a four-fold increase in the life of the ventral fins and cost savings over the life of the part. The success of aluminium MMCs performance led to further implementation into the F-16 design to solve a cracking problem in the fuselage corners of the fuel access doors presented in Figure 2–4 (b). The Atlantic Research Corporation developed titanium MMC nozzle actuator piston rods for two the Pratt & Whitney F119 engines for the F-22 Raptor. Discontinuously reinforced titanium MMCs were chosen for its low weight, high axial loads and stiffness. In addition, the titanium MMC are required to withstand cyclic fatigue loading at temperatures up to 450°C. Metal matrix composites have been implemented in Eurocopter EC120 helicopter, the Lockheed Martin U2 aircraft, the Lockheed Martin Gunship AC-130, Bell Boeing V-22 Osprey and the Boeing F/A-18E/F Super Hornet.

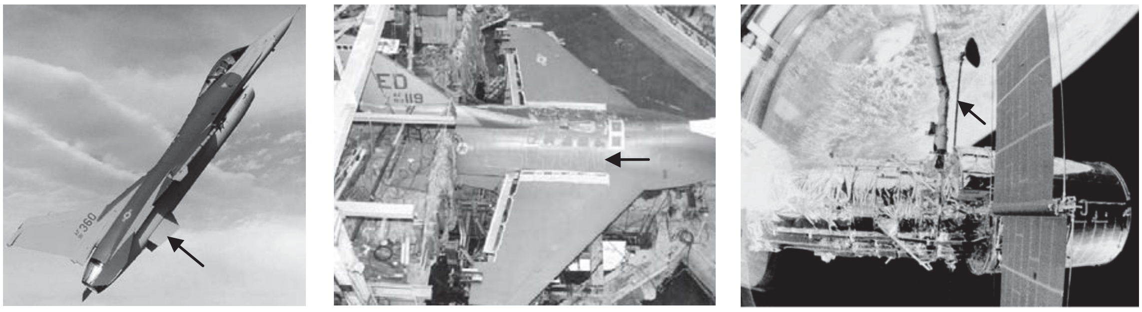

(a) (b) (c)

Figure 2–4. Metal matrix composites for the aerospace (a) F-16 fighter aircraft ventral fins (b) F-16 fighter fuselage doors and (c) Hubble space telescope high gain antennae wave guide boom [28, 34].

Metal matrix composites are becoming more prominent in the space industry with the development of several applications including 243 $6061/B/50_f$ monofilaments tubes for the space shuttle orbiter and $6061/C/40_f$ antennae wave-guide boom for the Hubble Space Telescope as presented in Figure 2–4 (c).

2.5 Processing routes

The processing routes for MMCs are well established and are summarized in Table 2-3. The choice for the processing route depends upon the desired metal matrix and reinforcement content. For example, the in-situ processing route deals with controlled unidirectional solidification of ceramic particulates in a eutectic alloy via stoichiometric reactions. The more traditional solid state and liquid state routes are preferred for continuous and discontinuous reinforced MMCs. There are numerous processing routes for MMCs and only the ones associated with this research are mentioned. These are the stir-cast and non-consumable vacuum arc remelting (VAR) techniques for processing aluminium and titanium MMCs, respectively.

Table 2-3. Processing routes for metal matrix composites.

Processing route	**Techniques**
Solid state processing	Powder metallurgy, explosive shock consolidation, diffusion bonding, roll bonding, forging and extrusion.
Liquid state processing **[22, 43]**	Liquid infiltration, squeeze-casting, stir-cast, spray co-deposition, reactive in-situ and non-reactive in-situ.
Gaseous state processing	Physical vapour deposition.

2.5.1 *Stir-cast process*

The stir-cast route involves mechanically mixing ceramic reinforcement with molten metal as presented in Figure 2–5. In addition, the reinforcements are made to be evenly distributed in suspension. Important variables associated with the stir-cast technique include temperature control, mixing speed, solidification rate, mixing and casting time. Common problems include flocculation or segregation of the reinforcement caused by reinforcement floating or sinking, wetting problems, porosity and chemical reactions between the matrix and reinforcement. After mixing, the suspended slurry are cast as either an extrusion billet, foundry ingot or rolling blank. Stir-cast products with volume fractions ranging from 10% to 40% can be achieved from this process. This process is widely used for applications that require high production volumes and low cost. In addition, the stir-cast technique is used extensively in the production of aluminium

MMCs [34]. For this research, the 7A04 aluminium alloy and 7A04/SiC_p MMCs are produced via stir-cast processing route.

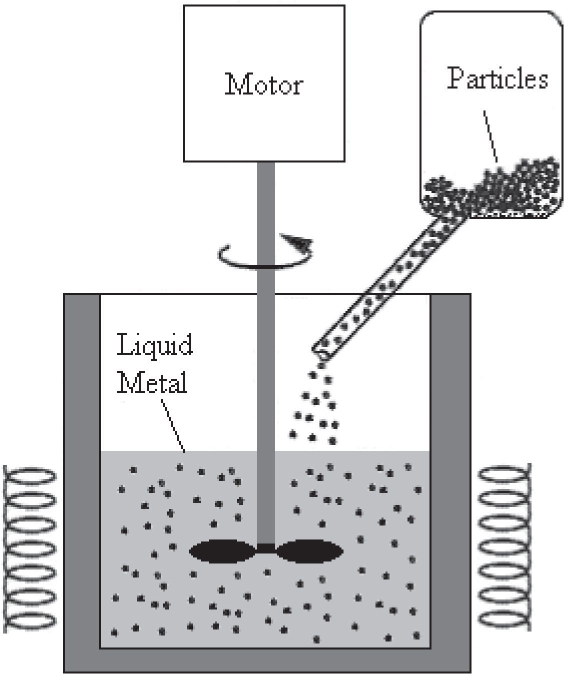

Figure 2–5. The stir-cast processing route for metal matrix composites [28].

2.5.2 *Vacuum arc remelting process*

The non-consumable vacuum arc remelting (VAR) furnace is often employed for processing MMCs especially for titanium which are reactive to oxygen at high temperatures [44-49]. Non-consumable VAR operates via a combination of traditional ingot metallurgy and self-propagation high-temperature synthesis (SHS) techniques to form the reinforcement via reactive in-situ process. Advantages associated with this process include low cost, high energy efficiency, easy operation, high purity of the reaction, clean thermodynamically stable matrix, reinforcement interface and fine sized reinforcements. A schematic diagram of the VAR furnace is presented below in Figure 2–6 (a).

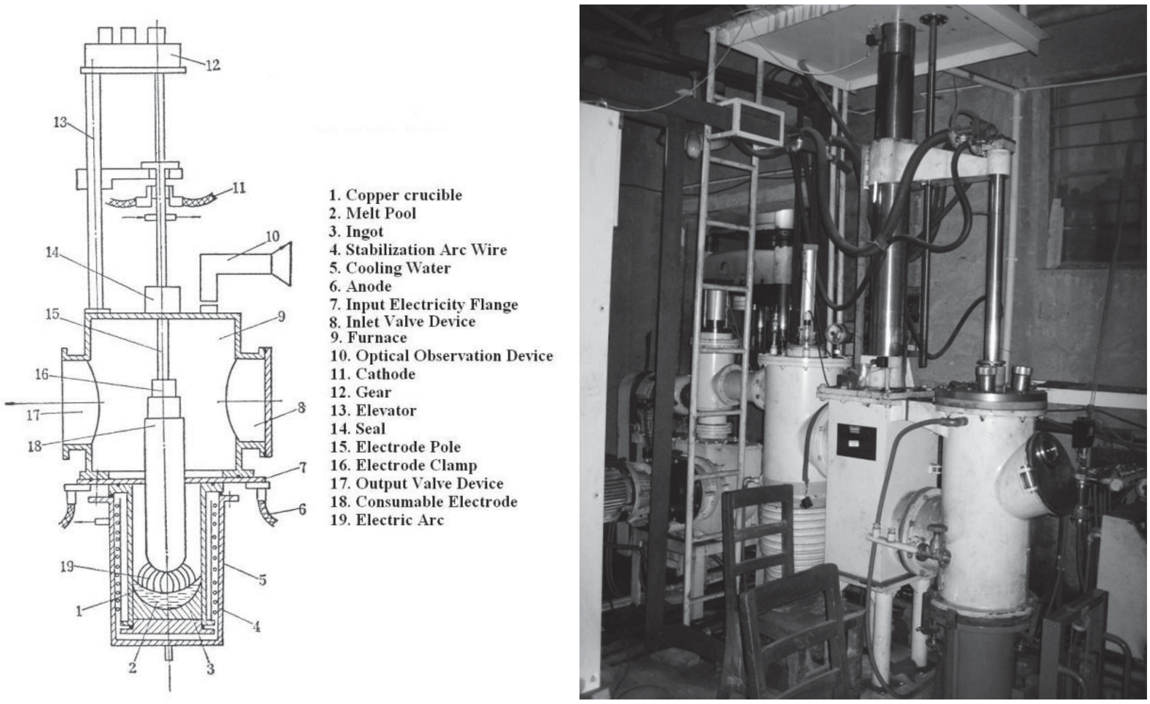

(a) (b)

Figure 2–6. Non-consumable vacuum arc remelting furnace (a) diagram and (b) furnace employed at the State Key Laboratory of Metal Matrix Composites.

A non-consumable VAR furnace as presented in Figure 2–6 (b) is employed for processing TiB_w and TiC_p reinforced Ti-6Al-4V MMCs. The process involved an initial blending of titanium sponge with alloying elements (Al, V), graphite powder and reactants (B_4C). The materials are then welded onto an electrode pole and inserted into the VAR furnace. A high voltage electric potential is applied to create an arc between the electrode and the copper crucible. The MMCs are then cast into ingots and the reinforcements TiB_w and TiC_p are then synthesized in-situ.

2.6 Concluding remarks

Metal matrix composites are now well established in the world market place which is expected to grow well into the future to meet the demands for high performance applications, however, improvements in processing routes and material choice are still required to improve the ductility and fracture toughness of these materials.

CHAPTER THREE

Mechanical Behaviour

3.1 Introduction

The mechanical behaviour of MMCs is dependent on the interaction of the metal matrix and the reinforcement phase. This chapter provides an overview of the tensile behaviour and fracture toughness of MMCs including the mechanisms that influence the strength and fracture behaviour for these materials.

3.2 Strength

There are many strengthening mechanisms that can influence the flow stress of an MMC. In terms of the metal matrix it is generally understood that the strength of a metal depends upon its resistance to dislocation initiation and dislocation movement under an applied external load [23]. Strengthening mechanisms can include grain-size-reduction, solid-solution alloying, strain hardening, precipitation hardening (age hardening) and dispersion strengthening and grain boundary strengthening mechanisms. Conversely, the ceramic reinforcement acts as a barrier to dislocation movement. This can lead to dislocation pile-up at the matrix/reinforcement interface, thereby increasing the strength of MMCs [50].

Other proposed strengthening mechanisms involved the ability of the MMC to transmit loads from the metal matrix to the high strength ceramic reinforcements. In this way the ceramic reinforcements bear the majority of externally applied loads [51].

Another factor that has an effect on the strength of MMCs is known as differential thermal contraction. Differential thermal contraction arises from large differences in the coefficient of thermal expansion (CTE) between the metal matrix and reinforcement phase [52, 53]. From a heat treatment process the metal matrix expands more than the reinforcement which leads to strains around the metal matrix and reinforcements interface. When the MMC cools, the metal matrix contracts more than the reinforcement phase. This mismatch in strains is sufficient to generate slip dislocations around the metal matrix and reinforcement interface [23].

Further factors that can affect the strength of an MMC are reinforcement geometry [54], orientation [55], size [56], shape [57], interparticle spacing [31] and distribution [31, 58]. For instance the tensile strengths have been shown to increase with decreasing particle size at constant volume fraction, this is attributed to a lowering of the probability of surface flaws on the reinforcement's surface [59]. It is important to note that reinforcements that have failed possess no load bearing capacity. Furthermore, any cracked regions are prone to void growth that can lead to premature failure of the MMCs.

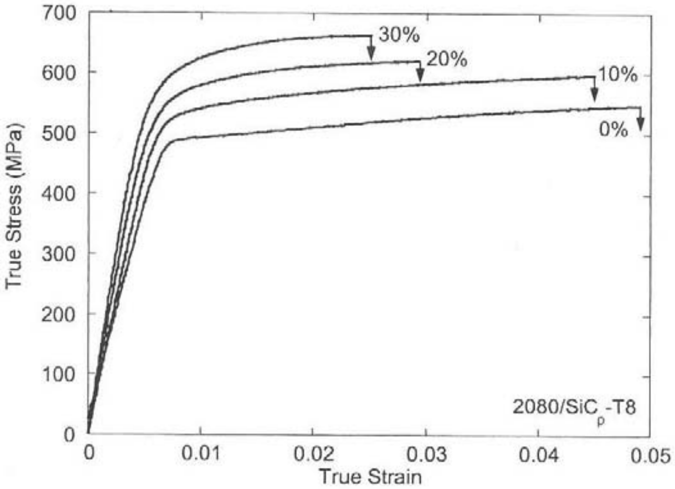

Figure 3–1. Tensile behaviour for Al-Cu-Mg 2080/SiC$_p$-T8 metal matrix composites with increasing reinforcement content [28, 50].

As observed in Figure 3–1 the overall flow stress of the Al-Cu-Mg 2080/SiC$_p$-T8 MMCs is increased with increasing additions of ceramic reinforcements. The elastic modulus is increased with increasing reinforcement and is due to the stiffness of the reinforcement phase. In addition, it is observed that the yield strength, ultimate tensile strength and fracture stress are improved with increasing reinforcements [55], however, a consequence of increasing the reinforcement content leads to lower ductility [21]. For instance it is observed in Figure 3–1 that the addition of 30 vol.% SiC$_p$ reinforcements leads to a halving of the MMC's ductility compared to its base alloy. This mechanical behaviour is supported by Kobayashi and Iwanari's research on 6061/SiC$_p$-T6 MMCs with increasing SiC$_p$ reinforcements. They found that with increasing reinforcement leads to increasing strength and a decrease in the ductility of the material [60].

3.3 Fracture toughness

The plane-strain fracture toughness, K_{1c} and J_{1c}, is a measure of a material's resistance to crack extension [61]. In terms of MMCs it is generally understood that the fracture toughness of particulate reinforced MMCs are lower compared to its their unreinforced counterparts [20, 28]. This is due to several factors including reinforcement content, interparticle spacing, particle strength, particle distribution [62], metal matrix microstructure and matrix/reinforcement interface. Chawla demonstrated that the plane-strain fracture toughness will decrease as the reinforcement content for the ceramic particulate reinforcement increase [28] for many types of aluminium MMCs as presented in Figure 3–2.

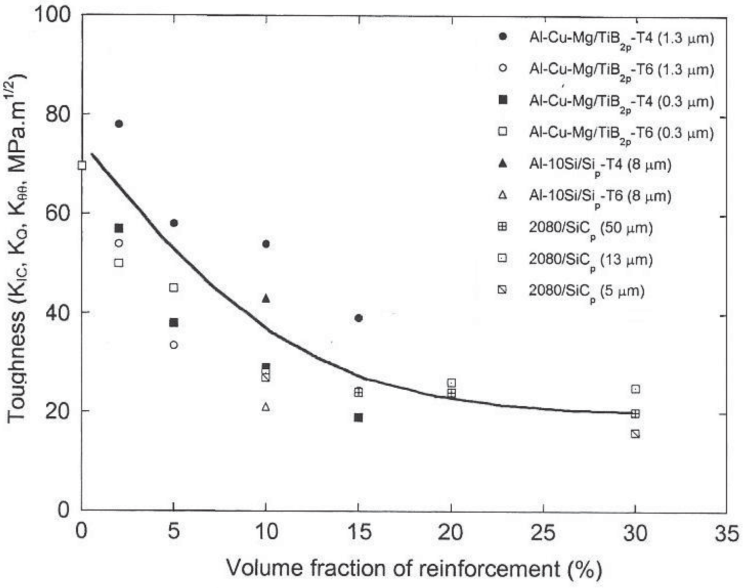

Figure 3–2. The fracture toughness for several particulate reinforced metal matrix composite with increasing reinforcement content [28, 63].

This can be explained by an increase in local stress triaxiality with increasing reinforcement content. According to Chawla the fracture toughness decreases with increasing reinforcements and levels off at around 20 vol.% reinforcement content [28]. Similar results are reported by Davidson who suggested the fracture toughness for MMCs are much lower compared to the unreinforced alloys due to the lower strains sustained at the crack tip for notched standard fracture toughness specimens. In addition, the MMCs fracture toughness is thought to be almost completely influenced by the work done within the plastic zone by the growing crack [64].

The effect of particle size is less clear than the effect of volume fraction. Flom and Arsenault conducted fracture toughness tests on MMCs with particle sizes which ranged from 2.4µm up to 250µm. They found that particle size showed limited effect on fracture toughness up to 20µm, after which the fracture toughness begins to decrease, [56]. These finding are further corroborated by Song et al. whom showed that particle size from 10µm to 50µm does lead to a decrease in the fracture toughness for MMCs, however, the effect is limited [65]. Zhao and Floyed conducted similar work with particles sizes ranging from 0.5µm to 2.5µm. They found that increasing particle sizes did lead to increased fracture toughness for very small sized particles [66].

3.4 Failure and fracture mechanism

The study of fracture mechanisms is important as it examines how a material can fail under an applied load or stress. This behaviour is further investigated by Arsenault et al. whom provided a comprehensive review of the deformation and fracture mechanisms of MMCs [53]. An understanding of the fracture mechanisms of MMCs is needed since the fracture toughness of MMCs is always less than their alloying counterparts in the same heat treated condition. Thus improvements in the design of these engineering materials will lead to improved fracture toughness values.

Ductile fracture in metals can be characterised into three stages known as microvoid initiation, nucleation and coalescence. Microvoids initiation sites arise from inclusions or second phase particles within the metal matrix. The fracture can occur either by interfacial decohesion or by particle cracking. Upon initiation the microvoid nucleates to a critical size followed by strain localisation between the microvoids. The microvoids experience necking followed by coalescence leading to the ultimate failure of the material. The ductile fracture mechanism plays an important role in the fracture toughness of metals. If the microvoids are large and deep and cover a large fraction of the fracture surface, then work required for nucleation is large and so is the fracture toughness, however, if microvoids only cover a small proportion of the fracture surface and/or if the microvoids are small then the contribution to fracture toughness is small. It is important to note that although MMCs may appear to fail in a brittle manner the underlying micro-mechanisms involves ductile failure of the metal matrix phase.

Brittle fracture mechanisms for metals are usually associated with cleavage fracture which is defined as rapid crack propagation along a crystallographic plane. Although cleavage fracture is associated with brittle fracture, the fracture can be preceded by large plastic strains. The preferred cleavage planes are those with the lowest packing density. For example cleavage is more likely to occur across a body centred cubic (BCC) than a face centred cubic (FCC) crystal structure which has more slip systems for dislocation movement. In general, cleavage is likely to occur when dislocation movement and plastic flow are restricted such as with an inclusion or second phase particles within the metal matrix. Often cleavage fracture is identified as the so called *River Pattern* since the cleavage planes converge to a point similar to the way an *Alluvial Fan* converges towards the main stream.

Another brittle fracture mechanism is intergranular crack propagation along the grain boundaries. There are a number of causes for intergranular fracture which include; precipitation along the grain boundary [67], hydrogen embrittlement, liquid metal embrittlement, environmental assisted cracking, intergranular corrosion, grain boundary cavitations and cracking at high temperatures.

For MMCs, examination of fracture surfaces showed a generally ductile topography with ruptured matrix ligaments. These ligaments are of two sizes: larger when nucleated by fracture reinforcement particles; or small when nucleated within the matrix. Therefore, despite reasonably brittle macro behaviour the fracture mechanism on a microscopic scale is one of void nucleation and coalescence that is ductile.

Fracture toughness is related to the work done within the material per unit area of new surface created. The magnitude of this work is determined by energy dissipating mechanisms that operate as the crack grows. These mechanisms that resist crack growth have been identified and are listed here in approximate order of its magnitude for relatively brittle materials in descending order [68]:

1. Deformation within the plastic zone.
2. Formation of voids along the fracture surface.
3. Fracture of the reinforcement along the crack path.
4. Interfacial failure between matrix and particle.
5. Fracture of the reinforcement in the plastic zone.
6. Matrix cracks near, but not contiguous with, the main crack.
7. Tortuosity of the fracture path increasing the surface area.

As might be expected energy absorption by the reinforcement as the crack grows is small. Any energy absorbed will be elastic and will be recovered when the crack passes. Thus most of the energy will be absorbed in the plastic zone of the matrix. For ductile metals void formation along the fracture surface is by far the most important energy absorbing mechanisms. In particulate reinforced MMCs the coverage and size of the dimples on the fracture surface varies wildly, from nearly zero for some [69] to a large fraction for others [70]. This is generally thought to be due to matrix composition and processing.

The addition of stiff particles result in a number of changes to material behaviour. Firstly the particles will inhibit dislocation movement as well as limit cross-slip and the operation of secondary dislocation sources. These effects would be likely to limit plastic zone size and therefore have a major influence on fracture toughness. The particles can also be expected to limit strain at the crack tip by decreasing the strain to failure and thereby altering the strain distribution in the plastic zone.

The effect of particles on yield stress is diverse. In general, there is the anticipated increase whilst for others a decrease without satisfactory explanation. The effect of yield stress comes about by the presence of the particles, residual stress of the matrix due to thermal mismatch between the matrix and particulate reinforcement, alterations of the recrystallisation of the matrix and alteration of the precipitation kinetics and precipitate distribution.

Particle debonding may influence the fracture toughness with particle size and particle matrix bond strength governing by how much [69-72]. A number of fracture mechanisms have been observed on a wide range of MMCs for example microvoid nucleation, growth and coalescence for SiC particulate reinforced aluminium 2009 MMC [69-73].

The ceramic particulate reinforcement is usually of a single monolithic crystalline structure with a mixture of covalent and ionic bonding. Ceramics do not possess close-packed structures therefore the dislocation movement is restricted. Thus the ceramic reinforcements often fail in a brittle manner.

The particulate reinforcement may fail if the strength of the interface is greater than the particle strength, then the particle will fracture via shear in concert with void formation in the metal matrix. On the other hand, if the particle strength is greater than the interfacial strength then there will be interfacial decohesion. After fracturing the particles carry no further loads and the fracture toughness is lowered in the presence of cracked particles which if stressed can lead to either the onset of crack propagation or microvoid nucleation.

Microconstraint around the particulate reinforcement affects the fracture toughness of MMCs by inhibiting plastic flow around the particle [74]. Microconstraint is influenced by particle shape and its relative location to adjacent particles. Microconstraint induces large tensile hydrostatic stresses in the matrix which increases the overall strength of the MMC, however, this leads to premature damage in the form of particle fracture, particle matrix decohesion and matrix microvoid growth [75]. Davidson and Heness showed that matrix deformation in the aluminium oxide reinforced 6061 T6 heat treated MMC was controlled by the strength of the matrix, shape of the reinforcement and the proximity of the crack tip. Constraint levels are measured and found to be higher when the particles are irregular in shape and lower when spherical. They also found larger fractions of particles provided more constraint in the matrix. Heness et al. also found that the yield strength affected the level of constraint as did particle shape and particle cracking [57].

Similarly particle clustering of the reinforcing particles can cause a significant decrease in the ductility and fracture toughness of the composite materials since the plastic flow is constrained around the cluster of particles. Moreover, particle clustering is thought to provide damage initiation sites. It is also observed that a crack will propagate towards a cluster of closely spaced particles. Furthermore, large average inclusion spacing between microvoid nucleating particles leads to increased fracture toughness whilst increasing volume fracture leads to decrease in fracture toughness.

Mortensen conducted an extensive review on the fracture toughness testing of MMCs [20]. He found that most plane-strain fracture toughness testing did not conform strictly to standard tests. The reason is due to the difficulty in fatigue cracking of the MMC specimens. Further development for alternative fracture toughness tests such as chevron-notch short rod or short bar test are introduced. The test can be conducted without the implementation of a fatigue crack. Furthermore, the specimen size is much smaller than standard tests, however, the test is still limited by size constraints. For this reason smaller test specimens are developed such as the small punch test that is applied in the plane-stress condition.

3.5 Concluding remarks

The mechanical behaviour for MMCs is governed by the reinforcement content. In general, it is observed that increase reinforcement content will lead to increased strength, however, the fracture toughness will be lowered. The fracture mechanisms for MMCs are diverse and complex exhibiting both brittle and ductile failure mechanisms. Moreover, MMCs exhibit ductile failure at the micro level, however, the overall behaviour observed at the macro level is predominantly brittle.

CHAPTER FOUR

FRACTURE TOUGHNESS TESTS

4.1 Introduction

The plane-strain fracture toughness, K_{1c}, is an important mechanical property and is a measure of a material's resistance to crack propagation in the presence of a flaw such as cracks, inclusion or voids and accounts for flaw size, component geometry and loading conditions. The approach is based on linear elastic fracture mechanics (LEFM) whereby it is assumed that the plasticity at the crack-tip is infinitely small so that yielding can be considered to be negligible. Often engineers apply the method in the design of in-service components to improve the safety and survivability of the component. The Irwin model in mode I as presented in Equation 4-1 is often applied when assessing the plane-strain fracture toughness of a material [76].

$$K_{1c} = Y\sigma\sqrt{\pi a_c} \qquad 4\text{-}1$$

Where K_{1c} is the plane-strain fracture toughness, Y is the dimensionless geometry factor, σ is the applied stress and a_c is the critical crack length [76].

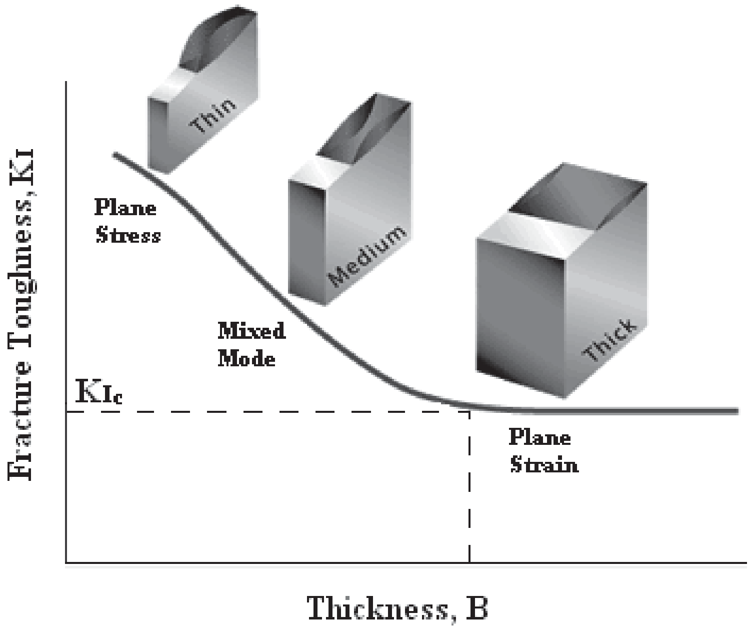

Figure 4–1. The effect of specimen thickness on fracture toughness [76].

The material size is an important factor to consider before conducting fracture toughness testing since different material thickness can lead to different stress-intensity values. If the thickness is too thin then the specimen will fracture in plane-stress, however, if a material thickness is thick enough then the material will fracture in plane-strain. In other words a critical thickness must be reached for plane-strain fracture toughness conditions [61].

Years of research on fracture toughness have culminated in standard and non-standard fracture toughness test methods [77-80]. Common fracture toughness mechanical properties include the plane-strain fracture toughness, K_{1c} and J_{1c}, J-Integral, and crack tip open displacement (CTOD) for engineering applications.

In this project the size of the as-received materials are limited by production capabilities. As a result fracture toughness testing methods that required small test volumes are sought. The following discussion comes from standard tests methods that require larger volumes of materials than is available through various methods leading to circumferential notch tension, CNT, test specimens.

In order to choose an appropriate fracture toughness test method, for this limited amount of material, a good understanding of standard test methods is developed so as to determine which of the non-standard tests would provide equivalent or close to equivalent plane-strain fracture toughness, K_{1c} and J_{1c}, values.

4.2 Standard fracture toughness test

Standard fracture toughness tests include the single-edged bend [SE(B)] [77], compact tension [C(T)] [77] and chevron-notched short rod or bar [78] tests. Researchers often refer to the American Society for Testing and Materials (ASTM) E 1820 – 09 [61, 77] publication of the “Standard Test Method for Measurement of Fracture Toughness” as a primary source and definitive guide to fracture toughness tests. Alternative international organisations that publish similar standards include the British Standard Institution (BSI) [81] and the International Organisation for Standardization (ISO) [82].

The tests can be used to determine the plane strain fracture toughness, K_{1c} and J_{1c}, J-Integral, crack tip open displacement (CTOD) and R-curve calculations. In this chapter only the plane-strain fracture toughness K_{1c} and linear fracture mechanics will be considered in addition to validity requirements.

4.2.1 *Single-edge bend test*

The well known single-edge bend [SE(B)] test [77] covers the determination of the plane-strain fracture toughness, K_{1c}. The SE(B) contains a notch that is sharpened with a fatigue crack for crack extension in accordance with ASTM E 1820 – 09 [77] standard. The SE(B) test is loaded in a three-point-bend. The ASTM configuration for the single-edge bend [SE(B)] test specimen is presented in Figure 4–2.

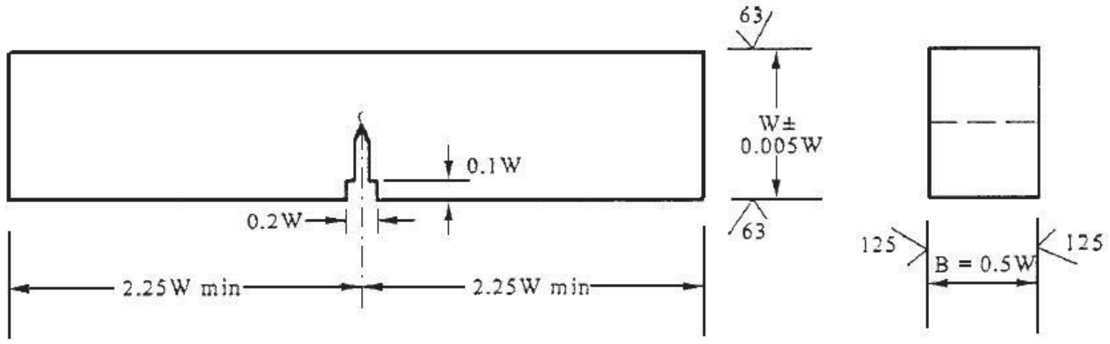

Figure 4–2. American Society for Testing and Materials single-edge bend test specimen [77].

The most important aspect about the SE(B) test is the notch configuration. The SE(B) incorporates either a straight-through, drilled hole or narrow notch configuration that is sharpened by a fatigue precrack. A fatigue precrack is produced through a three point cyclic load bending of the notched specimen to a range of 10^4 to 10^6 cycles. The process requires judicious selection of the lowest loads to induce a fatigue precrack. In addition, the loads can not exceed the maximum load, P_m. The fatigue crack size is required to be in the range of 0.45 to 0.55W for K_{1c} determination.

The fracture toughness test procedure involves loading the precracked SE(B) test specimen in three point bending. In this way the force and load-line displacement is recorded. The displacement is measured using a double cantilever clip gage that is mounted over sharp knife edges.

The fracture toughness is calculated from the plane-strain fracture toughness K_Q. If K_Q meets validity requirements set by the standard then K_Q becomes the plane-strain fracture toughness, K_{1c}.

$$K_Q = \left[\frac{P_i S}{(BB_N)^{\frac{1}{2}} W^{\frac{3}{2}}}\right] f\left(\frac{a_i}{W}\right) \qquad 4\text{-}2$$

Where P_i is the load, B is the thickness, B_N is the net thickness, W is the widths and a_i is the physical crack size.

After mechanical testing the stress-intensity factor qualifier, K_Q, is determined. The specimen is further subjected to validation requirements to determine whether K_Q meets standard fracture toughness test conditions for plane-strain fracture toughness, K_{1c}. The three main conditions are thickness, crack size measurements and maximum load limits which are described below.

The actual thickness of the specimen must be greater or equal to the thickness calculated from K_Q in order to qualify as K_{1c}. The thickness validity requirement ensures that the size of the specimen is sufficient to meet plane-strain conditions.

$$B \geq 2.5\left(\frac{K_Q}{\sigma_{YS}}\right)^2 \qquad 4\text{-}3$$

Where B is the specimen thickness, K_Q is the qualifying stress-intensity factor and σ_{YS} is the yield stress.

None of the nine measured original crack size and final physical crack size, a_p, shall differ more than five percent of the specimen thickness, B, from the averaged physical crack size. This is to ensure that the specimen fracture surface is not a mixed mode fracture surface.

The ratio of the P_{max} and P_Q must be equal or less than 1.10 in order for K_Q to be qualified as plane-strain fracture toughness, K_{1c}.

$$\frac{P_{max}}{P_Q} \leq 1.10 \qquad 4\text{-}4$$

Where, P_{max} is the maximum load and P_Q is a qualifying load which are determined from the fracture toughness load-displacement curve.

4.2.2 *Compact tension test*

The compact tension [C(T)] test covers the determination of the plane-strain fracture toughness, K_{1c}, and is an ASTM E 1820 – 09 standard test [77]. Similar to SE(B) the C(T) fracture toughness specimen incorporates a straight-through notch that is sharpened by a fatigue crack. In addition, the final K_Q validation requirements are the same as the SE(B) test. The main difference between the C(T) compared to the SE(B) test is that the loading of the specimen is in tension. According to the ASTM E 1820 – 09 the test is limited to testing materials that exhibit K_{1c} and linear elastic behaviour. Furthermore, the C(T) is a widely utilised fracture toughness test due to its relative size compared to SE(B). The ASTM compact tension C(T) test specimen is presented in Figure 4–3.

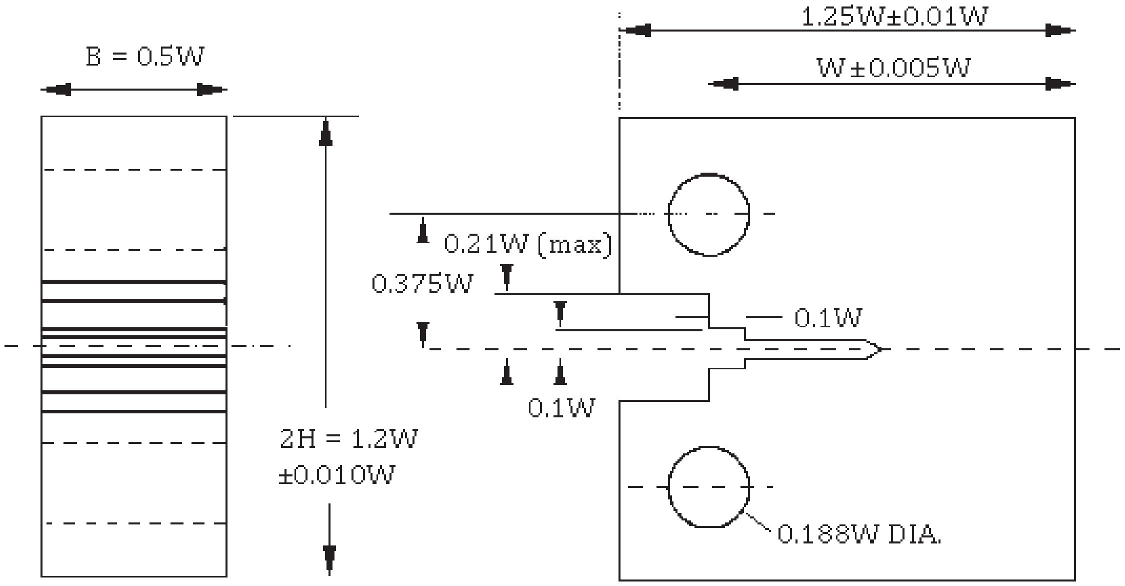

Figure 4–3. American Society for Testing and Materials compact tension test specimen [77].

The fracture toughness is calculated from the plane-strain fracture toughness K_Q. If the $K_{(i)}$ meets the validity requirements then K_Q becomes the plane-strain fracture toughness K_{1c}. Note, the validity requirements for C(T) are the same for SE(B) test.

$$K_Q = \left[\frac{P_i}{(BB_N W)^{\frac{1}{2}}}\right] f\left(\frac{a_i}{W}\right) \qquad 4\text{-}5$$

Where P_i is the load, B is the thickness, B_N is the net thickness, W is the widths and a_i is the physical crack size. The unit for the plane-strain fracture toughness, K_{1c} is $\text{MPa}\sqrt{\text{m}}$.

4.2.3 *Chevron-notched short rod or bar tests*

One of the first systematic attempts to reduce fracture toughness specimen size is the development of the chevron-notched short rod or bar. The development history of the chevron-notched (CN) short rod or short bar fracture toughness test in terms of metallic testing is mainly attributed to Barker [80]. The CN fracture toughness test was approved in 1989 as an ASTM standard and was recently re-approved in 2008. The published standard is ASTM E1304 – 97 for “Plane-Strain Chevron-Notched (CN) fracture toughness test of Metallic Materials” [78].

The CN short rod or bar test cover the determination of the plane-strain fracture toughness K_{1v}, K_{1vj} and K_{1vM} and characterise the material resistance to fracture by a slowly moving steady-state crack that is initiated at the chevron-notch tip. This distinguishes the CN test from the more conventional SE(B) and C(T) tests that utilise a sharp fatigue precrack notch configuration for crack extension. Furthermore, due to this difference the plane-strain fracture toughness values K_{1v} and K_{1c} are not interchangeable even though both values are based on Linear Elastic Fracture Mechanics (LEFM). The CN fracture toughness test is presented in Figure 4–4.

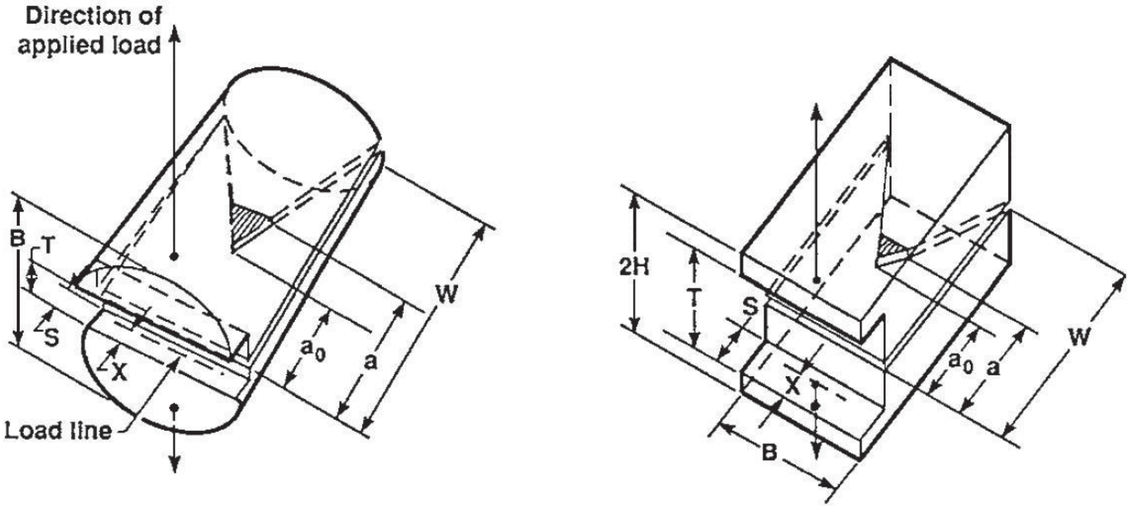

a)

b)

Figure 4–4. American Society for Testing and Materials chevron-notched (a) short rod and (b) short bar specimens [78].

The CN test is regarded as a useful alternative in circumstances when a fatigue precrack is difficult to produce such as with MMCs that are highly resistant to fatigue crack initiation. Further attributes include relatively small dimensional size, ease in machining and testing. It is for these reasons that many researchers have opted for the CN fracture toughness test as an approach for plane-strain fracture toughness testing. Researchers have noted good correlation between K_{1c} and K_{1v} for many materials exhibiting linear elastic behaviour [83], however, what remains as a concern is the stress field ahead of the crack tip may enlarge the plasticity thereby increasing that the overall stress intensity factor, K_{1v} compared K_{1c}.

Unloading-reloading cycles are performed for the determination of crack location, residual stress and the force used to calculate the plane strain fracture toughness value K_{1v} and K_{1vj}. The plane-strain fracture toughness K_{1v} and K_{1vj} are often utilised since all validity requirements are satisfied by the ASTM E1304 – 97 whilst the plane-strain fracture toughness K_{1m} lacks unloading and reloading validity checks for plasticity or excess residual stress. The plane-strain fracture toughness K_{1v}, K_{1vj} and K_{1m} are presented in Table 4-1.

Table 4-1. Stress intensity factors relevant to the chevron-notched short rod and bar fracture toughness test.

Stress intensity factor	Description
K_{1v}	Plane-strain fracture toughness for slowly advancing steady-state cracks[1].
K_{1vj}	Plane-strain (chevron-notched) fracture toughness for cracks that advance sporadically (crack jump behaviour)[1].
K_{1vM}	Plane-strain (chevron-notched) fracture toughness based on maximum load[2].

The fracture toughness is calculated from the conditional plane-strain fracture toughness K_{Qv}. If the K_{Qv} meets the validity requirements set by ASTM E1304 – 97 [78] then K_{Qv} qualifies as the plane-strain fracture toughness K_{1v}.

---

[1] The value is based on unloading and reloading the specimen in order to determine the critical crack length and thus the critical load.
[2] Determined by maximum load.

$$\mathrm{K_{Qv}} = \frac{\mathrm{Y_m^* P_c}}{\mathrm{B\sqrt{W}}} \qquad 4\text{-}6$$

Where Y_m^* is the stress intensity factor coefficient at minimum (occurs at maximum load), P_c is the force required to advance the critical crack length, B is the diameter and W is the length. The unit for the plane-strain fracture toughness, K_{QV} is $\mathrm{MPa}\sqrt{\mathrm{m}}$.

After mechanical testing the stress-intensity factor qualifier, K_{Qv}, is determined. The specimen is further subjected to validation requirements to determine whether K_{Qv} meets the conditions that need to be satisfied which is thickness, loading and maximum load limits.

The actual thickness of the specimen must be greater or equal to the thickness calculated from K_{Qv} in order to qualify as K_{1v}. The thickness validity requirement ensures that the size of the specimen is sufficient to meet plane-strain conditions. In addition, the specimen size is half that of the single-edge bend and compact tension test as presented in Equation 4-7 and Figure 4–5.

$$\mathrm{B} \geq 1.25\left(\frac{\mathrm{K_{Qv}}}{\sigma_{\mathrm{YS}}}\right)^2 \qquad 4\text{-}7$$

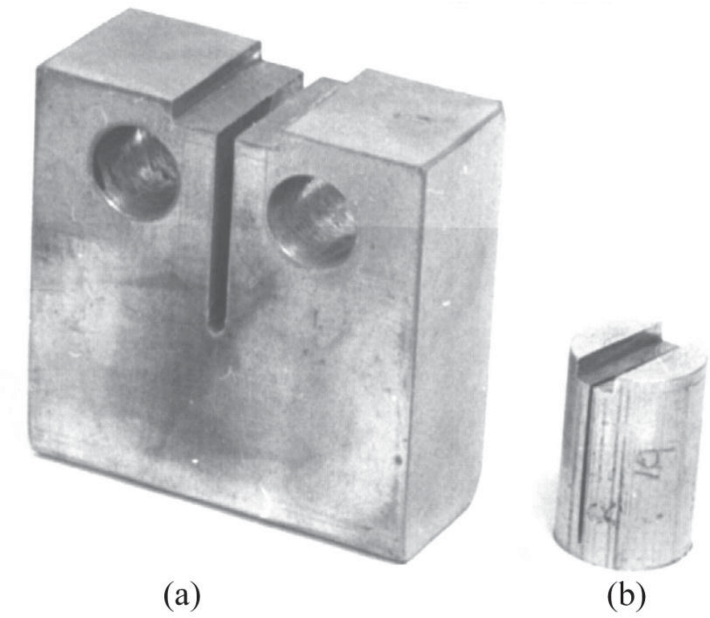

Figure 4–5. A comparison of the (a) compact tension and (b) chevron-notched short rod specimen [83].

Two unloading and reloading cycles are performed to provide validity checks on the load-displacement curve. ΔX is the distance between the effective unloading lines along the average force line. ΔX_O is the distance between the effective unloading lines along the zero force line. And p is the plasticity criterion, $p = \Delta X_O/\Delta X$. If the loading lines cross before reaching the zero load axis, then ΔX_O and p is considered to be negative, the test is only valid if;

$$-0.05 \leq \mathrm{p} \leq +1.10 \qquad 4\text{-}8$$

The ratio of the maximum load, P_M, and the force required to advance the crack, P_c, must be less than or equal to 1.10 in order for K_{Qv} to be qualified as plane-strain fracture toughness, K_{1v}.

$$\frac{P_M}{P_c} \leq 1.10 \qquad 4\text{-}9$$

Where the maximum load, P_M, and the load at intersection, P_c, are determined from the fracture toughness load-displacement curve.

4.3 Non-standard fracture toughness test

Fracture toughness specimens that do not conform to dimensional constraint imposed by standard test guidelines are known as non-standard test specimens. These non-standard test specimens are similar to the standard test specimens both in test methodology and procedure. In addition, the method provides reasonable approximation to standard plane-strain fracture toughness, K_{1c} and J_{1c} [79, 84-92], and CTOD values [93].

4.3.1 *Circumferential notch tension test*

The Circumferential Notch Tensile (CNT) test is mainly attributed to the work of Stark and Ibrahim [79]. The authors consider the CNT test as a valid plane-strain fracture toughness test that can deliver K_{1c} values since the full circumferential crack does not have an end in a plane stress region and thus plane strain condition is possible [86]. Very recent work includes CNT tests incorporating stress corrosion cracking (SCC) at the fatigue crack tip [84, 94] and CTOD [93].

The machining of the CNT specimen and v-notch is straightforward and inexpensive relative to the ASTM standard fracture toughness specimens. The present specimen dimensions are 9.5mm diameter specimen with a 60° angle v-notch. The v-notch depth is 1.25mm giving a minimum diameter of 7mm. The CNT test configuration is presented in Figure 4–6.

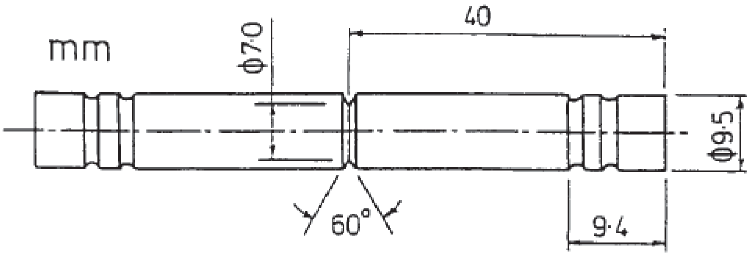

Figure 4–6. The circumferential notch tensile test configuration [95].

A fatigue precrack is introduced through rotational bending via a rotating beam fatigue test machine. The fatigue precrack depth can be controled through incremental loads and auto-stopped at a predetermined deflection via a deflection measurement gauge. The mechanical test simply involves uniaxial tension of the precracked CNT test specimen to determine the maximum load. The maximum load in addition to the final average crack length are then utilised for plane-strain fracture toughness, K_{1c}, determination.

$$K_{1c} = (\sigma_t + \sigma_b)\sqrt{\pi \bar{a} F} \qquad 4\text{-}10$$

Where σ_t is the tension stress, σ_b is the bending stress, $\bar{a}$ is the Irwin corrected crack depth and F is a parametric function describing geometry [96]. The unit for the plane-strain fracture toughness, K_{1c} is $\mathrm{MPa}\sqrt{\mathrm{m}}$.

According to Ibrahim and Stark, in order to satisfy validity requirements the deepest fatigue crack should be twice the Irwin plane-strain plastic zone correction r_o [86]. In addition, the mean axial stress in the final ligament should be no greater than 2.5 times the tensile yield strengths to avoid plasticity effects at the crack tip.

The primary validity requirement that governs the size of CNT plane-strain fracture toughness specimens are presented as follows.

$$D \geq 32.\, r_o \text{ or } D \geq 1.7\left(\frac{K_{1c}}{\sigma_{YS}}\right)^2 \qquad 4\text{-}11$$

Where D is the outside diameter, K_{1c} is the plane-strain fracture toughness and σ_{YS} is the yield strength. A comparison of the C(T) and CNT test specimen size demonstrate that CNT specimens are smaller compared to standard specimens as shown in Figure 4–7.

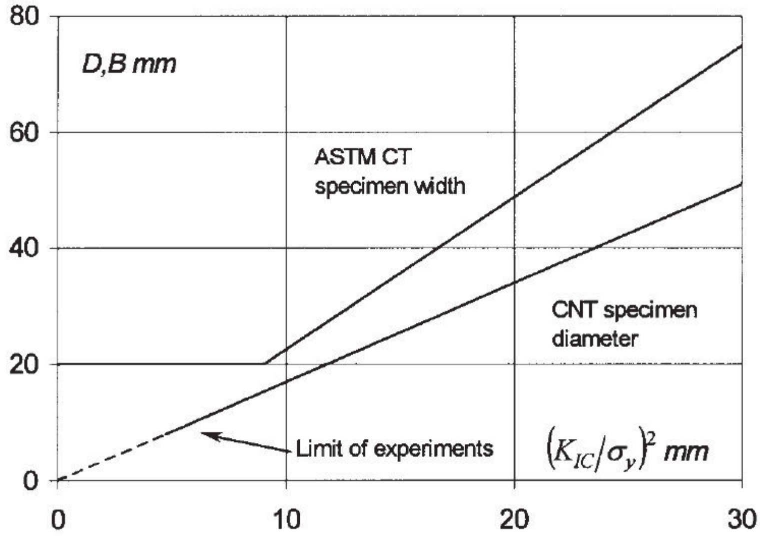

Figure 4–7. A comparison of the circumferential notch tension and the standard compact tension specimens test size [95].

$$a_f \geq 2r_f \qquad 4\text{-}12$$

Where a_f is the deepest fatigue crack and r_f is the Irwin correction factor [94].

$$\frac{\sigma_N}{\sigma_{YS}} \leq 2 \qquad 4\text{-}13$$

Where σ_N is the nominal applied stress and σ_{YS} is the yield strength [94].

The CNT test presents many advantages including small specimen size, ease in machining and mechanical testing. Disadvantages include eccentricity and non circularity of the final ligament which lead to increased scatter of the plane-strain fracture toughness, K_{1c}, results. Furthermore, very shallow fatigue crack depths can increase the overall measured fracture toughness value. Lastly Ibrahim et al. mention that the current CNT specimens incorporating 9.5mm diameter are suitable for many materials containing low fracture toughness values however a larger specimen diameters at 25mm would be more beneficial for materials exhibiting higher fracture toughness values [95].

The trend in fracture toughness testing has so far gone from very large sized specimens to smaller sized specimens that satisfy plane-strain conditions. Furthermore, the plane-strain fracture toughness testing can be achieved without a fatigue crack as in the case of the chevron-notched short rod or bar test which utilise a slowly moving steady-state crack. Still, the size of the specimens mentioned thus far can only be applied to instances where the materials are readily available for testing and in relative large amounts. Therefore, this research focuses on the small punch test that possesses no fatigue or slowly moving steady-state crack for the purpose of deriving plane-strain fracture toughness, K_{1c} and J_{1c}, values from significantly smaller plane-stress specimens.

4.4 Concluding remarks

Often there are limited materials for research and this is especially true in the case of MMCs. The trend towards ever smaller fracture toughness specimens to meet demand where material availability is limited continues. Further research in the development of small specimen tests that are capable of obtaining meaningful plane-strain fracture toughness values are sought.

CHAPTER FIVE

THE SMALL PUNCH TEST

5.1 Introduction

The small punch test (SPT) was first introduced just under 30 years ago by Manahan, M. P. [1, 2] as the Miniaturized Disk Bend Test (MDBT) at the Massachusetts Institute of Technology (MIT) in 1982 for extracting post irradiated mechanical behaviour and ductility from disk-shaped specimens not much larger than transmission electron microscopy specimens [1, 2, 97-99]. The key advantage of the SPT is the small volume of materials required for mechanical tests. This provides an effective method for monitoring in-service components exposed to high temperature environments and neutron irradiation without affecting the structural integrity and life of the component [100-102]. Monitoring of components is necessary for the optimisation of operating procedures, inspection, repair strategies and residual lifetime assessments. The mechanical properties such as yield strength, fracture appearance transition temperature (FATT), creep and fracture toughness have been assessed. The SPT has been applied to nuclear powered in-core structures, turbine rotors and pressure vessels. Furthermore, the SPT has been applied to welds, coatings [103], polymers [104], ceramics, metals [105] and composites [106-111]. An early SPT configuration employing disk-shaped SPT specimens that is simple supported is presented in Figure 5–1 [1].

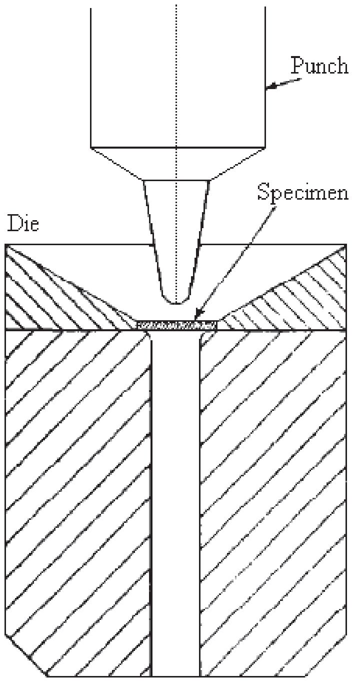

Figure 5–1. The Massachusetts Institute of Technology small punch test [98].

To date there have been several special technical publications (STPs) dealing with the SPT that provide a comprehensive overview of the development of the SPT for the evaluation of material mechanical properties. These publications include The Use of Small-Scale Specimens for Testing Irradiated Materials STP 888 [98, 99, 112-114], Small Specimen Test Techniques Applied to Nuclear Reactor Vessel Thermal Annealing and Plant Life Extension STP 1204 [115-119], Small Specimens Test Techniques STP 1329 [120-123], Small Specimen Test Techniques: Fourth Volume STP 1418 [124] and Small Specimen Test Techniques: Fifth Volume STP 1502 [125-127].

Research on the SPT continued in America, Japan and Europe. In 1998, a guide to the SPT was proposed by the Japanese Atomic Energy Research Institute, which provided recommended practices for the SPT [128]. Subsequently, standards are developed in America (ASTM F2183-02) [129] and in Europe (S.R. CWA 15627:2007) [130], however, consensus of an agreed universal standard has yet to be established. Very recently the People’s Republic of China has made progress towards a national standard of the SPT [131]. Looking towards the future, the SPT has the potential to become a multi-purpose multi-mechanical test for strength, toughness and creep assessment.

5.2 Defining the small punch test

Two variants of the SPT have arisen including the *small punch bulge test* and the *small punch drawing test* [130]. The small punch bulge test involves holding the small punch specimen in a clamped configuration thereby preventing disk sliding, conversely the small punch drawing test employs the un-clamped condition which allows for disk sliding. In the case of the small punch bulge test, the clamped region is not considered as part of the test section. Furthermore, finite element studies have shown measured loads to increase for the clamped case compared to the unclamped case [132].

The SPT can be employed as either a *time-dependant* (high temperature environment) or *time-independent* (low temperature environment) test. In general, the time dependant SPT focuses on creep resistance and life assessment of structural components. Test temperatures are usually in the creep range and the method can be referred to as the small punch creep (SPC) test. The time independent SPTs are mainly focused on assessing tensile and toughness properties, the tests are usually conducted at room temperature between 20˚C and 25˚C. The SPT is usually performed in air environment. For all intensive purposes this thesis focuses on the *time independent small punch bulge* test as an approach to obtaining meaningful tensile and fracture toughness properties.

The modern SPT configuration is composed of an upper and lower die and a spherical punch, as presented in Figure 5–2. The upper and lower die is held together with clamping screws.

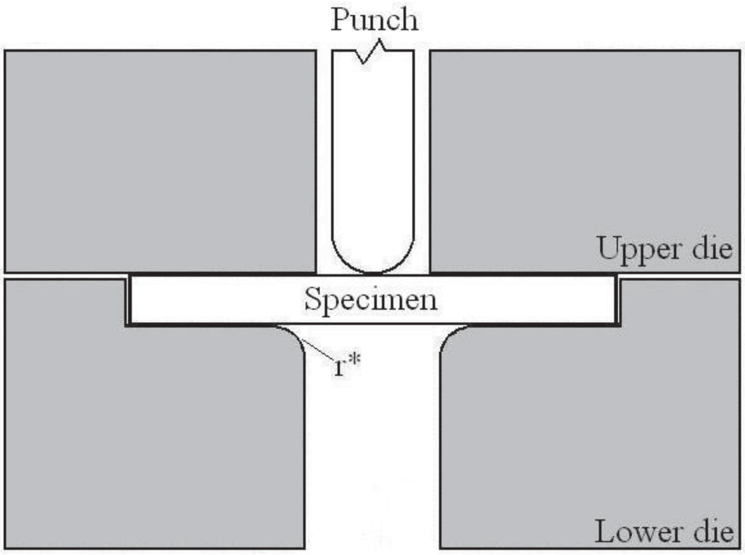

Figure 5–2. A schematic representation of the small punch test configuration.

Mao et al. [133-137] proposed the following SPT configuration where R_l is the radius of the lower die bore size, R_u is the upper die bore size and t_o is the SPT specimen thickness.

$$2R_l > 2R_u + 2t_o \qquad 5\text{-}1$$

Other notable factors when designing the SPT configuration are the radius of the spherical punch, radius of the lower die's chamfer edge *r**, clamping area and specimen dimensions. According to the European standard (S.R. CWA 15627:2007) a chamfer edge r* of 0.2mm is recommended. In addition, the hardness of the SPT configuration should be sufficient for mechanical tests. A hardness of 55 HRC is sufficient for most steels or a ceramic ball. There have been many SPT specimen and SPT die configurations that have been implemented in the past as presented in Table 5-1. Note, r_o is the punch radius.

Table 5-1. Small punch test specimen and die configurations.

Reference	**SPT specimen (mm)**	**SPT die (mm)**
Manahan et al. **[1]**	Ø = 3.00, $t_o = 0.25$	$r_o = 1.00$, $R_l = 1.50$
Foulds et al. **[120]**	Ø = 6.40, $t_o = 0.50$	$r_o = 1.25$, $R_l = 1.90$
Isselin et al. **[138]**	Ø = 9.00, $t_o = 0.50$	$r_o = 1.25$, $R_l = 2.00$
Abendroth and Kuna **[139]**	Ø = 8.00, $t_o = 0.50$	$r_o = 1.25$, $R_l = 2.00$, $r^* = 0.50$
Dobes and Milička **[140]**	Ø = 8.00, $t_o = 0.50$	$r_o = 1.25$, $R_l = 2.00$
Bulloch **[141]**	Ø = 10.0, $t_o = 0.50$	
Maribel et al. **[16]**	l = 10.0, w = 10.0, $t_o = 0.50$	$r_o = 1.2$, $R_l = 1.19$
Suzuki et al. **[142]**	l = 10.0, w = 10.0, $t_o = 0.50$	$r_o = 1.20$
Fleury and Ha **[143]**	l = 10.0, w = 10, $t_o = 0.50$	$r_o = 1.20$
Husain et al. **[144]**	l = 10.0, w = 10.0, $t_o = 0.50$	$r_o = 1.15$
Shekter et al. **[145]**	Ø = 10.0, $t_o = 0.50$	$r_o = 1.10$

Of course, alignments of the punch and die as well as load-line centre are critical in minimizing anisotropy effect caused by eccentricity. A steel ball can be employed as a useful method for load-line alignment of the punch [146]. Furthermore, adhering to strict design tolerances and preparing of specimens with constant thicknesses will reduce this effect. The SPT specimen dimensions can be either disc or square shaped in configuration since the SPT specimen is clamped. The SPT specimen size can range from as large as 10mm in diameter with 0.5mm thickness to a specimen size of 3mm in diameter with 0.25mm in thickness.

The dimensions of the SPT specimen do affect the load-displacement curve behaviour. In general decreasing the diameter and increasing thickness will increase the loads exhibited by the load-displacement curve. It has been demonstrated that an increase in specimen thickness will lead to an increase in overall load. In most cases due to the relative size of the SPT specimen relative to in-service component, the SPT specimen are considered as a *non-destructive test*. An example of the SPT is presented in Figure 5–3.

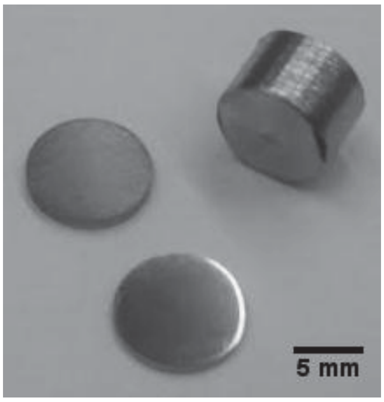

Figure 5–3. Small punch disk-shaped specimens cut from a cylindrical sample.

When conducting the SPT, the load-displacement is often applied by either a screw-driven or hydraulic source. The SPT should incorporate an accurate loading and displacement measurement system. The percent error for the force measurement should not exceed more than ±1% of the actual measured force and in compliance with tensile test standards. The percent error for the displacement measurement should not exceed more than ±1% of the SPT thickness. The displacement rate for the SPT is often chosen in accordance with standard tensile test rates [130]. In general, the displacement rate can range between 0.2 to 2mm/min, the former being the most utilised. Vaseline can be applied to minimise contact friction between the punch and the specimen, however, the effect of friction is minimal.

A number of devices can be employed at the centre of the specimen on the opposite side of the spherical punch. A linear variable differential transformer (LVDT) can be employed to measure displacement. When this option is employed the displacement is termed *deflection*. Several methods have been employed for identification of crack initiation. These methods include digital pinhole camera, electric potential drop method and acoustic emission sensor. A digital pinhole camera is often employed to observe the surface deformation behaviour and to identify the crack initiation point in-situ. Furthermore, an electric potential drop method could be employed to observed a drop in electric potential at crack initiation [147]. Similarly, an acoustic emission sensor is employed to identify the crack initiation point [146]. However, it is found that this method can be acoustically noisy when attempting to identify the fracture initiation event from some materials such as aluminium [105].

The SPT specimen fracture surface is often characterised using scanning electron microscopy (SEM). The technique provides superior resolutions over more conventional optical techniques and allows for clear identification of the cracked surface. Presently there has yet to be implementation of SEM techniques for in-situ observation of crack evolution and crack initiation point. This could be advantageous as the nature of failure can be identified. Furthermore, the crack initiation point is often utilised as a fracture criterion for the determination of fracture toughness [148]. Another advantage to in-situ analysis is the permitted high resolution observation of surface deformation and microstructural changes.

As a result of the SPT, a load-displacement curve is generated as presented in Figure 5–4 [149, 150]. The following load-displacement curve is divided into 6 regions for ductile steel. Finite element analysis illustrates theoretical deformation behaviour and crack propagation behaviour for each region.

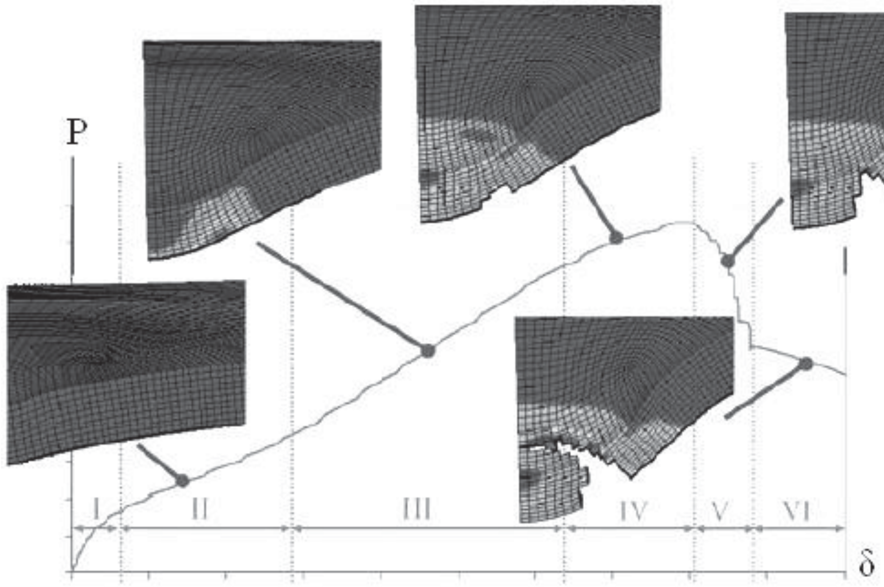

Figure 5–4. Small punch test load-displacement curve [149].

Region I. Is assumed to be mainly controlled by the elastic modulus and the Poisson's ratio on the elastic behaviour of the material. The initial curve is observed to be a straight line. The effect of the initial indentation by the spherical punch is assumed to be negligible.

Region II. Reflects the transition from purely elastic behaviour to elastic-plastic behaviour.

Region III. Membrane stretching. Specimen begins to bulge. Hardening mechanisms dominate. Void nucleation begins. Exhibits purely plastic behaviour. The crack initiation point may initiate within region III or IV.

Region IV. Softening mechanisms dominate leading to the maximum load and plastic instability. Void coalescence begins.

Region V. Exhibits the onset of failure and continuation of fracture softening.

Region VI. There has been limited research in this area however it represents the required load for continued crack propagation. The specimen is completely perforated by this stage.

Experimental observations of steels that have undergone SPT show the disappearance of inflexion points as the specimens are mechanically worked. More research into the various behaviour of the SPT load-displacement curve for various materials is required to assess these post-processing conditions.

5.3 Determination of the small punch elastic-plastic load, P_y

The determination of the yield strength often begins with the determination of the SPT elastic-plastic load P_y. The SPT elastic-plastic load P_y is identified as the transition load between the elastic region I and elastic-plastic region II. Two methods have arisen for the determination of the elastic-plastic load including the *offset* method [151] and the *2 tangent* method [152] as presented in Figure 5–5.

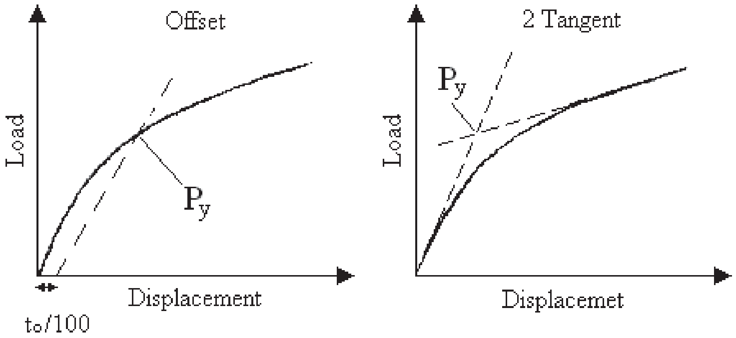

Figure 5–5. The *offset* method and *2 tangent* method for the determination of elastic-plastic load, P_y [152].

The *2 tangent* method consist of plotting two tangents on either side of the deviation point that ends the linear region at the beginning of the load-displacement curve. The load value at the intersection point is specified as the elastic-plastic load. The *offset* method consists of plotting a straight line through the linear portion of the load-displacement curve. The line is then offset by t_o/100mm where t_o is the thickness of the SPT specimen.

5.4 Determination of the small punch energy, E_{SP}

The SPT fracture energy E_{SP} can be defined as the area under the load-displacement curve. That is, up to the displacement at the onset of the fracture or failure which is defined by the Europe standard (S.R. CWA 15627:2007) as the small punch displacement at 20% load drop after the maximum load [153].

$$E_{SP} = \int_{0}^{\delta} F(\delta) d\delta \qquad 5\text{-}2$$

The function F(δ) can be approximated with a multivariate polynomial regression up to failure. Alternatively others have defined the fracture energy as the energy required for crack initiation at the free surface [148]. The SPT energy is often correlated with the plane-strain fracture toughness J_{1c} and the equivalent fracture strain ε_{qf} [154].

5.5 Determination of the small punch equivalent fracture strain, ε_{qF}

Chakrabarty et al. [155] proposed the following analytical solution as a fracture parameter for circular plate-shaped specimens based on membrane stretch theory and experimental observations of crack initiation after membrane stretching. The equivalent fracture strain, ε_{qF}, is an important SPT parameter since it has been shown to have good correlation to fracture toughness values. According to the theory the radial strain, ε_r, is equal to the circumferential strain, ε_θ, and the thickness strain, ε_t, is characterised by the following relation.

$$\varepsilon_t = \ln\left(\frac{t_o}{t}\right) \qquad 5\text{-}3$$

Where t_o is the original thickness, t is the final thickness. Considering the incompressible plastic case we come to the following relation.

$$\varepsilon_r + \varepsilon_\theta + \varepsilon_t = 0 \qquad 5\text{-}4$$

The radial strain, ε_r, equals the circumferential strain, ε_θ. The equivalent fracture strain is characterised as follows.

$$\varepsilon_q = 0.816\sqrt{\varepsilon_r^2 + \varepsilon_\theta^2 + \varepsilon_t^2} \qquad 5\text{-}5$$

Substituting

$$\varepsilon_q = \ln\left(\frac{t_o}{t}\right) \qquad 5\text{-}6$$

Mao et al [137] proposed the following relation which relate the equivalent fracture strain with the deflection δ^* of a SPT load-displacement curve.

$$\varepsilon_{qf} = \ln\left(\frac{t_o}{t_f}\right) = a\left(\frac{\delta^*}{t_o}\right)^b \qquad 5\text{-}7$$

Where t_o is the initial thickness, t_f is the minimum thickness at fracture, δ^* is the maximum deflection and a and b are empirically derived constants [4]. The final thickness at fracture can be determined from either direct measurement of the thickness at crack initiation with a measurement gauge device or by image analysis of the materials cross-section. Experimental results have shown that the crack initiation often occurs well in advance of the maximum load [146]. From experimental observation Foulds et al. [148] suggested that in the case of brittle materials, crack initiation occurs at peak load and drops in unstable crack growth whereas for ductile materials crack initiation occurs well before peak load followed by stable crack growth.

5.6 An analytical method for the determination of small punch maximum bend yield strength, σ_y

The yield stress can be determined from either an analytical or empirical solution. The analytical solution involves analysis of the elastic bend theory of plates and is based on the assumption that the elastic-plastic load, P_y, is governed purely by elastic deformation. Furthermore, elastic-plastic load is thought to be proportional to yield stress. The analytical approach involves solving the small punch maximum bend strength, σ_y, of a flat circular plate via the elastic bend theory of plates [102], in this way the yield strength is approximated. The conditions for the plate theory include flat surface, isotropic properties and non-hardening conditions. A schematic diagram depicting the loading and restraints is represented in Figure 5–6.

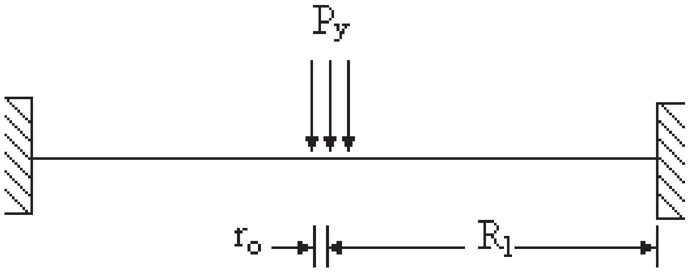

Figure 5–6. A flat circular plate with constant thickness [156]. Where P_y is the small punch elastic-plastic load, r_o is the radius of the spherical punch and R_l is the radius of the lower die bore.

Where the load P_y is uniform over a small central circular area of radius r_o. The edges of the flat circular plate are constrained. Considering P_y, the simple bending theory can be applied to obtain the maximum bending stress at the center of the free surface of the small test specimen and in turn estimate the yield stress of the material [156, 157].

For clamped condition

$$\sigma_y = \frac{3P_y(1+v)}{2\pi t_0^2}\ln\frac{R_l}{r'} \qquad 5\text{-}8$$

For simple supported

$$\sigma_y = \frac{3P_y}{2\pi t_0^2}\left[(1+v)\ln\frac{R_l}{r'}+1\right] \qquad 5\text{-}9$$

Where

$$r' = \sqrt{1.6r_0^2 + t_0^2} - 0.675t_0 \text{ for } r_o \le \frac{t_0}{2} \qquad 5\text{-}10$$

And

$$r' = r \text{ for } r_o \ge \frac{t_0}{2} \qquad 5\text{-}11$$

The determination of the small punch maximum bend strength, σ_y, is found to be higher compared to actual tensile yield strength values σ_{YS}. This is because of local deformation values are larger compared to the overall dimensions of the SPT specimen. In addition, there is a lot of uncertainty involved in the determination of the equivalent contact radius r′.

Fleury and Ha proposed an alternative expression for r′ in the following form. They recognised that the equivalent contact radius r′ is influenced by the elastic modulus of the spherical punch and specimen.

$$r' = 0.721(Pd\gamma)^{\frac{1}{3}} \qquad 5\text{-}12$$

Where P is the applied load, d is the diameter of the indenter.

And

$$\gamma = \frac{(1 - v_1^2)}{E_1} - \frac{(1 - v_2^2)}{E_2} \qquad 5\text{-}13$$

Where E_1, v_1 and E_2, v_2 are the elastic modulus and Poisson's ratio for the spherical punch and small punch test specimen, respectively.

As mention earlier the yield strength, σ_{YS}, can be determined through empirical correlations. A number of researchers have attempted this correlation as presented in Table 5-2. This involves a normalisation relationship of the tensile strength, σ_{YS}, and small punch elastic-plastic load, P_y. This can be accomplished by applying the least squares method to the yield stress plotted against the elastic-plastic load divided by original thickness, t_o, squared yields the normalisation relationship, α. The following relation is similar to Timoshenko's analysis of elastic plate bending as presented in Figure 5–6.

$$\sigma_y = \frac{P_y}{t_o^2} \times \alpha \qquad 5\text{-}14$$

Table 5-2. Reported yield strength correlation coefficients for the small punch test.

Reference	**Materials**	**SPT specimen (mm)**	**SPT die (mm)**	**Correlation coefficient, α**
Xu and Zhao **[158]**[3]	Steel		$R_l = 1.2$	0.48
Mao and Takahashi **[137]**	Steel	Ø = 3, $t_o = 0.25$	$R_l = 0.75$, $r_o = 0.5$	0.36
Cheon and Kim **[159]**	Steel	Ø = 3, $t_o = 0.25$	$R_l = 0.75$, $r_o = 0.5$	0.63

---

[3] For this case the correlation coefficient for the yield strength was derived analytically.

Cheon and Kim **[159]**	Steel	l = 10, w = 10, $t_o = 0.5$	$R_l = 2$, $r_o = 1.2$, $r' = 0.2$	0.6
Ruan et al. **[160]**[4]	Steel	Ø = 3, $t_o = 0.25$	$R_l = 0.75$, $r_o = 0.5$	0.5
Isselin and Shoji **[152]**	Steel	Ø = 3, $t_o = 0.25$	$R_l = 0.75$, $r_o = 0.5$, $r' = 0$	0.54

It is thought that the normalisation relationship α is predominantly influenced by the SPT configuration and is less to do with the mechanical properties of the materials [137, 159, 161]. It would be advantageous to develop a SPT configuration such that the normalisation relationship α is equal to 1.

Isselin et al. recently proposed an alternative empirical approach for the determination of yield strength based on the elastic deformation energy, EDE, [152] as presented in Equation 5-15. The EDE is the energy necessary to completely plasticize the SPT specimen and does not represent the plasticity at the center of the free surface [152]. The EDE is determined by loading the specimen up to yield and before crack initiation. The specimen is then allowed to unload. The elastic reverse displacement D_e is then measured. The EDE is then obtained as the area underneath the load-displacement curve up to the length D_e.

$$\mathrm{EDE} = \sigma_{\mathrm{center}}^2 \times \frac{2(1 - \mathrm{v}^2)\mathrm{a}^2\mathrm{t_o}}{3\mathrm{E}\pi(1 + \mathrm{v})^2} \qquad 5\text{-}15$$

From Equation 5-15 it is observed that the elastic deformation energy, EDE, is found to be proportional to the square of the stress at the center of the free surface. The proposed approach for correlating the yield strength, σ_{YS}, against the elastic deformation energy, EDE, is presented in Equation 5-16. This approach does not require measurement of the load unlike the *offset* method or *two tangents* method. Furthermore, Isselin et al. suggest

---

[4] The correlation coefficient was obtained through linear regression at the zero offset.

the proposed method exhibits scatter than can otherwise be obtained from the *offset* method or *two tangents* method.

$$\sigma_{YS}^2 = EDE \times \alpha \qquad 5\text{-}16$$

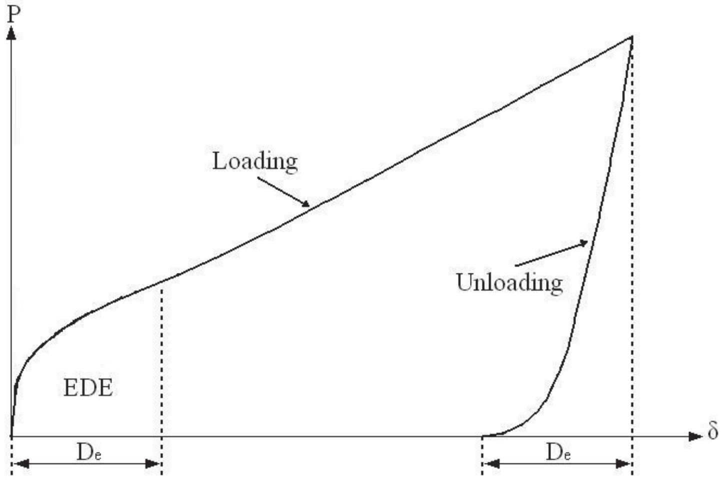

Figure 5–7. Method for the determination of the elastic deformation energy, EDE and the elastic displacement, D_e [152].

5.7 An empirical method for the determination of plane-strain fracture toughness, K_{1c} and J_{1c}

The plane-strain fracture toughness, K_{1c}, is an important mechanical property. It is a measure of a material’s resistance to fracture when a crack is present. Conventional SPT specimens do not conform to precrack conditions nor does the size of the SPT specimens qualify for plane strain conditions, however, this has not stopped researchers from further developing the SPT for fracture toughness analysis in the plane stress state. Furthermore, the plastic zone size is expected to be much larger than the initial crack size which further complicates determination of fracture toughness. If these conditions are not challenging enough the biaxial loading of the SPT means that the crack may propagate in mode I (opening), II (sliding) and III (tearing) crack loading.

Recently, researchers have made some efforts toward sharp notch or near precracked SPT specimens in order to satisfy the fracture toughness precrack condition [146, 157, 162]. Researchers often attempt extraction of the plane-strain fracture toughness, J_{1c}, compared to the more familiar K_{1c} value, since the SPT deformation behaviour is expected to be nonlinear elastic behaviour. The plane-strain fracture toughness, J_{1c}, and plane-strain fracture toughness, K_{1c}, have been obtained from empirical analytical, empirical, finite element and neural networks solutions.

Bayoumi and Bassim [26] first proposed a theoretical model relating the plane-strain fracture toughness, J_{1c}, and SPT equivalent fracture strain to an isotropic material as described in Figure 5–8.

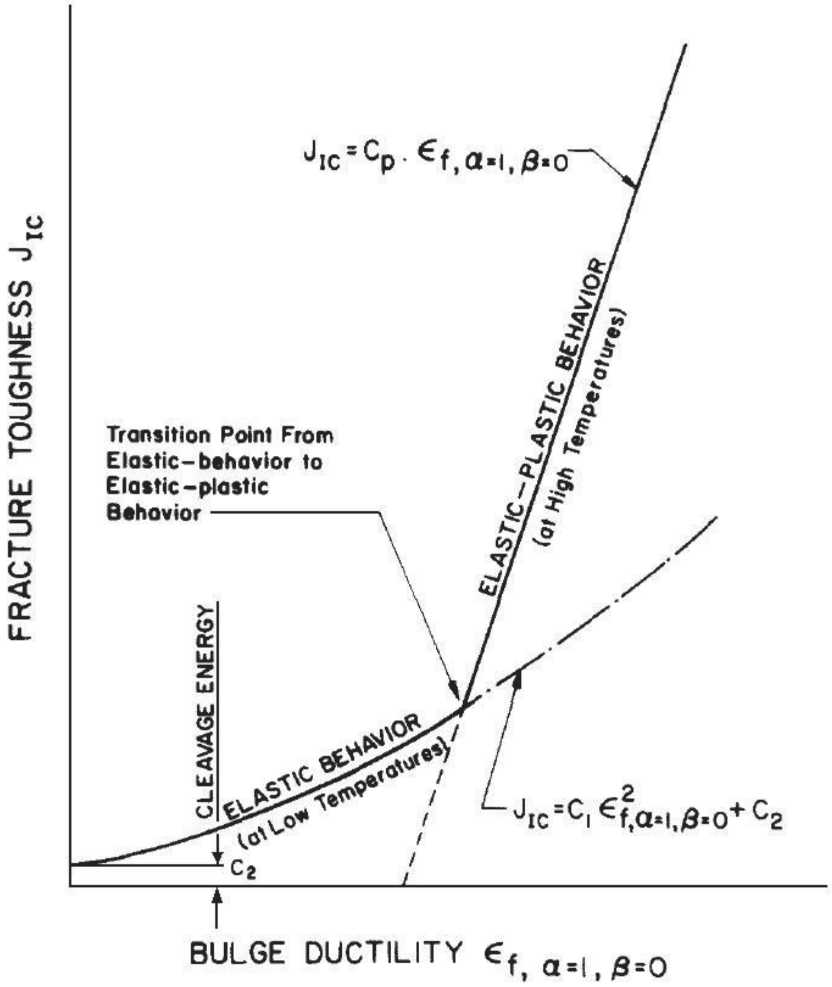

Figure 5–8. The theoretical plane strain fracture toughness J_{1c} and equivalent fracture strain relationship proposed by Bayoumi and Bassim [26].

According to Bayoumi and Bassim [26] the model is applicable to both elastic and elastic-plastic behaviour. The following relation describes elastic behaviour where plane-strain fracture toughness J_{1c} varies proportionally against the SPT equivalent fracture strain.

$$J_{1c} = S\rho^{*}(0.279)^{\frac{2}{n}}\varepsilon^{2}_{qF,\alpha=1\beta=0}f\big(E,K,n,\varepsilon_{y}\big) + 2\sigma_{f}^{2}\pi L_{e}^{*}\frac{(1-v^{2})}{E} \qquad 5\text{-}17$$

Or in general

$$J_{1c} = C_{1}\varepsilon^{2}_{qF,\alpha=1\beta=0} + C_{2} \qquad 5\text{-}18$$

Whereas in the case of elastic-plastic behaviour the plane-strain fracture toughness, J_{1c}, varies linearly against the SPT equivalent fracture strain.

$$J_{1c} = k\frac{m\sigma_{o}}{C}L_{p}^{*}\varepsilon_{qF,\alpha=1,\beta=0} \qquad 5\text{-}19$$

Or in general

$$J_{1c} = C_{p}\varepsilon_{qF,\alpha=1,\beta=0} \qquad 5\text{-}20$$

According to Bayoumi and Bassim [26] the three constants (C_1, C_2 and C_p) are easily determined through graphical evaluation. Mao and Takahashi expressed the elastic-plastic linear relationship as an empirical correlation of the plane-strain fracture toughness J_{1c} and the equivalent fracture strain [135, 163, 164], after Bayoumi and Bassim [26].

$$J_{1C} = k\varepsilon_{qf} - J_{o} \qquad 5\text{-}21$$

Where, k and J_o are empirically constants. In the case of brittle materials the plane-strain fracture toughness, K_{1c}, is proposed to be empirically correlated to SPT fracture stress by Mao et al. [135] where C is an empirical constant.

$$K_{1C} = C\big(\sigma_{f}^{SP}\big)^{\frac{2}{3}} \qquad 5\text{-}22$$

As mentioned earlier a sharp crack usually in a form of a fatigue crack is required for calculations of the stress intensity factor in accordance with the theory of fracture mechanics. This has led Ju et al. to apply fracture mechanics for the determination of a sharp notched SPT to obtain the stress intensity factor for steels [146, 165]. The stress intensity factor is obtained by analysing the stress fields near the crack tip. The fracture toughness is obtained from plate-shaped sharp notched SPT specimens as shown in Figure 5–9.

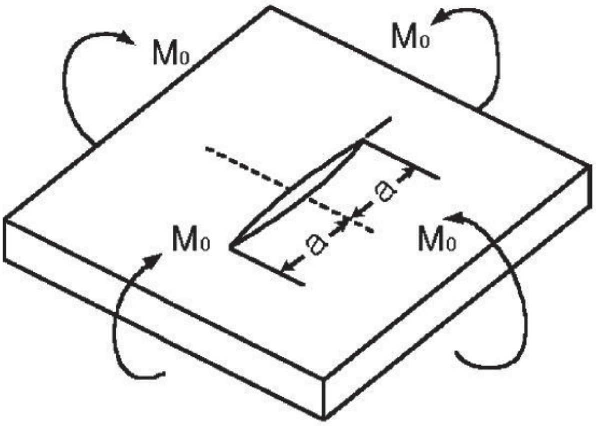

Figure 5–9. Infinite sharp notched plate-shaped small punch test subjected to uniform bending. Where M_o is the bending moment applied around the boundaries of an infinite plate.

The edges of the specimen are considered infinite therefore both plate-shaped and disk-shaped specimens that are in clamped configuration can be considered for fracture toughness, K_c, determination. The fracture toughness, K_c, equation for infinite sharp notched plate-shaped SPT subjected to uniform bending is presented in Equation 5-25.

$$K_1 = \frac{6M_o}{t_o^2}\sqrt{a} \qquad 5\text{-}23$$

Where

$$M_o = \frac{1+v}{4\pi}P\left(\ln\frac{R_l}{r'} + \frac{r'^2}{4R_l^2}\right) \qquad 5\text{-}24$$

So

$$K_c = \frac{3}{2}\frac{P_i(1+v)}{\pi t_o^2}\left(\ln\frac{R_l}{r'} + \frac{r'^2}{4R_l^2}\right)\sqrt{a} \qquad 5\text{-}25$$

Where R is the lower die bore radius, r' is the contact radius respectively, 2a is the crack length, P_i represents the load at crack initiation and the v is the Poisson’s ratio. Ju et al. achieved reproducible results for both brittle (77K) and ductile (298K) steels however their results for the ductile materials are significantly lower compared to standard fracture toughness values. This is because their analysis is based on linear elastic fracture mechanics.

Ha et al. estimated the plane-strain fracture toughness, K_{1c}, in the brittle regime by utilising the Richie-Knott-Rice criterion [166] which is based on the critical fracture stress and assumes that cleavage fracture occurs ahead of a sharp crack [167].

$$K_{1c} = \beta^{-[(n+1)/2]} l_o^{1/2}\left[\frac{\sigma_f^{(n+1)/2}}{\sigma_y^{(n-1)/2}}\right] \qquad 5\text{-}26$$

Where

$$\beta = f(n)\left[\frac{(1-v^2)}{\varepsilon_O I}\right]^{\frac{1}{n+1}} \qquad 5\text{-}27$$

Where β is a numerical constant [168] obtained from the Hutchinson-Rice-Rosengren small scale yielding solution [169-171], n is the hardening coefficient, σ_y is the yield stress and l_o is the grain size length. The Hutchinson-Rice-Rosengren small scale yielding solution is appropriate for plane strain conditions.

The total strain energy, W_T, as expressed in Equation 5-28 can be utilised to estimate the plane-strain fracture toughness, J_{1c}, in the ductile regime [167].

$$W_T = W_e + W_p + W_f \tag{5-28}$$

Where W_T is total strain energy, W_e is the elastic strain energy, W_p is the plastic strain energy and W_f is the energy at fracture. Since the elastic strain energy is small compared to the overall energies we can assume it to be negligible. The strain energy at fracture is of the following form.

$$W_f = 2\pi r_n t C_f J_{1C} \tag{5-29}$$

Where r_n is the radius in the necking area, t is the thickness, C_f is the cracked fraction of the necking line and J_{1c} is the plane-strain fracture toughness. Furthermore, the plastic strain energy is as follows.

$$W_p = (\pi r^{*2} t)\frac{\sigma \varepsilon^{n+1}}{n+1} \tag{5-30}$$

Where r^* is the radius of the lower die, t is the thickness, σ is a nominal stress, ε is a nominal strain and n is the strain hardening coefficient.

In order to take into account the formation of necking on the outside and inside the following equations are derived. The necking energies W_{inside} and $W_{outside}$ can take on the following form.

$$W_{inside} = \left[\pi\left(r^{*2} - r_f^2\right)t_1\right]\frac{\sigma_o \varepsilon_1^{n+1}}{n+1} \tag{5-31}$$

And

$$W_{outside} = \left(\pi r_f^2 t_2\right)\frac{\sigma_o \varepsilon_2^{n+1}}{n+1} \tag{5-32}$$

Where r_f is the radius of the necking at fracture. According to Ha et al. the necking energies can be obtained from integration of the load-displacement curve.

The plane-strain fracture toughness J_{1c} can then be determined in the following form.

$$J_{1c} = \frac{W_T - W_{inside} - W_{outside}}{2\pi r_n C_f t} \qquad 5\text{-}33$$

The plane-strain fracture toughness, J_{1c} can be related to the plane-strain fracture toughness, K_{1c} [172]. The relation is valid for isotropic, brittle and linear elastic materials.

$$J_{1c} = \frac{K_{1C}^2 (1 - v)^2}{E} \qquad 5\text{-}34$$

Or

$$K_{1c} = \left[\frac{EJ_{1C}}{(1 - v)^2}\right]^{\frac{1}{2}} \qquad 5\text{-}35$$

5.8 Finite element methods for the small punch test

The finite element method is a numerical technique for uncovering approximate solutions to partial differential and integral equations. The technique involves discretization of a mesh over a continuous domain to form sub-domains or *elements*. The combined elements form the mesh model of the structure to be analysed. Each element can adopt a specific geometric shape such as a triangle, square, tetrahedron or any appropriate shape with a specific internal basis function. Equilibrium equations between the external forces acting on the element and the displacements occurring at its corner points or *nodes* can be established from the basis function together with the actual geometry of the elements. There will be one equation for each degree of freedom for each node of the element. These equations are most conveniently written in matrix form for use in a computer algorithm. The finite element method has many applications in structural analysis, heat transfer, electromagnetism and fluid dynamics.

The complex nature of the SPT biaxial deformation process has lead to a number of researchers to implement the finite element method or the so called *inverse* method for the analysis of strength [152, 173] and fracture toughness properties [120, 148-150, 162, 174, 175]. The numerical solution is often carried out with finite element commercial code ABAQUS. Although the method may provide good agreement with experimental results, the methodology can be exhaustive and requires a significant amount of prior knowledge of the material.

The choice of the mesh model depends on whether the material properties are isotropic or anisotropic. A 2-D axis-symmetric mesh is often implemented for isotropic materials whereas a 3-D asymmetric mesh is appropriate for anisotropic materials. It is noted by Chawla that a 3-D model incorporating the true particulate reinforcement microstructure for MMCs should be implemented over the more generalised 2-D model [176]. In addition, Ayyer and Chawla recently modelled the crack growth behaviour within an MMC using linear elastic fracture mechanics, however, the analysis disregards particle fracture [177].

A finite element method for fracture toughness determination is introduced by Foulds et al. [120, 148]. The procedure requires only a single specimen and no prior knowledge of the material's mechanical properties. The procedure involves determination of the constitutive uniaxial stress-strain behaviour from the SPT load-displacement curve using the Ramberg-Osgood model. The constitutive uniaxial stress-strain is then used to determine the local strain energy density up to crack initiation. The SPT local strain energy density is then utilised as a fracture criterion.

$$\overline{\mathrm{w}}_{\mathrm{CT}} = \overline{\mathrm{w}}_{\mathrm{sp}} \qquad 5\text{-}36$$

Finite element analysis of a cracked ASTM standard compact tension test specimen is performed. The load level at which the fracture criterion corresponds with the critical strain energy density at the crack tip is measured and compared to fracture toughness values [120, 124, 178]. Ductile and plane-strain fracture toughness values are obtained from Hand Book. The procedure proposed by Foulds for fracture toughness determination is outlined in Figure 5–10.

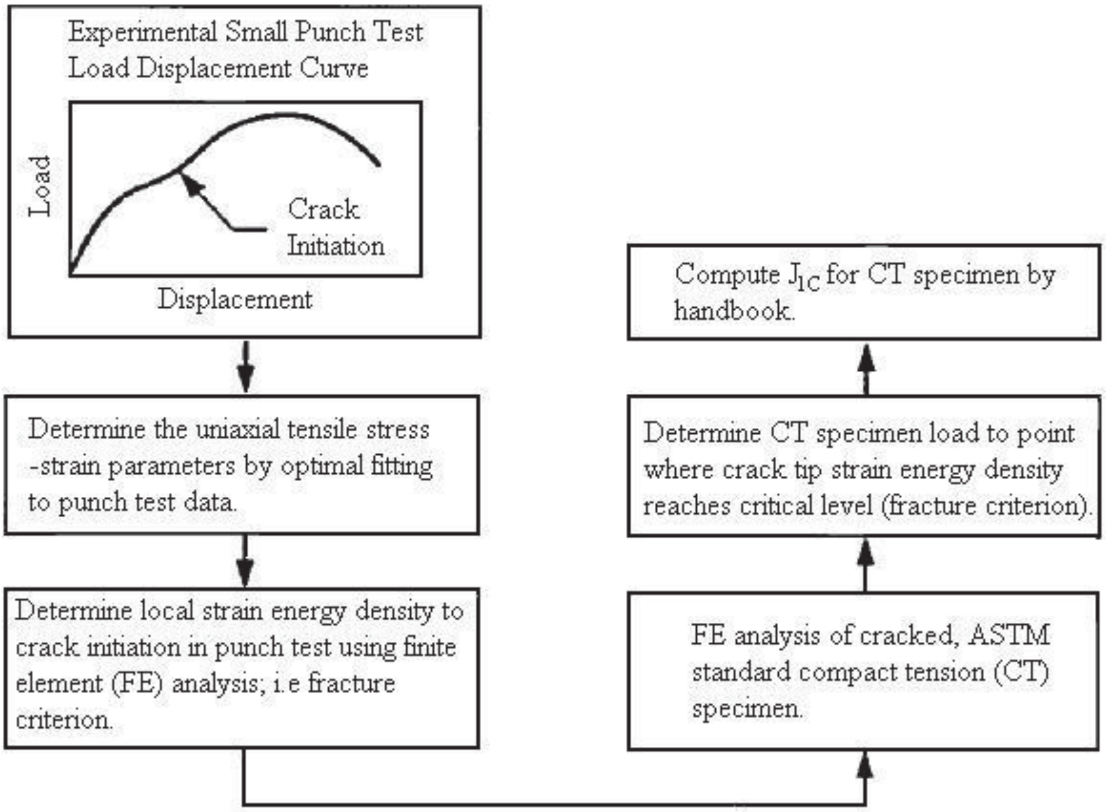

Figure 5–10. Procedure for estimating the fracture toughness by evaluating the local strain energy density from small punch test load-displacement curve [148].

Peñuelas et al. attempted to obtain the elastic-plastic and damage parameters for steels using the finite element method [149]. The finite element method for the evaluation of steels via SPT allows for characterisation of the macromechanical (E, v, σ_y, n, K) and micromechanical parameters (ε_n, f_n, f_c and f_F). These mechanical parameters are presented in Figure 5–11. The rest of the parameters can be obtained from literature [149].

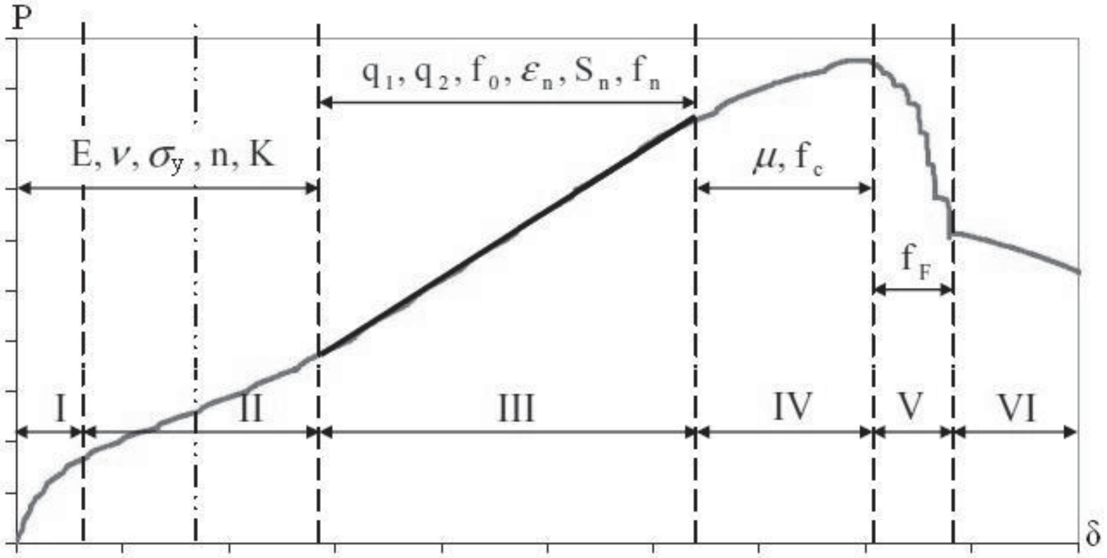

Figure 5–11. Parameters that govern each region of the small punch test load-displacement curve for structural steels [149].

From their study it is found that the elastic region I and elastic-plastic region II are enough to describe the creep behaviour of steels and in accordance with Hollomans's Law.

$$\sigma = K\varepsilon_p^n \qquad 5\text{-}37$$

Cuesta and Alegre applied the finite element method for pre-cracked SPT specimens for the purpose of determining the plane-strain fracture toughness value, K_{mat} [162]. The pre-cracked specimens are formed by laser-induced microcracking method. A combination of the failure assessment diagram and the SPT load-displacement curve is used to derive material's stress intensity factor K_{mat}.

Often researchers employ damage models into the finite element method in order to better approximate the evolution of damage to the material. The damage models include the Gurson-Tvergood-Neddleman, Johnson-Cook and Wilkins damage models. From these damage models Gurson-Tvergood-Neddleman is most often implemented in the finite element model of SPT for isotropic materials.

The Gurson-Tvergaard-Needleman damage model [139, 149, 150, 179-181] which accounts for the evolution of void nucleation, growth and coalescence has been used extensively in the finite element method of the small punch test. The damage parameter f describes the porosity of a material. The damage parameter can vary from f_o for an undamaged material to $f = 1$ for a completely damaged material. The model is using the yield condition

$$\Phi(q, p, \overline{\sigma}, f) = \left(\frac{q}{\overline{\sigma}}\right)^2 + 2.q_1.f^*.\cosh\left(-\frac{3.q_2.p}{2.\overline{\sigma}}\right) - (1 + q_3.f^{*2}) = 0 \qquad 5\text{-}38$$

Where q_1, q_2 and q_3 are fitting parameters introduced by Tvergaard et al., f characterises the porosity of the material, $\bar{\sigma}$ is microscopic flow stress, p is the macroscopic mean stress and $f*$ is the effective void volume fraction.

5.9 Neural networks for the small punch test

Artificial neural networks (ANN) can be utilised to predict the flow stress [174] and fracture toughness [182, 183] of a material through analysis of mechanical parameters. Furthermore, the method has been recently employed for analysing the mechanical properties of MMCs [184]. Abendroth and Kuna employed feed-forward neural network method on the SPT as presented in Figure 5–12. Their method employed training a feed-forward neural network via finite element to experimentally derived small punch load-displacement curves to obtain both ductile damage and fracture parameters [139, 179].

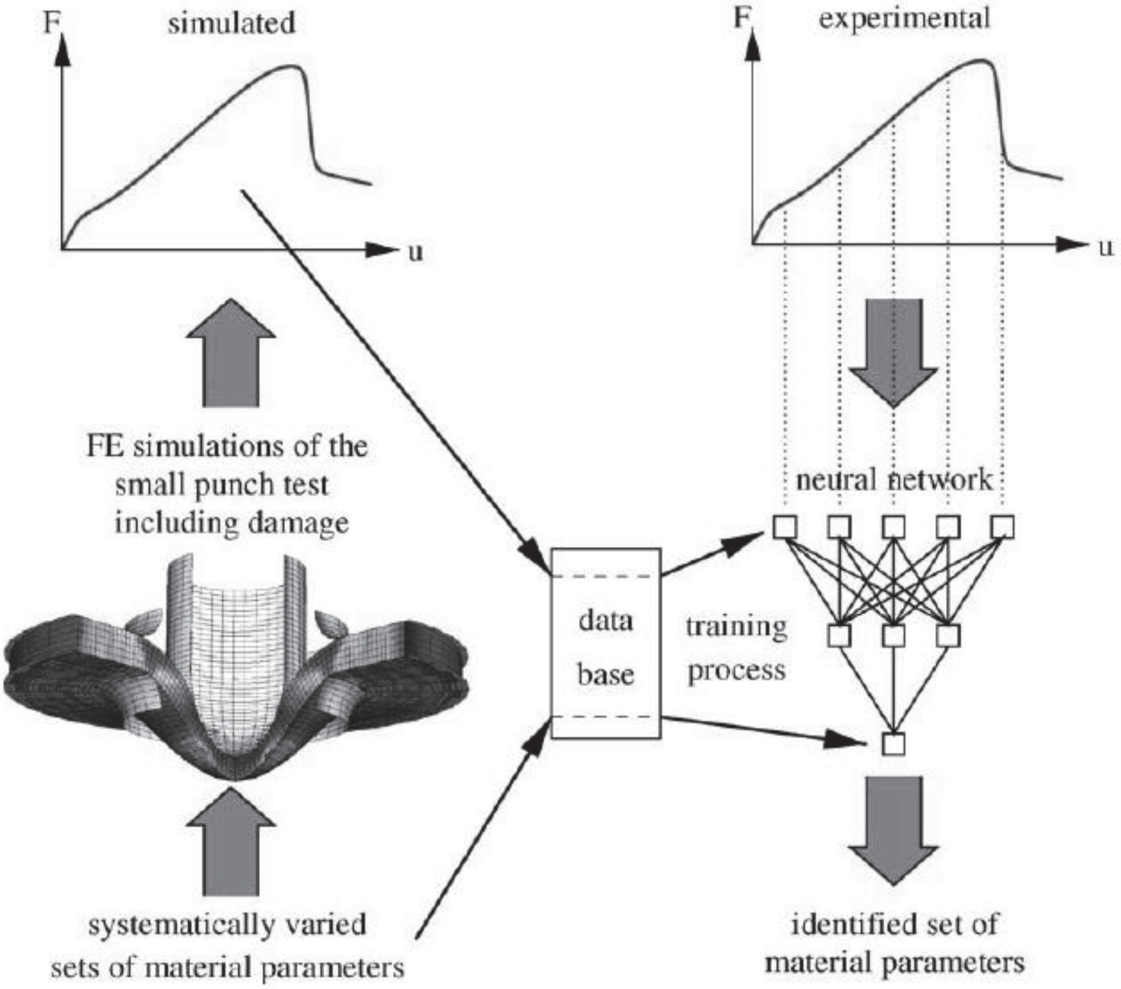

Figure 5–12. Neural network procedure to determine small punch test mechanical parameters [139].

5.10 Concluding remarks

The small punch test is an innovative test that is capable of assessing the mechanical behaviour of materials. Further research is needed to achieve correlations between the small punch mechanical values (P_y, ε_{qF} and E_{SP}) and conventional mechanical properties (σ_{YS}, K_{1c} and J_{1c}) whether it be through empirical, analytical or numerical techniques. The significance of the small specimen test can lead to the development of a multi-purpose multi-mechanical non-destructive test for assessing and monitoring advanced mechanical structures especially when material availability is limited.

CHAPTER SIX

EXPERIMENTAL METHOD

6.1 Introduction

The experimental method involves microstructural analysis and mechanical testing of aluminium and titanium alloys and MMCs. Scanning electron microscopy is conducted to assess the microstructure of the materials before and after mechanical tests. The mechanical tests involve tensile testing, plane-strain fracture toughness testing and small punch testing. In addition, finite element analysis is conducted to assess the experimental and theoretical small punch load-displacement behaviour.

6.2 Research materials

Aluminium and titanium research materials are provided by the State Key Laboratory of Metal Matrix Composites (SKLMMC), Shanghai Jiao Tong University (SJTU) Peoples Republic of China as part of the International Science Linkage (ISL) Program (Project No. CG110069 and CH080230) of the Department of Innovation, Industry, Science and Research. The aluminium materials included one base alloy and two MMCs. In addition, the titanium materials included one base alloy and two MMCs. Both the as-received aluminium and titanium materials are presented in Figure 6–1.

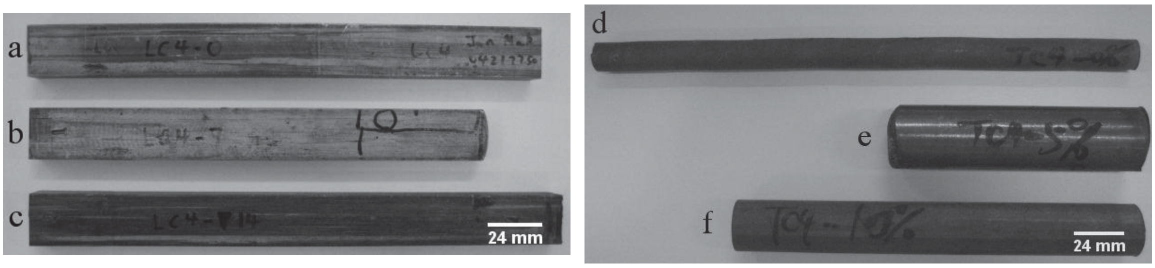

Figure 6–1. The as-received materials consist of (a) 7A04-T6, (b) 7A04/SiC/7.5p-T6, (c) 7A04/SiC/10p-T6, (d) TC4, (e) TC4/TiB, TiC/2.5w, 2.5p and (f) TC4/TiB, TiC/5w, 5p.

The nomenclature utilised in this research thesis for aluminium and titanium materials are presented in Table 6-1 and Table 6-2. The nomenclature system is based on AA – The Aluminium Association Inc. 1993, "Nomenclature System for Aluminium Metal Matrix Composites Materials", AA H35.5, IHS Standards Experts, USA. The alloy designation system used in this work is based on China’s National Standard Guóbiāo (GB) system. The system is regulated by the Standardisation Administration of the P. R. China (SAC).

6.2.1 *Aluminium materials*

The 7A04 base alloy and metal matrix consist of an Al-Zn-Mg alloy where aluminium is the predominant alloy and zinc is the primary alloying element. The 7A04 aluminium alloy possesses relatively high strength properties with good fatigue resistance relative to most aluminium alloys. Note, 7A04 was formally known as LC4 in an older China designation system. The MMCs reinforcement phase consists of SiC_p. The ceramic SiC_p reinforcement is utilised extensively in industry as a refractory material and as an abrasive. Silicon carbide is low in density whilst exhibiting high strength properties.

Table 6-1. The nomenclature for the aluminium research material.

Aluminium research materials	
Nomenclature	**Material description**
7A04-T6	7A04-T6 base alloy
7A04/SiC/7.5p-T6	7.5 vol.% SiC_p reinforced 7A04-T6 metal matrix composites
7A04/SiC/10p-T6	10 vol.% SiC_p reinforced 7A04-T6 metal matrix composites

The aluminium materials are fabricated using proprietary stir-cast processing. After stir-cast processing, the aluminium materials are extruded into bars and rods at a temperature between 400-450°C. The materials are then T6 heat treated in the following manner: Firstly, the materials are solution heat treated at 470°C for 60 minutes and water quenched. Secondly, the materials are artificially age hardened at 120°C for 24 hours and air cooled at room temperature.

6.2.2 *Titanium materials*

The titanium materials consist of a Ti-6Al-4V base alloy and metal matrix phase. The Ti-6Al-4V alloy employed in this research consists of α + β microstructure which is heat treatable to achieve moderate increases in strength. Furthermore, the alloy exhibits high strength-to-weight ratio, excellent strength and corrosion resistance. The particulate reinforcement consists of hard ceramic TiB_w and TiC_p. These reinforcements are formed in-situ during the non-consumable Vacuum Arc Re-melting (VAR) processing. Furthermore, the TiB_w and TiC_p reinforcement phases are at a 1:1 ratio.

After the non-consumable VAR process the resulting ingots are then hot forged at 1170°C from a section diameter of 120 down to 50mm then hot rolled at 1000-1050°C to the as-received bulk dimensions. The final step involved annealing at 750°C for one hour.

Table 6-2. The nomenclature for the titanium research materials.

Titanium research materials

Nomenclature	**Material description**
TC4	Ti-6Al-4V base alloy.
TC4/TiB, TiC/2.5w, 2.5p	5 vol. % (TiB_w + TiC_p) reinforced TC4 metal matrix composites
TC4/TiB, TiC/5w, 5p	10 vol. % (TiB_w + TiC_p) reinforced TC4 metal matrix composites.

6.3 Specimen orientation system

The specimen orientation system utilised for this thesis is based on the ASTM 1823 – 05a designation code for crack or notch configuration [185]. The system is used to describe both the microstructure and mechanical test orientations. Crack, notch or fracture plane orientation is designated by a hyphenated code with the first letter representing the direction normal to the crack plane and the second letter designating the expected crack propagation. The fracture toughness of a material usually depends on the crack direction and orientation in relation to the anisotropy of the mechanical working and grain flow according. The SPT and circumferential notch tension test specimen are L-T specimens since L is normal to the fracture plane and T is the expected crack propagation. The specimen orientation system utilised for this research are presented in Figure 6–2.

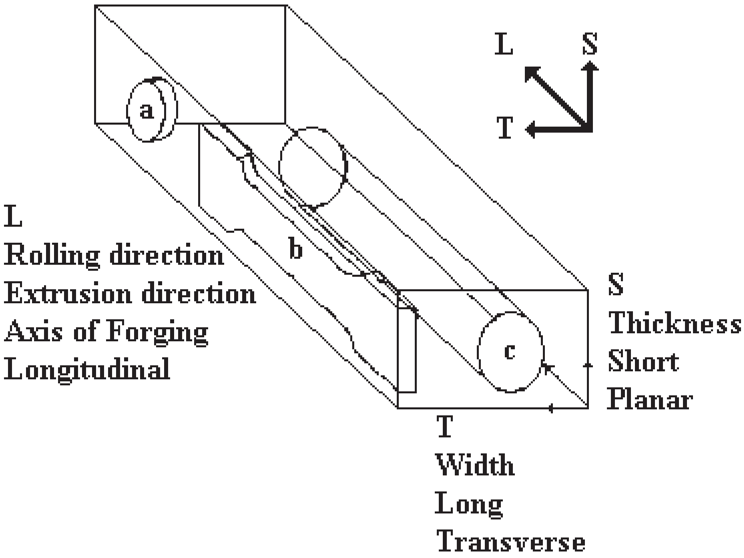

Figure 6–2. The as-machined mechanical test specimen orientation for the (a) SPT specimen, (b) tensile test specimen and (c) circumferential notch tension test specimen. Where L is the direction of the principle grain flow, T is the direction of least deformation and S is the third orthogonal direction.

6.4 Metallographic procedure

Metallographic preparation for both the aluminium and titanium materials is accomplished using the following method.

Large samples are initially sectioned using a silicon carbide cut-off wheel, however, if the samples are sufficiently small then sectioning using a precision diamond wafer blade could be used. Precision sectioning limits surface damage to around 100μm depth. Precision section should produce a fine surface that is smooth with little to no noticeably deformation.

Mounting is accomplished with either Bakelite or an epoxy resin in preparation for plane grinding. Cold mounting in an epoxy resin is preferred as mounting in Bakelite process may impart heat damage.

Mechanical grinding is accomplished with an automatic grinding machine with water lubricant. Initial grinding with Struers 1200 grit SiC paper (water, 300rpm, 150N, 30s) with an approximate particle size of 16μm is used to remove surface damage arising from sectioning. Grinding in one direction is made until all surface deformation arising from the previous step is removed. An optical microscope is used to assess progression of the grinding step.

Final fine grinding is made with Struers 4000 grit SiC paper (water, 300rpm, 150N, 30s) with an approximate particle size of 3μm. The 4000 grit SiC paper should be applied briefly to prevent the effects of particulate relief of the reinforcement phase. This is especially true if the matrix phase is softer than the reinforcement phase. The step produced a fine surface with a mirror-like finish. Final polish is achieved with chemical-mechanical polishing using 50nm colloidal silica (OP-S) and MD CHEM cloth. The polishing is made by gently by hand and with little force. The final step should produce a very fine surface such that grain boundaries and microstructure can be observed under optical and electron microscopy. The step should not take more than a few minutes to complete. Microstructure is revealed with the use of an etchant. It is observed that

Keller's and Kroll's reagent is appropriate for the aluminium and titanium materials, respectively [186, 187].

Methods are developed to overcome polishing problems such as particle pull-out from the matrix which can produce large scratch marks, relief, and the formation of comet-like dimples. This is caused by the diamond particle digging onto the surface of the titanium. Spot dimples form first followed by comet-like dimples formation as observed in Figure 6–3.

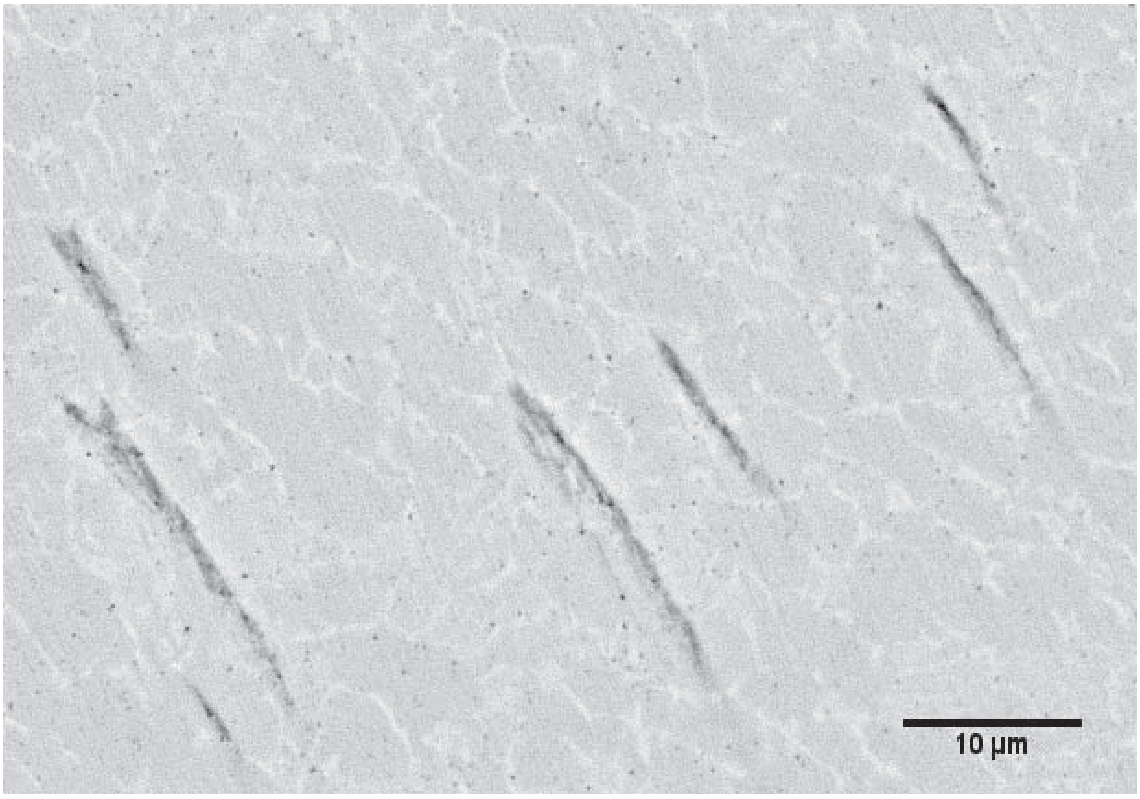

Figure 6–3. the formation of spot dimples or comet-like dimple on the surface of TC4 alloy after 1µm diamond polishing.

6.5 Microstructural examination

Microstructural examination on aluminium and titanium materials is performed using optical and scanning electron microscopy [188]. Optical microscopy in bright field mode is employed to obtain fractographic images of the specimens for the purpose of analysing the ductile, brittle and fatigue failure mechanisms in both the aluminium and titanium materials. Optical microscopy is further performed on both the single-edge bend SE(B) and circumferential notch tension (CNT) specimens for crack depth and fracture toughness analysis.

Scanning electron microscopy of the base alloy and MMCs are performed on the microstructure before and after mechanical testing. A Zeiss Supra 55 VP scanning electron microscope operating at 20kV acceleration voltage is employed for this task. The specimen is made conductive before scanning electron microscopy with either SPI Flash-Dry^{TM} Silver Paint, SPI double sided adhesive carbon filled conductive discs and 3M copper conductive tape. High resolution and high contrast micrographs is obtained using a back scatter electron detector for analysis of the grain and particulate morphology. Scanning electron microscopy with the back scatter electron detector is also carried out on the fracture surface of the SPT and CNT test specimens.

6.6 Compositional analysis

6.6.1 *Aluminium materials*

The chemical composition for the aluminium based materials is carried out using energy dispersive spectroscopy. The chemical composition for 7A04-T6 base alloy is presented in Table 6-3. The spectrum is ZAF corrected (bulk standardless). The parameters included 2000cps, 15mm working distance, dead time of 25% and 20kV acceleration voltage.

Table 6-3. The chemical composition (wt.%) for the 7A04-T6 base alloy.

Sample	Cu	Cr	Fe	Mg	Mn	Zn	Al
7A04-T6	1.6	0.2	0.4	2.3	0.4	6.9	Balance
Nominal	1.4-2	0.1-0.3	-	1.8-2.8	0.2-0.6	5-7	Balance

6.6.2 *Titanium materials*

The chemical composition for the titanium based materials is carried out using energy dispersive spectroscopy. The chemical composition for TC4 alloy is presented in Table 6-4. The spectrum is ZAF corrected (bulk standardless). The parameters included 1000cps, 15mm working distance, dead time of 20%, 10kV acceleration voltage and a dead time of 20%.

Table 6-4. The chemical composition (wt.%) for the TC4 base alloy.

Sample	Al	V	Ti
TC4	6.8	2.7	Balance
Nominal	6	4	Balance

6.7 Quantitative x-ray mapping

Quantitative x-ray mapping utilising both energy dispersive spectrometers (EDS) and wavelength dispersive spectrometers (WDS) is carried out on the aluminium and titanium material's. The quantitative x-rays map is a useful tool for the determination of the materials elemental distribution [189-191]. This is especially important for the identification of the elemental distribution of the particulate reinforcement, therefore providing the identification of the particulate distribution of the MMCs. Furthermore, quantitative x-ray mapping is carried out on the base alloy.

A scanning electron microscope fitted with multi-detector energy dispersive spectrometers are utilised for the analysis of the elemental distribution of the particulate reinforcement. Compositional analysis is performed using Moran Scientific quantitative x-ray mapping software. The software is capable of producing quantitative maps, pseudo colour maps [189] and scatter diagrams [192]. The characteristics of the detectors must be accurately determined first before the x-ray maps can be summed to achieve high resolution Quantitative x-ray mapping.

6.8 Tensile testing

Standard tensile testing is conducted according to Australian Standards. The following provides a detail overview of the material preparation methodology and mechanical testing procedure.

6.8.1 *Flat tensile test specimens*

The standard tensile test specimens are machined into flat rectangular specimens (dog-bone shape) according to Australian Standards AS 1391-2007 [153]. The aluminium and titanium tensile specimens are machined by conventional and wire electric discharge machining, respectively. Wire electric discharge machining is chosen as it provided the best route to limit hardening effects, however, the aluminium MMCs proved difficult to cut with this method due to the non-conductive nature of the SiC_p

reinforcement which led to a poor finish. Conversely the titanium MMCs produced excellent results within a relatively short amount of time with limited material wastage. Therefore a decision is made to machine all aluminium materials using conventional machining methods whilst all titanium materials are machined by wire electric discharge machining.

According to AS 1391-2007, the specimens are regarded as tensile flats since the cross-section is rectangular in shape incorporating a thickness that is equal to 3mm, width that is 6±0.03mm, total length, L_t, of 70mm, parallel length, L_c, of 36mm and the transition radius is set to 6mm. All dimensional tolerances are set to 0.03mm as required by the standard. Furthermore, the original gauge length, L_o, and original cross-sectional area of the parallel length, S_o, is calculated to be 24mm and 18mm^2, respectively. The specimen configuration of the machined test specimens are presented in Figure 6–4.

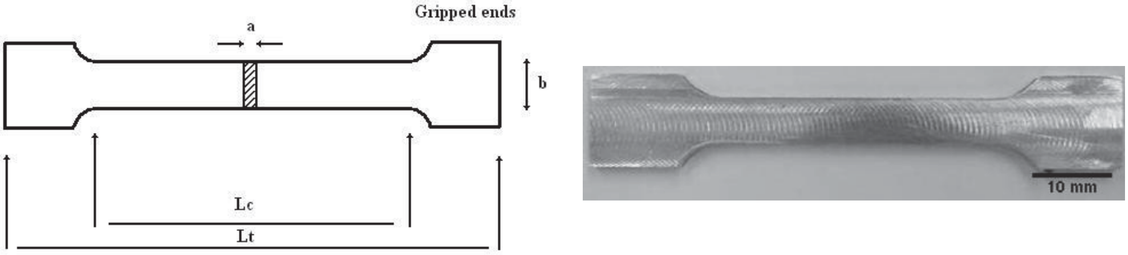

(a) (b)

Figure 6–4. Australian Standard tensile specimen [153] (a) specimen configuration and (b) machined specimen. Where a represents the thickness, L_c is the parallel length, b is the parallel lengths and L_t is the total length of the test piece.

The specimens are regarded as proportional test specimens according to Equation 6-1.

$$L_o = k\sqrt{S_o} \qquad 6\text{-}1$$

Where L_o is original gauge length, k is the international adopted number of 5.65 and S_o is the original cross-sectional area of the paralleled length.

The tensile tests are conducted using a universal tensile testing machine and the test conducted according to AS 1391-2007. The mechanical test involves uni-axial straining of a test piece at room temperature in order to determine tensile properties.

The stress and strain behaviour for the materials is recorded using a DataTaker DT800. The load cell is calibrated to have the electrical pulse such that 1mV corresponded to 1kgF. In the case of the aluminium materials an electrical pulse of 2500mV is set for a load scale of 2500kgF. In the case of the titanium materials an electrical pulse of 5000mV is set for a load scale of 5000kgF. These load scales are above the relative range of the maximum loads of 1090kgF and 2025kgF imparted by the aluminium and titanium materials, respectively.

The extension is measured via a clip-on strain gauge extensometer. The extensometer is calibrated to have the electrical pulse such that 5000mV corresponded to a physical displacement of 2.5mm.

The cross head is set to a constant speed at 2mm/min. In addition, a constant stress rate for the materials is maintained between 6 to 20MPa/s.

Tension wedge grips are employed to hold the flat tensile test specimens. The original gauge length of 24mm is scribed onto the tensile test specimen for the determination of percentage elongation after fracture. The tensile test is conducted at ambient room temperature 25°C.

Engineering stress-strain behaviour is determined for the aluminium and titanium materials including the elastic modulus, yield stress, ultimate tensile strength and percent and elongation.

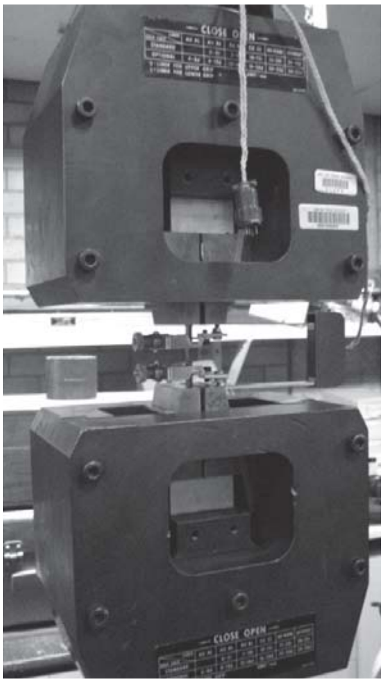

Figure 6–5. The tensile test setup with a flat tensile specimen clamped between two pairs of tension wedge grips. An extensometer is attached to the tensile specimen for strain measurement. The load capacity of the wedge grips are 100kN.

The tensile test gripping length of 11mm provided enough area to conduct a tensile test, however, problems are encountered during tensile testing due to the limited size of the specimen gripping ends. The first type of grips employed for the test are Hounsfield wedge grips with a rated gripping capacity of 20kN. During tensile testing the grips suffered dynamic brittle failure, which is a consequence of limited gripping area. Another method involved machining a hole within the tensile specimen gripping area and inserting hardened cast iron steal. During the test the cast iron steal pin failed via shear.

Finally wedge grips with a load bearing capacity of 100kN are employed for the tensile test. For the test the extensometer are modified and calibrated to measure a shorter gauge length, this in turn provided extra room for extensometer to be clipped onto the tensile specimen. Although the standard allows for flexibility in the shape and size of the grips to be determined by the user, in future, calculations should made to determine the load capacity of the grips before the start of the mechanical tests. Furthermore, enough gripping length should be provided in order to conduct the test.

6.9 Fracture toughness testing

6.9.1 *Single-edge bend testing*

The single-edge bend, SE(B), test is performed according to the ASTM E1820 – 09 standard. Qualification requirements included adhering to machining tolerances, precrack tolerances, precrack procedures and test procedures. In general, it is necessary to abide by section 9.1 and A5.4 of the ASTM E1820 – 09 standard. The machined SE(B) specimen dimensions and tolerances for the SE(B) are presented in Figure 6–6.

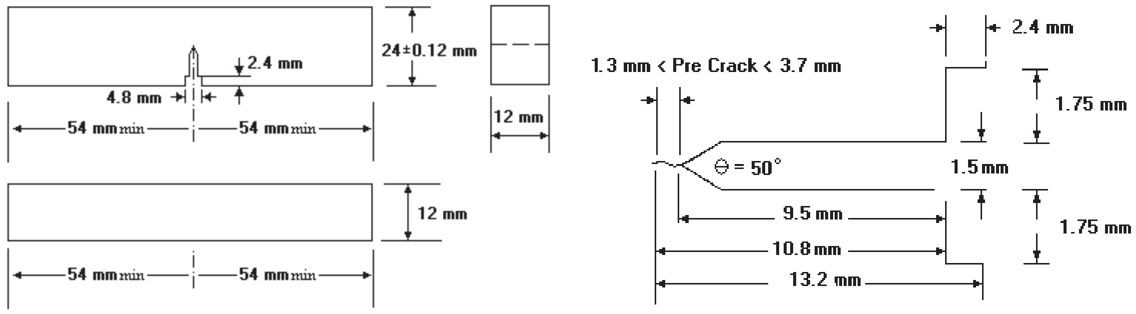

(a) (b)

Figure 6–6. (a) single-edge bend fracture toughness test specimen and (b) straight-through notch.

For pre-cracking, the SE(B) specimen is positioned in a three-point bend configuration using a universal testing machine. A strain gauge is adhered to the front face of the specimen. The force and the strain gauge are calibrated using a Keithley 197A measurement device and Instruments Division Strain Indicator, respectively.

The specimen is then mounted into the precracker as shown in Figure 6–7. The initial pre-cracking load is calculated according to the standard. Loads are increased incrementally every 10^5 cycles until crack growth is detected. The maximum and minimum loads are maintained at $R = 0.1$.

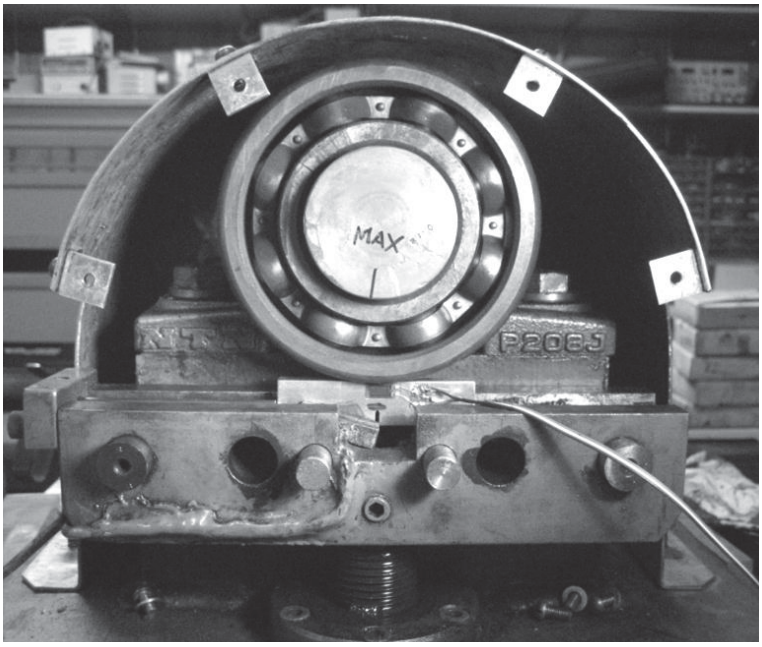

Figure 6–7. The high speed fatigue precracker.

An important factor associated with standard fracture toughness testing is to ensure the test meets validity requirements for plane-strain conditions. This is why most standard fracture toughness tests specimens are machined to relatively large specimen thicknesses. It is therefore prudent to machine the fracture toughness specimen to as large a size as can be allowed. In this case the specimens are machined to a final thickness B of 12mm. Larger specimen thickness could not be achieved due to the as-received specimen sizes and limited available materials. An extensometer is attached to measure the crack open displacement. The displacement of the extensometer is calibrated using Vernier scale from a travelling microscope.

6.9.2 *Circumferential notch tension testing*

The circumferential notch tension test specimens are essentially cylindrical bars with a circular v-notch. The following provides a detail overview of circumferential notch tension test specimen material preparation methodology and mechanical testing procedure [79].

The aluminium and titanium circumferential notched tension test specimens are machined by conventional and wire electric discharge machining techniques. The circumferential notch tension test specimen had a total length of 80mm and a diameter of 9.5mm. The v-notch had a depth of 1.25mm and an angle of 60º. The v-notch is machined using a solid tungsten carbide blade. The saw teeth are sharp with a cutting angle of 60º corresponding to the v-notch configuration. Further sharpening of the v-notch can be made with scalpel blades or sharps. It is important that the v-notch be made as sharp as possible to reduce impedance to crack initiation. The circumferential notch tension test specimen configuration and test piece is presented in Figure 6–8 (a).

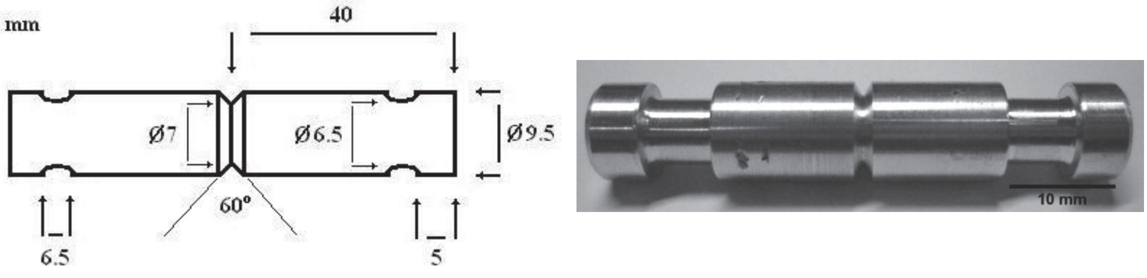

(a) (b)

Figure 6–8. The circumferential notched tension test (a) specimen configuration and (b) machined specimen.

Grooves are incorporated into the design at the ends of the circumferential notch tension test specimen as observed in Figure 6–8 (b). The grooves provide a means for gripping the specimen via split collets during uniaxial testing. The grooves are employed due to limited material availability of the test and gripping area. The original gripping method employed v-serrated mechanical wedge action grips, however, the wedge grips would collapse due to the limited length of the circumferential notch tension test piece.

Fatigue pre-cracking is required before circumferential notch tension testing can commence. In addition, the grooves have yet to machine into the specimen at this stage. This step requires the use of a high speed rotational-bending fatigue machine as presented in Figure 6–9.

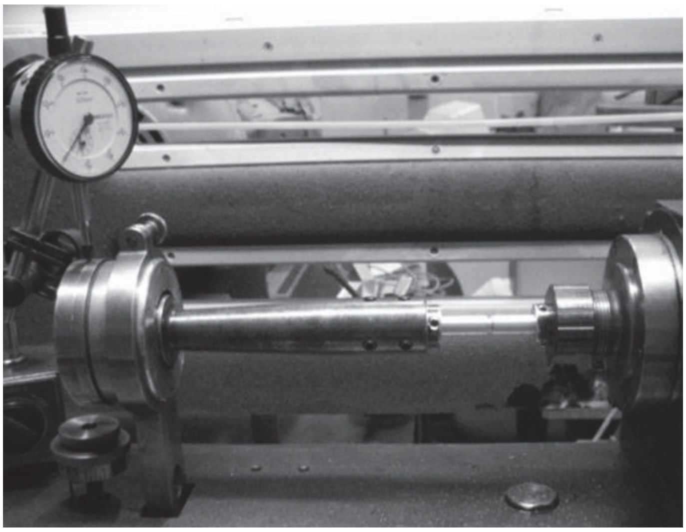

Figure 6–9. Rotational-bend fatigue machine, to induce a precrack in the circumferential notch tension test specimen.

The rotational-bending fatigue machine employs Rubber-Flex collets that are used to hold either the circumferential notch tension test specimen or machined specimen adapters as shown above. The specimen adaptors are employed to hold the specimen using $^{3}/_{32}$ inch cast iron grub screws. Attached to one of the specimen adapters is a beam, this beam is allowed to rotate whilst connected to a lever load system. A Mitutoyo dial indicator (HFS684) is used to measurement beam deflection. It is important that the beam be aligned and balanced such that minimal deflections or vibrations are observed on the Mitutoyo dial indicator, the dial should only register the fatigue cracking (beam deflection). The rotational-bending fatigue machine is calibrated in order to determine crack depth with respect to beam deflection. It is found that a crack depth of 1mm corresponded to a deflection of 0.1mm.

The circumferential notch tension test specimen underwent rotation bending. This rotational-bending fatigue machine setup is similar to the cantilever experiment where a load is applied on one end of the test specimen. This load is manually controlled by using a lever system. As the specimen rotates higher stresses is experience at the v-notch tip, it is likely that a fatigue crack will form at the tip of the v-notch. The stress can be estimated by using Equation 6-2 which considers simple beams of uniform cross-section.

$$f_z = \frac{64YW}{\pi d^4}(L - x) \qquad 6\text{-}2$$

Where f_z is the maximum stress (Pa) at point x from the support, Y is the distance from the extreme fiber to the neutral axis, W is the total load, d is the depth of beam, L is the length of beam and x is the distance along the beam from the support [193]. The stress employed for high speed crack fatigue testing should always be below the yield stress of the material.

Beam deflection is an important parameter when performing high speed fatigue crack testing. The fatigue cracking process is automatically stopped after beam deflection of 0.1mm. A beam deflection of 0.1mm typically produced a fatigue crack of 1mm in depth. If no deflection is detected in 10^7 cycles, the machine is stopped and the load increased before restarting the test again.

Identification of a fatigue crack is made though optical microscopy after a beam deflection of 0.1mm via the dial gauge as shown in Figure 6–9. A dye penetrant is employed to identify whether a fatigue crack had formed on the groove of the circular v-notch.

The mechanical test involved uni-axial loading of a circumferential notched test piece at room temperature in order to determine maximum load before failure. The stress intensity factor K_1 is then determined from measurement of the load and the size of the fatigue crack [86, 94-96].

The load behaviour for the materials is recorded using a DataTaker DT800. The load cell is calibrated to have the electrical pulse such that 1mV corresponded to 1kgF. For the aluminium and titanium materials electrical pulse of 5000mV is set for a full scale of 5000kgF. The cross head speed is maintained at 2mm/min, this is the same speed utilised for the tensile test. The circumferential notch tension test setup is shown in Figure 6–10.

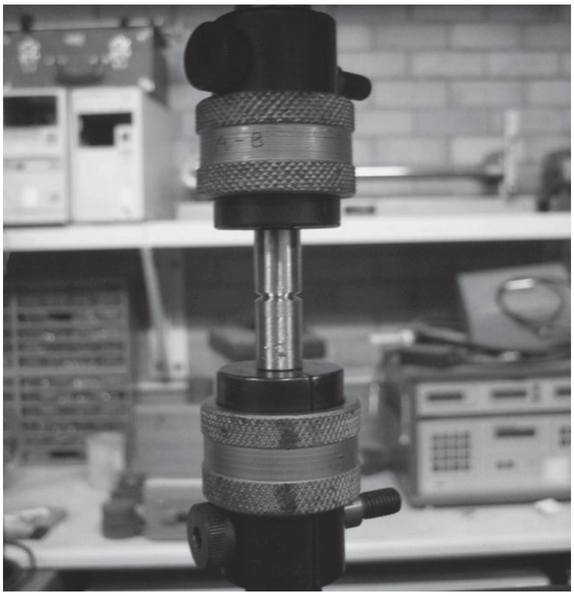

Figure 6–10. Circumferential notch tension test (a) specimen held by split-collet grips.

6.9.3 *Small punch testing*

The SPT specimens are disc shaped. The following provides a detail overview of SPT specimen material preparation methodology and mechanical testing procedure. The test can be used to evaluate the tensile and fracture behaviour of a material.

The six SPT specimens are machined into disk-shaped specimens with a diameter of 6mm and a thickness of 0.7mm. This is accomplished with conventional machining methods such as from a lathe or wire electric discharge machining (WEDM).

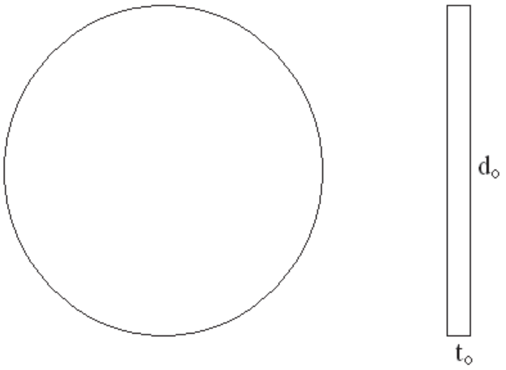

Figure 6–11. The small punch test specimen configuration.

Samples are initially machined into 6mm diameter rod-shaped samples. A Struers Accutom-50 cut-off machine with a 459CA diamond wafer blade is used to slice the specimen into disk-shaped specimens. The blade's thickness in addition to the small punch disc's thickness should be accounted for as this will determine the number of specimens that can be produced from the rod sample.

Table 6-5. Accutom-50 cut-off saw parameters for aluminium based materials.

Cutting Parameter	
Wheel	459CA
Feed	0.015mms^{-1}
Water	On
Speed	5000rpm
Thickness	0.7mm

The preparation of the SPT test specimens involved the use of Struers Accustop-30 specimen holder for controlled grinding to within 20μm accuracy. The following steps are developed in order to produce thin, parallel sided specimens:

1. Measure all six of the machined SPT specimens' thickness using the Mitutoyo Digimatic Indicator. Measure 5 points around the specimens to ascertain overall specimen thickness.
2. Place the Struers Accustop-30 insert mount (ASPAR) onto a hot-plate and set to 121ºC. Melt a small amount of Crystalbond^{TM} onto the mount surface for the six SPT specimens. Adhere the SPT specimens onto the mount surface in a hexagonal pattern. Remove the mount from the hot-plate.
3. Apply equal amount of pressure to the SPT specimens using a load device. This is to maintain similar Crystalbond^{TM} thickness. Allow the mount to cool.
4. Once cooled place the mount onto two glass slides with equal thicknesses.
5. Then place the Struers Accustop-30 holder over the insert mount and clamped into place. Parallelism should be within ± 5μm.
6. Initially grind down the SPT specimens with 1200 grit SiC paper to 50μm. This should be done with an automatic grinding machine. Followed by another 30μm with 2500 grit SiC paper and finally a further 10μm with 4000 grit SiC paper.
7. Once completed, repeat steps 1 to 6 on the other side of the machine SPT specimens. Adjust grinding as necessary to achieve a tolerance of around 10 μm for the final polish.
8. Then polished down the specimen to 0.5 ± 0.005mm thickness using MD-Chem pad with OP-S colloidal Silica (50nm) by hand. The surface finish should be mirror-like which would obstruct observation if too much glare is present therefore the specimens should be etched before the commencement of the small punch test.

Note that it is, it is important to prevent gradients and multiple faces from forming during the grinding stage. In addition, the grinding for each step should be completed before moving to the next step.

The SPT procedure involved loading a disk-shaped specimen via spherical punch as presented in Figure 6–12 (a). The SPT may be referred to as the small punch bulge test since the SPT specimens are clamped into position. The SPT jig consisted of an upper and lower die that is firmly clamped together by four screws. Furthermore, the screws flatness are tightened with a torque wrench to around 2Nm, this is to maintain an even downward pressure and to constrain the SPT specimen. In addition, the jig is aligned with alignment rods for the upper and lower die. The SPT jig incorporated a spherical punch diameter of 2mm with a lower die bore diameter of 4mm and a lower die chamfer edge of 0.22mm. The spherical ball punch is made of cast iron and incorporates a hardness of 55 HRC.

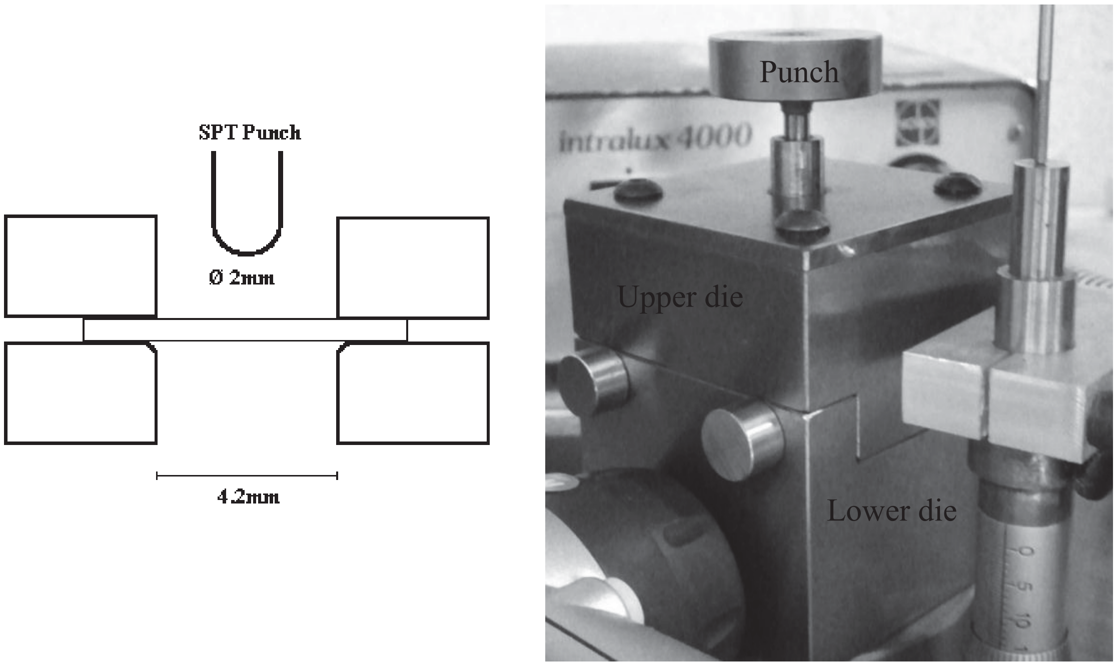

(a) (b)

Figure 6–12. The small punch test configuration (a) schematic diagram (b) experimental setup at the University of Technology, Sydney.

A 5kN load cell Instron 8562 universal mechanical testing machine is utilised for the SPT. The actuator resolution is 0.01mm.The load and displacement is monitored and recorded using Instron Blue Hill mechanical test software. SPT is recorded until load drop then stopped. The tests are set to a constant displacement rate of 0.2 mm/min. The surface deformation of the SPT specimen is monitored with a borescope attached to an ELMO-3 Chip charge coupling device (CCD). The SPT is conducted in ambient temperature. Further improvement would involve SPT inside a SEM for in-situ analysis and observation of crack formation. Accurate identification of the crack initiation is probably the most important aspect of analysis.

6.10 Finite elemental analysis of small punch test

The ABAQUS student edition version 6.6-2 is employed for finite element modelling and analysis of the SPT research materials [144, 194-196]. The finite element model is a 2-D axisymmetric model of SPT configuration and conforms to the dimensions of test. The small punch disc specimen is specified as a homogeneous model and is based on continuum stress-strain deformation properties of the material. The experimental elastic and plastic properties for the materials are inputted into the finite element program. The elastic properties included the elastic modulus and Poisson's ratio. The plastic properties included tensile true stress-strain behaviour for the materials. The SPT specimen model is descretized into six hundred four node axis-symmetric quadrilateral reduced integration hybrid elements. The clamped surfaces are constrained for the method. A sliding contact surface is implemented for the punch and the specimen top surface. The Von Mise's stress contour maps are generated for each type of material studied, APPENDIX I. Note, the *step time* utilised for the FEM is equivalent to displacement in millimetres. In addition, the SPT load-displacement curve is generated from the finite element method. The 2-D axisymmetric finite element model of SPT configuration is presented in Figure 6–13.

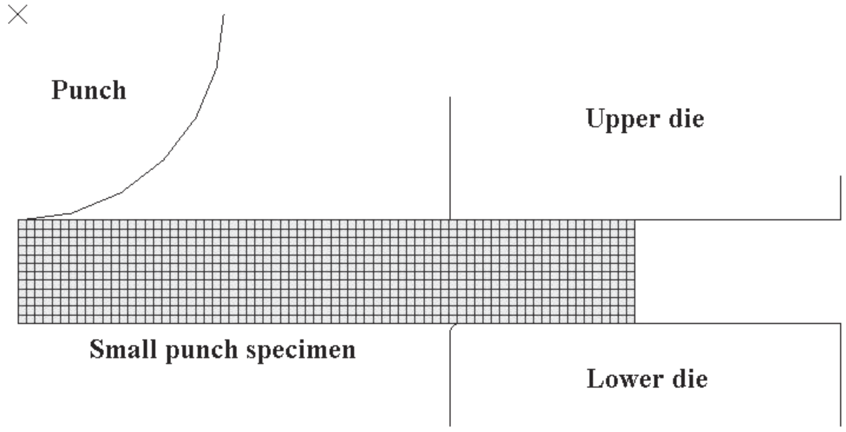

Figure 6–13. The finite element model of the small punch test configuration.

6.11 Concluding remarks

Metallographic techniques are developed to reveal the microstructure for the alloys and MMCs. Kroll's and Keller's reagents proved useful in revealing the fine microstructural features in both the aluminium and titanium materials. Scanning electron microscopy revealed microstructures and for both the alloy and MMCs. In addition, energy dispersive spectroscopy and quantitative x-ray mapping are used to identify the reinforcement content. Fractography is conducted after mechanical testing. Conventional tensile, single-edge notched bend and circumferential notched tension preparation and test techniques are successfully completed in obtaining the yield strength, σ_{YS}, and plane-strain fracture toughness, K_{1c} and J_{1c}, properties. Material preparation and testing methodology for the SPT specimens are introduced. The methods developed from this research should prove useful for future conventional and small punch testing.

CHAPTER SEVEN

RESULTS AND DISCUSSION

7.1 Introduction

Chapter seven presents the results and discussion on the microscopy, mechanical testing and finite element analysis of the 7AO4-T6 aluminium and TC4 titanium materials. Scanning electron microscopy is utilised to characterise the microstructure and composition of the materials. Furthermore, fractography is utilised to assess the fracture surfaces of the materials after mechanical testing. Mechanical tests involved small punch, tensile and fracture toughness assessment.

7.2 Aluminium results

7.2.1 *The microstructure*

Scanning electron microscopy is conducted on stir-cast 7A04-T6 aluminium base alloy, 7A04/SiC/7.5p-T6 aluminium MMC and 7A04/SiC/10p-T6 aluminium MMC in the longitudinal, transverse and planar sections as presented in Figure 7–1 and Figure 7–2. The chemical composition for the 7A04-T6 aluminium base alloy is presented previously in Table 2-1. Scanning electron microscopy revealed the metal matrix to exhibit a textured appearance with fine grains that are aligned along the extrusion and longitudinal axis. The grain boundaries are revealed by Keller’s etchant. In the transverse section the metal matrix appeared to exhibit a dendritic microstructure that is common for cast material. Scanning electron microscopy confirmed the presence of SiC_p (dark) reinforcements in both the 7A04/SiC/7.5p-T6 aluminium MMC and 7A04/SiC/10p-T6 aluminium MMC. The SiC_p are observed to be homogeneously distributed within the 7A04 aluminium MMCs. The shape of the SiC_p can be characterised as equiaxed exhibiting sharp edges. Clean interfacial wetting between the 7A04 metal matrix and the SiC_p is evident, as shown in Figure 7–1.

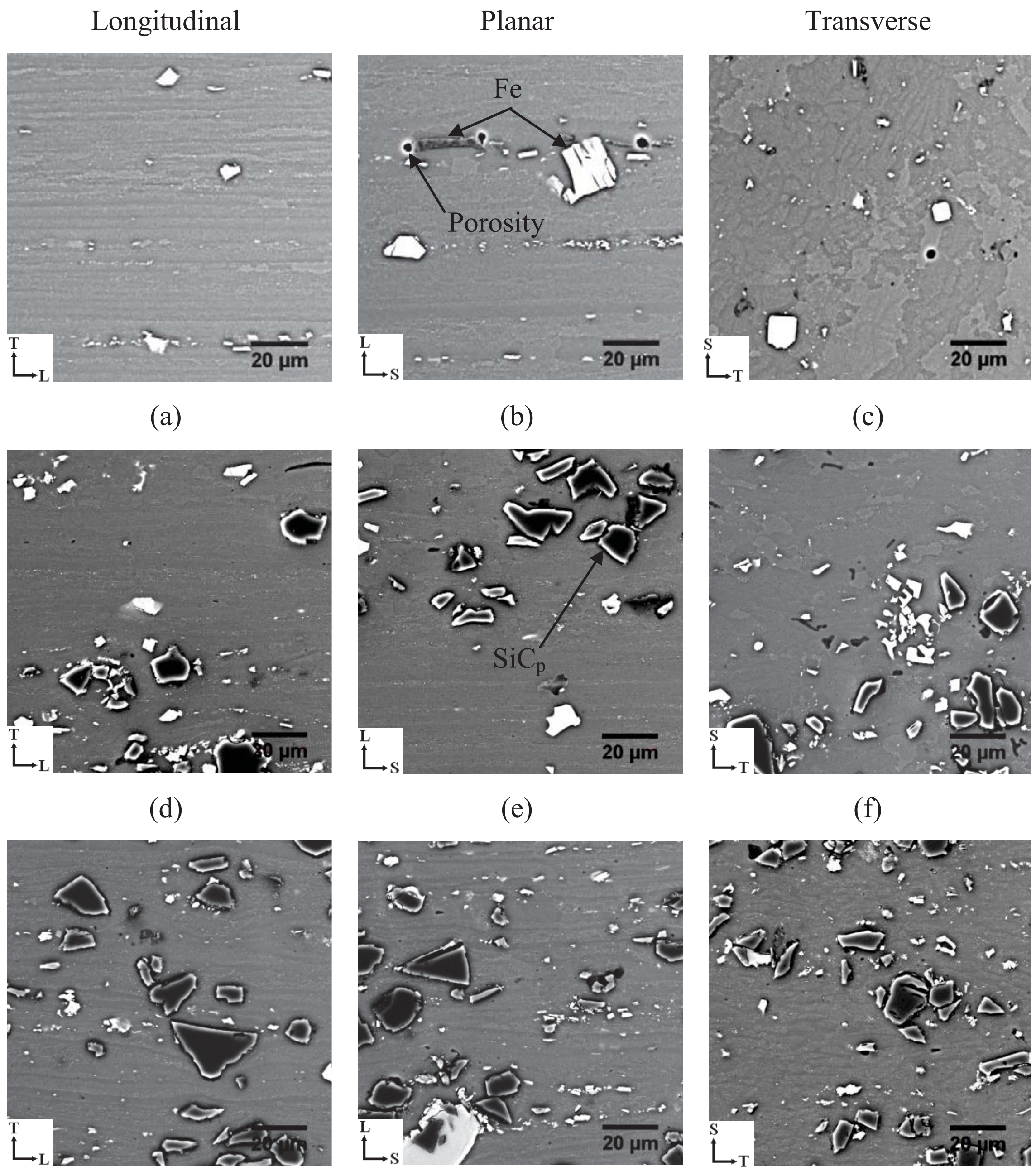

(a) (b) (c)

(d) (e) (f)

(g) (h) (i)

Figure 7–1. Backscatter electron micrographs for the as-received (a, b, c) 7A04-T6 aluminium alloy, (d, e, f) 7A04/SiC/7.5p-T6 aluminium MMC and (g, h, i) 7A04/SiC/10p-T6 aluminium MMC.

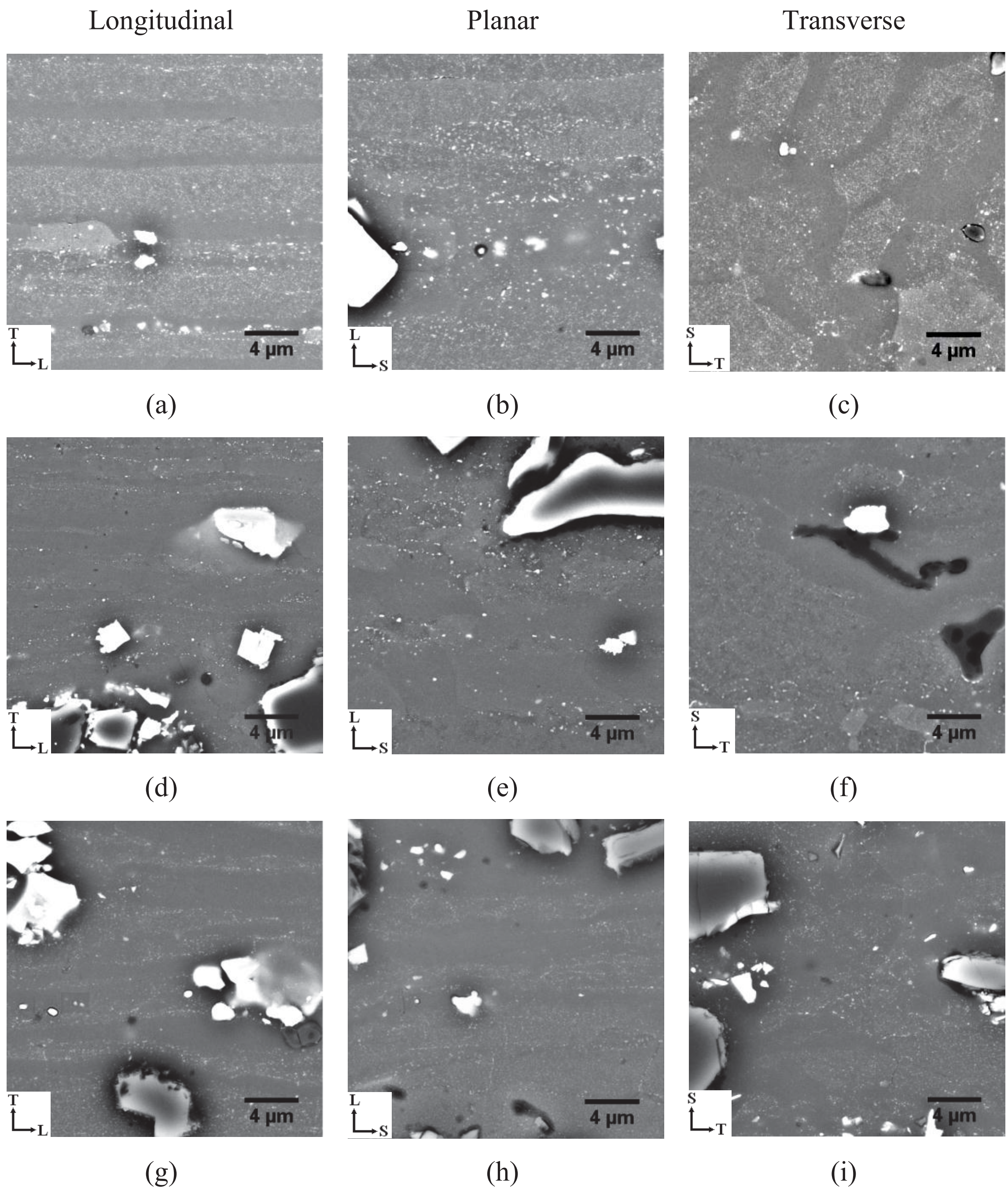

(a) (b) (c)

(d) (e) (f)

(g) (h) (i)

Figure 7–2. Backscatter electron micrographs for the as-received (a, b, c) 7A04-T6 aluminium alloy, (d, e, f) 7A04/SiC/7.5p-T6 aluminium MMC and (g, h, i) 7A04/SiC/10p-T6 aluminium MMC.

Iron inclusions (white) are evident in both the 7A04-T6 aluminium alloy and the 7A04-T6 aluminium MMCs as observed in Figure 7–1 and Figure 7–2. The iron inclusions are mainly observed as white rectangular equiaxed structures whilst some appear as dark grey plate-like structures. Energy dispersive spectroscopy revealed that the iron inclusions are 99% pure. In addition, microvoids are observed to have formed around the ends of the dark grey plate-like iron inclusions as observed in Figure 7–1 (b). The size of these iron inclusions is generally smaller than the SiC_p reinforcement, however, the size can range from 0.01μm up to 20μm in length. These iron inclusions are observed throughout the metal matrix, both within the grains and along the grain boundaries. The presence of iron inclusions is a consequence of an iron ball milling process that is implemented for the preparation of aluminium powder before stir-casting. There is evidence of crack formation in the iron inclusions and SiC_p reinforcements, these cracking events are attributed to post-processing. The average particle size, volume percent and mean free path of the particulate reinforcement for the aluminium MMCs are presented in Table 7-1. Ten BSE micrographs are obtained at a magnification 100x. Image analysis is performed on these micrographs and the particles are then counted. The average particle size is determined by measurement of the particle's major-axis length. The volume percent is determined from area measurement and by assuming stereological equivalence of the particle area and volume. The standard deviation of the measured particles is taken as the error of the measurement. The mean free path is determined from Equation 7-1 [197].

$$\mathrm{M.F.P.} = \frac{4\mathrm{r}(1-\mathrm{V})}{3\mathrm{V}} \qquad 7\text{-}1$$

Where M.F.P. is the mean free path, r is the particle radius, and V is the volume fraction.

These results indicate that the average particle size for the SiCp reinforcement is around 10µm. The analysis is based on measuring the surface of the SiCp that are embedded within the metal matrix. This limited the measurement to the portion of the SiCp that are in view. Nevertheless the upper limits of the particle size could be argued to be no more than around 20µm.

Table 7-1. The particle size and volume percent of SiC$_p$ for aluminium metal matrix composites.

Materials	Particle size SiC$_p$ (µm)	Volume SiC$_p$ (%)	Mean free path (µm)
7A04/SiC/7.5p-T6	9.8 ± 6.8	7.5 ± 2.1	242
7A04/SiC/10p-T6	9.4 ± 6.2	10.2 ± 1.3	166

Quantitative x-ray mapping (QXRM) is conducted on the aluminium base alloy and MMCs. Pseudo colour maps are produced via post-processing of the QXRM as presented in Figure 7–3. The elements aluminium, zinc, magnesium, silicon and iron are assigned with colour labels. In this way the precipitates and particulate distributions are identified. Weighted averaging is applied to the x-ray map.

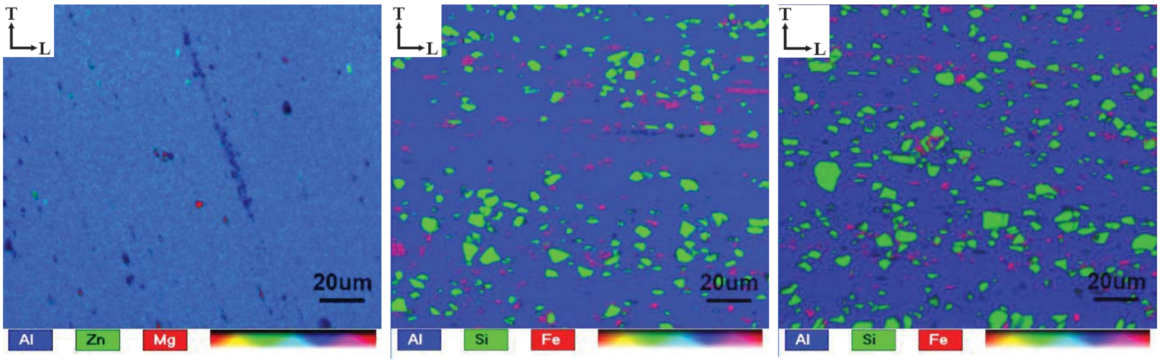

(a) (b) (c)

Figure 7–3. Pseudo colour quantitative x-ray mapping for the as-received (a) 7A04-T6 aluminium alloy, (b) 7A04/SiC/7.5-T6 aluminium MMC and (c) 7A04/SiC/10-T6 aluminium MMC. The mapping parameters included 6000cps, 20kV and 512x512 pixels resolution.

The elemental distribution is easily identified in the pseudo colour maps. Zinc-rich and magnesium-rich phases are observed to have formed with additions of iron inclusions (dark regions) as presented in Figure 7–3 (a). Again the iron inclusions are aligned along the extrusion direction. The SiC_p distribution is coloured green and is easily identifiable in the pseudo colour map. In the case of the MMCs the iron inclusions are assigned the colour red. Note that chromium and manganese are not chosen to be visualised in the QXRM.

7.2.2 *The tensile test*

Standard tensile tests are performed on the aluminium materials in order to assess the effect of increasing SiC$_p$ reinforcements on tensile properties and to obtain the yield strength, σ_{YS} for fracture toughness evaluation. In general, at least four tensile tests are conducted for each type of material. The strain rate is set to 0.2mm/min. Typical tensile curves are presented in Figure 7–4 and the results are presented in Table 7-2.

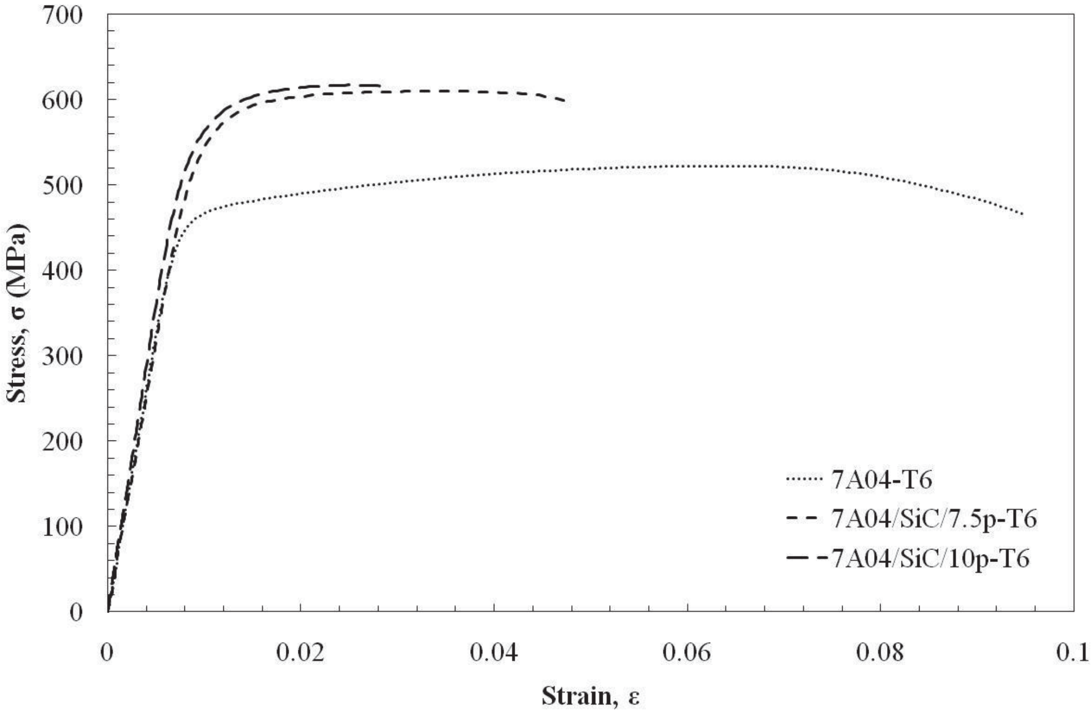

Figure 7–4. Engineering stress-strain behaviour for 7A04-T6 aluminium alloy, 7A04/SiC/7.5p-T6 aluminium MMCs and 7A04/SiC/10p-T6 aluminium MMCs.

It is observed that as SiC$_p$ reinforcement increases so does the overall stiffness and elastic modulus. This effect although minor is a consequence of the high stiffness properties imparted by the SiC$_p$ reinforcements. Furthermore, the yield strength and ultimate tensile strength increase with increasing SiC$_p$ reinforcement. This is a consequence of the constraint strengthening mechanism imparted by the reinforcement phase, this strengthening behaviour has been confirmed by numerous investigators [57, 74, 75]. Moreover, it is observed that the ductility is significantly decreased with increasing SiC$_p$ reinforcement. This expected decrease in ductility is caused by SiC$_p$

reinforcement acting as a barrier to dislocation movement. This early failure is attributed to an early onset of microplasticity around the sharp edges of the particulate reinforcement leading to increasing constraint [53]. The strength properties for the MMCs are similar, which suggested additional SiC_p reinforcement would not yield further significant increases in strength. The tensile mechanical properties for the aluminium materials are presented below in Table 7-2. The error is based on the standard deviation.

Table 7-2. Tensile mechanical properties for 7A04-T6 aluminium alloy, 7A04/SiC/7.5p-T6 aluminium MMC and 7A04/SiC/10p-T6 aluminium MMC.

Materials	Elastic modulus (GPa)	Yield Strength (MPa)	Ultimate Tensile Strength (MPa)	Elongation (%)
7A04-T6	75 ± 8	462 ± 10	525 ± 20	13 ± 1
7A04/SiC/7.5p-T6	79 ± 13	555 ± 4	593 ± 150	4 ± 1
7A04/SiC/10p-T6.	85 ± 12	557 ± 9	607 ± 9	2 ± 1

7.2.3 *The single-edge bend test*

This section discusses the factors encountered during research on the standard single-edge bend, SE(B), fracture toughness test on both the 7A04 aluminium alloy and MMCs which eventually lead to the decision to employ the circumferential notch tension (CNT) test method for the determination of the plane-strain fracture toughness, K_{1c}, values. The decision to choose the CNT test proved successful for the evaluation of plane-strain fracture toughness, K_{1c}, for both the aluminium and titanium MMCs.

The original experimental research aim involved SE(B) fracture toughness tests according to the ASTM E1820 – 09 standard [77] procedures to determine the plane-strain fracture toughness, K_{1c}, values for both the 7A04 aluminium alloy and MMCs. The fracture toughness values from the SE(B) test can then be empirically correlated with the small punch energy, E_{SP}, and equivalent fracture strain, ε_{qF}, values. An empirical relationship between K_{1c} and ε_{qF} can then be established for aluminium alloy and aluminium MMC materials. Furthermore, the effect of increasing reinforcement content can be studied. In addition, the empirical relationship arising from this research can then be compared with literature values. Unfortunately the single-edge bend specimens are found to yield invalid K_{1c} values and had to be discontinued. The experimental setup used for this research is shown in Figure 7–5. In general, at least three tests are conducted for each type of material.

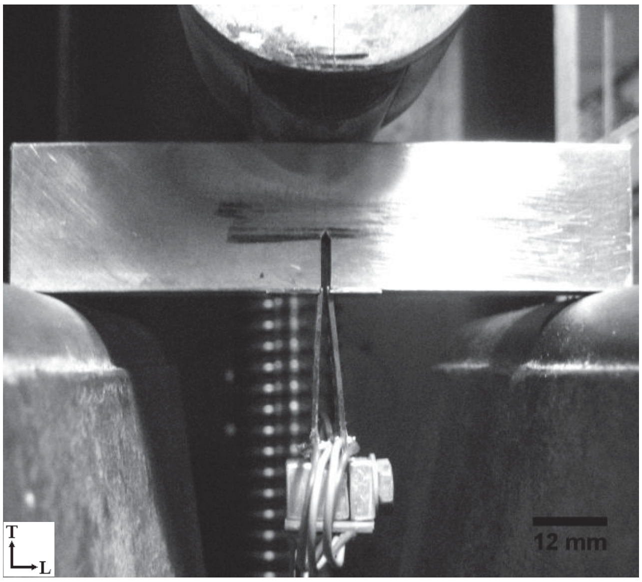

Figure 7–5. Single-edge bend test specimen in a three point bending configuration.

The load verse crack tip open displacement (CTOD) curves are then derived as presented in Figure 7–6, Figure 7–7 and Figure 7–8. Pop-in is observed for two of 7A04 aluminium alloys [77]. The qualifying load P_Q is identified from the intersection of the 95% secant and K_Q is determined from the test.

In order to meet the qualification requirements of the ASTM E1820 – 09 standard, the qualifying ligament size b calculated from K_Q must be less than the initial un-cracked ligament, b_o, which is 12 mm and in accordance with Equation 4-3. Unfortunately this is not the case for the three 7A04 aluminium alloy SE(B) specimens that are tested. The ligament sizes calculated from K_Q are all found to be larger than the machined initial un-cracked ligament size b_o of 12mm and it is not possible to machine larger ligament sizes. Therefore the SE(B) test failed to meet the ASTM E1820 – 09 qualification requirements. Successive attempts are made to minimise the precrack length and increase the uniformity of the fatigue precrack front, however, all without success. The results for the SE(B) test are presented in Table 7-3.

Table 7-3. The 7A04-T6 aluminium base alloy single-edge bend loads, validity requirements and fracture toughness values. The 0.2% off-set yield strength, σ_{YS}, for the 7A04-T6 aluminium base alloy is 462MPa.

Test	P_Q (N)	P_{max} (N)	P_{max}/P_Q[5]	B[5] (mm)	a_p[5] (mm)	K_Q ($MPa\sqrt{m}$)	J_Q (kJ/m^2)
1	3512	3886	1.11	14	3.8	35	16
2	4948	5418	1.09	18	4.8	39	19
3	6815	7267	1.07	22	3.4	43	22

It is observed from Table 7-3 that most validity requirements are essentially met, all measured fatigue crack lengths, a_p, is within the validity requirements. All P_{max}/P_Q are met except for Test 1 which is just larger than the required ratio of $P_{max}/P_Q = 1.10$. It is the initial specimen thickness calculated from K_Q that did not satisfy the validity requirements since the utilised as-received specimens had a thickness of 12mm. The result of K_Q suggested larger specimens are required to satisfy ASTM E1820 – 09 SE(B) fracture toughness standards. In fact the procedure suggested an increase of the initial un-cracked ligament size of 18mm, $1.5b_o$, should meet the minimum requirements for plane-strain fracture toughness, K_{1c}, conditions. Despite this the K_Q values obtained from the SE(B) test could be used to compare with plane-strain fracture toughness, K_{1c}, values determined from CNT test.

---

[5] Most parameters met the validity requirements set by the standard except for the minimum thickness, B, which was determined from K_Q.

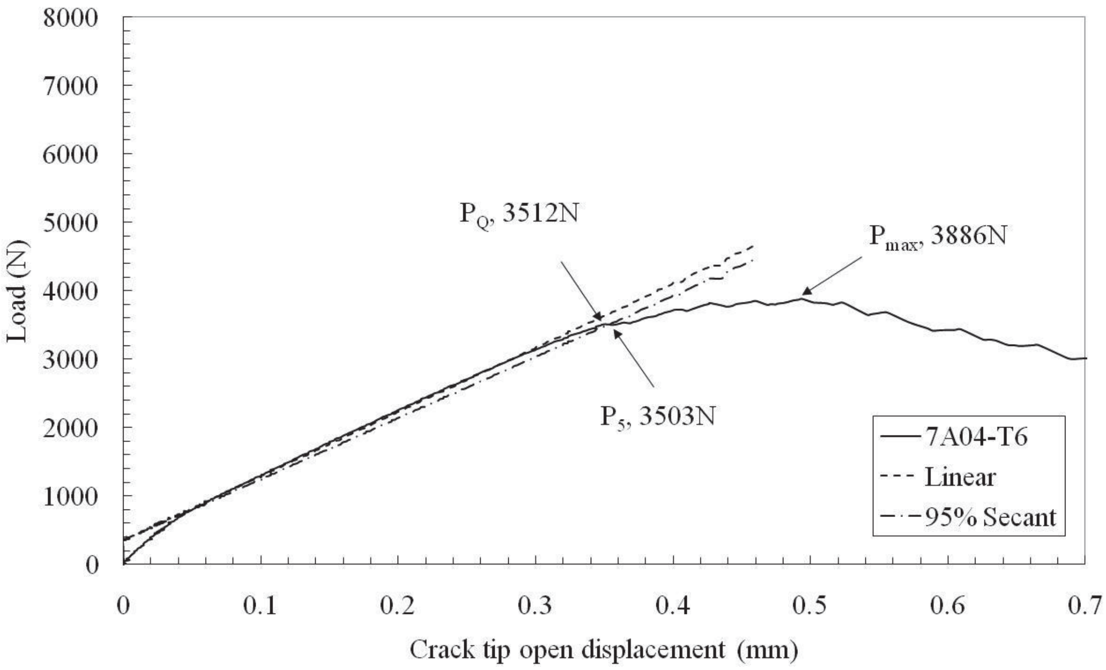

Figure 7–6. Fracture toughness load-displacement curve for 7A04-T6 aluminium alloy.

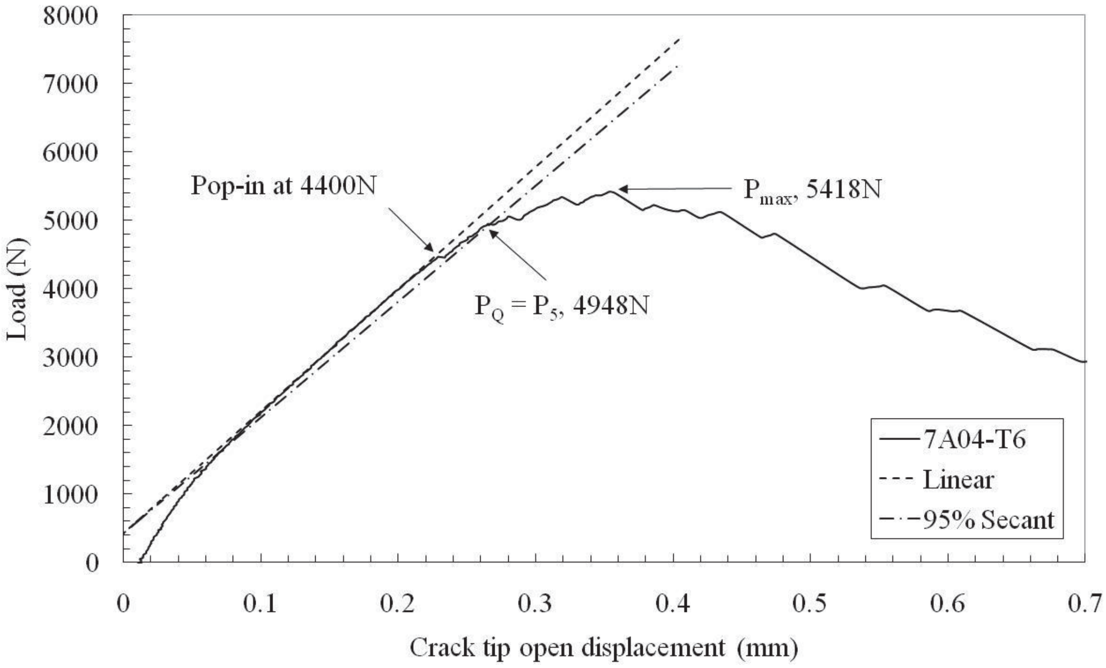

Figure 7–7. Fracture toughness load-displacement curve for 7A04-T6 aluminium alloy.

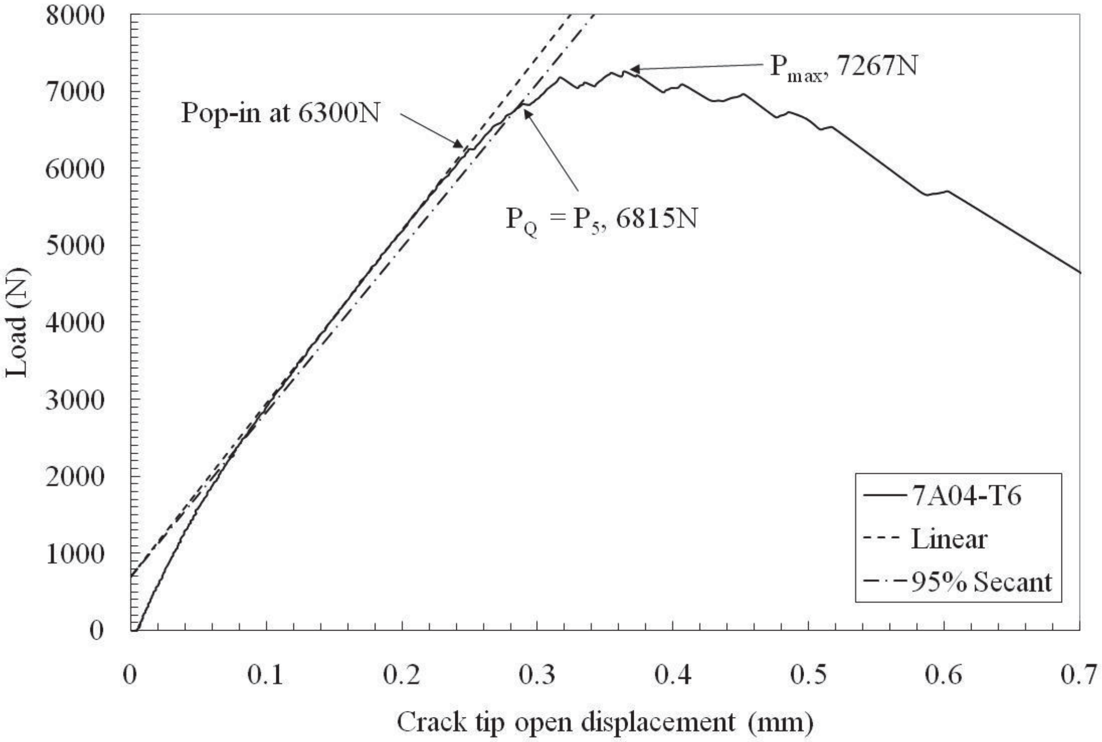

Figure 7–8. Fracture toughness load-displacement curve for 7A04-T6 aluminium alloy.

In the case of the MMCs, attempts to induce a fatigue precrack at the straight-through notch proved unsuccessful. Furthermore, the MMCs would experience fast fracture and fail in brittle manner even though cyclic compressive forces are kept well below the peak compressive force, P_m, as described in the standard at all times during the fatigue process. The specimens are first loaded to a very low precrack load and this load is increased in small increments every 10^5 cycles until crack initiation is observed. It is found that fracture initiated at much lower loads than the base alloy. A number of attempts are made to overcome abrupt failure including decreasing the compresive loads, increasing fatigue time, varying the sharpness of the notch, all without success, however, some sign of a formation of a fatigue precrack for the MMCs are observed. The presence of a shallow fatigue crack up to 200μm in depth within the fracture surface is observed in Figure 7–9. Some *beachmarks* are evident within this region confirming fatigue had occurred. As the crack propagates along, subtle changes in topography is observed with the appearance of dimple-like structures.

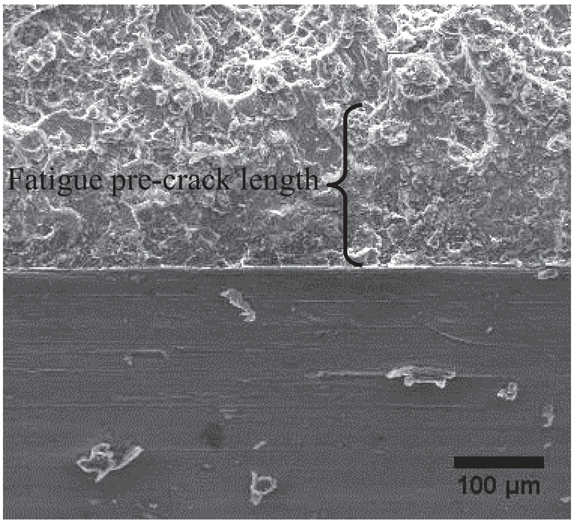

Figure 7–9. Secondary electron image of the aluminium MMCs fracture surface at the crack tip. The shallow crack length is approximately 200µm as indicated in the micrograph.

At low magnification many dimple structures are observed as presented in Figure 7–10. Above the shallow fatigue crack are dimple structures and many of the reinforcement particulates can be found inside these structures. These dimple structures are small and are only 5 to 10µm in size. This micro-ductility fracture mechanism are typical of MMCs that still show overall brittle behaviour.

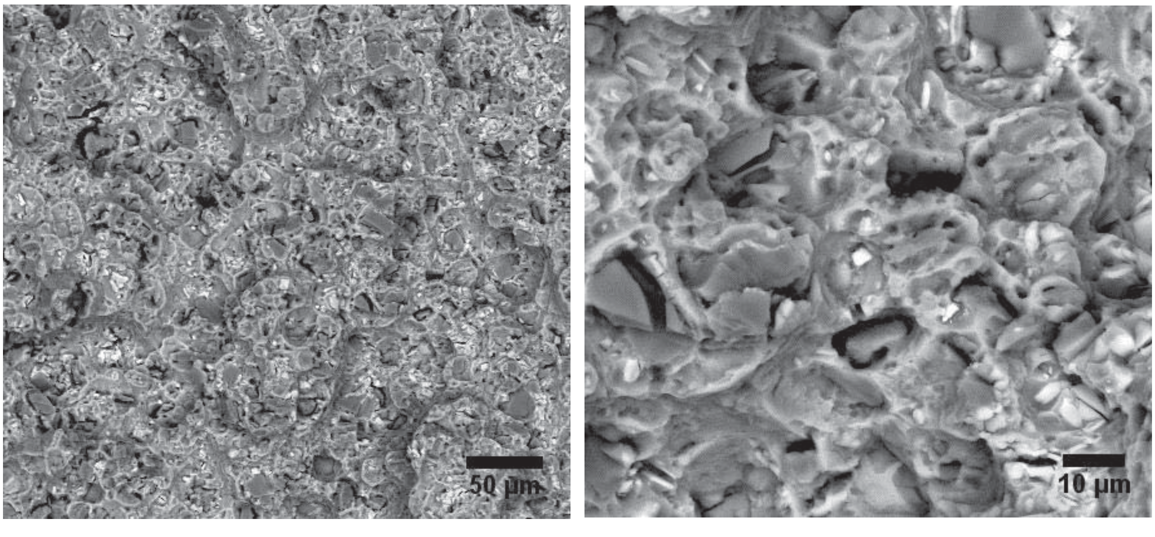

(a) (b)

Figure 7–10. Backscatter secondary electron image of the aluminium MMCs fracture surface.

In general, there are limited available materials for conducting research. Several factors that cannot be overcome include:

- Insufficient volume of materials for fracture toughness testing.
- The as-received 7A04 aluminium base alloy specimen thickness proved to be insufficient to meet ASTM plane-strain thickness validity requirements.
- The as-received 7A04 aluminium MMCs failed during the fatigue precrack stage.

As a result of being unable to produce a stable precrack in the MMCs with the equipment available and the fact that valid fracture toughness values could not be achieved with the aluminium alloy, a decision is made to investigate the use of the circumferential notch tension test specimens for plane-strain fracture toughness testing. Although the CNT testing proved successful in obtaining K_{1c} values the pre-cracking for the MMCs remained a problem as will be discussed in the next section.

7.2.4 *The circumferential notch tension test*

Circumferential notch tension test fracture toughness tests are employed to assess the plane-strain fracture toughness, K_{1c} values. In general, at least three tests are conducted for each type of material. After pre-cracking, fractography is conducted to determine the precrack profile, size, geometry and eccentricity of the final ligament. The fracture surfaces for 7A04-T6 aluminium alloy, 7A04/SiC/7.5p-T6 aluminium MMC and 7A04/SiC/10p-T6 aluminium MMC are presented in Figure 7–11, Figure 7–13 and Figure 7–16, respectively. In addition, the maximum load at fracture for the alloys and MMCs are presented in Figure 7–12, Figure 7–15 and Figure 7–18.

7A04-T6 A 7A04-T6 B 7A04-T6 C

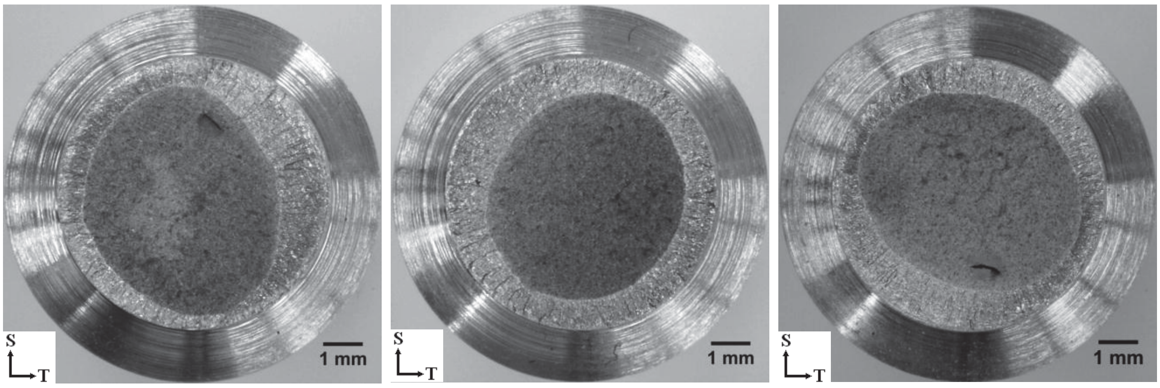

Plane-strain Plane-strain Plane-strain

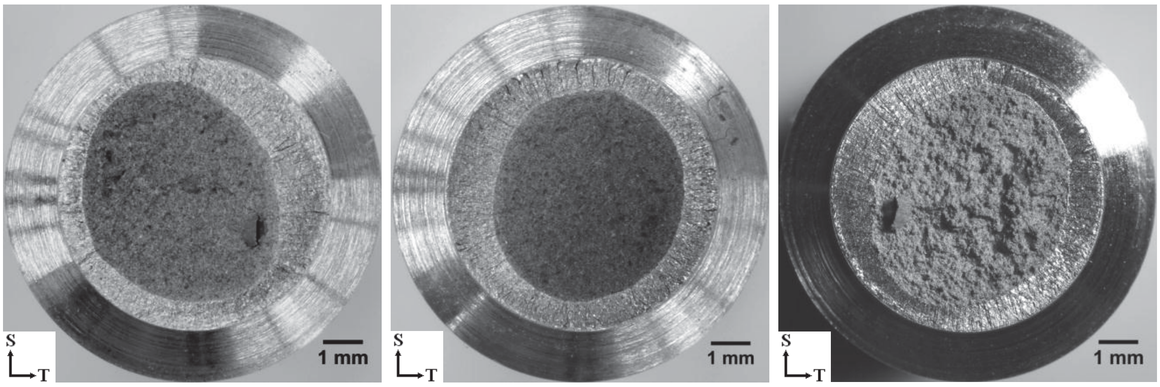

Figure 7–11. Circumferential notch tension precrack fracture surface for 7A04-T6 alloys. The top and bottom fractographs for each column are the matching fracture halves for each specimen. The letters A, B and C are used in this section to designate the test specimens.

Optical microscopy and SEM revealed the presence of a *stringer* that had run along the extrusion axis of the 7A04 base alloy, that is a region exhibiting a difference composition. This *stringer* is clearly observed in Figure 7–11 for specimen's 7A04-T6 A and C. This *stringer* affected the circumferential notch tension test load-displacements results with the specimen that clearly demonstrated the *stringer* effect possessing increased displacements as exhibited by specimens 7A04-T6 A and C. Good correlations is observed for the materials that clearly exhibited the *stringer* flaw except for specimen 7A04-T6 B which had less observable diplacement. Although the *stringer* had affected the displacement values the overall loads for the 7A04-T6 alloy remained similar. It is found from this study that the presence of the *stringer* had a limited effect on the overall fracture toughness of the alloy as shown in Table 7-4. Furthermore, the CNT plane-strain fracture toughness values are found to be comparable to the plane-strain fracture toughness values determined by SE(B) as presented in Table 7-3.

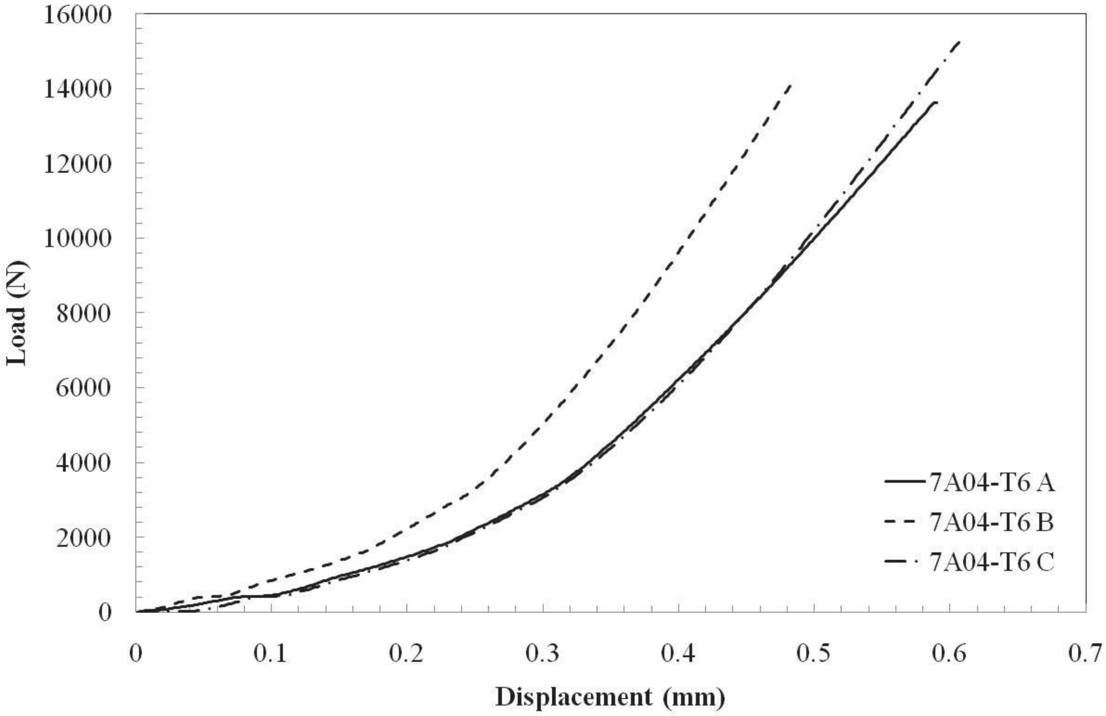

Figure 7–12. Circumferential notch tension load curves for the 7A04-T6 aluminium materials. The letters A, B and C are used in this section to designate the test specimens.

Table 7-4. Circumferential notch tension plane-strain fracture toughness, K_{1c}, values for the 7A04-T6 aluminium materials. The letters A, B and C are used in this section to designate the test specimens.

Material	Plane-strain fracture toughness, K_{1c} ($MPa\sqrt{m}$)
7A04-T6 A	42.5 ± 0.7
7A04-T6 B	40 ± 1.1
7A04-T6 C	42.5 ± 0.7

Circumferential notch tension testing is conducted on the metal matrix composites for the purpose of obtaining plane-strain fracture toughness values as presented in Figure 7–13. Analysis of the fracture surface revealed that specimens 7A04/SiC/7.5p-T6 A and C exhibited what appeared to be mix-mode I/II behaviour. Furthermore, it is observed that fracture surface is not flat as can be clearly seen in Figure 7–14. Moreover specimens 7A04/SiC/7.5p-T6 A and C exhibited lower maximum fracture loads as shown in Figure 7–15. It should be noted that it is not clear in the current work what would have initiated this type of failure. Nevertheless, it is determined only specimens that exhibited a flat surface and plane-strain conditions [79, 86, 87, 92] could qualify as plane-strain fracture toughness, K_{1c} and J_{1c},. Circumferential notch tension testing is conducted on the 7A04/SiC/10p-T6 MMCs as presented in Figure 7–16. In this case specimen 7A04/SiC/10p-T6 C exhibited a similiar crack profile and mix/mode I/II behaviour. Specimens 7A04/SiC/10p-T6 A and B are deemed to be flat and exhibit plane-strain conditions. Furthermore plane-strain fracture toughness values for specimens 7A04/SiC/10p-T6 A and B are found to be similar. Kamat et al. found that mix/mode behaviour exhibited lower fracture toughness when compared against mode I and this is consistant with these research findings [198, 199].

7A04/SiC/7.5p-T6 A　　7A04/SiC/7.5p-T6 B　　7A04/SiC/7.5p-T6 C

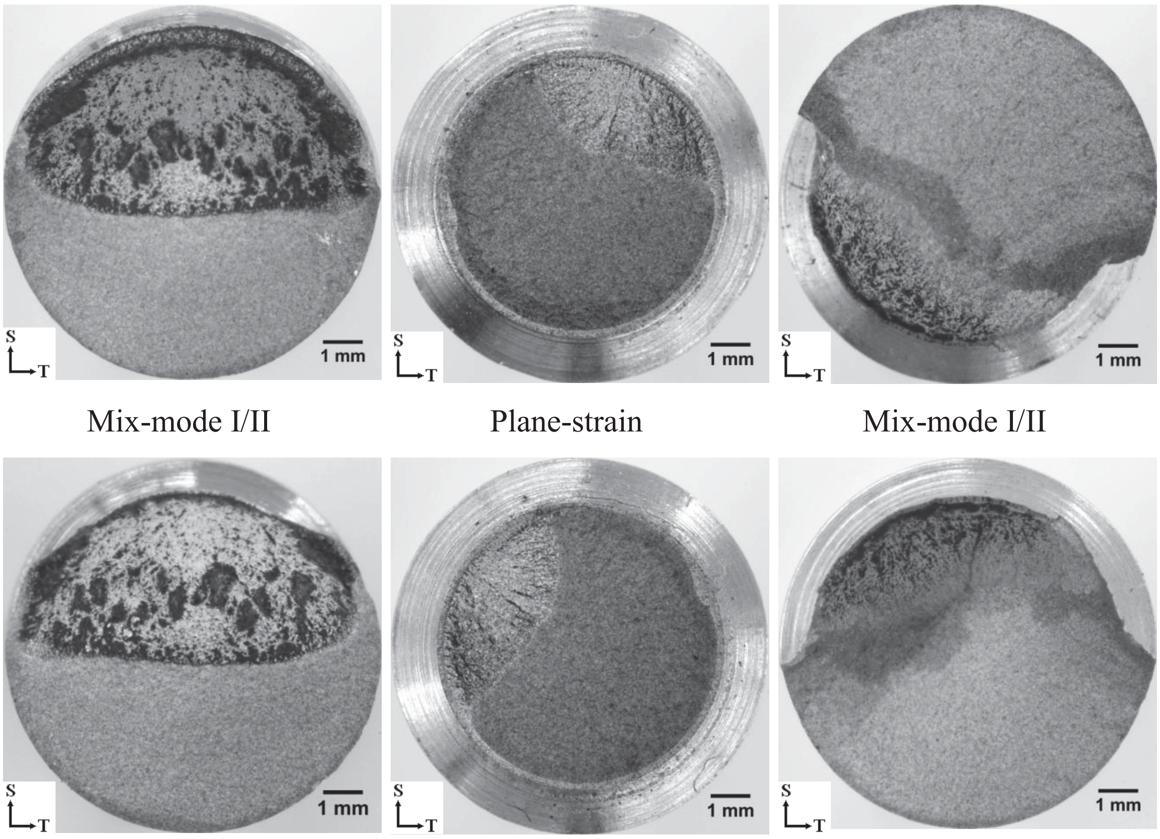

Mix-mode I/II　　Plane-strain　　Mix-mode I/II

Figure 7–13. Circumferential notch tension precrack fracture surface for the 7A04/SiC/7.5p-T6 aluminium materials. The top and bottom fractographs for each column are the matching fracture halves for each specimen. The letters A, B and C are used in this section to designate the test specimens.

7A04/SiC/7.5p-T6 A　　7A04/SiC/7.5p-T6 B　　7A04/SiC/7.5p-T6 C

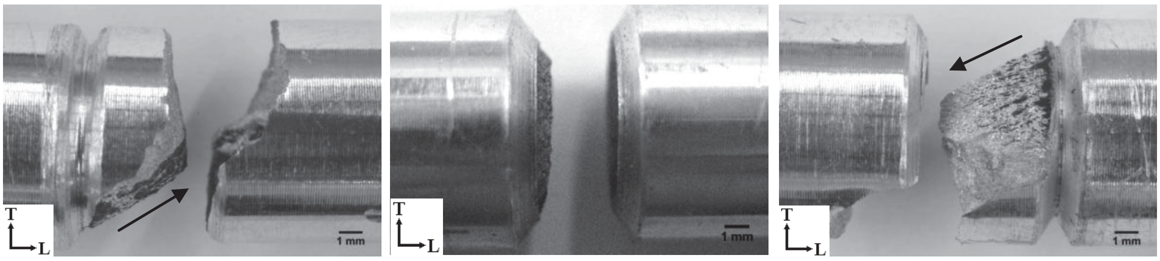

Figure 7–14. Side view of the circumferential notch tension precrack fracture surface for the 7A04/SiC/7.5p-T6 aluminium materials. The letters A, B and C are used in this section to designate the test specimens.

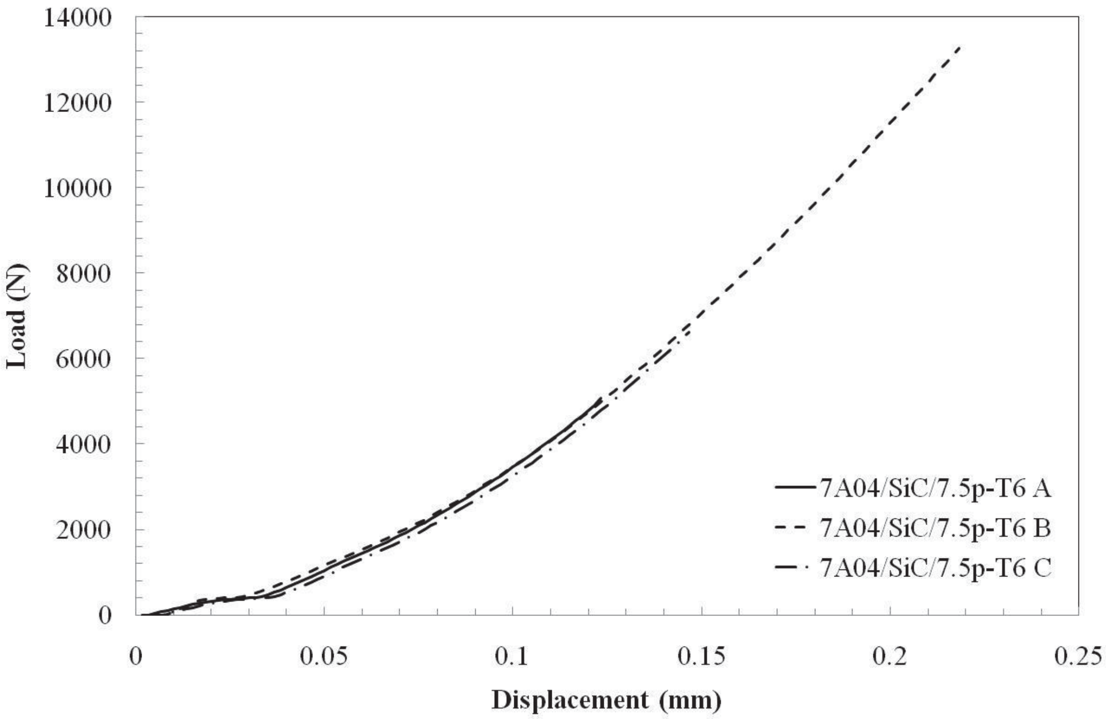

Figure 7–15. Circumferential notch tension load curves for the 7A04/SiC/7.5p-T6 aluminium materials. The letters A, B and C are used in this section to designate the test specimens.

Table 7-5. Circumferential notch tension plane-strain fracture toughness, K_{1c} values for the 7A04/SiC/7.5p-T6 aluminium materials. The letters A, B and C are used in this section to designate the test specimens.

Material	Plane-strain fracture toughness, K_{1c} ($MPa\sqrt{m}$)
7A04/SiC/7.5p-T6 A	16.5 ± 0.7
7A04/SiC/7.5p-T6 B	38 ± 0.7
7A04/SiC/7.5p-T6 C	16.5 ± 2.1

7A04/SiC/10p-T6 A 7A04/SiC/10p-T6 B 7A04/SiC/10p-T6 C

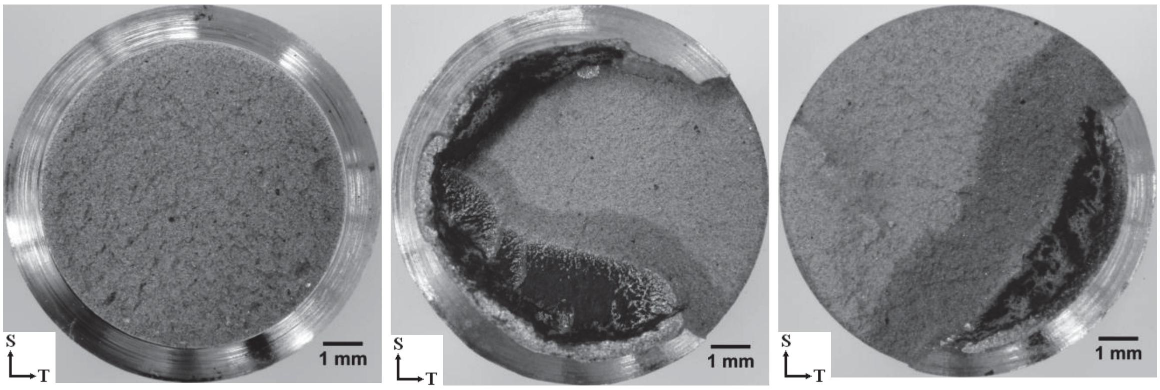

Plane-strain Plane-strain Mix-mode I/II

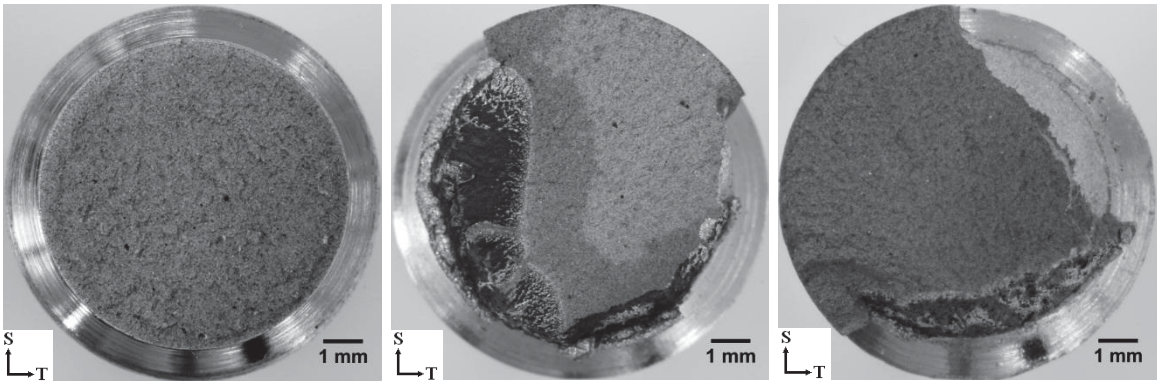

Figure 7–16. Circumferential notch tension precrack fracture surface for 7A04 /SiC/10p-T6 MMCs. The top and bottom fractographs for each column are the matching fracture halves for each specimen. The letters A, B and C are used in this section to designate the test specimens.

7A04/SiC/10p-T6 A 7A04/SiC/10p-T6 B 7A04/SiC/10p-T6 C

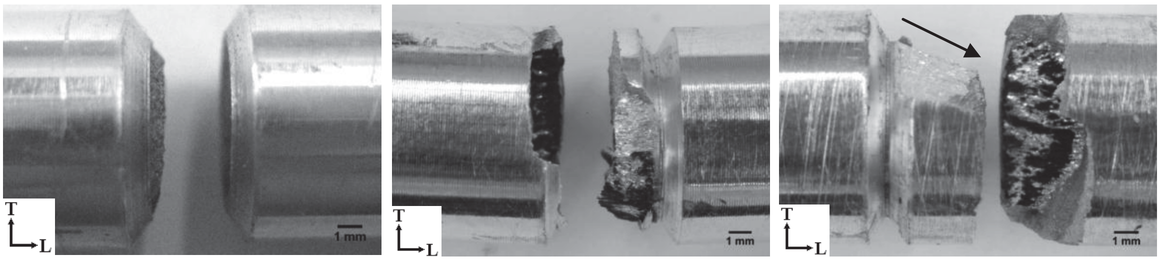

Figure 7–17. Side view of the circumferential notch tension precrack fracture surface for the 7A04/SiC/10p-T6 aluminium materials. The letters A, B and C are used in this section to designate the test specimens.

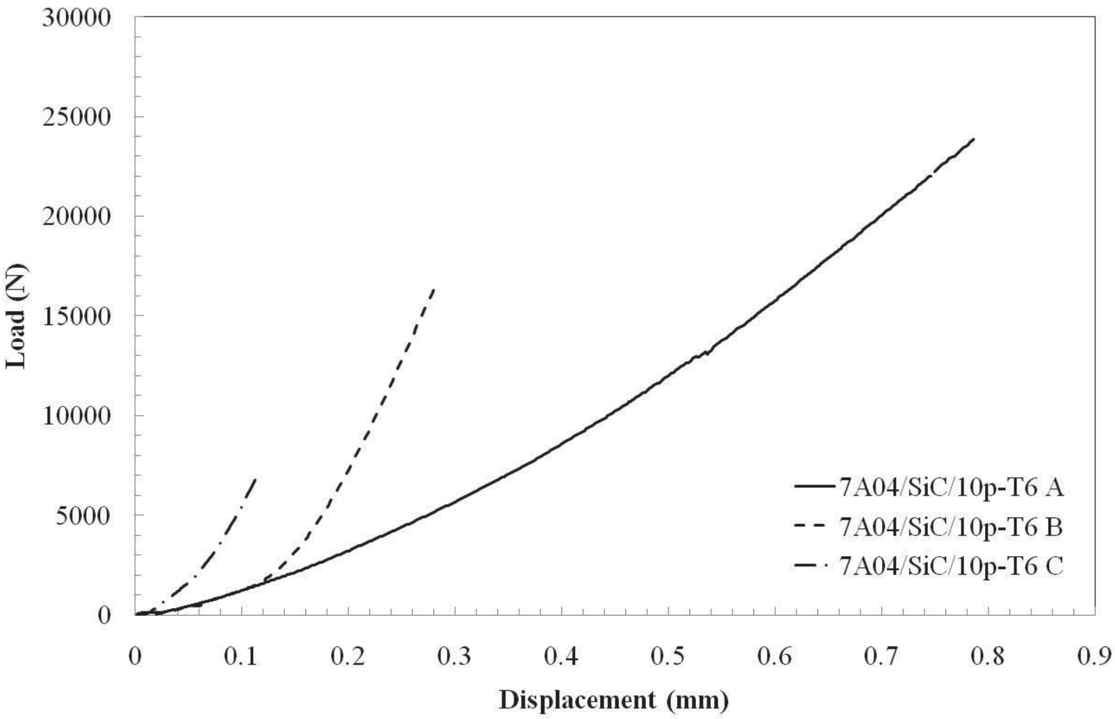

Figure 7–18. Circumferential notch tension load curves for 7A04/SiC/10p-T6 aluminium materials. The letters A, B and C are used in this section to designate the test specimens.

Table 7-6. Circumferential notch tension plane-strain fracture toughness, K_{1c} values for the 7A04/SiC/10p-T6 aluminium materials. The letters A, B and C are used in this section to designate the test specimens.

Material	**Plane-strain fracture toughness, K_{1c} ($MPa\sqrt{m}$)**
7A04/SiC/10p-T6 A	26
7A04/SiC/10p-T6 B	28.5 ± 0.7
7A04/SiC/10p-T6 C	10 ± 2.8

All specimens passed validity requirements set by Ibrahim [86]. The 7A04-T6 aluminium alloy presented in Figure 7–11 exhibited plane-strain fracture conditions. In addition, the results are found to be consistent with the SE(B) plane-strain fracture toughness results as presented in Table 7-3. This finding further provided evidence that plane-strain fracture toughness values could be achieved with smaller sized specimens. Note, the rotational bend fatigue pre-cracking loads for fatigue crack initiation and propagation are found to be higher for MMCs compared to its base alloy counterpart.

Circumferential notch tension fatigue pre-cracking of the aluminium MMCs revealed that some of the MMCs exhibited irregular fatigue precrack behaviour, as can be seen in Figure 7–14 and Figure 7–17. This fracture behaviour is unexpected. A survey of the literature found that this behaviour has not been encountered by other researchers.

The fatigue precrack is observed to initiate at the CNT v-notch from where it begins to propagate towards the longitudinal axis and into the specimen. The crack path appeared to follow the grain and particulates alignment which arose from extrusion post-processing. These MMCs appeared to exhibit mix-mode I/II fracture behaviour where there is a combination of opening and shearing behaviour. The specimens that exhibited a flat surface are accepted as possessing plane-strain conditions. The results of these specimens are accepted as valid plane-strain fracture toughness, K_{1c} for this test. The MMCs fatigue crack profile can be due to:

1. An increased probability of fatigue crack initiating flaws, clusters and machine damage in the MMCs.
2. The rotating bending forces acting on that flaw.

It is determined that specimens 7A04/SiC/7.5p-T6 A, 7A04/SiC/7.5p-T6 C and 7A04/SiC/10p-T6 C which exhibited relatively lower plane-strain fracture toughness, K_{1c} values of $16\mathrm{MPa}\sqrt{\mathrm{m}}$, $16\mathrm{MPa}\sqrt{\mathrm{m}}$ and $10\mathrm{MPa}\sqrt{\mathrm{m}}$, respectively be left out of the final results since these specimens did not meet plane-strain criteria and conditions. These results are summarised in Table 7-7.

The final CNT plane-strain fracture toughness results for the aluminium materials are presented in Table 7-8. The results further reinforce the findings by previous authors, that increasing reinforcement content leads to MMCs with lower fracture toughness values [200]. Furthermore, although the particulate reinforcement served to increase the overall strength of the material, it is the constraint imparted by the reinforcements that limited the fracture toughness of MMCs. Further improvements to the material's fracture toughness could come from reducing concentrated stress points produced by the reinforcement content which often leads to an early onset of failure, limiting clustering of particulates could also increase the toughness values.

Table 7-7. Summary of the valid circumferential notched tension test fracture toughness specimens.

Material	7A04-T6	7A04/SiC/7.5p-T6	7A04/SiC/10p-T6
A	Yes	No	Yes
B	Yes	Yes	Yes
C	Yes	No	No

Table 7-8. Circumferential notched tension fracture toughness results.

Material	Plane-strain fracture toughness, K_{1c} ($MPa\sqrt{m}$)	Valid values
7A04-T6	41.7 ± 1.4	Yes
7A04/SiC/7.5p-T6[6]	38 ± 0.7	Yes
7A04/SiC/10p-T6	27.3 ± 1.8	Yes

---

[6] Value taken from a single specimen.

Scanning electron microscopy is conducted on the 7A04-T6 CNT test specimens to identify a feature that is found on the fracture surface as presented in Figure 7–19. This feature is initially assumed to be a consequence of CNT testing, however, a literature search revealed no mention of such feature. Energy dispersive spectroscopy (EDS) then confirmed that this feature is due to a change in composition. The feature is probably a *stringer* that had been extruded along the length of the bar.

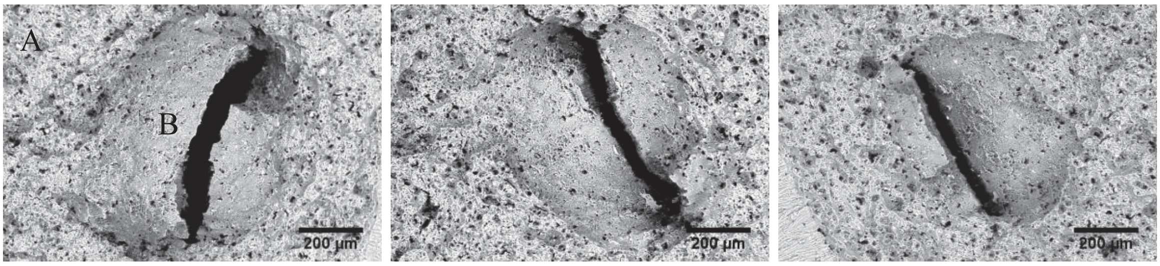

(a) (b) (c)

Figure 7–19. The 7A04-T6 aluminium alloy fracture surface exhibiting a common flaw.

The elemental composition in weight percent for 7A04-T6 aluminium alloy taken at locations A and B as presented in Table 7-9.

Table 7-9. Compositional analysis of 7A04-T6 aluminium alloy.

7A04-T6	C	Cu	Cr	Fe	Mg	Mn	Si	Zn	Al
A	0	2.6	0.3	1.3	4	0.6	0	10.7	Balance
B	0	10.4	0.2	1	2.2	0.5	0	47.6	Balance

The results indicate that this feature is not a consequence from the CNT test rather it arose from the way 7A04-T6 aluminium specimens are processed and cast. Furthermore, the zinc and copper weight percentages for the *stringer* are higher compared to the overall composition of the 7A04-T6 aluminium alloy. In addition, almost half of the *stringer's* composition is found to be composed of zinc. Moreover the zinc and copper content for the *stringer* is found to be 5 and 4 times that of the original as-received 7A04-T6 aluminium alloy, respectively.

7.2.5 *Small punch test*

The SPT load at crack initiation is identified by concurrently observing both the load and initial crack initiation on the surface of the SPT specimen as it underwent mechanical deformation. The equivalent fracture strain, ε_{qF}, is determined from the final specimen thickness at crack initiation in accordance with Equation 5-7. The loads at crack initiation and equivalent fracture strain are presented in Table 7-10. The equivalent fracture strain of a circular plate shaped specimen is based on membrane stretch theory proposed by Bayoumi and Bassim [26, 27].

The typical SPT load-displacement curves for the aluminium base alloy and the aluminium MMCs are shown in Figure 7–20, Figure 7–21 and Figure 7–22. In general, at least four tests are conducted for each type of material. The curves demonstrate that the SPT exhibited good reproducibility.

The averaged small punch load-displacement curves for the aluminium base alloy and the aluminium MMCs are shown in Figure 7–23 using individual data points. It can be seen that the MMCs exhibit a lower displacement with load when compared to the alloy. On crack initiation, the slope of the curves or stiffness reduced to a level below that of the alloy. This can be attributed to damage accumulation in the MMCs reinforcement content leading to faster crack growth.

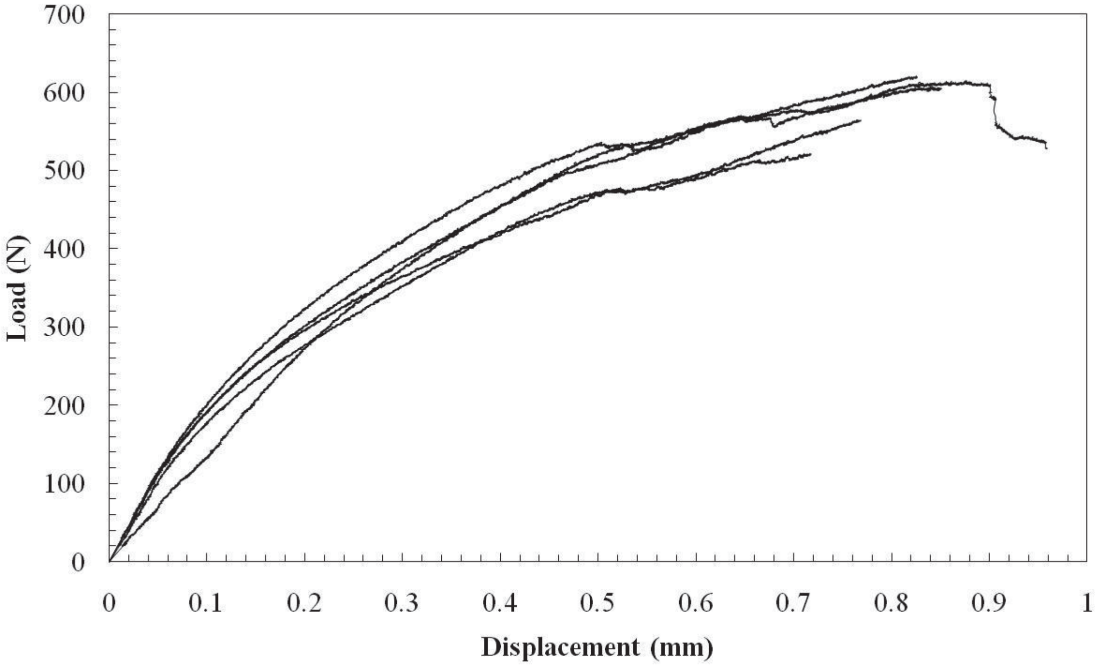

Figure 7–20. Typical small punch test load-displacement curves for 7A04-T6 aluminium alloy.

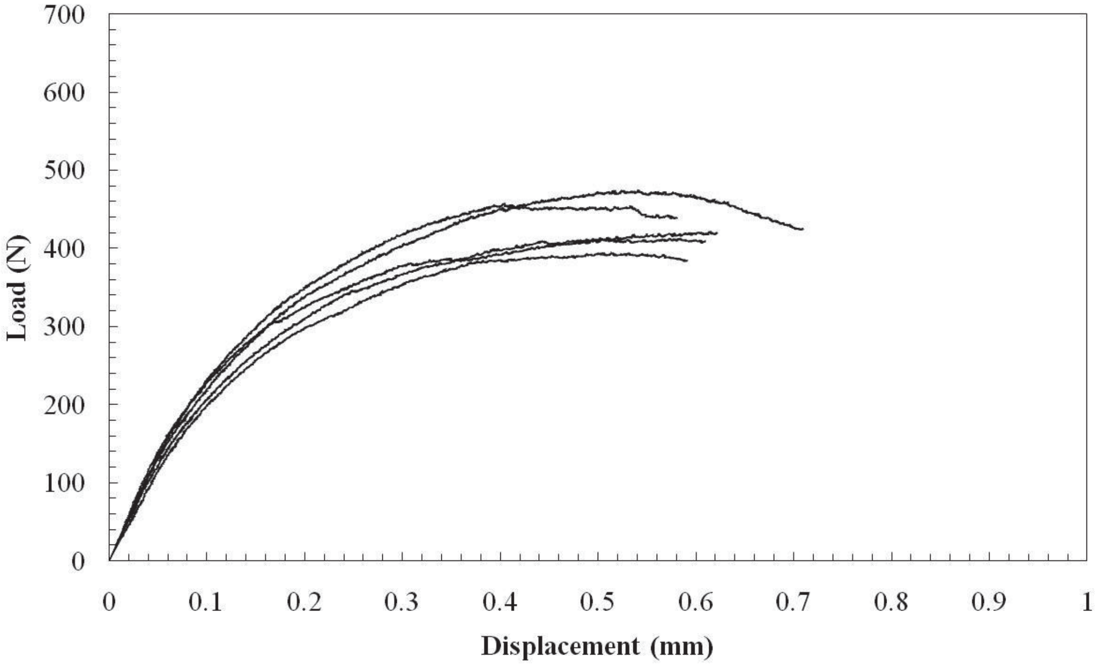

Figure 7–21. Typical small punch test load-displacement curves for 7A04-T6/SiC/7.5p-T6 aluminium MMC.

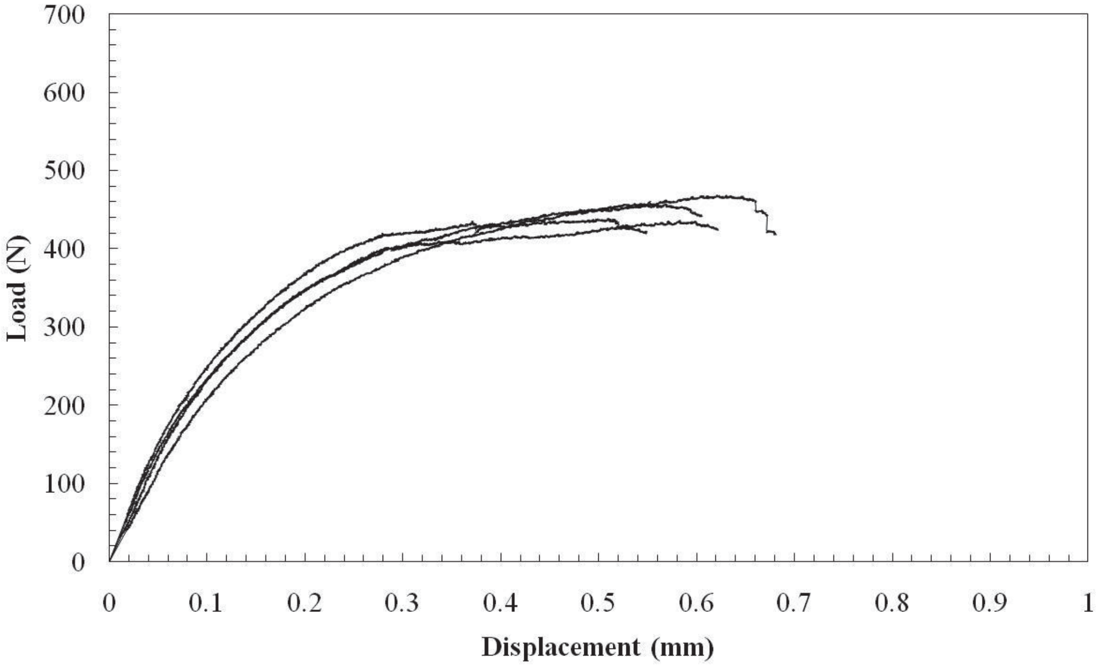

Figure 7–22. Typical small punch test load-displacement curves for 7A04-T6/SiC/10p-T6 aluminium MMC.

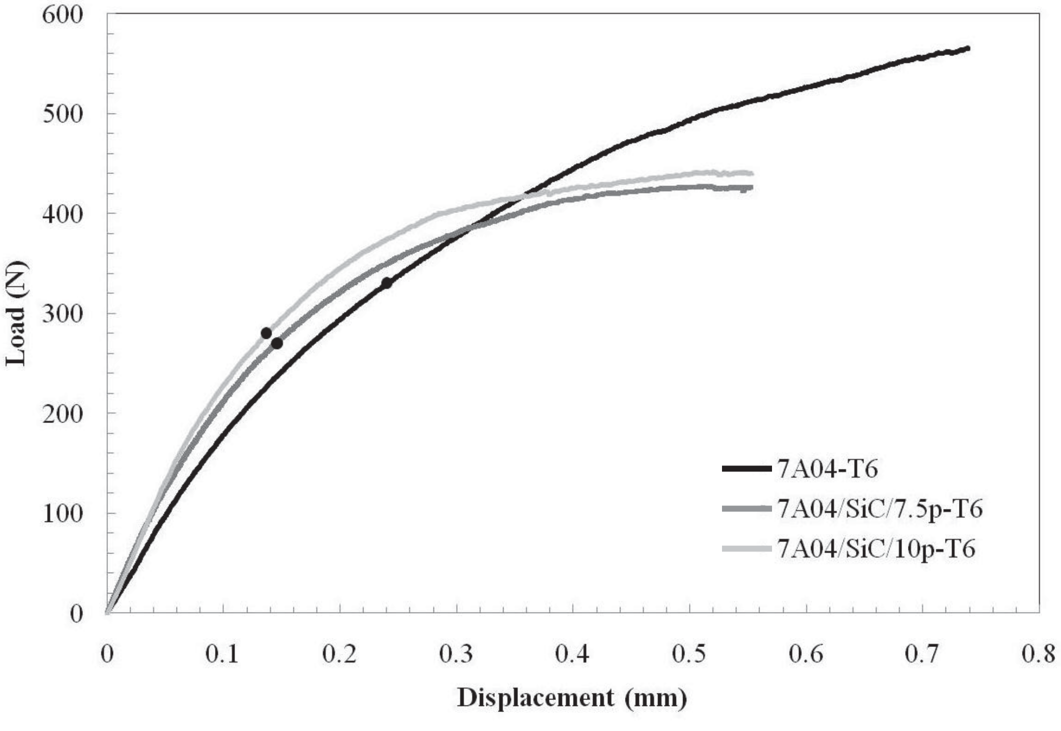

Figure 7–23. Averaged small punch test load-displacement curves for 7A04-T6 aluminium alloy, 7A04/SiC/7.5p-T6 aluminium MMC and 7A04/SiC/10p-T6 aluminium MMC. The dots indicate the observed load at crack initiation.

Table 7-10. Small punch test properties for the as-received aluminium based materials.

Material	Elastic-plastic load[7] , P_y (N)	Load at crack initiation, P_i (N)	Equivalent fracture strain, ε_{qF}	Total small punch energy, E_{SP} (J)
7A04-T6	89 ± 2.8	330 ± 90	0.14 ± 0.002	0.32 ± 0.05
7A04/SiC/7.5p-T6	97.0 ± 2.1	270 ± 60	0.07 ± 0.002	0.19 ± 0.01
7A04/SiC/10p-T6.	117 ± 2	280 ± 40	0.06 ± 0.003	0.20 ± 0.02

It is observed that the load at crack initiation for the base alloy is generally higher compared to the MMCs. This is attributed to the overall fracture toughness of the base alloy and its ability to resist crack propagation compared its reinforced counterpart. Comparing the MMCs it is observed that higher loads are observed with increasing reinforcement material. In general a decrease in strain is observed for the high reinforcement. The SPT energy, E_{SP}, is derived from the area under the small punch load-displacement curve. As expected the alloy exhibited higher energies when compared to the MMCs. This is due to the alloy's higher fracture toughness. With respect to the MMCs a t-test is performed as presented in Table 7-11 to ascertain whether there is any significant statistical difference between the 7A04/SiC/7.5p-T6 and

---

[7] The method utilized in this Thesis for the determination of the elastic-plastic load is explained in page 159.

7A04/SiC/10p-T6 small punch energy, E_{SP}. The basic analysis found that there is no real difference between the two from a statistical point of view.

Table 7-11. The statistical difference between two small punch energy, E_{SP}, 7A04-T6 aluminium MMCs.

t-Test: Two-sample assuming unequal variances		
Materials	7A04/SiC/7.5p-T6	7A04/SiC/10p-T6
Mean	0.169	0.199
Variance	0.001	0.000
Observations	5.000	4.000
Hypothesized Mean Difference	0.000	
df	7.000	
t Stat	-1.837	
P(T<=t) one-tail	0.054	
t Critical one-tail	1.895	
P(T<=t) two-tail	0.109	
t Critical two-tail	2.365	

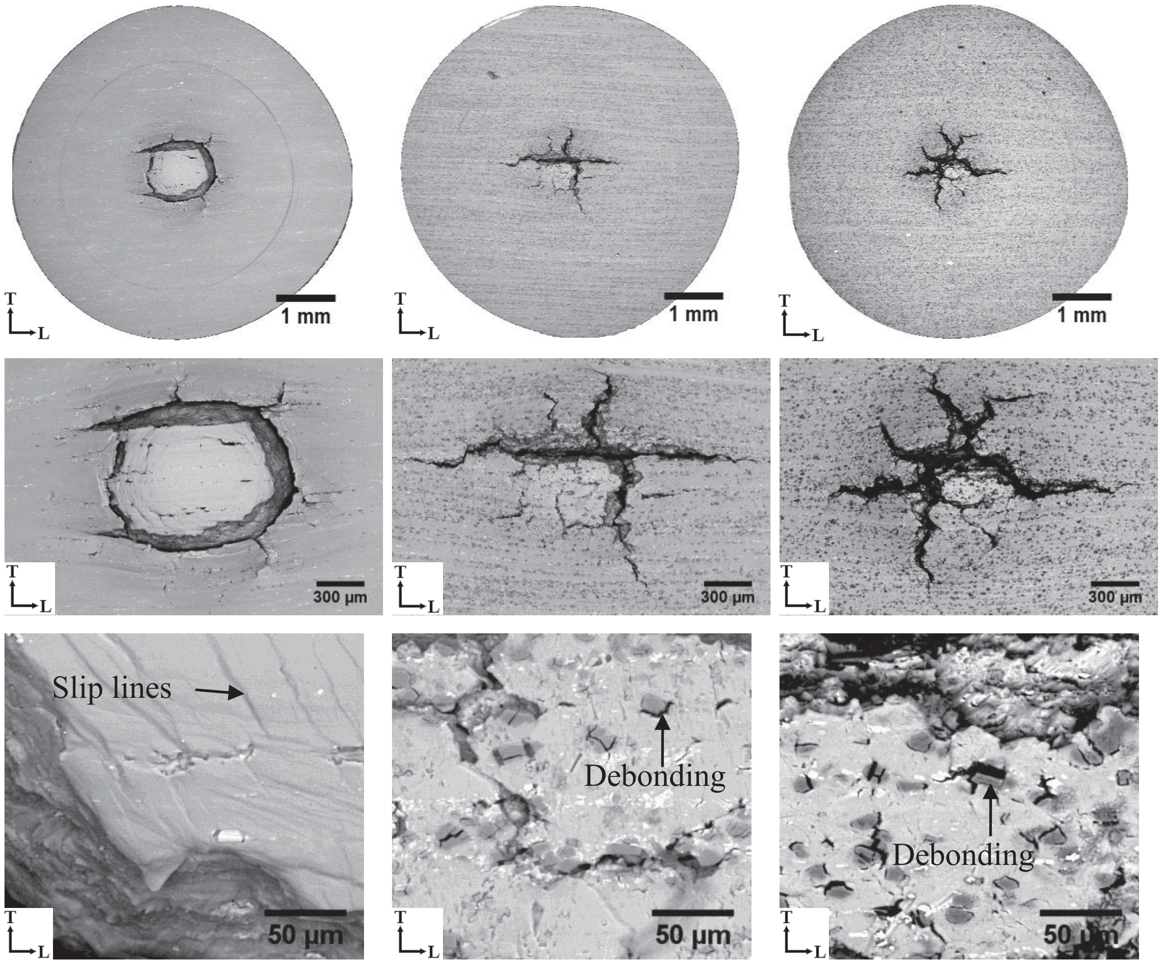

(a) (b) (c)

Figure 7–24. Micrographs illustrating the small punch test crack profile for (a) 7A04-T6, (b) 7A04/SiC/7.5p-T6 and (c) 7A04/SiC/10p-T6 aluminium materials.

Backscatter electron images of the fracture surfaces of the SPT specimens are presented in Figure 7–24. The base alloy exhibited the usual complex circumferential crack behaviour as commonly observed for conventional alloys with some secondary surrounding cracks, the crack formation could be characterised as a form of hoop stress. Furthermore slip-lines are observed at higher magnifications. The MMCs exhibited clear multiple-crack behaviour, which is mainly due to the presence of the SiC_p reinforcement as shown in Figure 7–24 (b) and (c). Particle fracture and particle-matrix decohesion are observed. Also of note is the way the main crack is aligned in the longitudinal direction or extrusion direction for the MMCs and texture of microstructure. The fracture appearance for MMCs appeared almost like a star with secondary cracking propagating perpendicular and away from the main crack event.

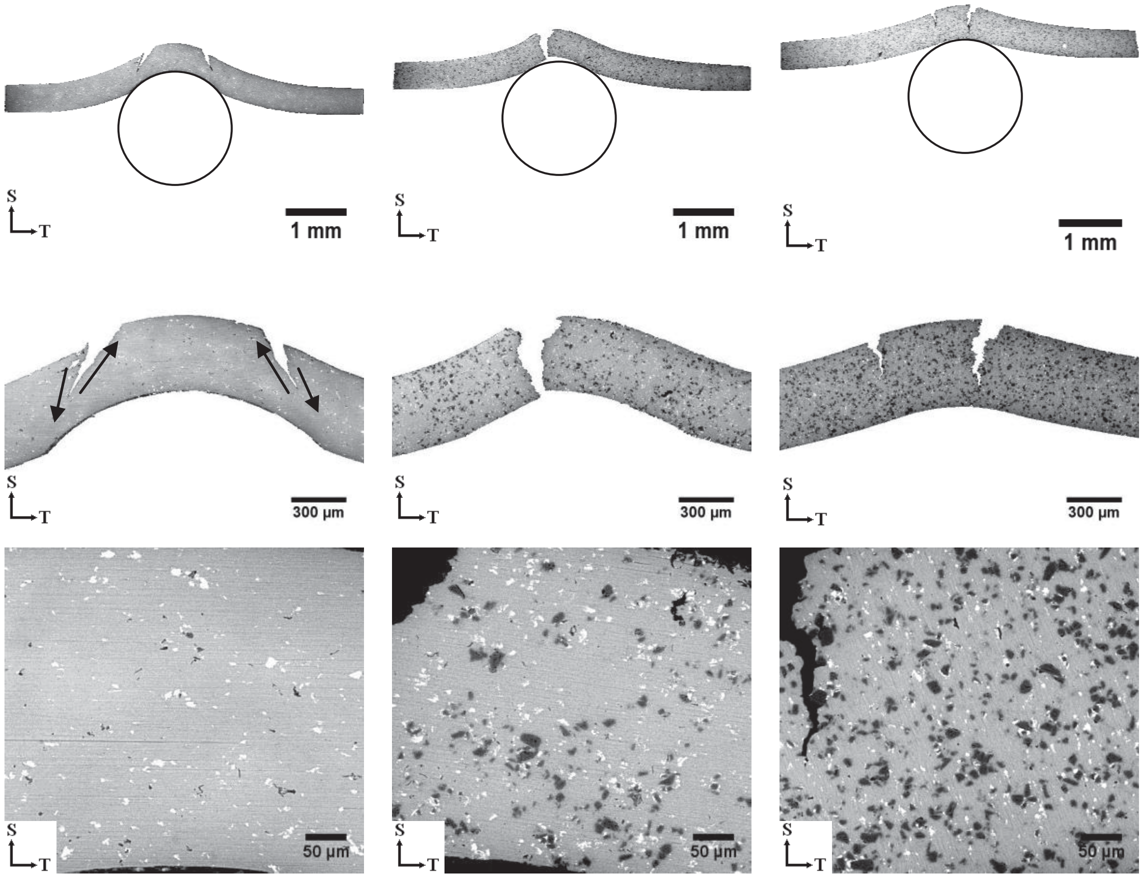

(a) (b) (c)

Figure 7–25. Backscatter electron micrograph illustrating the cross-section of the small punch test crack profile for (a) 7A04-T6, (b) 7A04/SiC/7.5p-T6 and (c) 7A04/SiC/10p-T6 aluminium materials.

The aluminium alloy exhibited smooth shear-like crack behaviour that appeared to conform with the shape of the spherical punch as shown in Figure 7–25 (a). In addition, large plasticity for the alloy are observed. Small void cavities are observed to have formed within the 7A04-T6 aluminium alloy. Ma and Yoon observed similar deformation and fracture behaviour for 2024 aluminium alloy [201]. The MMCs did not exhibit smooth crack behaviour due to the presence of SiC_p reinforcements as shown in Figure 7–25 (b) and (c). Furthermore, as the reinforcement increases, there is less observable deformation owing to MMCs decreased ductility, as shown by the equivalent fracture strain results as presented in Table 7-10. Moreover, the crack initiation appeared to form nearer towards the center for MMC SPT specimens.

7.2.6 *Finite element analysis*

An attempt is made to describe the SPT behaviour via finite element analysis as shown in Figure 7–26. The load-displacement diagram is modelled with the simple approach of using longitudinal stresses. The MMCs are modelled simply using global elastic modulus, E, and yield strength, σ_{YS}, values. No particle distribution is considered for the model. Despite this, the FEA showed that the two composite curves are above the alloy and are close together. This mirrored the actual experimental SPT results. However, the FEA overestimated the load-displacement behaviour for all the materials. This is due to the model not taking into account the debonding of the particles, and the linking of these many interfacial cracks was the failure mechanism in these materials. That is, as is well known in materials science and engineering, the load-displacement behaviour is structured sensitive. Also the FEA did not predict a decrease in stiffness once the crack formed. Another mechanical behaviour that the FEA did not account for is strain-hardening effects.

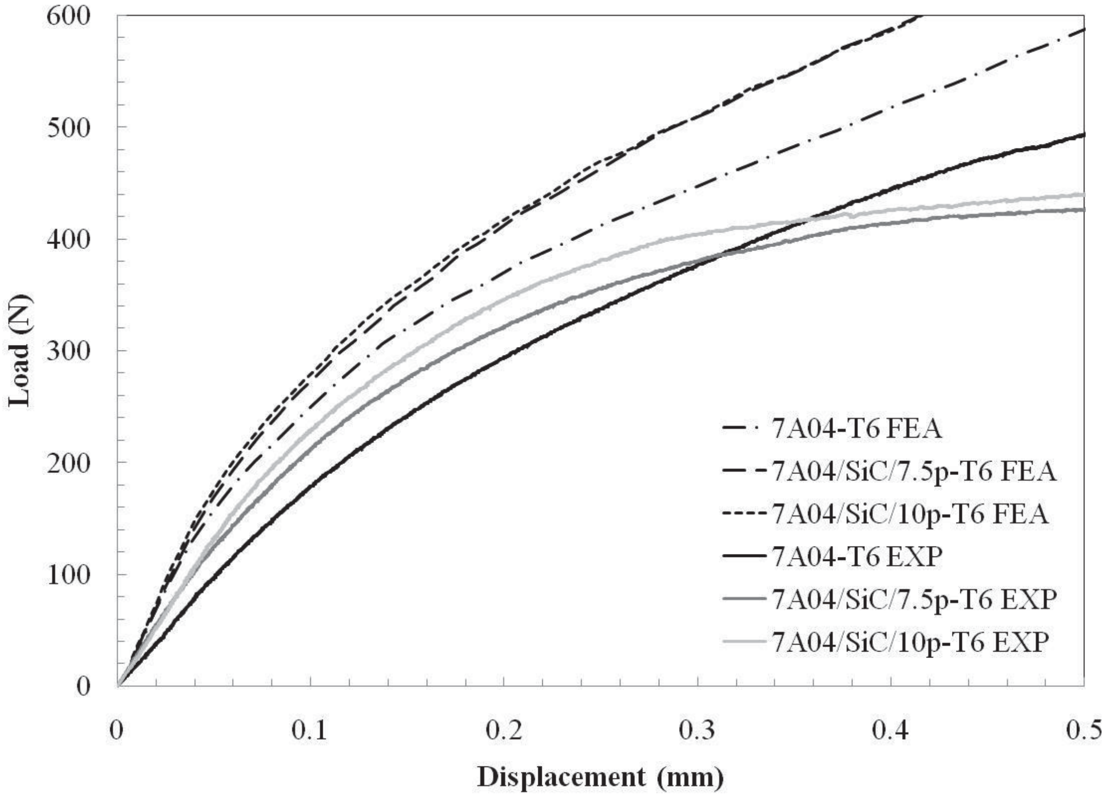

Figure 7–26. Finite element prediction of the small punch load-displacement curve for aluminium materials.

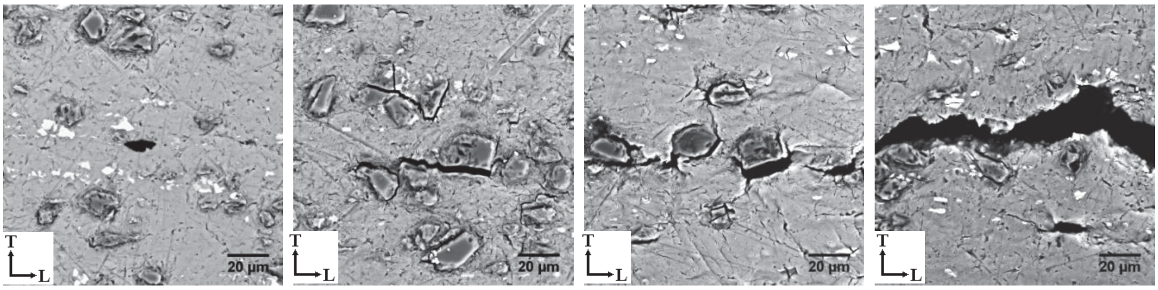

100N 200N 300N 400N

Figure 7–27. Crack initiation and propagation behaviour for 7A04/SiC/7.5p-T6 aluminium MMC with increasing loads.

Further work is implemented to ascertain the deformation and crack initiation mechanism on the aluminium materials. This is achieved by loading the SPT specimens up to predetermined loads. The following images demonstrate developing crack growth for 7A04/SiC/7.5p-T6 and 7A04/SiC/10p-T6 aluminium MMCs as presented in Figure 7–27 and Figure 7–28, respectively. All micrographs are imaged at the center of the specimen. Scanning electron microscopy revealed crack formation as low as 200N and appeared much sooner than is previously observed with light optical methods. It is identified that cracks often formed around clustered particles. In the case of the aluminium MMCs, crack initiation is confirmed to be due to particle debonding between the reinforcement and the metal matrix. In addition, the iron inclusions are observed to fail at around 200N. This gave further evidence that inclusion lowered the strength and toughness of materials.

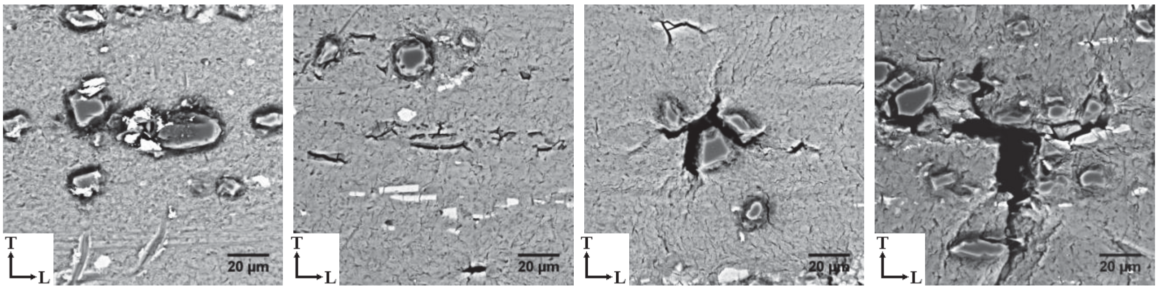

100N 200N 300N 400N

Figure 7–28. Crack initiation and propagation behaviour for 7A04/SiC/10p-T6 aluminium MMC with increasing loads.

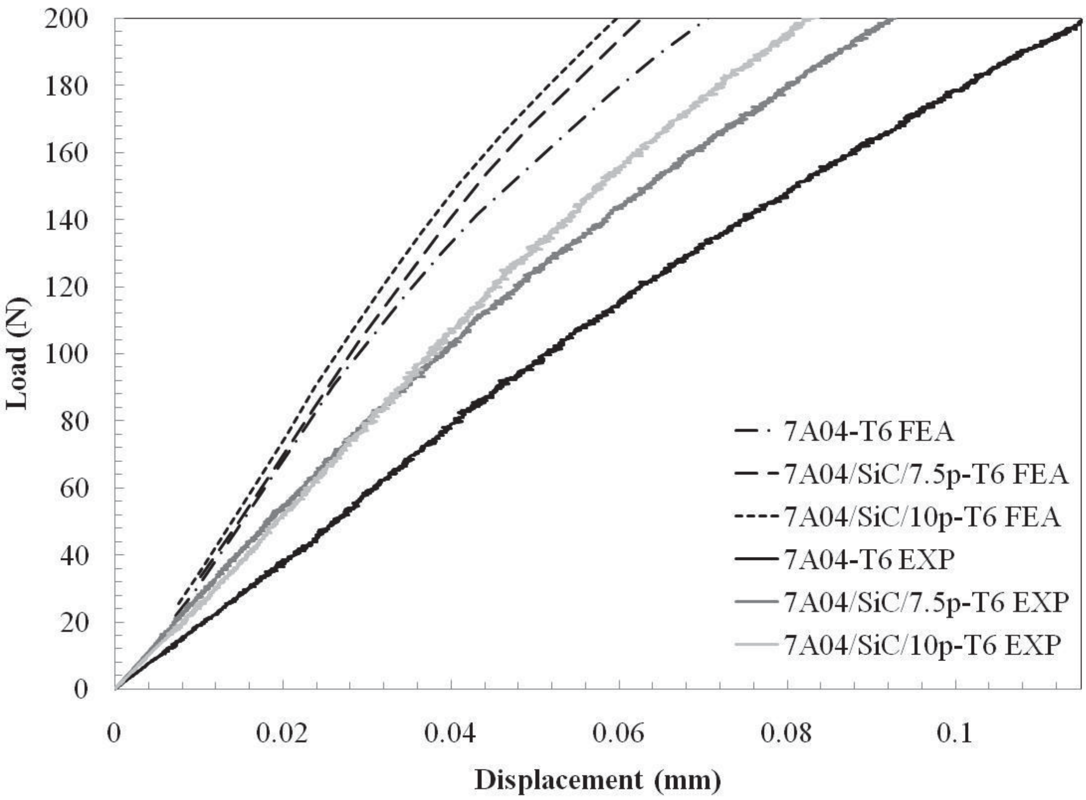

Figure 7–29. Finite element prediction of the small punch load-displacement curve for aluminium materials up to 200N.

The finite element model of the load-displacement curves up to 200N is shown in Figure 7–29. The evidence that crack initiation occurred somewhere between 100N to 200N explained why the experimentally derived loads fell away where as finite element model predicted continued increasing loads as shown in Figure 7–26. Furthermore, particle debonding, particle fracture and void nucleation should be considered when implementing the finite element method. Further work on the FEA of MMCs was discontinued due to the exhaustive modelling techniques that are beyond the scope of this research and would constitute another research thesis.

7.3 Titanium results

7.3.1 *The microstructure*

Scanning electron microscopy is conducted on TC4 titanium base alloy, TC4/TiB, TiC/2.5w, 2.5p titanium MMC and TC4/TiB, TiC/5w, 5p titanium MMC in the longitudinal, transverse and planar sections as presented in Figure 7–30 and at higher magnifications in Figure 7–31. The chemical composition for the TC4 titanium base alloy is presented previously in Table 6-4. Scanning electron microscopy revealed that all materials exhibited alpha grains (dark grey), acicular alpha grains (needle-like) and retained beta (white) within the metal matrix microstructure. This microstructure is revealed by Kroll's etchant and is typical for TC4 based materials. Although all materials exhibited similar matrix microstructure, the TC4/TiB, TiC/5w, 5p titanium MMC appeared to exhibit finer alpha, α, and acicular alpha, α', grain structure. This is perhaps due to the increasing reinforcement's effect on the metal matrix microstructure.

Scanning electron microscopy on the MMCs confirmed the presence of in-situ synthesized TiC_p and TiB_w and is characterised respectively as globular and whisker-like in structure. Clean interfacial bonding is observed between the matrix and reinforcements interface. In addition, the TiB_w is observed to align along the longitudinal direction which is a consequence of the casting process. The reinforcements in both TC4/TiB, TiC/2.5w, 2.5p titanium MMC and TC4/TiB, TiC/5w, 5p titanium MMC are observed to be homogeneously distributed within the TC4 titanium matrix alloy. Evidence of microvoid formation is observed at the ends of the TiB_w and is similar to what is observed with the whisker-like iron precipitates observed for the aluminium materials. Furthermore, some of the TiB_w had fractured which is due to post-processing and forging.

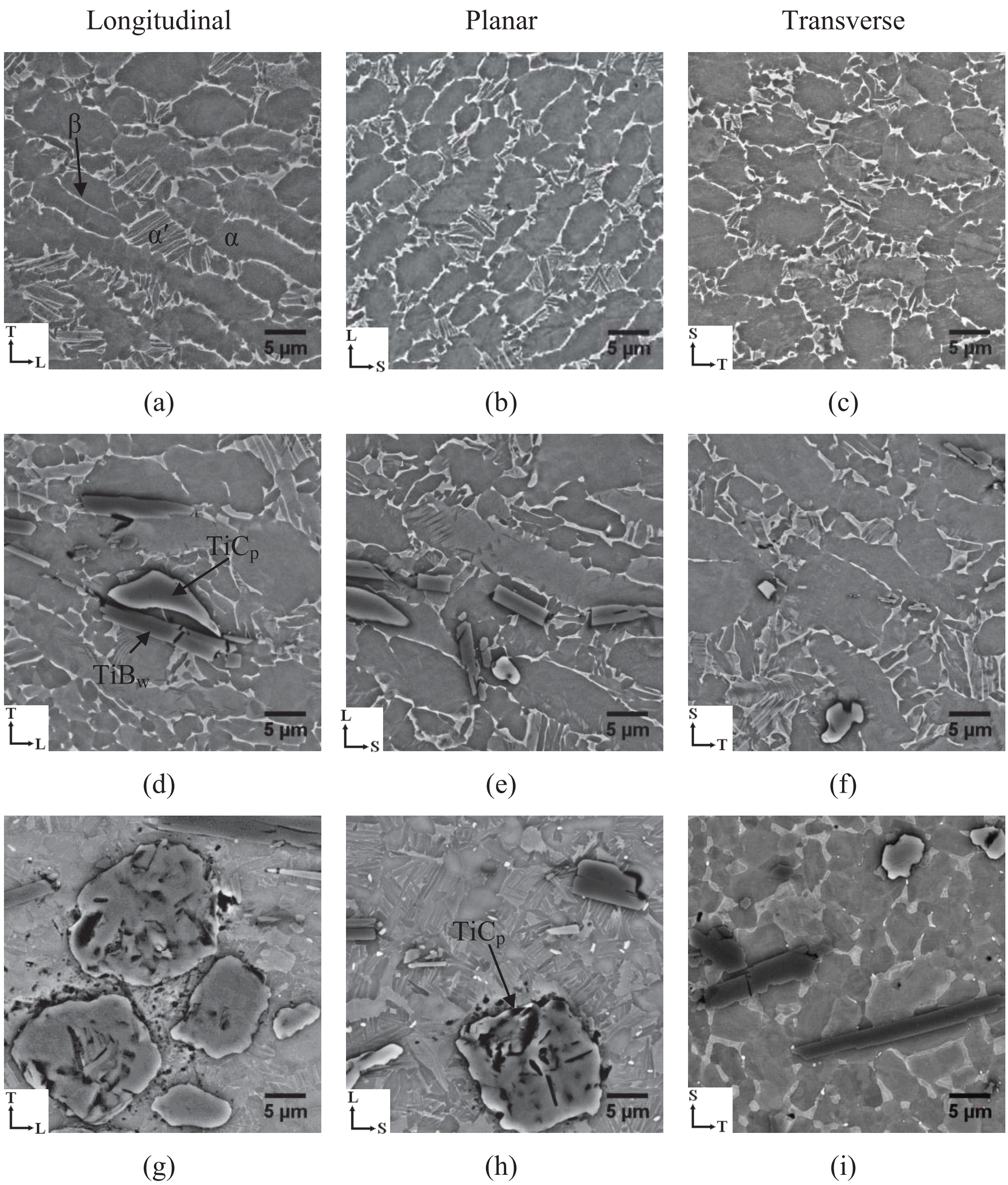

(a) (b) (c)

(d) (e) (f)

(g) (h) (i)

Figure 7–30. Backscatter secondary electron micrographs for the as-received (a, b, c) TC4 titanium alloy, (d, e, f) TC4/TiB, TiC/2.5w, 2.5p titanium MMC and (g, h, i) TC4/TiB, TiC/5w, 5p titanium MMC.

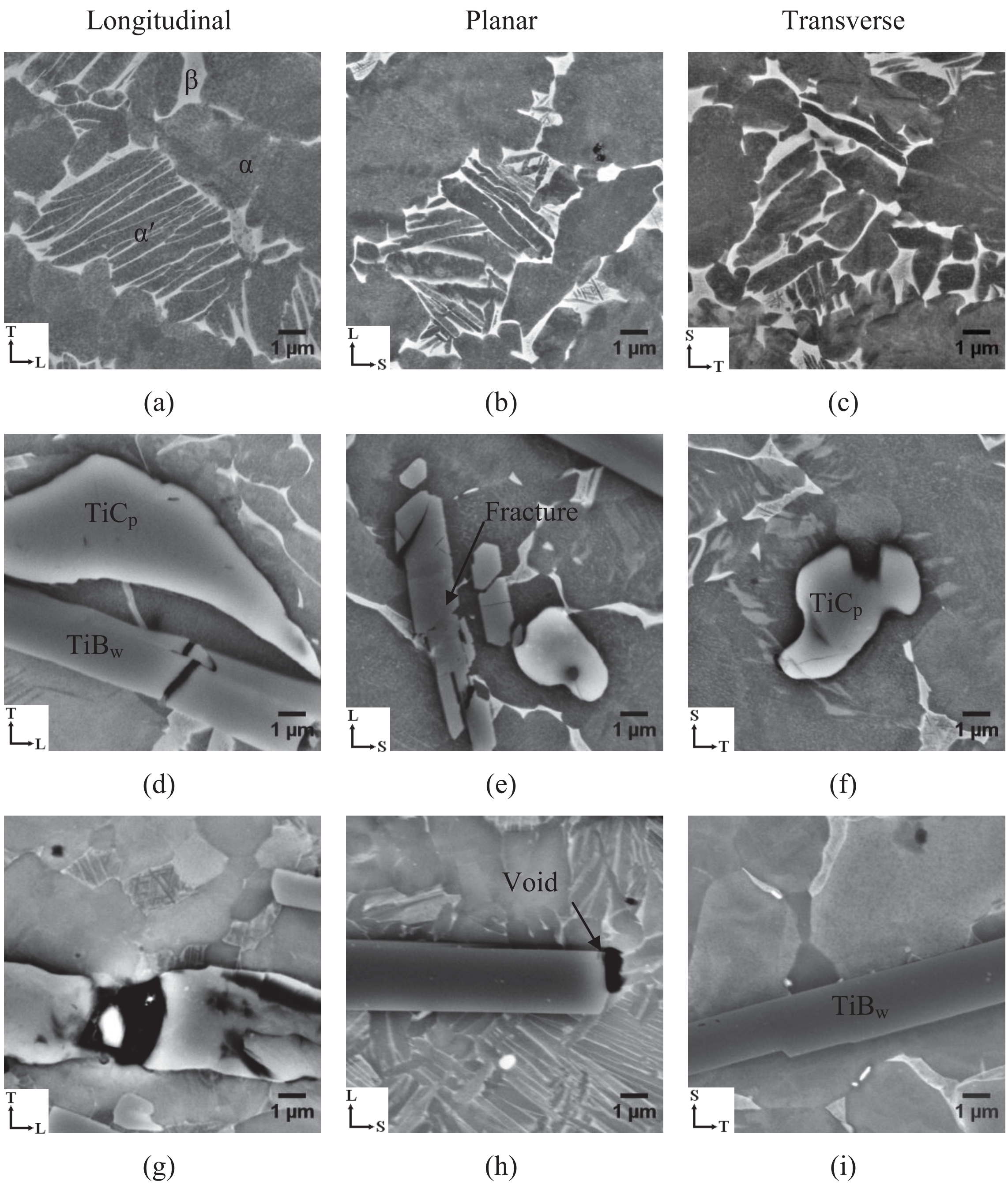

Longitudinal Planar Transverse

(a) (b) (c)

(d) (e) (f)

(g) (h) (i)

Figure 7–31. Backscatter secondary electron micrographs for the as-received (a, b, c) TC4 titanium alloy, (d, e, f) TC4/TiB, TiC/2.5w, 2.5p titanium MMC and (g, h, i) TC4/TiB, TiC/5w, 5p titanium MMC.

Image analysis is conducted on the titanium MMCs reinforcement content to determine the average particle size and volume percent as presented in Table 7-12. The procedure involved collecting ten backscatter secondary electron (BSE) micrographs at a magnification 400x. Image analysis is performed on these micrographs and the particles are then counted. The average particle size is determined by measurement of the particle’s major-axis length. The volume percent is determined from area measurement and by assuming stereological equivalence of the particle area and volume. The mean free path is determined from Equation **7-1** [197]. Note, TiB_w and TiC_b are treated as a single type of reinforcement.

Table 7-12. The particle size and volume percent for titanium MMCS.

Materials	**Particle size (µm)**	**Volume (%)**	**Mean free path (µm)**
TC4/TiB, TiC/2.5w, 2.5p	5.3 ± 3.8	4.8 ± 1.3	210
TC4/TiB, TiC/5w, 5p	8.9 ± 7.2	10 ± 1	160

The image analysis of the titanium MMCs revealed that there are differences between the reinforcement’s size. This is probably due to the vacuum arc remelting technique and the difficulty in controlling the size for these in-situ synthesized reinforcements. The volume fractions are as expected for the materials which are predetermined by stoichiometric calculations and controlled material additions of B_4C and carbon.

Quantitative x-ray mapping (QXRM) is conducted in order to characterise the titanium materials elemental distribution. In addition, QXRM is utilised to confirm the presence of TiB_w and TiC_c reinforcement. Quantitative x-ray mapping is performed using Moran Scientific X-Ray Mapping system. Pseudo colour maps generated from the X-Ray Mapping system allowed for identification of the elemental distribution of boron and carbon. Thus the location of the TiB_w and TiC_p reinforcement are identified in the MMCs system.

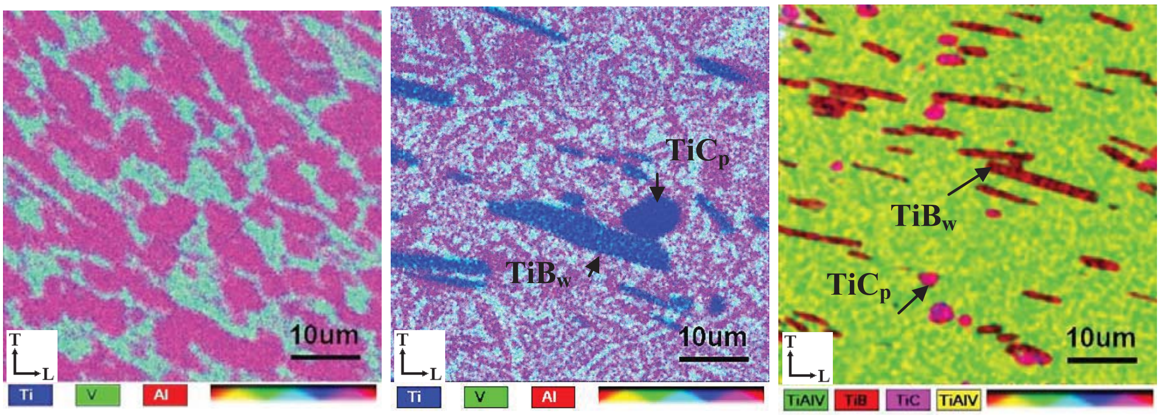

(a) (b) (c)

Figure 7–32. Pseudo coloured Quantitative x-ray mapping for as-received (a) TC4 titanium alloy (b) TC4/TiB, TiC/2.5w, 2.5p titanium MMC and (c) TC4/TiB, TiC/5w, 5p titanium MMC. The image size is set to 512x512 pixels, 16kV acceleration voltage. All Quantitative x-ray mapping is weighted averaged.

The elemental distribution is easily identified in the pseudo colour maps. The TC4 titanium alloy possessed a Ti-6Al-4V metal matrix as shown in Figure 7–32 (a). The emerald coloured phase suggested much of the vanadium and titanium elements existed within the retained beta, β, and acicular alpha phase, α′. The primary alpha, α, phase mainly consisted of aluminium and titanium elements. No interfacial reaction products are identified between the metal matrix and reinforcement content. Problems arose when identifying energy levels for the boron element using energy dispersive spectroscopy (EDS). It is resolved, however, with the use of wave-length dispersive spectroscopy (WDS) which identified very low atomic numbered elements as shown in Figure 7–32 (c) where the TiB_w is shown as red and TiC_p is shown as pink.

7.3.2 *The tensile test*

Standard tensile tests is performed on TC4 titanium alloy, TC4/TiB, TiC/2.5$_w$, 2.5$_p$ titanium MMC and TC4/TiB, TiC/5$_w$, 5$_p$ titanium MMC in order to assess the effect of increasing reinforcement content on tensile properties and mechanical behaviour. In general, at least three tensile tests are conducted for each type of material. The results of the tensile tests are presented in Figure 7–33 and Table 7-13.

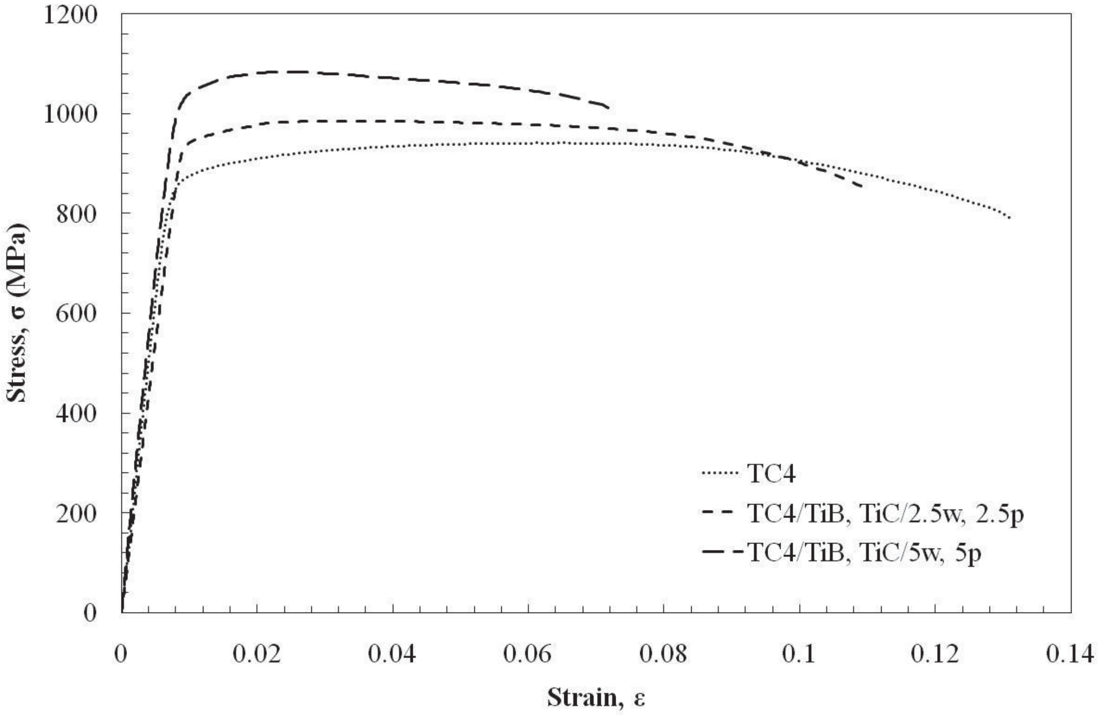

Figure 7–33. Engineering stress-strain behaviour for TC4 titanium alloy, TC4/TiB, TiC/2.5w, 2.5p titanium MMC and TC4/TiB, TiC/5w, 5p titanium MMC.

As observed in Figure 7–33 as the reinforcement weight percentage increased so did the elastic modulus. In addition, the yield and ultimate tensile strength experience an increase in strength with increasing reinforcement with a decrease in elongation indicating a lowering of ductility. This is attributed to an early onset of microplasticity around the sharp edges of the particulate reinforcement leading to increasing working hardening of the material. Furthermore, the material experienced increased void nucleation which led to final fracture and failure of the material.

Table 7-13. Tensile properties for TC4 titanium alloy, TC4/TiB, TiC/2.5w, 2.5p TC4/TiB, TiC/5w, 5p MMC.

Material	Elastic modulus (GPa)	Yield strength (MPa)	Ultimate tensile strength (MPa)	Elongation (%)
TC4	116 ± 7	900 ± 40	941 ± 6	13 ± 3
TC4/TiB, TiC/2.5w, 2.5p	124 ± 21	909 ± 28	976 ± 10	11 ± 1
TC4/TiB, TiC/5w, 5p	126 ± 20	1023 ± 11	1085 ± 4	3 ± 2

The tensile properties for the titanium materials as presented in Table 7-13 follow a similar trend to that of the aluminium materials presented in Table 7-2. As can be expected, the elastic modulus increased with increasing reinforcement. The yield strength and ultimate tensile strength increased with increasing reinforcement, however, the elongation decreased indicating a loss of ductility.

7.3.3 *The circumferential notch tension test*

There are insufficient materials to conduct the single-edge bend, SE(B), test on the titanium materials, however, there is enough to conduct CNT and SPT testing. Only one test is conducted for each condition due to limited materials. Circumferential notch tension test is conducted to assess the fracture toughness values for the titanium materials as presented in Table 7-14. Note, the error as stated in Table 7-4 is achieved by considering both fracture surfaces after the specimen is broken, in this way two fracture toughness values could be achieved for a single specimen. Problems arose when conducting CNT on the titanium materials as shall be discussed.

The plane-strain fracture toughness for the Ti-6Al-4V titanium alloy is expected to be around 44 to 66 $\mathrm{MPa}\sqrt{\mathrm{m}}$ [29], however, this value is not observed for the Ti-6Al-4V alloy. Applying Equation 4-11 which is the CNT's validity requirement for diameter size indicated that a minimum ligament thickness of between 4.1 to 9.1 mm is required for the test. Unfortunately, the minimum ligament for the Ti-6Al-4V alloy is measured after fracture to be 2.7 mm which is due to a large fatigue crack depth as observed in Figure 7–34 (a). The determination of the crack initiation is easy enough for this type of test, however, it is difficult to determine crack depth.

Since what is observed is the crack at the surface of the CNT v-notch and not how deep the fatigue crack penetrated into the specimen. A future solution to this problem could involve incorporating an electric potential drop technique for assessing a change in ligament size.

Another problem involved attempts at inducing fatigue crack into the titanium MMCs. According to Ibrahim et al. the fatigue crack depth has to be at least twice that of Irwin's correction, r_y, in depth to satisfy plane-strain fracture toughness conditions [96]. Furthermore, this requirement is only required to be satisfied at the deepest crack. Unfortunately, fatigue crack depths induced for the MMCs are found to be shallow, however, the Irwin's correction, r_y, is found to be at least satisfied. This result led to much higher fracture toughness values than otherwise would be expected and which is more than what is expected for the TC4 titanium alloy as observed in Table 7-14.

Furthermore, it is observed that the load-displacement curves for the TC4/TiB, TiC/2.5w, 2.5p and TC4/TiB, TiC/5w, 5p presented in Figure 7–35 are much higher than for the TC4 base alloy which further provided evidence that the crack is quite shallow. The finding shown in Table 7-14 runs contrary to the findings of the literature whereby fracture toughness decreases with introduction of reinforcement content.

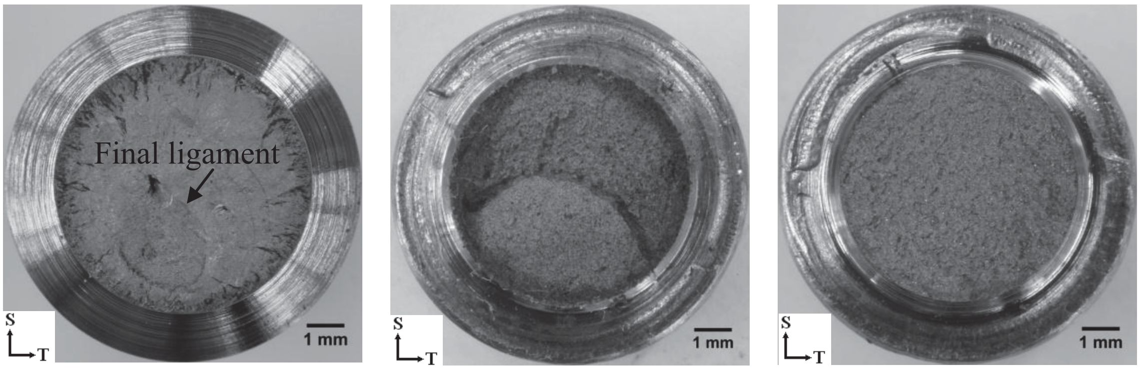

Plane-stress Plane-strain Plane-strain

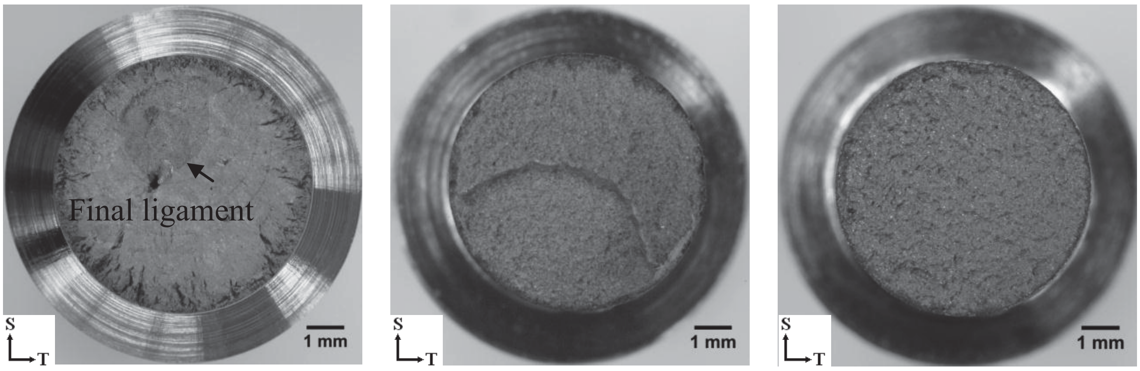

(a) (b) (c)

Figure 7–34. Circumferential notch tension test fracture surface for the (a) TC4, (b) TC4/TiB, TiC/2.5w, 2.5p and (c) TC4/TiB, TiC/5w, 5p. The top and bottom fractographs for each column are the matching fracture halves for each specimen.

Nevertheless, TC4/TiB, TiC/5w, 5p are found to exhibit a lower fracture toughness value when compared to TC4/TiB, TiC/2.5w, 2.5p as stated in Table 7-14. Furthermore the fracture surface for the TC4/TiB, TiC/2.5w, 2.5p and TC4/TiB, TiC/5w, 5p are found to be flat. The MMCs satisfied all validity requirements including Irwin's correction, r_y. This lead to a decision to regard TC4/TiB, TiC/5w, 5p TC4/TiB, and TiC/2.5w, 2.5p to exhibit plane-strain conditions and regard the TC4 base alloy to exhibit plane-stress behaviour.

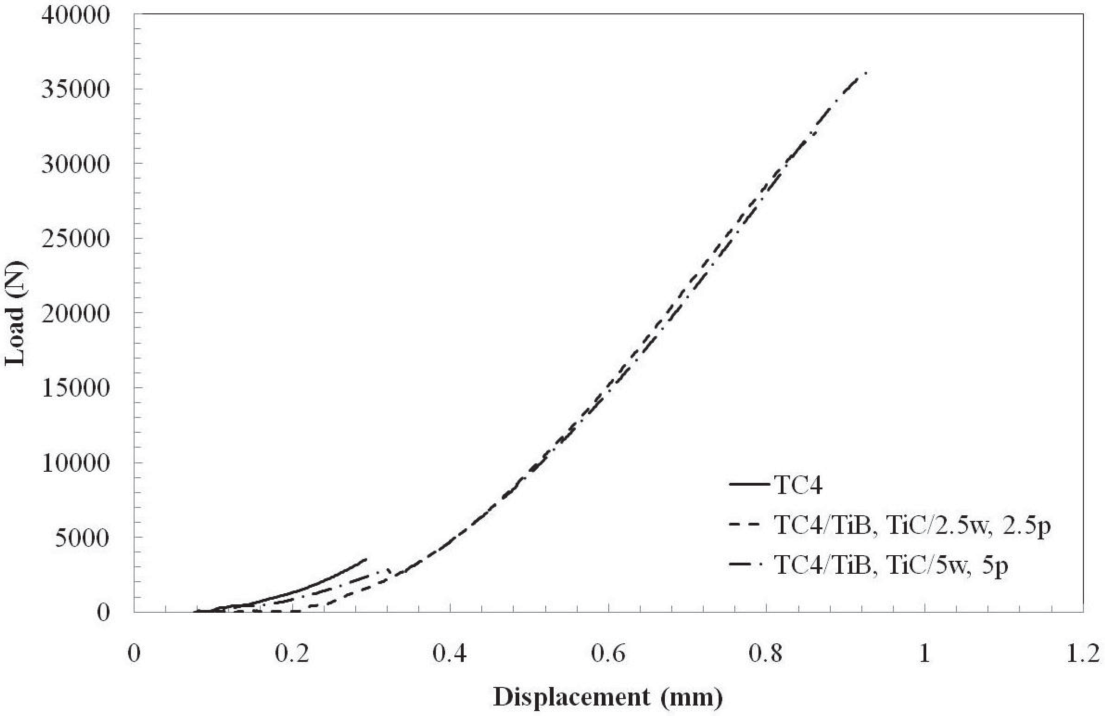

Figure 7–35. Circumferential notch tension load curves for titanium materials.

Table 7-14. Circumferential notch tension plane-strain fracture toughness, K_{1c} values for the titanium materials.

Material	Plane-Strain Fracture Toughness, K_{1c} (MPa$\sqrt{m}$)	Valid values
TC4	10	No[8]
TC4/TiB, TiC/2.5w	72	Yes
TC4/TiB, TiC/5w, 5p	71	Yes

The fracture toughness value for the as-received TC4 base alloy is considered to be in plane-stress conditions therefore this value is not incorporated into the SPT correlations in chapter eight.

---

[8] TC4 base alloy is considered to exhibit plane-stress conditions.

7.3.4 *Small punch test*

The small punch load-displacement curves for the titanium alloy and MMCs are presented in Figure 7–36, Figure 7–37 and Figure 7–38. In general, at least six tests are conducted for each condition. It is observed that curves presented produced relatively low scatter at the early stages of the SPT, however, scatter did increases as the load and displacement increased which is attributed to the increase in damage sites that accumulated within the bulk sample. In addition, a reason for the relatively low scatter is due to the accuracy in preparing the small punch disc specimen. The small punch load-displacement behaviour for the titanium materials are similar to what is observed for the aluminium small punch load-displacement behaviour. In that, it is observed that a distinct transition from the initial linear behaviour to nonlinear behaviour existed for all small punch load-displacement curves. Furthermore, the loads began to fall off at higher loads. This is especially true in the case of the MMCs. This fall in the loads is due to particle cracking and crack initiation, as damage to the particulate reinforcement accumulated limiting the MMCs ability to carry loads which is in contrast to that of the titanium alloy.

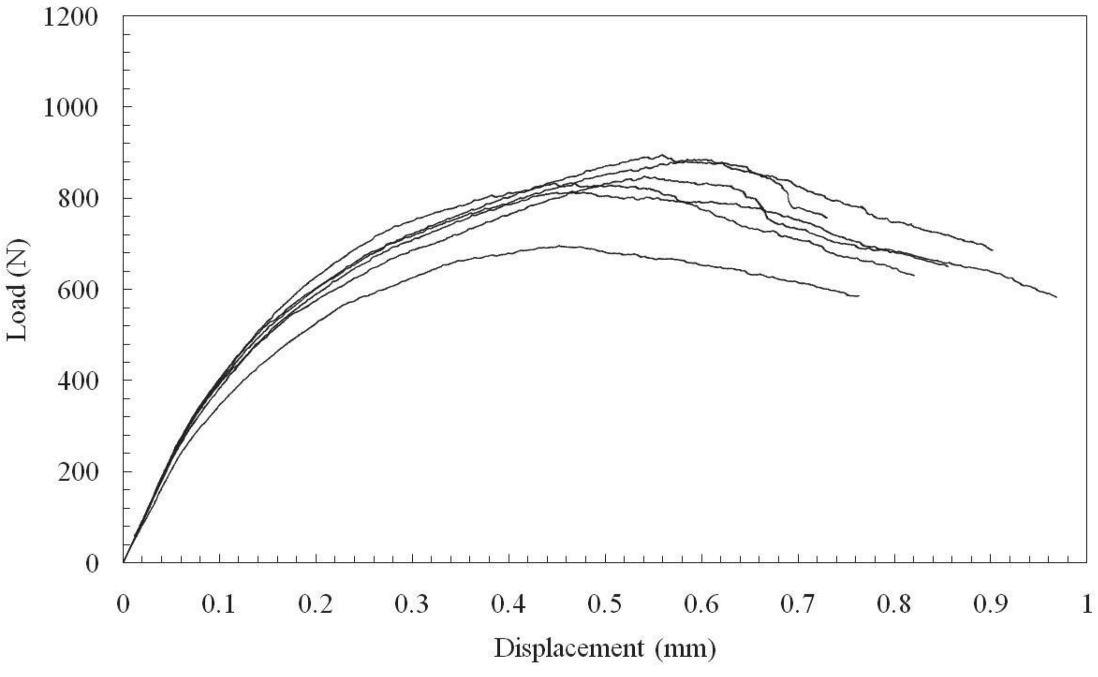

Figure 7–36. Typical small punch test load-displacement curves for TC4 titanium alloy.

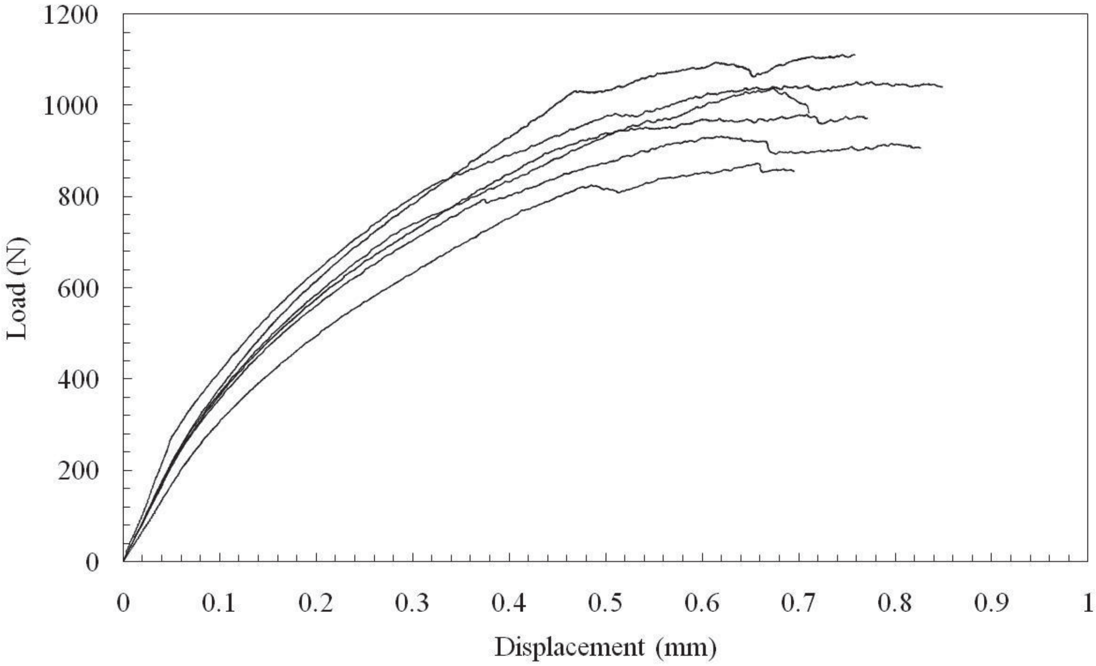

Figure 7–37. Typical small punch test load-displacement curves for TC4/TiB, TiC/2.5w, 2.5p titanium MMC.

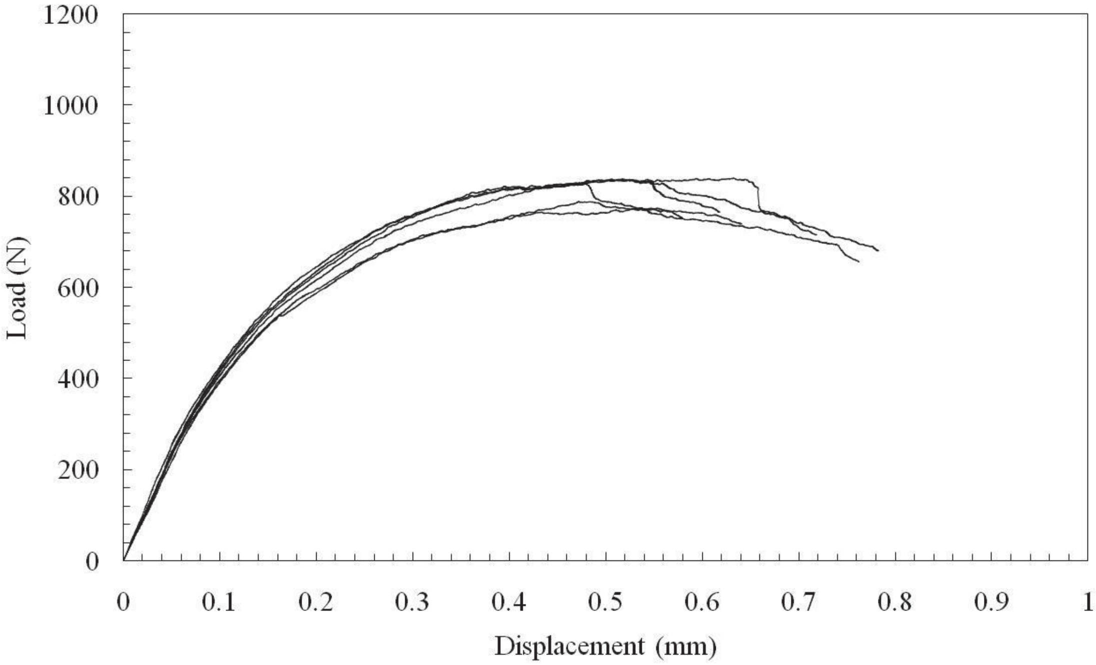

Figure 7–38. Typical small punch test load-displacement curves for TC4/TiB, TiC/5w, 5p titanium MMC.

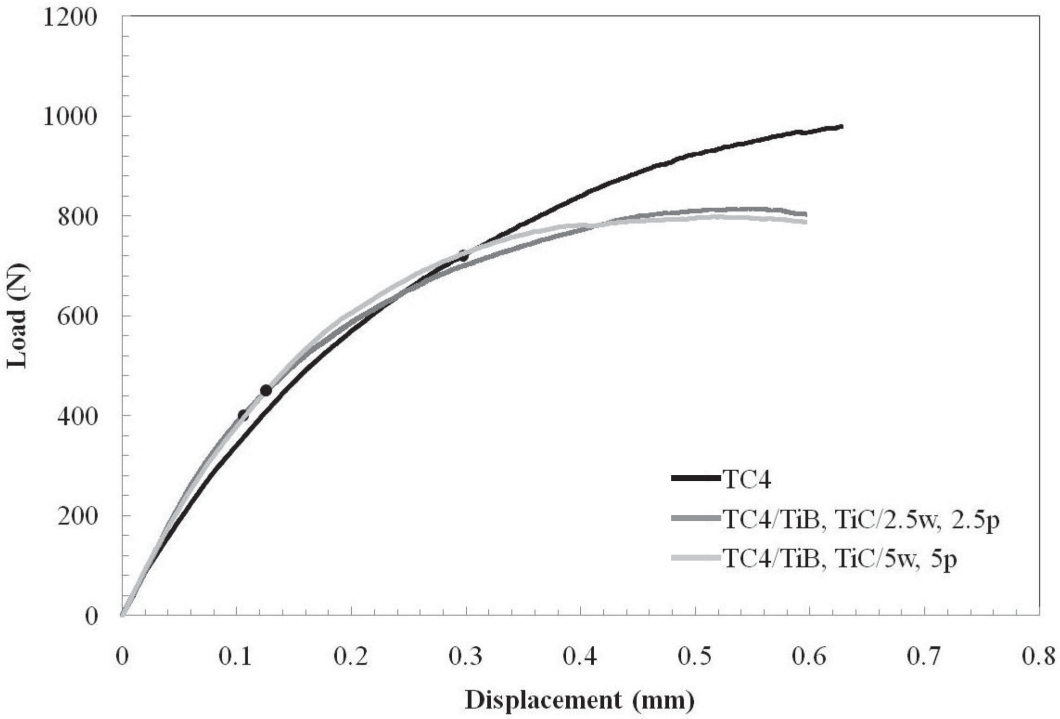

Figure 7–39. Averaged small punch test load-displacement curves for TC4 titanium alloy, TC4/TiB, TiC/2.5W, 2.5p titanium MMC and TC4/TiB, TiC/5W, 5p titanium MMC. The dots indicate the observed load at crack initiation.

Wanjara, et al. conducted a brief study on the shear punch load-displacement behaviour for Ti-6Al-4V/TiC MMCs as presented in Figure 7–40 [202, 203]. The shear punch test is similar to the SPT in that the difference is mainly due to the utilisation of a flat tip punch instead of a spherical punch. From their studies, the shear punch load-displacement curve and observed fracture mechanisms are found to be similar to uniaxial tensile behaviour as observed in Figure 7–40. Furthermore, the loads for their Ti-6Al-4V/TiC$_p$ MMC exhibited much higher loads when compared to the Ti-6Al-4V (MA) and Ti-6Al-4V (PM) base alloy which corresponds to the findings of this research where the initial loads of the aluminium and titanium MMCs are in fact higher than the alloy as observed in Figure 7–23 and Figure 7–39, respectively. Wanjara et al. stated that the shear punch load-displacement behaviour is a consequence of strengthening, work hardening and ductile behaviour of the alloys and MMCs material. Furthermore, the displacement values for the alloy are found to be more than the MMCs which confirmed that the alloys ductility is greater than the MMCs. Similarly, fracture and failure mechanisms for the MMCs involved void nucleation, growth and coalescence of the metal matrix. In addition, particle fracture and debonding is observed.

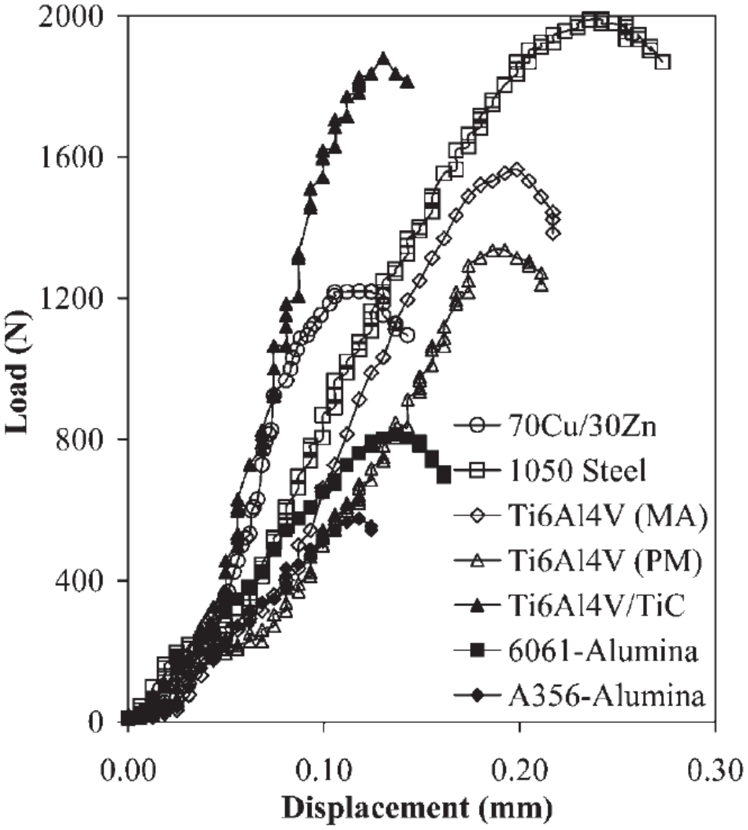

Figure 7–40. Shear punch load-displacement curve for various materials including MMCs [202, 203].

Small punch values are determined for the as-received titanium materials as presented in Table 7-15. The small punch values included the small punch elastic-plastic load, P_y, small punch load at crack initiation, P_i, small punch equivalent fracture strain, ε_{qF}, and small punch energy, E_{SP}. The small punch load at crack initiation is determined by observing crack initiation via a CCD camera. When the crack is observed the load is recorded. The equivalent fracture strains are calculated using an approximation method proposed by Mao et al. [10]. The results are presented in Table 7-15 and are similar to the results obtained for the aluminium materials as presented in Table 7-10.

Table 7-15. Small punch test properties for the as-received titanium materials

Materials	**Elastic-plastic load, P_y (N)**	**Load at crack initiation, P_i (N)**	**Equivalent fracture strain, ε_{qF}**	**Total small punch test energy, E_{SP} (J)**
TC4	200 ± 2.3	720 ± 17	0.16 ± 0.006	0.51 ± 0.1
TC4/TiB, TiC/2.5w, 2.5p	220 ± 3.5	400 ± 60	0.07 ± 0.001	0.30 ± 0.06
TC4/TiB, TiC/5w, 5p	230 ± 4.1	450 ± 20	0.05 ± 0.001	0.32 ± 0.05

It is observed that the load at crack initiation for the base alloy is generally higher compared to the MMCs. This attributed to the overall toughness of the base alloy and its ability to resist crack initiation compared to its reinforced counterpart. Comparing the

MMCs it is observed that higher loads are observed with increasing reinforcement. In general a decrease in strain is observed for increasing reinforcement.

A student's t-Test is performed on the TC4/TiB, TiC/2.5w, 2.5p and TC4/TiB, TiC/5w, 5p titanium MMCs to ascertain whether there is any statistical difference in the derived small punch energies, E_{SP}, as presented in Table 7-16. Similar to the t-Test performed for the aluminium materials the t-test found that there is no real difference between the two small punch energies, E_{SP}, from a statistical point of view. This may indicate that the experimental SPT configuration may not possess the necessary energy resolutions to ascertain the differences in small punch energies for MMCs exhibiting similar volume fractions with a difference of only 5 vol.%.

Table 7-16. The statistical difference between two small punch energy, E_{SP}, TC4 titanium MMCs.

t-Test: Two-sample assuming unequal variances		
Materials	TC4/TiB, TiC/2.5w, 2.5p	TC4/TiB, TiC/5w, 5p
Mean	0.300	0.322
Variance	0.003	0.003
Observations	6.000	6.000
Hypothesized Mean Difference	0.000	
df	10.000	
t Stat	-0.686	
P(T<=t) one-tail	0.254	
t Critical one-tail	1.812	
P(T<=t) two-tail	0.508	
t Critical two-tail	2.228	

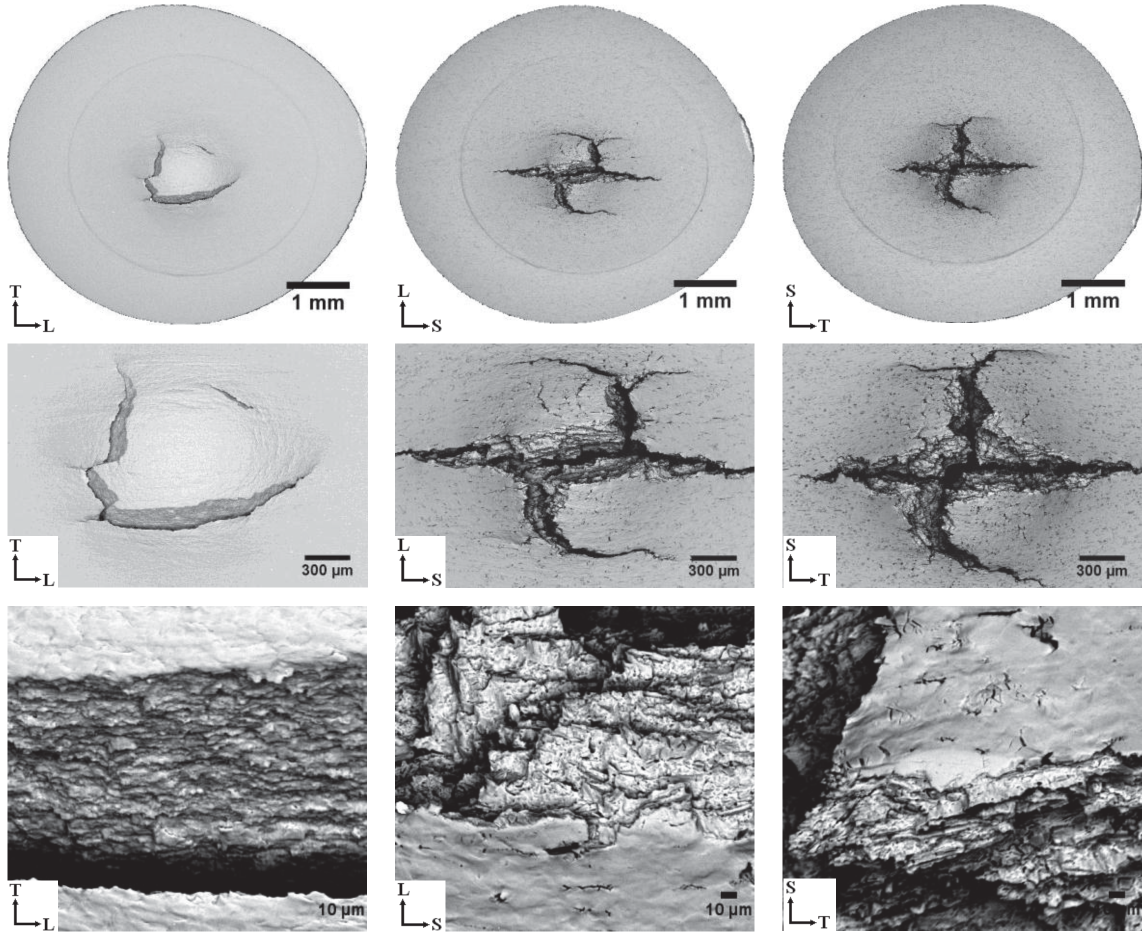

(a) (b) (c)

Figure 7–41. Fractographs showing the cracking profile of (a) TC4 titanium alloy, (b) TC4/TiB, TiC/2.5w, 2.5p titanium MMC, (c) TC4/TiB, TiC/5w, 5p titanium MMC at increasing magnifications.

Fractography is conducted using scanning electron microscopy on the top and side views of the titanium materials as presented in Figure 7–41 and Figure 7–42, respectively. The fracture surface for the TC4 base alloy as presented in Figure 7–41 (a) exhibited a circumferential complex crack formation whilst multi-crack formation is evident on the fracture surface of the titanium MMCs, as shown in Figure 7–41 (b) and (c). The crack behaviour for the titanium MMCs is dissimilar to the titanium alloy which suggested that the fracture mechanisms for alloy and MMCs are distinct. Furthermore, with respect to the MMCs, the primary crack is often found to be aligned along the longitudinal and extrusion axis.

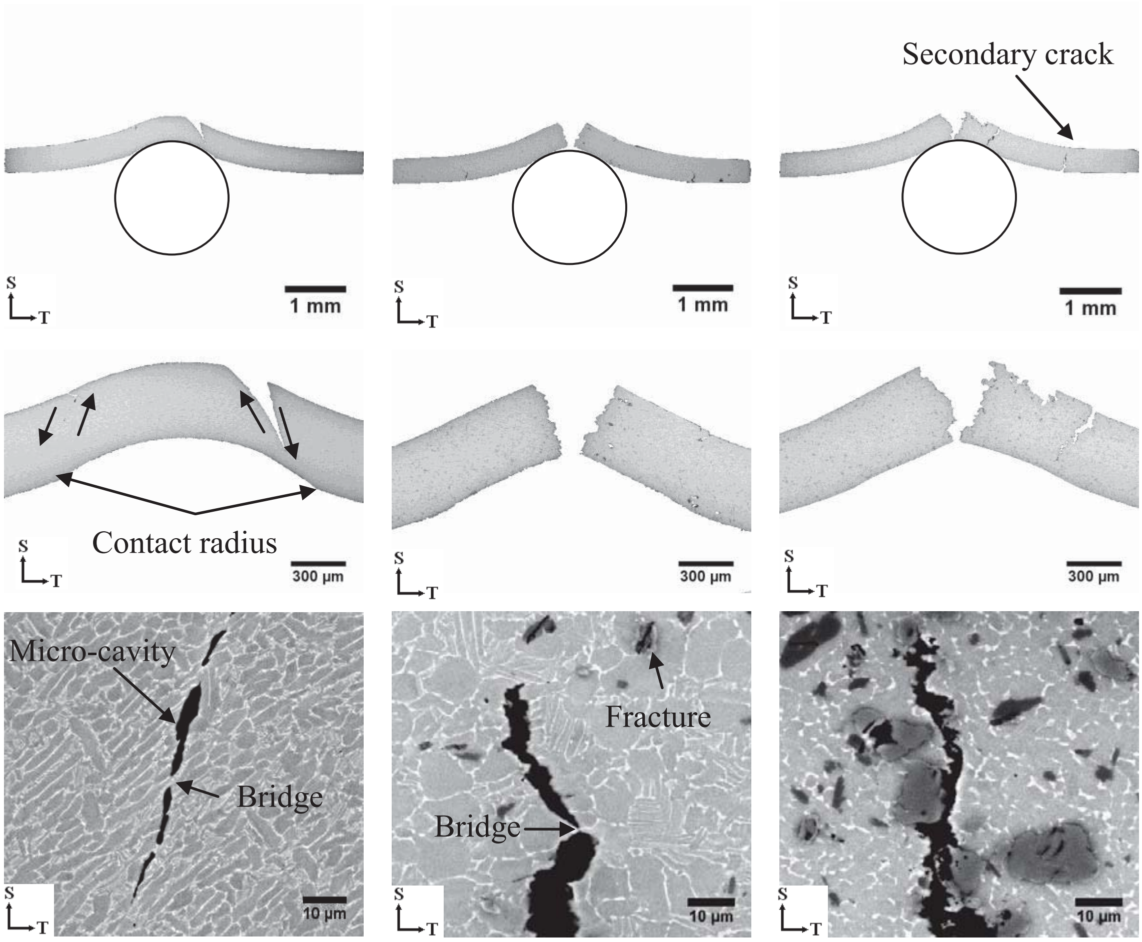

(a) (b) (c)

Figure 7–42. Side view of the small punch test crack profile for (a) TC4 titanium alloy, (b) TC4/TiB, TiC/2.5w, 2.5p titanium MMC and (c) TC4/TiB, TiC/5w, 5p titanium MMC.

Scanning electron microscopy is conducted on the side view of the titanium materials as presented in Figure 7–42. As is the case for the aluminium materials, the alloy for the titanium exhibited a smooth crack profile that began at free surface and ran up to the point where it meets the edge of the contact radius of the spherical punch. The formation of micro-cavities could be observed at the tip of this smooth line. In addition, bridging is observed for the titanium alloy as seen in Figure 7–42 (a). The titanium MMCs exhibited tortuosity of the crack path which is a consequence of the particulate reinforcement as shown in Figure 7–42 (c). In addition, fracture of the TiC_p reinforcement is observed as shown in Figure 7–42 (b).

7.3.5 *Finite element analysis*

Finite element analysis is conducted on the titanium materials in order to assess the small punch load-displacement behaviour for the titanium materials which is compared against the experimental data as presented in Figure 7–43. The modelling processes incorporated elastic and plastic properties of the titanium materials. Similar to the analysis that is applied to the aluminium materials, the finite element analysis of the titanium materials predicted higher loads when compared against the experimentally derived data. Furthermore the finite element analysis could not account for the load drop as exhibited by the MMCs. This behaviour is again attributed to increase damage brought on by the reinforcement content. A finite element model of the MMCs should account for particle fracture, matrix-particle debonding and failure of the matrix such as void nucleation and coalescence. Again, research on the finite element method is discontinued due to the complexity of modelling of the MMCs' deformation and fracture behaviour which is concluded to be beyond the scope of this research.

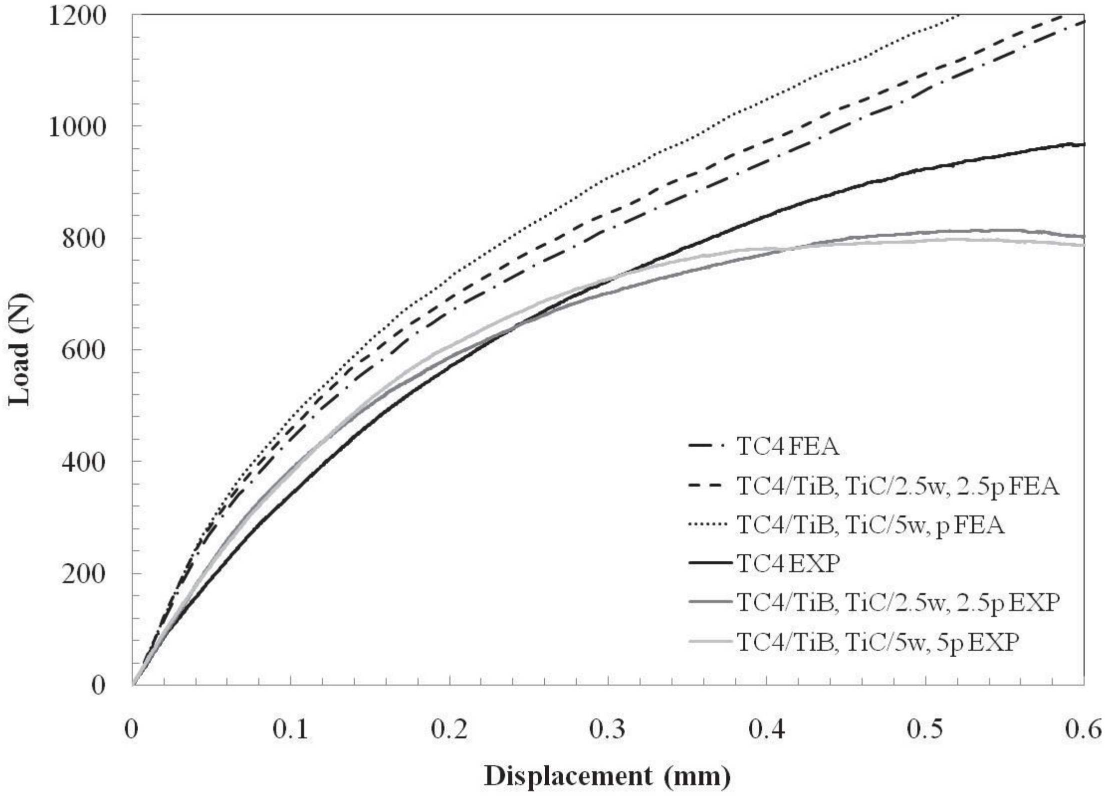

Figure 7–43. Finite element prediction of the small punch load-displacement curves for titanium materials.

The crack initiation load, P_i, describes the point at which the material begins to fracture which will lead to unstable crack growth. Furthermore identifying the small punch load at crack initiation, P_i, has proven to be difficult in the past since identification involved light optical techniques which have limited resolution range. Moreover such techniques cannot resolve the early failure event due to reflectance and effects arising from optical aberrations. The titanium materials are tested under predetermined loads to identify the load at crack initiation for the TC4/TiB, TiC/2.5w, 2.5p and TC4/TiB, TiC/5w, 5p MMCs as presented in Figure 7–44 and Figure 7–45, respectively.

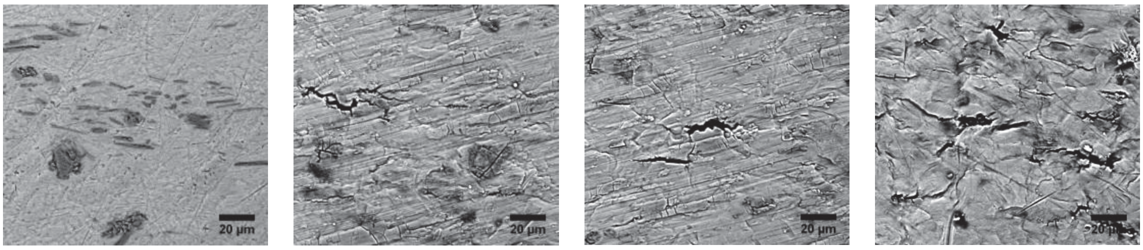

200N 300N 400N 500N

Figure 7–44. Crack initiation and propagation behaviour for TC4/TiB, TiC/2.5w, 2.5p titanium MMC with increasing loads.

It is found that crack initiation load, P_i, occurred between 200N to 300N for TC4/TiB, TiC/2.5w, 2.5p and TC4/TiB, TiC/2.5w, 2.5p titanium MMCs. In both cases initial failure occured via particle fracture of the globular TiC_p reinforcement and decohesion between the metal matrix and whisker-like TiB_w reinforcement content. Reinforcements that have fractured have no loading bearing capacity. Therefore the rate of load increase began to steadily decrease leading to load drop and unstable crack growth as observed in Figure 7–39.

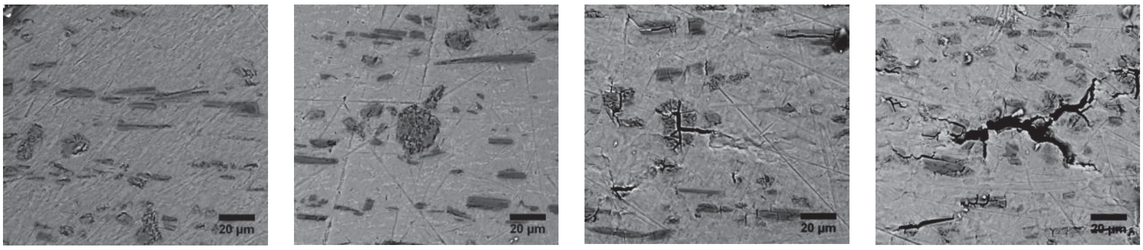

100N 200N 300N 400N

Figure 7–45. Crack initiation and propagation behaviour for TC4/TiB, TiC/2.w, 2.5p titanium MMC with increasing loads.

The finite element model of the small punch load-displacement behaviour up to 300N is presented in Figure 7–29. The evidence of crack initiation occurring between 200N to 300N explained why the experimentally derived loads fell away when compared to finite element prediction. Furthermore, it is suggested by this author that particle debonding and fracture should be considered to improve the finite element method. Again, further work on the FEA of MMCs is discontinued as the work required would constitute another thesis.

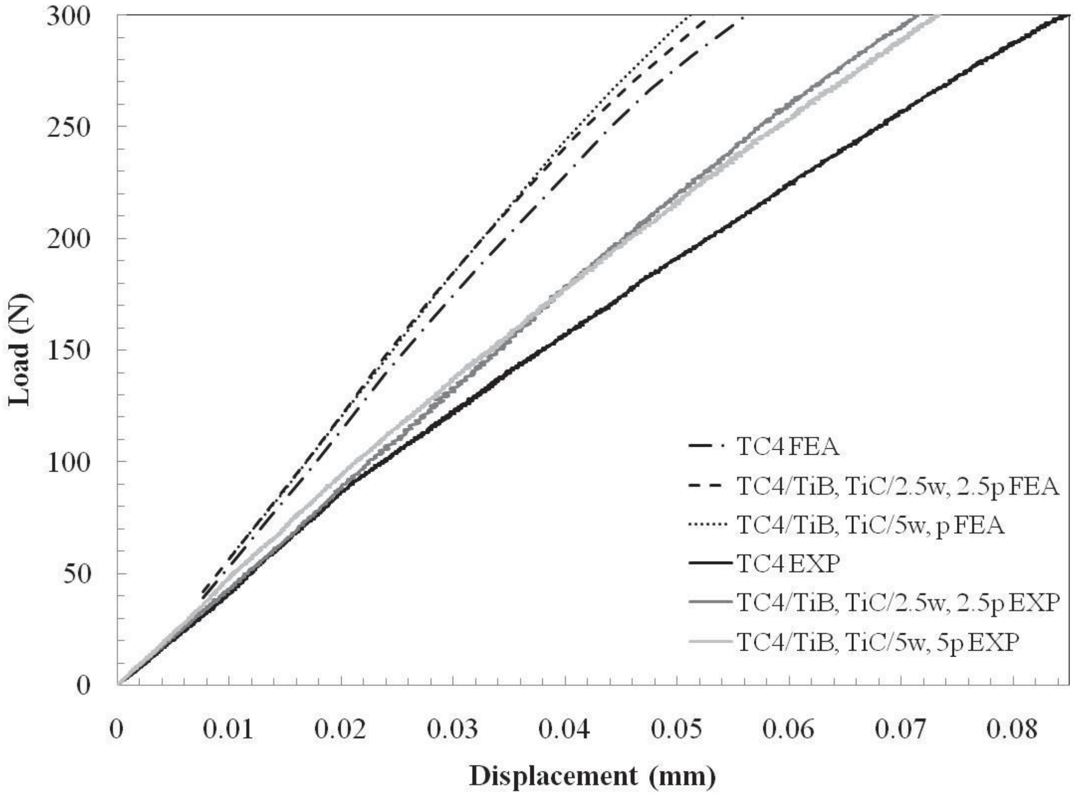

Figure 7–46. Finite element prediction of the small punch load-displacement curve for titanium materials up to 300N.

7.4 Concluding remarks

The microstructure, mechanical properties and fracture behaviour for the as-received aluminium and titanium materials have been assessed and discussed. In addition tensile test, fracture toughness test and small punch test data has been obtained.

Scanning electron microscopy of the small punch specimen's fracture surface revealed that alloys exhibited circumferential complex cracking behaviour whilst the MMCs exhibited the multi-cracking event which appeared *star-like*. Furthermore, initial failure for the aluminium MMCs arose from debonding between the SiC_p and metal matrix whilst the titanium MMCs initial failure arose from either debonding of TiB_w or by TiC_p fracture.

Scanning electron microscopy revealed that the small punch crack initiation load, P_i, occurred at much earlier loads when compared to conventional optical techniques. The initial crack is a steady-state crack which could lead to unstable crack growth and failure of the material.

Basic finite element analysis found that the rate in load reduction for the MMCs is attributed to increasing damage brought on by the reinforcement content. The finite element method should account for damage mechanism associated with MMCs.

The small punch elastic-plastic load, P_y, equivalent fracture strain, ε_{qF}, and small punch energy, E_{SP}, has been derived. These values shall now be correlated against conventional yield strength, σ_{YS}, and plane-strain fracture toughness, J_{1c}, values in the following chapter in order to assess the small punch role as a multi-mechanical test.

CHAPTER EIGHT

SMALL PUNCH TEST CORRELATIONS

8.1 Introduction

The aim of this thesis is to determine if there are any correlations between data from the SPT and conventional tensile yield strength, σ_{YS}, and plane-strain fracture toughness, K_{1c} and J_{1c}, properties. This is to establish whether it is possible to predict reasonable mechanical values from small sized specimens especially in the case when limited materials are available or when specimen sizes do not meet the requirements as specified by the standard tests. To ascertain this, the data presented in chapter seven will now be compared and the relationships derived. The SPT mechanical values (P_y, ε_{qF} and E_{SP}) presented in Table 8-1 are compared against mechanical properties (σ_{YS}, K_{1c} and J_{1c}) presented in Table 8-2 as the reinforcement content varies.

The small punch elastic-plastic load, P_y, small punch equivalent fracture strain, ε_{qF}, and small punch energy, E_{SP}, where chosen since they are considered to be intimately related to conventional mechanical test properties. For instance, the small punch elastic-plastic load, P_y, is considered to be related to yield strength, σ_{YS}, [137, 152, 158-160]. The small punch equivalent fracture strain, ε_{qF}, [123, 141, 147, 154, 204] and the small punch energy, E_{SP}, [26, 27, 105, 163, 205-207] is considered to be related to the plane-strain fracture toughness, K_{1c} and J_{1c}, values. The small punch and conventional mechanical properties is compared for the purpose of this chapter as presented in Table 8-3.

Table 8-1. Summary of the small punch test P_y, ε_{qF} and E_{SP} values for aluminium and titanium materials.

Materials	**Small punch elastic-plastic load, P_y (N)**	**Small punch equivalent fracture strain, ε_{qF}**	**Total small punch fracture energy, E_{SP} (J)**
7A04-T6	89 ± 2.8	0.14 ± 0.002	0.32 ± 0.05
7A04/SiC/7.5p-T6	97 ± 2.1	0.07 ± 0.002	0.19 ± 0.01
7A04/SiC/10p-T6	117 ± 2	0.06 ± 0.003	0.2 ± 0.02
TC4	200 ± 2.3	0.16 ± 0.006	0.51 ± 0.1
TC4/TiB, TiC/2.5w, 2.5p	220 ± 3.5	0.07 ± 0.001	0.30 ± 0.06
TC4/TiB, TiC/5w, 5p	230 ± 4.1	0.05 ± 0.001	0.32 ± 0.05

Table 8-2. Summary of conventional mechanical properties σ_{YS}, K_{1c} and J_{1c}, values for aluminium and titanium materials.

Materials	**Yield strength, σ_{YS} (MPa)**	**Plane-strain fracture toughness, K_{1c} ($\mathrm{MPa}\sqrt{\mathrm{m}}$)**	**Plane-strain fracture toughness, J_{1c} ($\mathrm{kJ/m^2}$)**
7A04-T6	462 ± 10	41.7 ± 1.4	20.6 ± 1.3
7A04/SiC/7.5p-T6	555 ± 4	38 ± 0.7	16.4 ± 1.3
7A04/SiC/10p-T6	557 ± 9	27.3 ± 1.8	9.4 ± 1
TC4	900 ± 40	10.0 ± 0.2	0.81
TC4/TiB, TiC/2.5w, 2.5p	909 ± 28	72 ± 1.4	38 ± 1.4
TC4/TiB, TiC/5w, 5p	1023 ± 11	71.0 ± 2.1	36.4 ± 2.2

Table 8-3. Comparison of small punch and conventional mechanical properties.

Small punch test values		Mechanical properties
P_y	vs.	σ_{YS}
ε_{qF}	vs.	K_{1c}, J_{1c}
E_{SP}	vs.	K_{1c}, J_{1c}

8.2 Empirical correlations between the small punch and mechanical values

8.2.1 *Correlating yield strength, σ_{YS}, and small punch elastic-plastic load, P_y*

As mentioned earlier the small punch elastic-plastic load, P_y, is described as the load at which the specimen begins to yield which is defined as the transition point between elastic region I and elastic-plastic region II from the small punch load-displacement curve as described in Figure 5–4. The small punch elastic-plastic load, P_y, is thought to be an important value as it is considered to be related to the tensile yield strength, σ_{YS} [137, 152, 158-160]. The small punch elastic-plastic load, P_y, is identified from the small punch load-displacement curve. A number of authors have attempted to identify the small punch elastic-plastic load, P_y, using methods such as the *offset*, *2 tangent*, *elastic deformation energy* (EDE) and *finite element method* (FEM) with varying levels of success [137, 151, 152, 173]. A qualitative representation of the small punch elastic-plastic, P_y, is presented in Figure 8–1 (c). In the case of this research, the small punch elastic-plastic load, P_y, is recorded at the point of onset of nonlinear behaviour. The *offset* and *2 tangent* methods presented in Figure 8–1 (a) and (b) are not used since these methods tended to identify the small punch elastic-plastic load, P_y, above the transition point and at higher loads. If we refer back to chapter seven on the load crack initiation graphs we find that SEM analysis found that crack initiation loads, P_i, occurs much earlier than what would be expected if optical techniques are applied.

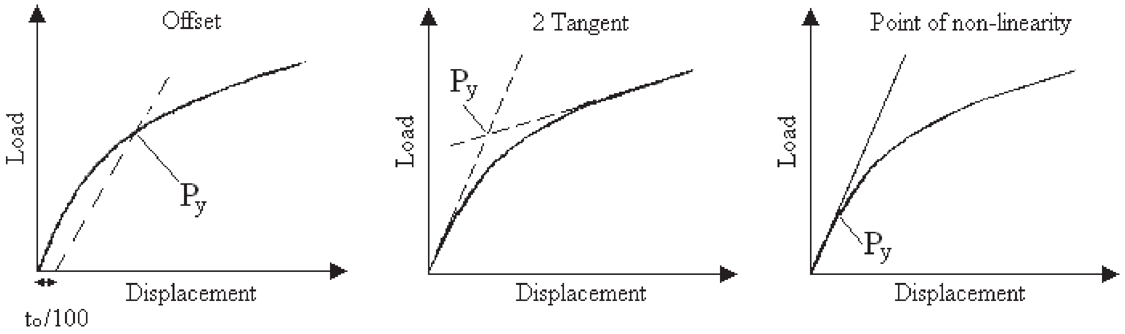

(a) (b) (c)

Figure 8–1. A qualitative comparison of the methods for deriving small punch elastic-plastic load, P_y.

This indicates that the tensile yield stress on the free surface must be reached at very early loads. In fact, it is found for the aluminium MMCs that crack initiation occurred somewhere between 100N to 200N as presented in Figure 7–27, whilst for the titanium MMCs crack initiation occurred around 200N to 300N as presented in Figure 7–44 and Figure 7–45. Therefore, yielding has to occur before the onset of failure.

Furthermore, the *2 tangent* method and the *offset* method tended to introduce large errors [152]. The *offset* method exhibited less scatter than *2 tangent* method and is similar to the *point of non-linearity* method except the offset is at zero.

It is important to identify the small punch elastic-plastic load, P_y, at loads since studies in this research area have found the yielding event occurs earlier than might expected as identified from small-punch load-displacement curves and explained in chapter seven. Finite element analysis utilising Von Mise's stress contour plots as presented in APPNEDIX I clearly predicts that the stress required for yielding occurs for all materials at low loads. Furthermore, as observed by the FEM, significant yielding will be experienced by the materials for small punch displacements as low as 0.1mm. Note, the *step time*, seconds, utilised for the FEM is equivalent to displacement in millimetres. Isselin found that the *2 tangent* and the *offset* techniques provided a consistent technique for the evaluation of the small punch elastic-plastic load, P_y [152] but disagreed with the hypothesis that the small punch elastic-plastic load, P_y, can be compared to the tensile yield strength, σ_{YS}. Nevertheless, it is found that in both studies the onset of plasticity is identified to occur at low loads within the bulk small punch specimen which corresponds well with this research's numerical findings shown in APPNEDIX I. Therefore, early identification of the small punch elastic-plastic load, P_y, is needed.

The deviation from the so called initial elastic region may be influenced by another deformation mechanism which is observed in both Figure 7–25 (a) and Figure 7–42 (a) in which at some point the small punch specimen began to experience shear stress, τ_{YS}. This finding is supported by Ma et al. who identified that final fracture occurs via shear failure [201]. In addition, this observation is similar to the Von Mise's yield relation observed by Lucas who had conducted shear punch tests [208, 209] as presented in Equation 8-1.

$$\sigma_{YS} = \frac{1}{\sqrt{3}}\tau_{YS} \qquad 8\text{-}1$$

If this is the case then it becomes even more important to obtain the small punch elastic-plastic load, P_y, before the shearing effects become significant.

The change from linearity is a subtle event and must be observed closely at the early stages of the small punch load-displacement curve. Moreover, the techniques involving the *offset* and *2 tangent*, *elastic* method tend to produce large scatter thereby complicating yield strength, σ_{YS} correlations [152]. This is why this author believes good correlations between the small punch elastic-plastic load, P_y, have yet to be established due to inaccurate estimate of the small punch elastic–plastic load, P_y. Furthermore, much of the elastic and plastic deformation occurs at very low loads. Evidence for identifying the small punch elastic-plastic load, P_y, is confirmed through scanning electron microscopy which revealed that the transition point occurs at much earlier loads than is previously thought and in most cases well before the maximum small punch load, P_{max}, as described in previous results shown in Figure 7–27, Figure 7–28, Figure 7–44 and Figure 7–45.

The small punch elastic-plastic load, P_y, is obtained by analysing the end of linearity through linear-regression analysis and identifying the first point which behaves nonlinearly on the small punch load-displacement curve. The analysis can be implemented by first drawing a line intercepting zero. The next step would be to find the tangent to the small punch load-displacement curve. The small punch elastic-plastic load, P_y, can then be determined as the last point which deviates from linearity.

The empirical correlation for the small punch elastic-plastic load, P_y, and tensile yield strength, σ_{YS}, for both the aluminium and titanium materials are presented in Figure 8–2 and Figure 8–3, respectively. As can be expected an increase in the small punch elastic-plastic load, P_y, follows an increase in yield strength, σ_{YS}, values for both materials as reinforcement content increases. Although this is the case there appears to be evidence of a linear relationship for both the aluminium and titanium materials when applying linear least squares regression.

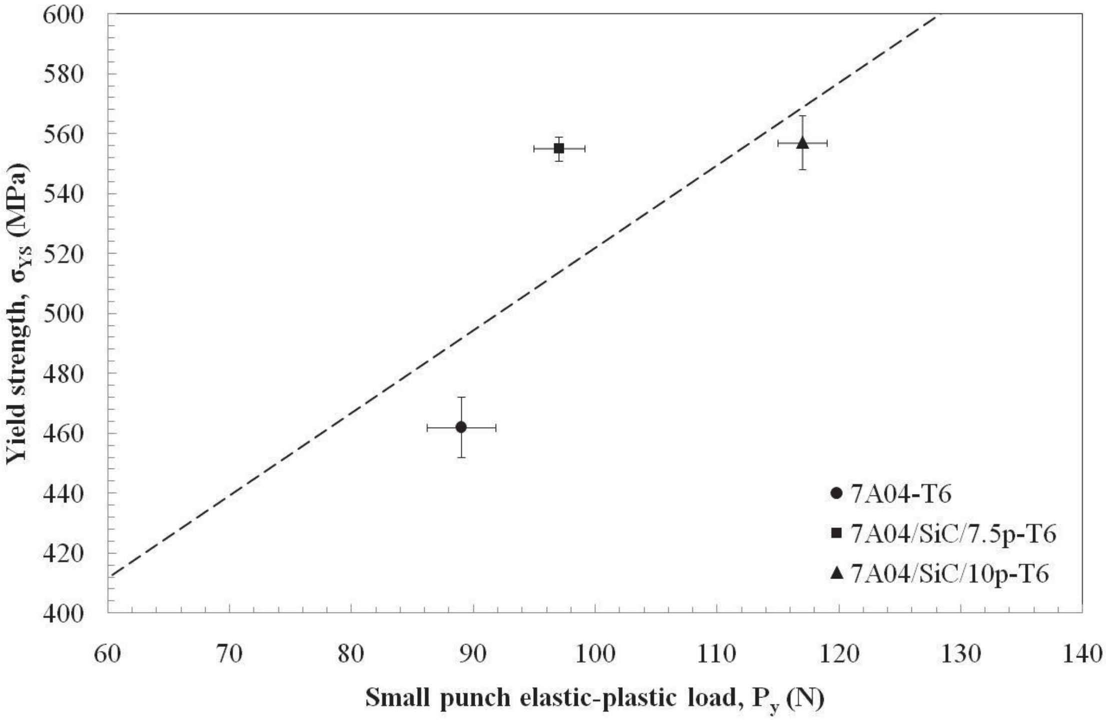

Figure 8–2. Correlation of the yield strength, σ_{YS}, and the small punch elastic-plastic load, P_y, for aluminium materials.

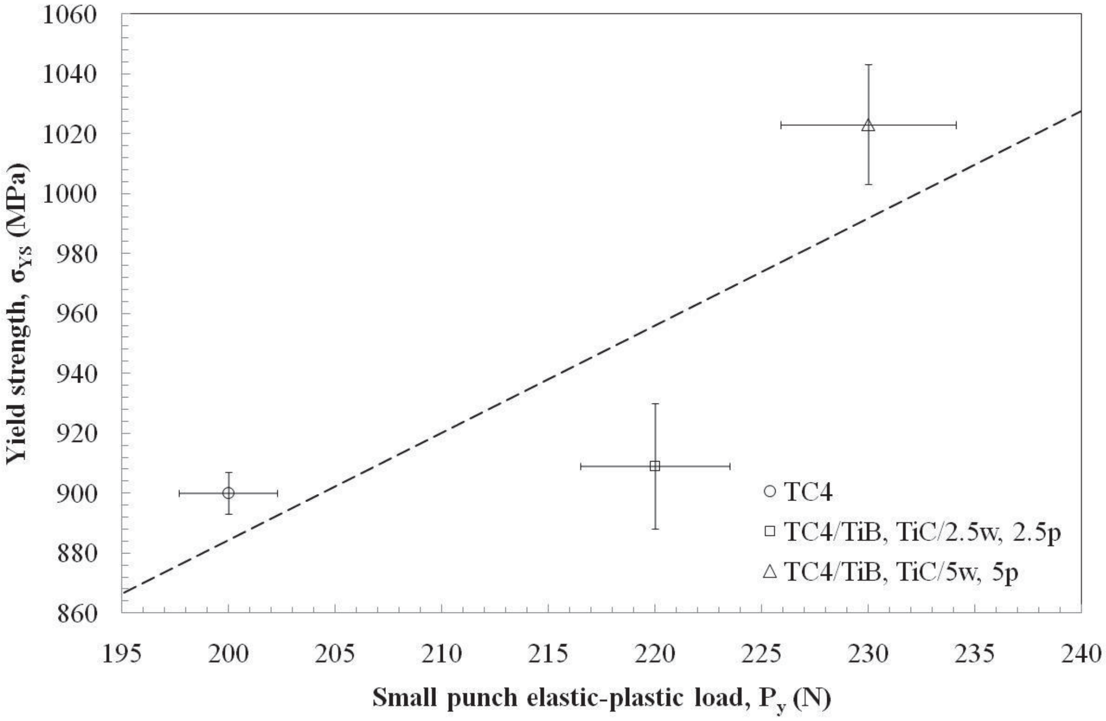

Figure 8–3. Correlation of the yield strength, σ_{YS}, and the small punch elastic-plastic load, P_y, for titanium materials.

The aluminium and titanium are then combined together as presented in Figure 8–4. A clearer relationship is now observed for the both the aluminium and titanium materials, as there is evidence of a linear relationship between the small punch elastic-plastic load, P_y, and tensile yield strength, σ_{YS} values. Furthermore, it can be seen that the error bars are fairly small indicating low scatter in the results. The overall linearity of small punch elastic-plastic load, P_y, and tensile yield strength, σ_{YS}, suggest that there is a good correlation between the two values. From this relationship, analytical solutions can be implemented to obtain direct yield strength values from the SPT as shall be discussed in this chapter.

As stated previously in chapter five, the tensile yield strength, σ_{YS}, and small elastic-plastic load, P_y can be correlated together using a normalisation relationship known as the correlation coefficient, α, which is described in Equation 5-14. The calculated correlation coefficient, α, for the as-received aluminium and titanium materials are presented in Table 8-4.

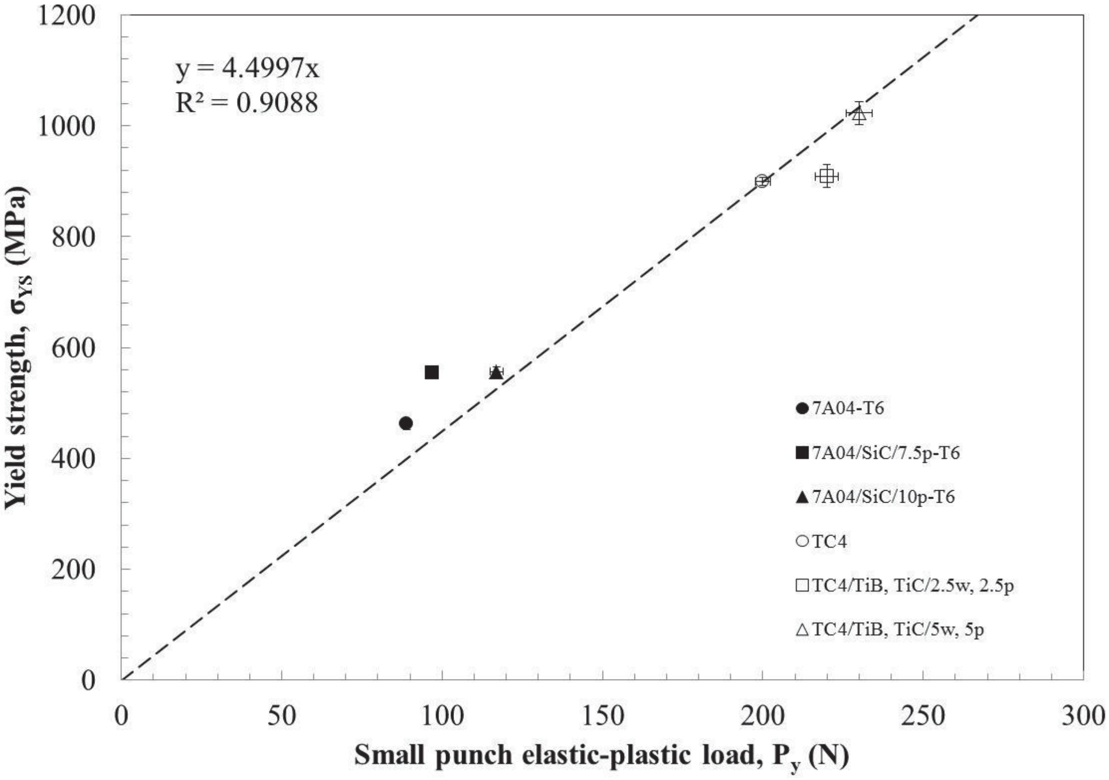

Figure 8–4. Correlation of the yield strength, σ_{YS}, and the small punch elastic-plastic load, P_y, for both aluminium and titanium materials.

Table 8-4. Correlation coefficients, α, for the aluminium and titanium materials.

Materials	Correlation coefficient, α
7A04-T6	1.3
7A04/SiC/7.5p-T6	1.4
7A04/SiC/10p-T6	1.2
TC4	1.1
TC4/TiB, TiC/2.5w, 2.5p	1
TC4/TiB, TiC/5w, 5p	1.1

The correlation coefficients, α, are in general, larger when compared to literature values as presented in Table 5-2. This is explained by the method employed for this research to identify the small punch elastic-plastic load, P_y, which is taken at lower loads. The slightly higher correlation coefficients, α, values exhibited by the aluminium materials is less clear since literature states that the correlation coefficient, α has less to do with mechanical properties and more to do with die geometry [137, 159, 161]. It is worth noting that the literature values are for steel. Nevertheless, the correlation coefficients, α, for the aluminium and titanium materials are similar and can be used to empirically correlate the small punch elastic-plastic load, P_y, and tensile yield strength, σ_{YS}, values. The empirical equation for the correlation coefficient, α, derived from this research is presented in Equation 8-2.

$$\sigma_{YS} = 0.9018\frac{P_y}{t_o^2} + 161.4 \qquad 8\text{-}2$$

It is important to note that the correlation coefficient, α, is made over a large yield range. Therefore, the above empirical correlation should cover a large range of materials with similar yield strength values.

The correlation coefficient, α, is an empirical correlation for determining the tensile yield strength, σ_{YS}, values from small punch elastic-plastic load, P_y. The correlation coefficient, α, accounts for the SPT die configuration including lower die bore size, spherical punch diameter and specimen thickness. Furthermore, the correlation coefficient, α, is thought to be a constant that has less to do with the mechanical properties of the small punch specimen and more to do with the SPT die configuration. Therefore, the tensile yield strength, σ_{YS}, can be assessed once the correlation coefficient, α, is known. Of course, the equations for the empirical correlations coefficient, α, will vary with different kinds of die geometries.

8.2.2 *Correlating plane-strain fracture toughness, J_{1c} and small punch equivalent fracture strain, ε_{qF}*

The intimate relationship between ductility and fracture toughness has led to many studies in the field of fracture mechanics. One such study first proposed by Bayoumi and Bassim [26] involved a theoretical model between the small punch equivalent fracture strain, ε_{qF}, [155] and the plane-strain fracture toughness, J_{1c} and K_{1c}, as presented previously in Figure 5–8. The theoretical model described a nonlinear relationship for materials that exhibited predominant elastic behaviour and linear behaviour for materials that exhibited elastic-plastic behaviour. Many authors have verified this linear relationship for elastic-plastic materials [16, 137, 210, 211], however, limited studies have been done for the non-linear case.

The small punch equivalent fracture strain, ε_{qF}, can be used to quickly obtain the plane-strain fracture toughness, J_{1c} and K_{1c}, by measuring the initial thickness, t_o, and minimum thickness at fracture, t_f, as described in Equation 5-3. The small punch equivalent fracture strain, ε_{qF}, is compared against the plane-strain fracture toughness, J_{1c}, for the aluminium and titanium materials as presented in Figure 8–5 and Figure 8–6, respectively. Note, the ductile plane-strain fracture toughness, J_{1c}, is derived from brittle plane-strain fracture toughness K_{1c}, values in accordance with Equation 5-34. A large part of the uncertainty in deriving the small punch equivalent fracture strain, ε_{qF}, arose from identifying and measuring the minimum thickness at fracture, t_f. Often measurement of this small punch minimum thickness at fracture, t_f, can only be done after the mechanical test is completed.

The effect of elastic recovery can affect the measurement of the small punch minimum thickness at fracture, t_f, however, the extent of this effect remains unknown. Another factor to consider is the way the measurement is made, for example in this research the thickness is measured using a Mitutoyu Digimatic Indicator which has sharpened ends for measuring the SPT minimum specimen thickness. This method although capable in performing this task can be difficult to perform since the specimen has to be held in place whilst the thicknesses are measured.

The general trend found when empirically correlating the plane-strain fracture toughness, J_{1c}, and small punch equivalent fracture strain, ε_{qF}, with increasing reinforcement content is presented in Figure 8–5 and Figure 8–6. The plane-strain fracture toughness, J_{1c}, and equivalent fracture strain, ε_{qF}, empirical correlation for both materials show that an increase in the ductility will result in an increase in fracture toughness. A comparison of both the aluminium and titanium materials as presented in Figure 8–7 demonstrates that the fracture toughness for the titanium materials are larger when compared to the aluminium materials. The points for the aluminium and titanium materials are not collinear as what might be expected. The points for the titanium are shifted up and show that despite much higher values of fracture toughness, J_{1c}, they have similar small punch equivalent fracture strain, ε_{qF}. Also, it is expected that the small punch equivalent fracture strain, ε_{qF}, values for the titanium materials be more than the aluminium. Although, the tensile elongation results as presented in Table 7-2 and Table 7-13 for both materials are similar which may explain the similar small punch equivalent fracture strain, ε_{qF}, values.

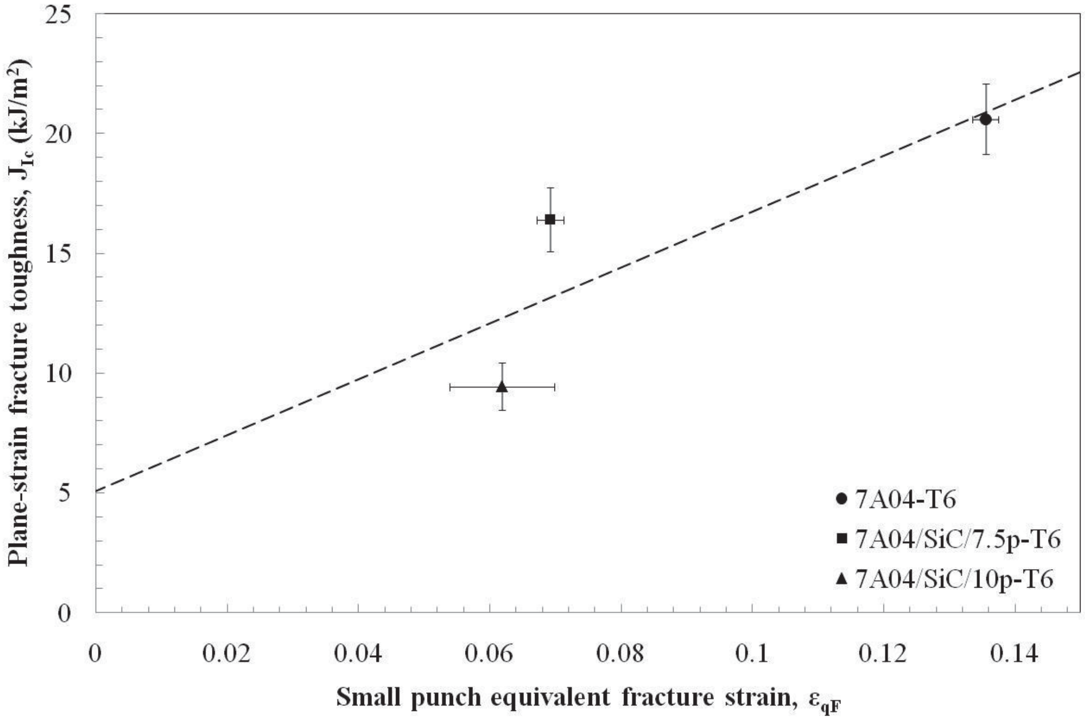

Figure 8–5. A correlation of the plane-strain fracture toughness, J_{1c}, and equivalent fracture strain, ε_{qF}, for aluminium materials.

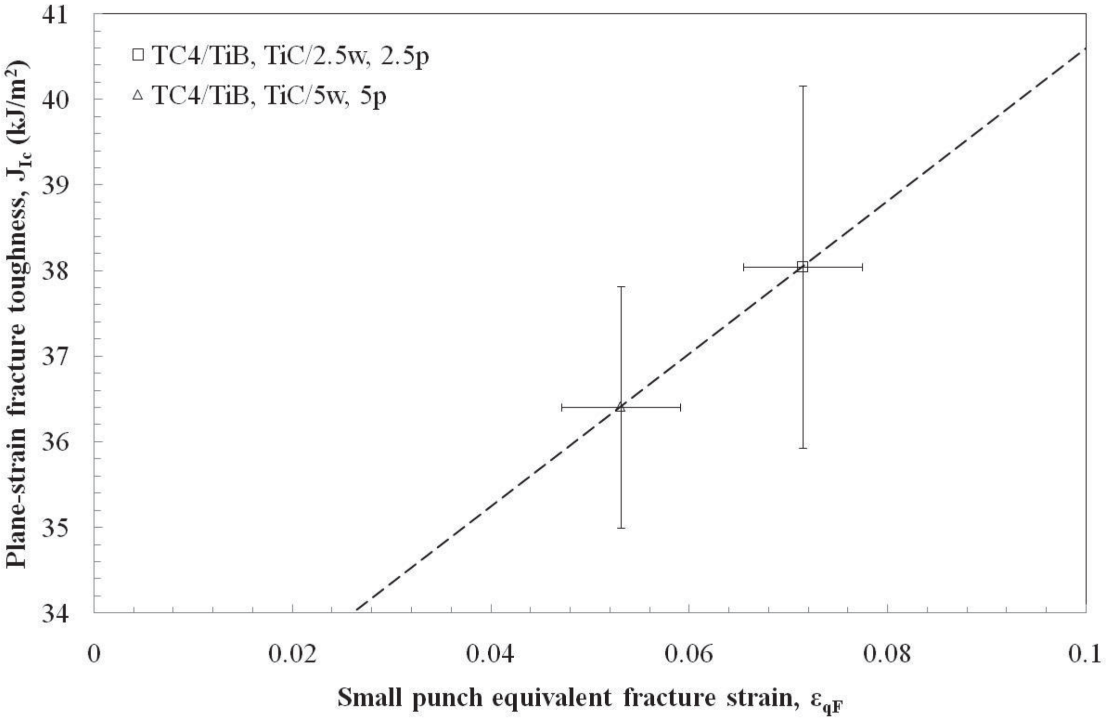

Figure 8–6. A correlation of the plane-strain fracture toughness, J_{1c}, and equivalent fracture strain, ε_{qF}, for titanium materials.

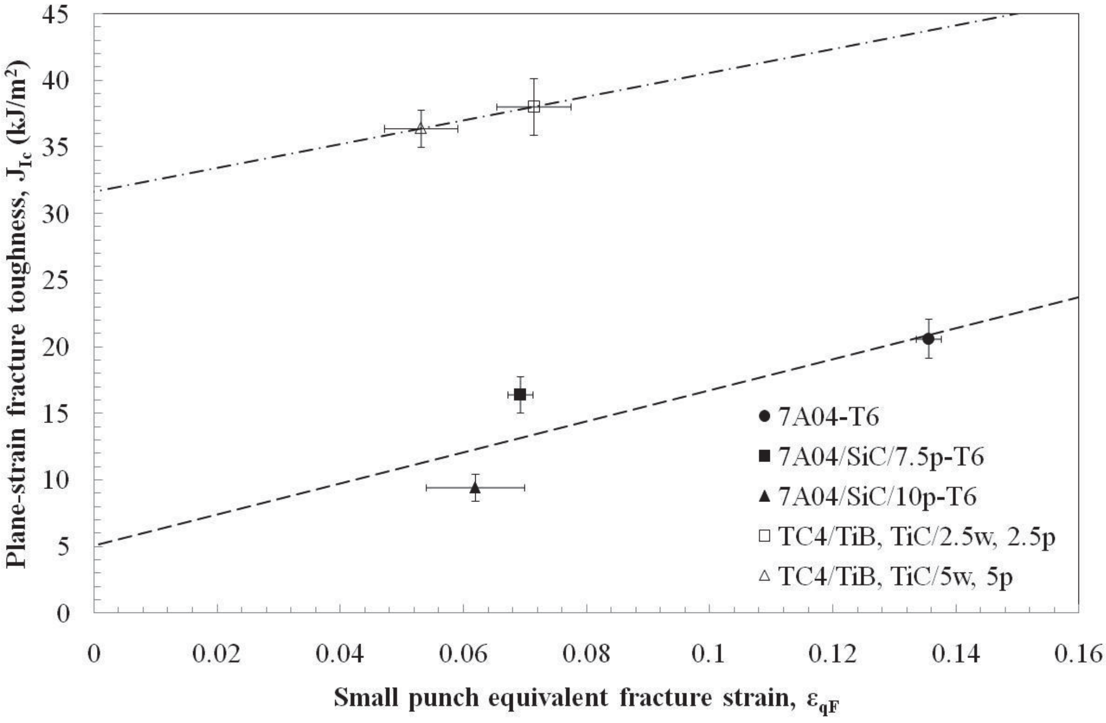

Figure 8–7. A correlation of the plane-strain fracture toughness, J_{1c}, and equivalent fracture strain, ε_{qF}, for both aluminium and titanium materials.

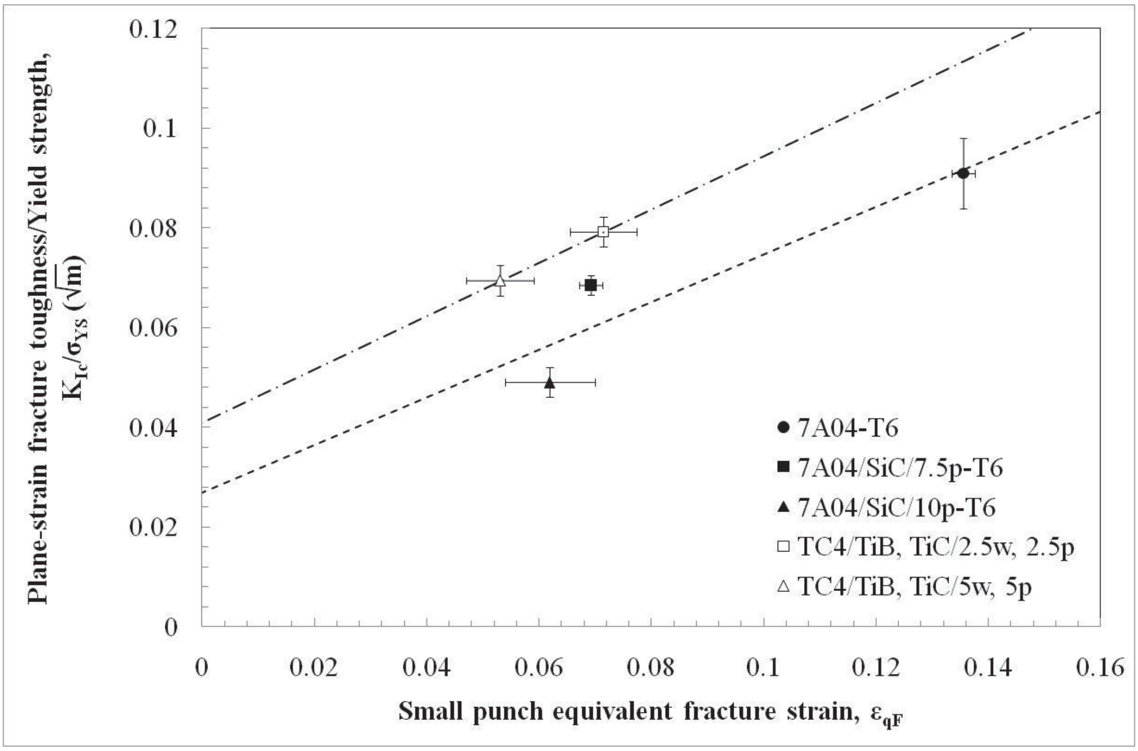

Figure 8–8. A correlation of normalised plane-strain fracture toughness/yield strength, K_{1c}/σ_{YS}, and equivalent fracture strain, ε_{qF}, relationship for both aluminium and titanium materials.

The parallelism as observed in Figure 8–7 of the titanium and aluminium materials are further analysed by normalising the brittle plane-strain fracture toughness, K_{1c}, with the yield strength, σ_{YS}, of the material as presented in Figure 8–8. The goal is to see whether the results could be collapsed into a single line to derive some kind of relationship. Unfortunately, this could not be achieved for both J_{1c} and K_{1c} calculations. It may be argued that the fracture toughness for the titanium is overestimated. The high fracture toughness exhibited by the titanium material may be due to the small fatigue crack size as observed in Figure 7–34 (b) and (c). A crack size that is larger than twice the theoretical Irwin correction factor, r_y, proposed by Ibrahim may be needed in the case of MMCs [94]. The small crack size led to an overall increase in the measured CNT maximum load which may have increased the fracture toughness values. A lack of materials allowed only a single test for each of titanium CNT specimens which further complicated the results, however, the overall trend is clear that increase strain will correspond with an increase in fracture toughness. Nevertheless, it will be shown in the following sections that a clear relationship exists for J_{1c} and ε_{qF}.

8.2.3 *Correlating plane-strain fracture toughness, J_{1c}, with the small punch energy, E_{SP}*

Baik et al. defined the area underneath the small punch load-displacement curve as the small punch energy [97, 114]. For this research the small punch energy, E_{SP}, is approximated with the use of a polynomial curve and integrated to obtain the energy for the material. Recently, the small punch energy, E_{SP}, is defined as the energy required up to the displacement at the onset of fracture/failure after 20% load drop from the maximum load, P_{max} [130], however, as discussed earlier crack initiation and failure is observed to form well before the maximum load, P_{max}. Therefore, the total small punch energy, E_{SP}, in fact describes the energy required to elastically and plastically deform a material whilst the crack forms.

In this research, the test is stopped soon after the first load drop is observed, instead of allowing the test to run through a 20% load drop, since it is believed that no more useful mechanical behaviour can be derived after significant damage and failure to the material. For this reason, the small punch maximum load, P_{max}, is employed as the limit of the small punch energy and not the 20% load drop method. The small punch energy can be applied to three situations as described in Figure 8–9.

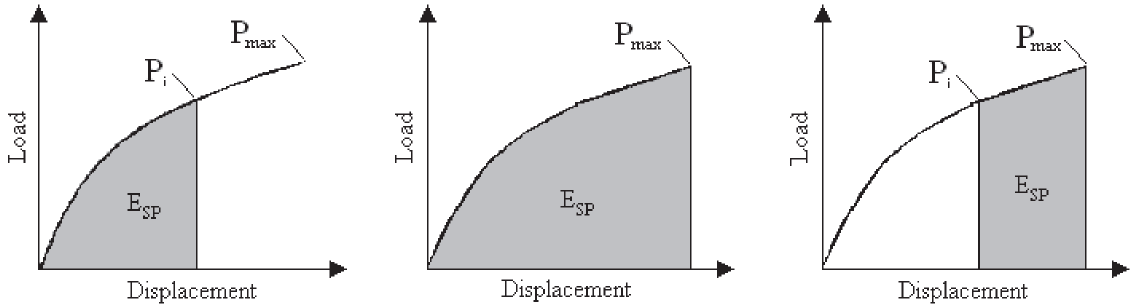

(a) (b) (c)

Figure 8–9. A qualitative comparison of the methods for deriving small punch energy, E_{SP}. Where (a) is the energy up to crack initiation, (b) is the total small punch energy and (c) is the energy after crack initiation.

The results for the small punch fracture energies are presented in Table 8-5. Generally, it is found from this research that the small punch fracture energies for the alloy are much higher when compared to the MMCs. Calculated small punch energies as described in Figure 8–9 are presented in Table 8-5. In general, the small punch energy, E_{SP}, for the alloy is found to be higher when compared to the MMCs. This is to be expected, however, a linear trend is not observed when comparing the fracture toughness and small punch energy, E_{SP}, with increasing reinforcement. The fracture toughness and the total small punch energy, E_{SP}, for aluminium and titanium materials is presented in Figure 8–10.

Table 8-5. Calculated small punch energies.

Materials	**Small punch energy up to crack initiation, E_{SP} (J)**	**Total small punch energy, E_{SP} (J)**	**Small punch energy after crack initiation, E_{SP} (J)**
7A04-T6	0.05± 0.02	0.32 ± 0.05	0.27 ± 0.03
7A04/SiC/7.5p-T6	0.02 ± 0.03	0.19 ± 0.01	0.17 ± 0.03
7A04/SiC/10p-T6	0.03 ± 0.04	0.20 ± 0.02	0.17 ± 0.02
TC4	0.11 ± 0.02	0.51 ± 0.1	0.4 ± 0.04
TC4/TiB, TiC/2.5w, 2.5p	0.03 ± 0.04	0.3 ± 0.06	0.26 ± 0.05
TC4/TiB, TiC/5w, 5p	0.05 ± 0.03	0.32 ± 0.05	0.27 ± 0.06

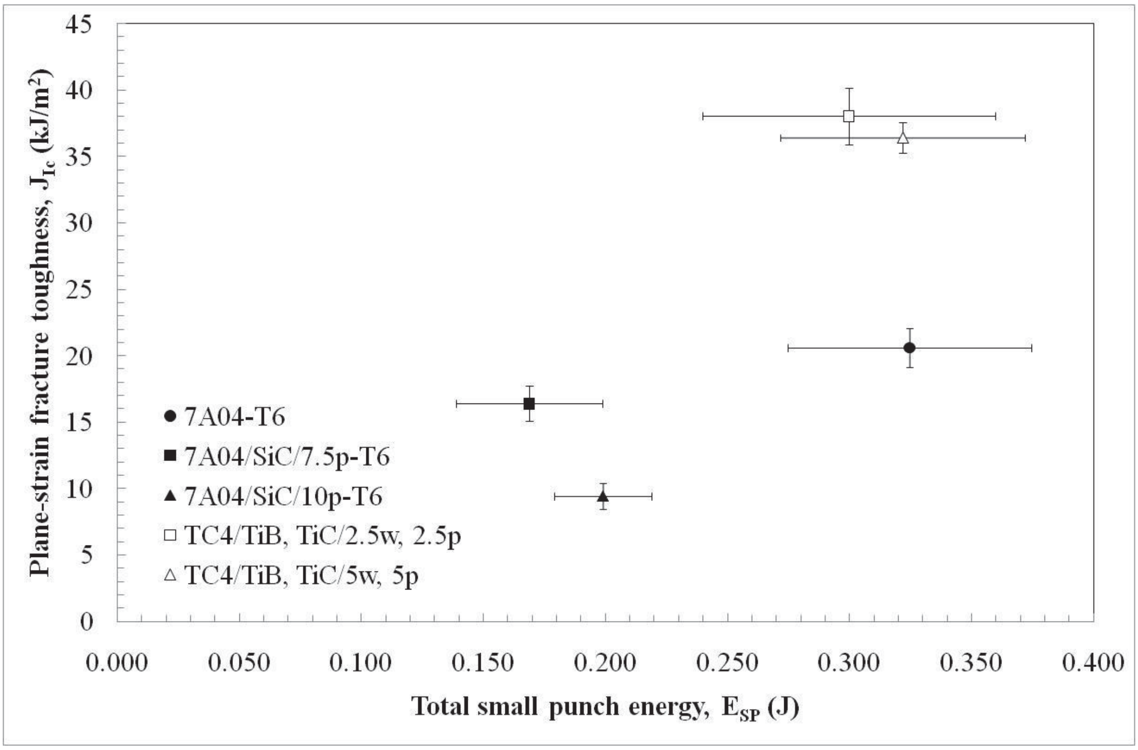

Figure 8–10. A correlation of the plane-strain fracture toughness, J_{1c}, and total small punch energy, E_{SP}.

As expected the plane-strain fracture toughness, J_{1c}, is found to decrease as the reinforcement increases [28]. Similarly, it is expected that the small punch energy, E_{SP}, would decrease as well. This is not the case, in fact, an inverse relationship is observed for the reinforced materials. Referring back to the SPT results for the aluminium and titanium materials as presented in Figure 7–23 and Figure 7–39 show that there is limited difference in displacement for the MMCs, however, as expected load increase is observed for increasing reinforcement which may explain this inverse trend. From this observation, it may be that the yield strength, σ_{YS}, has the largest effect on the small punch energy, E_{SP}, for reinforced materials. Again the same effect as observed for Figure 8–7 is found whereby the titanium points are shifted up, though normalisation by yield strength, σ_{YS}, did not collapse the data into a linear relationship.

A factor that may influence small punch energy, E_{SP}, results could be due to the minor difference in reinforcement content which is not significant for both the aluminium and titanium materials. A larger range in materials volume fractions would provide a clearer trend, however, this could not be achieved due to limited available materials for this research.

A *two-sample assuming unequal variance* student's t-test with a p-value of 5% is performed between the 7A04/SiC/7.5p-T6 and 7A04/SiC/10p-T6 aluminium MMCs total small punch energy, E_{SP}. The statistical analysis found that there is an 11% probability that the two samples are the same. From this basis it can be argued that there is no statistical difference between 7A04/SiC/7.5p-T6 and 7A04/SiC/10p-T6 aluminium MMCs total small punch energies. The t-test is performed again on the TC4/TiB, TiC/2.5p, 2.5w and TC4/TiB, TiC/5p, 5w titanium MMCs which gave a probability of 51% that the two samples are the same. And similarly, the statistical difference between TC4/TiB, TiC/2.5p, 2.5w and TC4/TiB, TiC/5p, 5w titanium MMCs total small punch energies are found to limited. The calculations for the *two-sample assuming unequal variance* student's t-test with a p-value of 5% for the aluminium and titanium materials are presented in Table 7-11 and Table 7-16, respectively.

It may be put forward that the current experimental setup of the SPT may not possess the necessary energy resolution that is required for discerning small differences in reinforcement content. In this case, improvements in both material preparation and experimental procedures may be required.

8.3 An analytical approach for the determination of the small punch maximum bend strength, σ_y

In this research, empirical correlations of the small punch elastic-plastic load, P_y, and the yield strength, σ_{YS}, are found to give further impetus towards developing an analytical solution and an approach towards direct derivation of tensile yield strength, σ_{YS}, values from the SPT data. A literature survey of past papers is then undertaken. The survey found that a number of researchers including Cheon [159] and Vorlicek [212] attempted analytical solutions to approximate tensile yield strength values, σ_{YS}. Recently, Cicero and Lacelle [157] mentioned that the yield strength, σ_{YS}, can be obtained by considering small punch elastic-plastic load, P_y, and applying the General Theory of Plates developed by Timoshenko's linear-elastic deformation theory on disc plates and is described in Equation 5-8, however, a solution to the spherical contact radius remained a problem. Börger et al. [213, 214] while working on a similar problem concerning the ball-on-three-balls test on ceramic based materials found that approximations introduced by Westergaard [215], Godfrey [216] and Shetty [217] are insufficient for the task [213]. Therefore an analytical solution to this problem is developed here and is based on the geometric analysis of a spherical punch as described in Figure 8–11. This geometric model characterises the length of the small punch contact radius, r', as the small punch displacement, δ, varies down the z-axis.

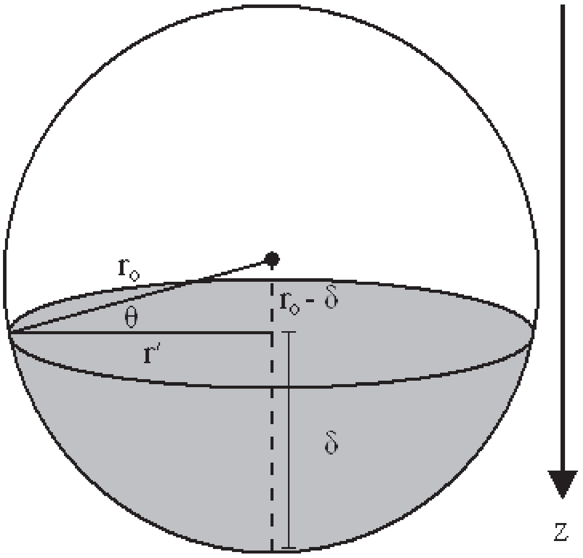

Figure 8–11. A geometric method for determining the small punch equivalent contact radius, r′.

The model assumes that the spherical punch is infinitely rigid compared to the material of concern which may affect the contact radius, however, it is expected that this effect will be limited for ductile materials.

The following solution can be employed to approximate the yield strength value for alloys and MMCs. The analytical solution for the small punch maximum bend strength, σ_y, first introduced in Chapter seven is presented again in Equation 8-3.

$$\sigma_y = \frac{3P_y(1+v)}{2\pi t_0^2}\ln\frac{R_l}{r'} \tag{8-3}$$

The proposed analytical small punch equivalent contact radius, r′, as described in Figure 8–11 is presented in Equation 8-4.

$$r' = \sqrt{2r_o\delta - \delta^2} \tag{8-4}$$

Where r′ is the small punch equivalent contact radius, δ is the small punch displacement and r_o is the radius of the spherical punch.

The above solution for the small punch equivalent contact radius, r′, can be used to correlate the small punch elastic-displacement displacement, δ, up to the small punch displacement at fracture, δ^*. In addition, it can be used to predict the small punch elastic-plastic displacement, δ_y, which is required for the determination of the small punch equivalent contact radius, r′, at yield. Timoshenko's solution incorporating the small punch equivalent contact radius, r′, is presented in Equation 8-5 (1).

$$\sigma_y = \frac{3P_y(1+v)}{2\pi t_0^2}\ln\left(\frac{R_l}{\sqrt{2r_o\delta_y - \delta_y^2}}\right) \tag{8-5}$$

Where σ_y is the small punch maximum bend strength, P_y is the small punch elastic-plastic load and δ_y is the small punch elastic-plastic displacement.

As mentioned earlier Westergaard [215], Godfrey [216] and Shetty [217] developed a solution for the equivalent contact radius, r′. Here we have Timoshenko’s solution incorporating Westergaard solution for the equivalent contact radius, r′, as presented in Equation 8-6 (2).

$$\sigma_y = \frac{3P_y(1+v)}{2\pi t_0^2}\ln\left(\frac{R_l}{\sqrt{1.6r_0^2+t_0^2}-0.675t_0}\right) \qquad 8\text{-}6$$

The described analytical solutions for the small punch maximum bend strength, σ_y, are plotted against the small punch elastic-plastic load, P_y, as presented in Figure 8–12. A comparison of Westergaard’s solution and the geometric solution found that there is a clear difference in the calculated stresses for both solutions. Furthermore, Westergaard’s solution for the equivalent contact radius, r′ tends to underestimate the strength for the material. Of course, identifying higher small punch elastic-plastic loads, P_y, would increase the value for the small punch maximum bend strength, σ_y, however, as is described earlier identifying higher small punch elastic-plastic load, P_y, is incorrect since plastic yielding occurs at very early loads. Moreover, Westergaard’s solution does not account for changes in the contact radius of the spherical punch, instead the contact radius is treated as a constant utilising only the small punch disc radius, r_o, and small punch original thickness, t_o.

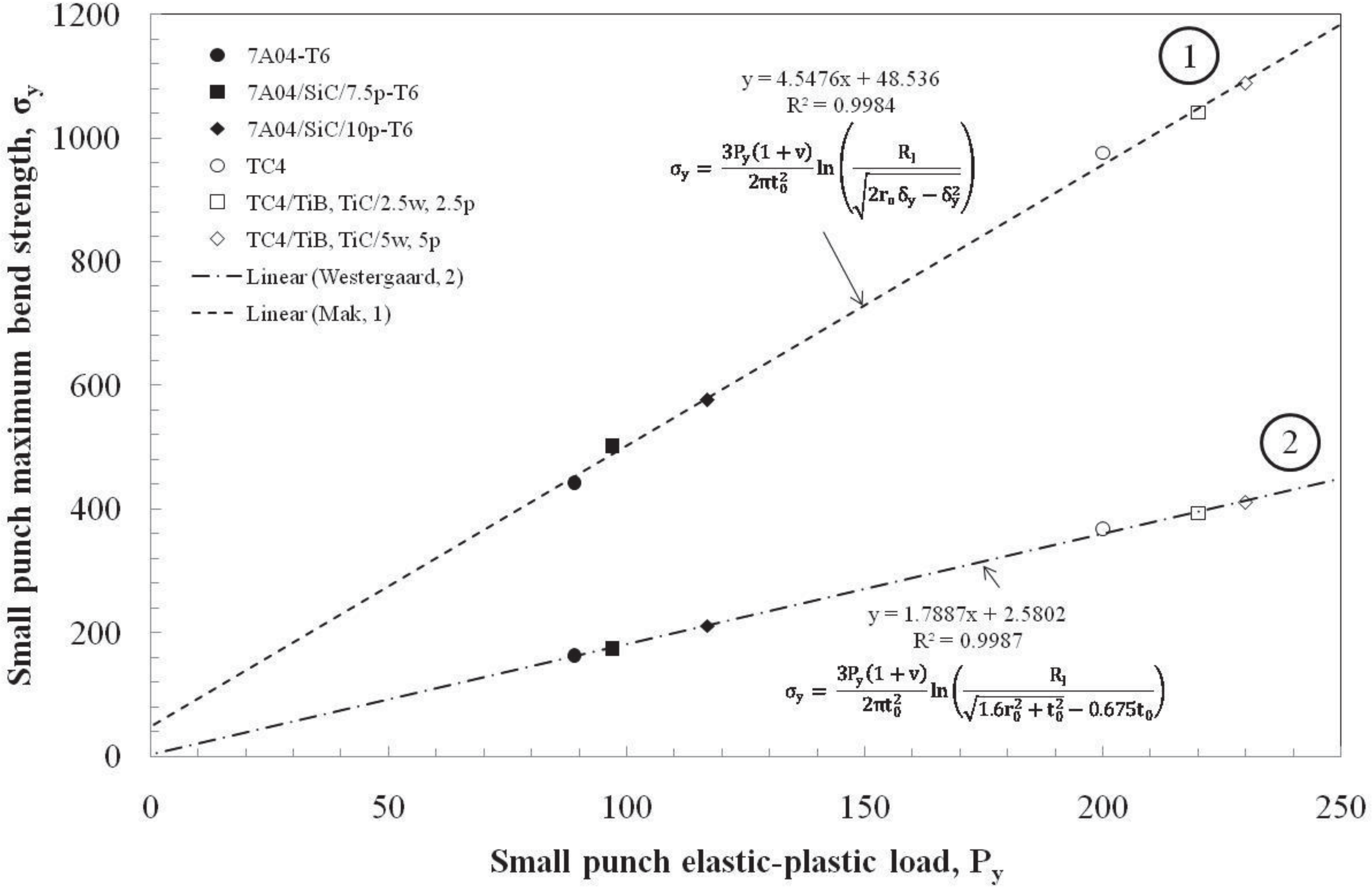

Figure 8–12. Analytical solutions for solving the small punch maximum bend strength, σ_y. Where (1) is the geometric solution and (2) is Westergaard's solution.

Small punch maximum bend strength, σ_y, data so obtained are then plotted against measured tensile yield strength, σ_{YS}, data and is presented in Figure 8–13. In addition, data is collected from literature which included STE690 steel, 12Cr-1Mo steel, 6061 aluminium and zircaloy-4 [178, 179, 205, 206]. Curve B represents the measured tensile yield strength, σ_{YS}, empirical relationship with P_y/t_o^2 which represents the yield stress for the SPT and in accordance to Equation 8-2 and as described in chapter five.

It is clear that Westergaard's solution provides a clear linear approximation to tensile yield strength, σ_{YS}, however, these values are overestimated. The relationship for tensile yield strength, σ_{YS}, and small punch yield strength, σ_y, derived from Timoshenko and Westergaard's solution is presented in Equation 8-7.

$$\sigma_{YS} = 1.87\sigma_y + 220 \qquad \text{8-7}$$

The modified solution based on the radius of spherical cap provides a better solution since the solution accounts for the small punch load and displacement as described above. In this way the solution accounts for the evolution of the small punch contact radius, r'. The relationship for tensile yield strength, σ_{YS}, and small punch yield strength, σ_y, derived from Timoshenko and from this research solution is presented in Equation 8-8.

$$\sigma_{YS} = 0.73\sigma_y + 143 \qquad \text{8-8}$$

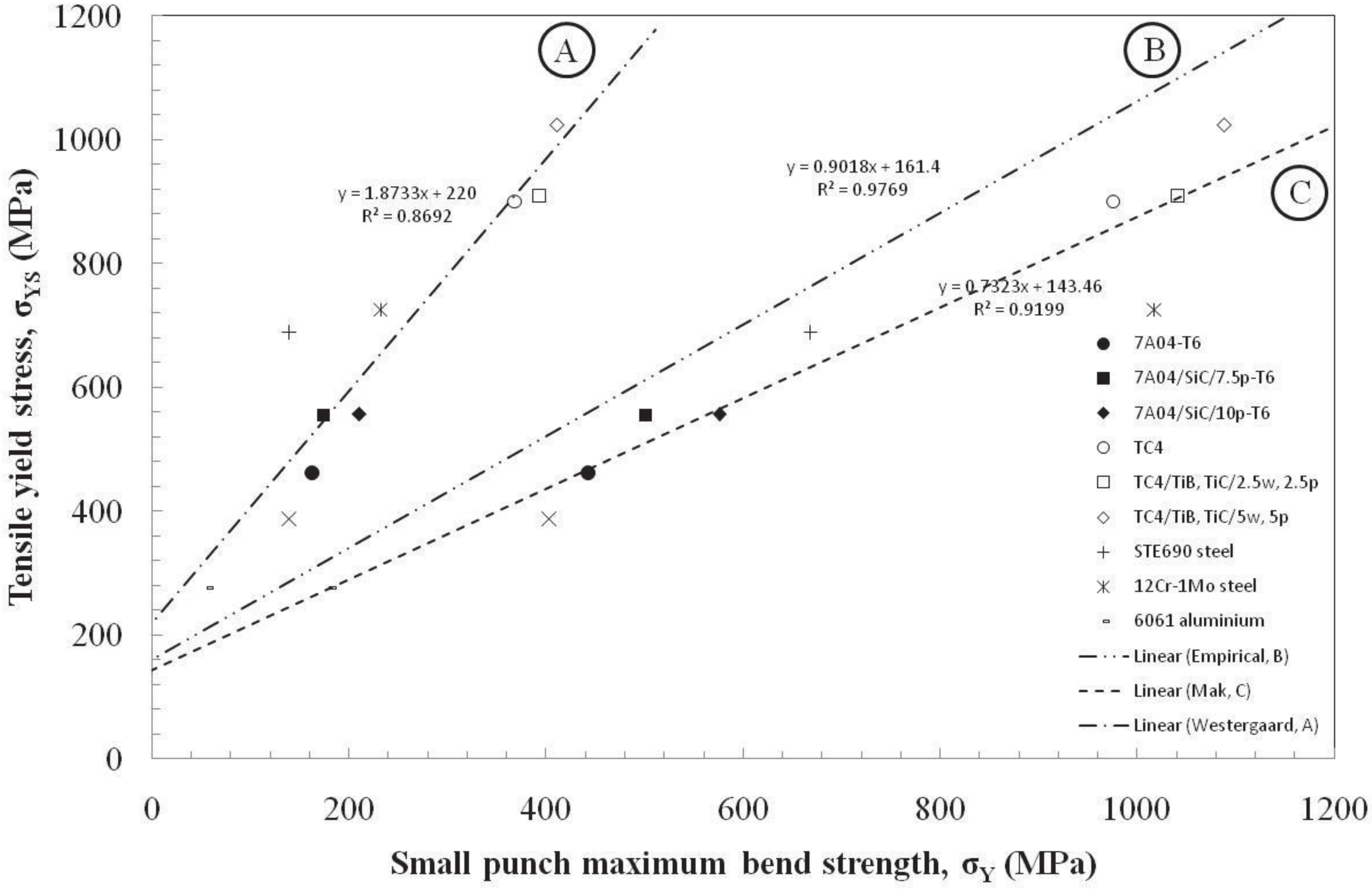

Figure 8–13. A correlation of the tensile yield strength, σ_{YS}, plotted against small punch maximum bend strength, σ_y.

Lucas et al. contributed many studies on small specimen testing, especially on the shear punch test where a shear punch effective stress, σ_{eff}, is first correlated against tensile yield stress, σ_{YS} [218, 219].

Studies involving small punch shear tests have been performed on both alloys [208, 209, 219-221] and MMCs [202, 203]. A clear linear correlation is observed for yield strength, σ_{YS}, and shear punch effective stress, σ_{eff}. The shear punch effective stress, σ_{eff}, is based on the following relationship as shown in Equation 8-9 [218].

$$\sigma_{eff} = \frac{P - P_f}{2\pi r_o t_o} = C\sigma_{YS} \qquad 8\text{-}9$$

Where P is the shear load, P_f is the friction load, r_o is the shear punch radius, t_o is the shear punch thickness and C is a constant derived linear regression analysis.

Many features of the shear punch test are similar to the SPT in that a flat-faced punch is utilised rather than a spherical punch. Furthermore, the shear punch test is dominated by shear rather than by the complex biaxial bending and tension forces experienced by the SPT. Nevertheless, both studies have found that a linear correlation exists for the tensile yield strength, σ_{YS}, and by measurement of experimental loads such as the shear load, P, or the small punch elastic-plastic load, P_y.

8.4 A literature survey of the plane-strain fracture toughness, J_{1c}, and small punch equivalent fracture strain, ε_{qF}

An extensive literature survey is conducted to provide a global overview of the small punch equivalent fracture strain, ε_{qF}, relationship to plane-strain fracture toughness, J_{1c}, as presented in Figure 8–14. The relationship confirms Bayoumi and Bassim's proposed model [26]. A non-linear behaviour is observed up to a small punch equivalent fracture strain, ε_{qF}, of 0.4 followed by linear behaviour as the small punch equivalent fracture strain, ε_{qF}, and plane-strain fracture toughness, J_{1c}, values increase. In addition, the model appears to follow a polynomial relationship. Therefore Equation 5-18 for the non-linear region and Equation 5-20 for linear region are combined to yield the following relationship as presented in Equation 8-10.

$$J_{1c} = C_1\varepsilon_{qF}^2 + C_2 + C_p\varepsilon_{qF} \qquad 8\text{-}10$$

Where the parameters C_1 and C_p are derived from J_{1c}-ε_{qF} relationship as shown in Figure 8–14. The parameter C_2 which describes the minimum cleavage energy is assumed to be small. Thus a decision is made to set the intercept to zero.

A polynomial curve based on this study is then fitted to the small punch J_{1c}-ε_{qF} values. The small punch J_{1c}-ε_{qF} relationship obtained from this research is shown below in Equation 8-11.

$$J_{1_c} = 115\varepsilon_{qF}^2 + 164\varepsilon_{qF} \qquad 8\text{-}11$$

This empirical correlation can be used to approximate the plane-strain fracture toughness, J_{1c}, if the small punch equivalent fracture strain, ε_{qF}, is known and constitutes the first use of a polymeric curve that has been utilised for determining small punch J_{1c}-ε_{qF} values. With further improvements in SPT methodologies and procedures it is expected that this empirical relationship will be further defined. This empirical correlation for the plane-strain fracture toughness, J_{1c}, and equivalent fracture strain, ε_{qF}, is presented in Figure 8–14.

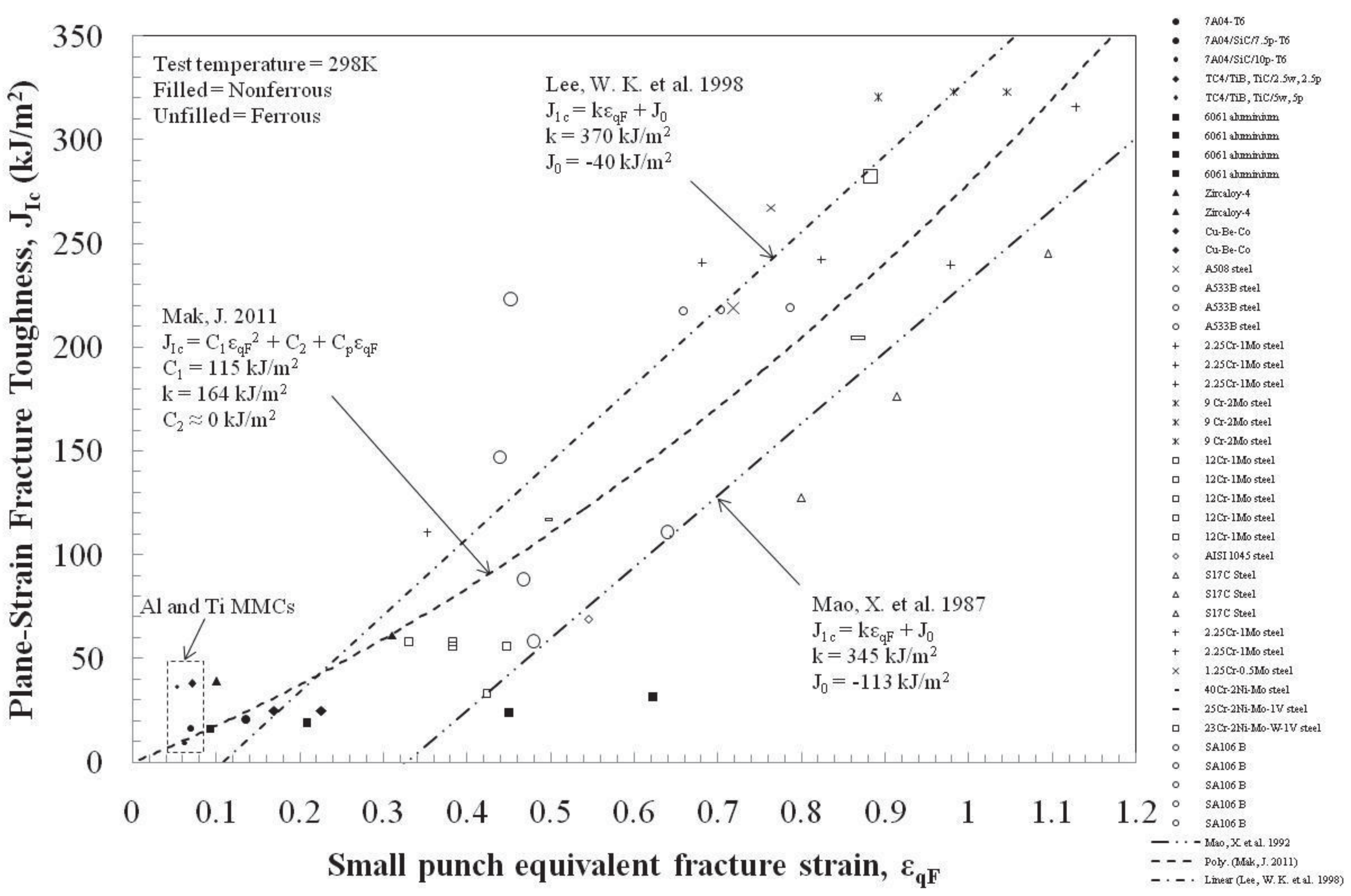

Figure 8–14. A global overview of the relationship between plane-strain fracture toughness, J_{Ic}, and the small punch equivalent fracture strain, ε_{qF}.

The small punch J_{1c}-ε_{qF} relationship includes data from the as-received research materials as well from the following materials, obtained from the literature including: 6061 aluminium, zircalloy-4, Cu-Be-Co, A508 steel, A533B steel, 2.25Cr-1Mo steel, 9Cr-2Mo steel, 12Cr-1Mo steel, AISI 1045 steel, S17C steel, 1.25Cr-0.5Mo steel, , 40Cr-2Ni-1Mo-1V steel, 23Cr-2Ni-1W-1V steel, 25Cr-2Ni-1Mo-1V steel and SA106 B steel [27, 105, 205-207, 222].

It is observed, that both the aluminium and titanium materials exhibited much lower fracture toughness and ductility compared to the global small punch J_{1c}-ε_{qF} relationship as seen in Figure 8–14. This is not surprising since this region is predominately made of materials exhibiting elastic behaviour, however, this region does not preclude materials that exhibit elastic-plastic behaviour. Furthermore, it is expected that future studies on the SPT of MMCs will be made within this non-linear region. Much research is still required to improve the fracture toughness and ductility of advanced MMCs.

Mao et al. contributed many studies on the linear part of the small punch J_{1c}-ε_{qF} relationship [205]. In this study, their empirical correlation is found to characterise the upper bound of the small punch J_{1c}-ε_{qF} relationship. The proposed empirical correlation is presented in Equation 8-12.

$$J_{1c} = 345\varepsilon_{qF} - 113 \tag{8-12}$$

In addition, Lee et al. contributed as well to the linear part of the small punch J_{1c}-ε_{qF} relationship [123, 154]. The empirical correlation for their study is found to characterise the lower bound of the small punch J_{1c}-ε_{qF} relationship. The proposed empirical correlation is presented in Equation 8-13.

$$J_{1c} = 370\varepsilon_{qF} - 40 \tag{8-13}$$

8.5 A potential small punch analytical solution to derive the plane-strain fracture toughness, J_{1c}

One of the goals of this thesis is to develop a method for the determination of plane-strain fracture toughness, J_{1c}, values from small specimens. Over the course of this research a number of methods had been researched [77, 78], however, these methods could not be employed due to small specimen sizes and limitations set by standards.

One such method known as the Ritchie-Knott-Rice, RKR, micromechanical model may provide a way for achieving plane-strain fracture toughness, J_{1c}, values from small specimens [166]. A brief literature review found that some research progress had been made toward this field especially on the *characteristic distance* [223, 224], which according to RKR, characterises the distance for cleavage fracture in pre-cracked steels. The model suggests that in a pre-cracked specimen cleavage fracture occurs when the critical cleavage fracture stress is exceeded by some normal maximum tensile stress at some *characteristic* distance ahead of the crack tip, usually forming microvoids [223]. Dieter, G. E. briefly mentions the RKR model as shown below in Equation 8-14 [76], however, provides no further mention of where it comes from or how it is derived.

$$J_{1c} = \sigma_o \varepsilon_F l_o \qquad \text{8-14}$$

Where J_{1c} is the ductile plane-strain fracture toughness, σ_o is the yield strength, ε_F is the true fracture strain and l_o is the *characteristic distance*.

Applying this solution to the TC4 base alloy yields plane-strain fracture toughness, J_{1c}, value of 21 J/mm^2 or 52 MPa$\sqrt{\mathrm{m}}$. For yield strength, σ_y, of 900MPa, small punch equivalent fracture strain, ε_{qF}, of 0.16 and *characteristic distance*, l_o, of 0.144mm. Note, in this case, the true tensile fracture strain, ε_F, is replaced with the small punch equivalent fracture strain, ε_{qF}. The *characteristic distance* is measured from the furthest microvoid to the tip of the fracture surface.

The plane-strain fracture toughness value of 52 MPa$\sqrt{\mathrm{m}}$ is is within the range of what would be expected from the TC4 base alloy. Further work is required in this area to assess the validity of this finding.

8.6 Concluding remarks

This research further develops the application of the SPT which may lead to an inexpensive straightforward multi-purpose multi-mechanical non-destructive test technique for advanced alloys and MMCs.

This study found very good empirical and analytical solutions for the small punch maximum bend strength, σ_y, as presented in Equation 8-15.

$$\sigma_y = 0.9018\frac{P_y}{t_o^2} + 161.4 \qquad \text{8-15}$$

A modified analytical solution based on Timoshenko's plate theory, which incorporates both small punch elastic-plastic load, P_y, and small punch elastic-plastic displacement, δ_y, is presented in Equation 8-16. The yield strength, σ_{YS}, values derived from the SPT are found to be reasonably close to yield strength, σ_{YS}, values obtained from tensile tests as presented in Figure 8–13.

$$\sigma_y = \frac{3P_y(1+\nu)}{2\pi t_0^2}\left(\ln\frac{R_l}{\sqrt{2r_o\delta_y - \delta_y^2}}\right) \qquad \text{8-16}$$

The small punch energy, E_{SP} has been calculated for the aluminium and titanium materials. It has been found that materials containing the reinforcement content in general had exhibited lower small punch fracture energies when compared to the unreinforced material. This finding corroborates with the findings of Wanjara [202] who conducted similar studies on MMCs.

The small punch J_{1c}-E_{SP} relationship appears to show an inverse relationship for the reinforced materials. A statistical analysis showed small punch energy, E_{SP}, is unable to resolve the difference between the reinforced materials. It may be put forward that the current experimental setup of the SPT may not possess the necessary energy resolution that is required for discerning small differences in reinforcement content. In this case, improvements in both material preparation and experimental procedures may be required.

Chapter eight provides a more thorough study on the non-linear part of the J_{1c}-ε_{qF} relationship. The finding suggests that both elastic and elastic-plastic materials can be found in this region. Furthermore, it is found that most materials identified in the non-linear region thus far are nonferrous alloys. In fact, according to the literature survey, linear behaviour appears to be predominantly made up of ferrous materials.

This research shows excellent correlation for the small punch J_{1c}-ε_{qF} relationship. The small punch equivalent fracture strain, ε_{qF}, has been demonstrated as a viable method for estimating the plane-strain fracture toughness, J_{1c} and K_{1c}, of a material. In addition, the ε_{qF}-J_{1c} empirical correlation has been extended for the assessment of MMCs. It's important to note that empirical correlations have been made with different combinations of SPT configurations and for different kinds of materials with a wide range of fracture toughness values. Standardisation of the small punch mechanical test procedure will further reduce scatter of the results.

The polynomial curve presented in this research provides a good average between these two extremes and closely predicts the relationship between ε_{qF} and J_{1c}. The empirical equation of the SPT J_{1c}-ε_{qF} is presented in Equation 8-17 and can be utilised to predict plane-strain fracture toughness, J_{1c}, values from small sized specimens.

$$J_{1c} = 115\varepsilon_{qF}^{2} + 164\varepsilon_{qF} \qquad 8\text{-}17$$

CHAPTER NINE

CONCLUSION

9.1 Conclusions regarding the small punch test

A number of fracture toughness tests are investigated in order to overcome the problem of limited availability of these developmental materials. This led to a number of *standard* fracture toughness tests configurations being assessed.

- Single-edge bend test, SE(B) as discussed in section 4.2.1.
- Compact tension tests, C(T) as discussed in section 4.2.2.
- Chevron v-notch short rod or bar test, CN as discussed in section 4.2.3.
- Circumferential notched tension test, CNT as discussed in section 4.3.1.

A literature review of fracture toughness tests lead to a judicious decision to employ CNT test specimens as the best candidate for fracture toughness testing when only limited amounts of material are available, which is a significant problem for this research. Circumferential notched tension tests are then carried out on the 7A04-T6 aluminium and TC4 titanium materials. There are problems with the CNT test namely gripping problems due to limited amounts of material as discussed in chapter six and seven. This then led to the decision to machine circular grooves around the CNT test specimen for the purposes of conducting uniaxial tests and improve gripping with split-collets as shown in Figure 6–8. Another problem involved the irregular fatigue precrack formation exhibited by the aluminium MMCs as presented in Figure 7–13 (a, c) and Figure 7–16 (c). This is determined to be mix mode I/II fracture behaviour and is found to reduce the fracture toughness values for these materials [198, 199]. These problems are overcome through a well thought-out decision to employ the CNT test which allowed for the determination of valid plane-strain fracture toughness, K_{1c}, values in accordance with literature requirements [86]. The following are the conclusions of this Thesis:

- This research as far as the author understands constitutes a first in the SPT of MMCs. Furthermore, SPT results are obtained for developmental 7A04-T6 aluminium and TC4 titanium MMCs as presented in Table 7-10 and Table 7-15, respectively.

- Fractography of the small punch 7A04-T6 aluminium and TC4 titanium specimens as shown in Figure 7–24 and Figure 7–41, respectively. The analysis revealed that alloys exhibited circumferential complex crack profile indicative of ductile materials, whilst MMCs exhibited multi-crack profile which is a consequence of the reinforcement content and is similar to crack profiles found in brittle materials. Furthermore, scanning electron microscopy revealed that the crack initiation event occurred much earlier and at lower loads when compared against light optical techniques.

- Empirical correlation of the small punch elastic-plastic load, P_y, and tensile yield strength, σ_{YS}, values demonstrated an overall linear relationship. Furthermore, this research found previous methods tended to overestimate the small punch elastic-plastic load, P_y. This led to a new technique for determining the small punch elastic-plastic load, P_y, described as the *small punch point of nonlinearity* contained in Figure 8–1.

- An analytical solution for determining yield strength, σ_{YS}, is presented in 8-16. The solution is based on Timoshenko's strength analysis of circular plates. In particular, the small punch elastic-plastic load, P_y, and corresponding small punch elastic-plastic displacement, δ_y, value are utilised. Furthermore a new method for determining the small punch equivalent contact radius, r′ is introduced in Equation 8-4.

- The small punch energy, E_{SP}, is compared against the plane-strain fracture toughness, J_{1c} and K_{1c} values. It is found that in general the alloys exhibited higher energies when compared to MMCs. This corresponded with alloys which have higher plane-strain fracture toughness when compared to MMCs.

- This research found excellent empirical relationship of the small punch equivalent fracture strain, ε_{qF}, and the plane-strain fracture toughness, J_{1c} and K_{1c} as proposed by Bayoumi and Bassim [26, 27] and observed in Figure 8–14. In particular, MMCs are demonstrated to belong in the non-linear region. This finding is compared against literature values to provide a global overview of this empirical relationship. From this relationship an empirical solution is developed as presented in Equation 8-11.

- This study further progresses the development of the SPT as a multi-purpose multi-mechanical non-destructive test to be considered as an economically viable solution to be employed on all kinds of alloys and advanced MMCs. To this end, more research is required to standardise the test method and procedures which will further improve mechanical evaluation of material properties.

CHAPTER TEN

FUTURE WORK

The following provides a brief overview of the most important areas of research that is needed for the SPT. Namely, standardisation of the SPT, refinement of the small punch J_{1c}-ε_{qF} relationship and investigation of the *characteristic distance*, l_o.

- It is proposed that further work be applied for the standardisation of the SPT methodologies and procedures which will lead to an international recognised standard. Standardisation will lead a pathway for researchers to easily compare their results and research finding for other materials. Furthermore, the refinement of material preparation, mechanical testing and analysis should lead to reduced errors and scatter in the results. Specifically, research is needed in assessing the small punch J_{1c}-ε_{qF} relationship especially to reduce the scatter and improve the empirical correlations.

- Further investigation on the small punch crack initiation event is needed through in-situ studies involving scanning electron microscopy which is superior to conventional optical techniques in terms of its high resolution and superior depth of field. The experimental setup can allow for real-time observation and recording of crack initiation and propagation. Furthermore, identification of particle cracking, debonding or failure of the metal matrix can be quickly assessed.

- More work is required to investigate the *characteristic distance*, l_o, for materials with a wide range of J_{1c} values. The purpose is to investigate whether the SPT can be used to obtain indirect plane-strain fracture toughness, J_{1c}, values from the following relation as shown in Equation 10-1 or of a similar relation incorporating the *characteristic distance*, l_o, of a material. The results may lead to a direct method for the determination of plane-strain fracture toughness, J_{1c}, from a very small plane-stress specimen.

$$J_{1c} = \sigma_o \varepsilon_F l_o \qquad 10\text{-}1$$

REFERENCES

1. Manahan, M.P., A.S. Argon, and O.K. Harling, *The development of a miniaturized disk bend test for the determination of postirradiation mechanical properties.* Journal of Nuclear Materials, 1981. **104**: p. 1545-1550.
2. Manahan, M.P., *The developement of a miniaturized disk bend test for the determination of post-irradiation mechanical behaviour*, in *The Department of Nuclear Engineering*. 1982, Massachusettes Institute of Technology: Massachusettes. p. 277.
3. Jaekel, D.J., D.W. MacDonald, and S.M. Kurtz, *Characterization of PEEK biomaterials using the small punch test.* Journal of the Mechanical Behavior of Biomedical Materials. **In Press, Corrected Proof**.
4. Mao, X., T. Shoji, and H. Takahashi, *Characterization of fracture behaviour in small punch test by combined recrystalization-etch method and rigid plastic analysis.* Journal of Testing and Evaluation, 1987. **15**(1): p. 30-37.
5. Giddings, V.L., et al., *A small punch test technique for characterizing the elastic modulus and fracture behavior of PMMA bone cement used in total joint replacement.* Biomaterials, 2001. **22**(13): p. 1875-1881.
6. Russo, T., et al., *Poly(ε-caprolactone) reinforced with sol-gel synthesized organic-inorganic hybrid fillers as composite substrates for tissue engineering.* Journal of Applied Biomaterials & Biomechanics, 2010. **8**(3): p. 146-52.
7. Serre, I. and J.-B. Vogt, *Mechanical properties of a 316L/T91 weld joint tested in lead-bismuth liquid.* Materials & Design, 2009. **30**(9): p. 3776-3783.
8. Kato, T., et al., *High-temperature strength analysis of welded joint of RAFs by small punch test.* Journal of Nuclear Materials, 2009. **386-388**: p. 520-524.
9. Carr, D.G., et al., *Residual stress measurements in a zircaloy-4 weld by neutron diffraction.* Acta Materialia, 2004. **52**(14): p. 4083-4091.
10. Parker, J.D. and B. Wilshire, *Non-destructive life assessment of high temperature components and weldments.* International Journal of Pressure Vessels and Piping, 1992. **50**(1-3): p. 337-347.
11. Shekhter, A., et al., *Assessment of temper embrittlement in an ex-service 1Cr-1Mo-0.25V power generating rotor by Charpy V-Notch testing, KIc fracture toughness and small punch test.* International Journal of Pressure Vessels and Piping, 2002. **79**(8-10): p. 611-615.
12. Nambu, T., et al., *Enhanced hydrogen embrittlement of Pd-coated niobium metal membrane detected by in situ small punch test under hydrogen permeation.* Journal of Alloys and Compounds, 2007. **446-447**: p. 588-592.
13. Lucas, G.E., A. Okada, and M. Kiritani, *Parametric analysis of the disc bend test.* Journal of Nuclear Materials. **141-143**(Part 1): p. 532-535.
14. Lucas, G.E., et al., *Recent progress in small specimen test technology.* Journal of Nuclear Materials, 2002. **307-311**(Part 2): p. 1600-1608.
15. Lucas, G.E., et al., *The role of small specimen test technology in fusion materials development.* Journal of Nuclear Materials, 2007. **367-370**(Part 2): p. 1549-1556.
16. Saucedo-Muñoz, M.L., et al., *Correlationship between JIC and equivalent fracture strain determined by small-punch tests in JN1, JJ1 and JK2 austenitic stainless steels.* Cryogenics, 2001. **41**(10): p. 713-719.

17. Misawa, T., et al., *Fracture toughness evaluation of fusion reactor structural steels at low temperatures by small punch tests.* Journal of Nuclear Materials, 1989. **169**: p. 225-232.
18. Suresh, S., Mortensen, A., Needleman, A., *Fundamentals of metal matrix composites*. 1993, Boston Butterworth-Heinemann. 342.
19. Mortensen, A. and I. Jin, *Solidificationprocessing of metal matrix composites.* International Materials Reviews, 1992. **37**(3): p. 101-128.
20. Mortensen, A., *A review of the fracture toughness of particle reinforced aluminium alloys*, in *Proceedings of the International Conference: Fabrication of Particulates Reinforced Metal Composites*. 1990, ASM: Montreal, Canada. p. 217-233.
21. Mortensen, A.L., Javier *Metal Matrix Composites.* Annual Review of Materials Research, 2010. **40**: p. 243-270.
22. Tjong, S.C. and Z.Y. Ma, *Microstructural and mechanical characteristics of in situ metal matrix composites.* Materials Science and Engineering: R: Reports, 2000. **29**(3-4): p. 49-113.
23. Ibrahim, I.A., F.A. Mohamed, and E.J. Lavernia, *Particulate reinforced metal matrix composites — a review.* Journal of Materials Science, 1991. **26**(5): p. 1137-1156.
24. Chawla, N. and K.K. Chawla, *Microstructure based modelling of the deformation behavior of particle reinforced metal matrix composites.* Journal of Materials Science, 2006. **41**(3): p. 913-925.
25. Kainer, K.U., ed. *Metal Matrix Composites* Custom-made Materials for Automotive and Aerospace Engineering. 2006, Wiley-VCH: Weinheim.
26. Bayoumi, M.R. and M.N. Bassim, *Study of the relationship between fracture toughness (JIC) and bulge ductility.* International Journal of Fracture, 1983. **23**(1): p. 71-79.
27. Bayoumi, M.R. and M.N. Bassim, *Experimental correlation between ductility and J-integral in the transition region of 1045 steel.* Engineering Fracture Mechanics, 1983. **18**(3): p. 679-691.
28. Chawla, N. and K.K. Chawla, *Metal Matrixs Composites*. 2006, New York: Springer.
29. Callister, W.D., *Materials Science and Engineering: An Introduction*. 7th ed. 2007, New York: John Wiley & Sons, Inc. 811.
30. Goh, K.L., R.M. Aspden, and D.W.L. Hukins, *Review: finite element analysis of stress transfer in short-fibre composite materials.* Composites Science and Technology, 2004. **64**(9): p. 1091-1100.
31. Li, Q.F. and D.G. McCartney, *A review of reinforcement distribution and its measurement in metal matrix composites.* Journal of Materials Processing Technology, 1994. **41**(3): p. 249-262.
32. Ouyang, Q.B., et al., *Friction and Wear Properties of Aluminum Matrix Composites and its Application.* Key Engineering Materials, 2007. **351**: p. 147-150.
33. Miracle, D.B. and S.L. Donaldson, *Introduction to Composites*. ASM Handbook, ed. D.B. Miracle and S.L. Donaldson. Vol. 21. 2001, Ohio: ASM International.
34. Miracle, D.B., *Metal matrix composites - From science to technological significance.* Composites Science and Technology, 2005. **65**(15-16): p. 2526-2540.

35. Swift, C., *Metal Matrix Composites: The Global Market*. 2009, BBC Research: Wellesley, Massachusetts. p. 229.
36. Hunt Jr, W.H., et al., *Metal Matrix Composites: Applications*, in *Encyclopedia of Materials: Science and Technology*. 2001, Elsevier: Oxford. p. 5442-5446.
37. Mahendra, K.V. and K. Radhakrishna, *Castable composites and their application in automobiles*, in *Proceedings of the Institution of Mechanical Engineers -- Part D -- Journal of Automobile Engineering*. 2007. p. 135-140.
38. Weber, L. and R. Tavangar, *Diamond-based Metal Matrix Composites for Thermal Management made by Liquid Metal Infiltration.* Advanced Materials Research, 2009. **59**: p. 111-115.
39. Ouyang, Q., et al., *Light Weight and High Modulus Aluminium Matrix Composites and its Application into Aerospace.* Materials Science Forum, 2007. **546-549**: p. 1551-1554.
40. Rawal, S., *Metal-Matrix Composites for Space Applications.* JOM, 2001. **53**(4): p. 14-17.
41. Shelley, J.S., R. LeClaire, and J. NicholsDOI, *Metal-matrix composites for liquid rocket engines.* JOM 2001. **53**(4): p. 18-21.
42. Swift, C. *GB-108N Metal Matrix Composites in the 21st Century: Markets and Opportunities*. 2005 [cited 2006 6 July]; Available from: http://www.bccresearch.com/advmat/GB108N.html.
43. Aldas, K. and M.D. Mat, *Experimental and theoretical analysis of particle distribution in particulate metal matrix composites.* Journal of Materials Processing Technology, 2005. **160**(3): p. 289-295.
44. Geng, K., et al., *In situ preparation of titanium matrix composites reinforced by TiB and Nd2O3.* Materials Letters, 2003. **57**(24-25): p. 4054-4057.
45. Geng, K., W. Lu, and D. Zhang, *In situ synthesized (TiB + Y2O3)/Ti composites.* Journal of Materials Science Letters, 2003. **22**(12): p. 877-879.
46. Geng, K., W. Lu, and D. Zhang, *Microstructure and tensile properties of in situ synthesized (TiB+Y2O3)/Ti composites at elevated temperature.* Materials Science and Engineering A, 2003. **360**(1-2): p. 176-182.
47. Zhang, X., et al., *In situ technique for synthesizing (TiB+TiC)/Ti composites.* Scripta Materialia, 1999. **41**(1): p. 39-46.
48. Lu, J., et al., *Microstructure and tensile properties of in situ synthesized (TiB+TiC)/Ti-6Al-4V composites.* Key Engineering materials, 2009. **351**: p. 201-207.
49. Lu, W.J., et al., *Microstructure and tensile properties of in situ (TiB+TiC)/Ti6242 (TiB:TiC=1:1) composites prepared by common casting technique.* Materials Science and Engineering A, 2001. **311**(1-2): p. 142-150.
50. Chawla, N., et al., *The effect of matrix microstructure on the tensile and fatigue behaviour of SiC particle--reinforced 2080 Al matrix composites.* Metallurgical and Materials Transactions A, 2000. **31a**(2): p. 531-541.
51. Zong, B.Y., et al., *Strengthening mechanism of load sharing of particulate reinforcements in a metal matrix composite.* Journal of Materials Science, 2007. **42**(12): p. 4215-4226.
52. Arsenault, R.J. and N. Shi, *Dislocation generation due to differences between the coefficients of thermal expansion.* Materials Science and Engineering, 1986. **81**: p. 175-187.

53. Arsenault, R.J., S. Fishman, and M. Taya, *Deformation and fracture behavior of metal-ceramic matrix composite materials.* Progress in Materials Science, 1994. **38**: p. 1-157.
54. Lim, L.G. and F.P.E. Dunne, *The effect of volume fraction of reinforcement on the elastic-viscoplastic response of metal-matrix composites.* International Journal of Mechanical Sciences, 1995. **38**(1): p. 19-39.
55. Ganesh, V.V. and N. Chawla, *Effect of particle orientation anisotropy on the tensile behavior of metal matrix composites: experiments and microstructure-based simulation.* Materials Science and Engineering A, 2005. **391**(1-2): p. 342-353.
56. Flom, Y. and R.J. Arsenault, *Effect of particle size on fracture toughness of SiC/Al composite material.* Acta Metallurgica, 1989. **37**(9): p. 2413-2423.
57. Heness, G.L., et al., *Development of a finite element micromodel for metal matrix composites.* Computational Materials Science, 1999. **13**(4): p. 259-269.
58. Yang, N., J. Boselli, and I. Sinclair, *Simulation and quantitative assessment of homogeneous and inhomogeneous particle distributions in particulate metal matrix composites.* Journal of Microscopy, 2001. **201**(2): p. 189.
59. Prangnell, P.B., et al., *The effect of particle distribution on damage formation in particulate reinforced metal matrix composites deformed in compression.* Materials Science and Engineering A, 1996. **220**(1-2): p. 41-56.
60. Kobayashi, T., H. Iwanari, and K. Yamamoto, *Evaluations of toughness and mechanical properties in Al/SiC$_p$ composite*, in *Metal & ceramic matrix composites: Processing, modelling and mechanical behavior*, R. Bhagat, et al., Editors. 1990, TMS, Minerals, Metals & Materials Society: Warrendale, PA. p. 227-234.
61. Anderson, T.L., *Fracture Mechanics: Fundamentals and Applications*. 2nd ed. 1995, Boca Raton: CRC Press. 688.
62. Sabirov, I., et al., *Equal channel angular pressing of metal matrix composites: Effect on particle distribution and fracture toughness.* Acta Materialia, 2005. **53**(18): p. 4919-4930.
63. Park, B.G., A.G. Crosky, and A.K. Hellier, *Fracture toughness of microsphere Al2O3–Al particulate metal matrix composites.* Composites Part B: Engineering, 2008. **39**(7–8): p. 1270-1279.
64. Davidson, D., *Fracture characteristics of Al-4 pct Mg mechanically alloyed with SiC.* Metallurgical and Materials Transactions A, 1987. **18**(12): p. 2115-2128.
65. Song, M. and B. Huang, *Effects of particle size on the fracture toughness of SiCp/Al alloy metal matrix composites.* Materials Science and Engineering: A, 2008. **488**(1-2): p. 601-607.
66. Dan, Z. and F.R. Tuler, *Effect of particle size on fracture toughness in metal matrix composites.* Engineering Fracture Mechanics, 1994. **47**(2): p. 303-308.
67. Kameda, J., *Effect of Solute Segregation on Fracture Toughness in a Ni-Cr Steel.* Metallurgical and Materials Transactions A, 1981. **12**(12): p. 2039-2048.
68. Davidson, D.L., *Fracture toughness of particulate metal matrix composites*. Metal Matrix Composites: Mechanisms and Properties, ed. R.J. Arsenault and R.K. Everett. 1991, New York: Academic Press.
69. Davidson, D., *Fracture surface roughness as a gauge of fracture toughness: aluminium-particulate SiC composites : Davidson, D. L. Journal of Materials Science Vol 24 (1989) pp 681-687.* Composites, 1989. **20**(5): p. 495-495.

70. Crowe, C.R., R. Gray, and D.F. Hasson, *Microstructure controlled fracture toughness of SiC/Al metal matrix composites*, in *Proceedings of the 5th International Conference on Composite Materials*, W. Harrigan, J. Strife, and A. Dhingra, Editors. 1985, TMS-AIME: San Diego, CA. p. 843-866.
71. Dewald, D.K., et al., *Dislocation structures ahead of advancing cracks.* Scripta Metallurgica, 1989. **23**(8): p. 1307-1312.
72. Brown, L.M. and J.D. Embry, *The Initiation and Growth of Voids at Second Phase Particles*, in *Proceedings of the 3rd International Conference of the strength of metals and alloys* 1973, Institute of Metals: London. p. 164-169.
73. Somerday, B.P., Y. Leng, and R.P. Gangloff, *Elevated temperature fracture of particulate-reinforced aluminium part 1: Fracture Toughness.* Fatigue & Fracture of Engineering Materials & Structures, 1995. **18**(5): p. 565-582.
74. Davidson, D.L., *Optimization the design of particulate composites for maximum fracture resistance through modeling.* International Journal of Fracture 1999. **96**: p. 359-370.
75. Somerday, B. and R. Gangloff, *Global constraint-insensitive fracture in SiC particulate-reinforced AA 2009.* Metallurgical and Materials Transactions A, 1994. **25**(7): p. 1471-1479.
76. Dieter, G.E., *Mechanical Metallurgy*. 1988, London: McGraw-Hill.
77. *Standard Test Method for Measurement of Fracture Toughness*. 2009, American Society for Testing and Materials.
78. *Standard Test Method for Plane-Strain (Chevron-Notch) Fracture Toughness of Metallic Materials*. 1997, American Society for Testing and Materials.
79. Stark, H.L. and R.N. Ibrahim, *Estimating fracture toughness from small specimens.* Engineering Fracture Mechanics, 1986. **25**(4): p. 395-401.
80. Barker, L.M., *A simplified method for measuring plane strain fracture toughness.* Engineering Fracture Mechanics, 1977. **9**(2): p. 361-364, IN5-IN6, 365-369.
81. *Metallic materials. Determination of plane-strain fracture toughness*. 2005, British Standards Institution.
82. *Metallic materials -- Determination of plane-strain fracture toughness*. 2010, International Organization for Standardization.
83. Heness, G.L. and Y.W. Mai. *The Fracture Toughness of Some Metal Matrix Composites - Comparison of Techniques*. in *Proceedings of the 10th International Congress of Fracture*. 2001. Honolulu: Elsevier Science.
84. Singh Raman, R.K., R. Rihan, and R.N. Ibrahim, *Validation of a novel approach to determination of threshold for stress corrosion cracking (KISCC).* Materials Science and Engineering: A, 2007. **452-453**: p. 652-656.
85. Rihan, R., R.K.S. Raman, and R.N. Ibrahim, *Circumferential notched tensile (CNT) testing of cast iron for determination of threshold (KISCC) for caustic crack propagation.* Materials Science and Engineering: A, 2005. **407**(1-2): p. 207-212.
86. Ibrahim, R.N. and H.L. Stark, *Validity requirements for fracture toughness measurements obtained from small circumferentially notched cylindrical specimens.* Engineering Fracture Mechanics, 1987. **28**(4): p. 455-460.
87. Bayram, A., A. Uguz, and A. Durmus, *Rapid determination of the fracture toughness of metallic materials using circumferentially notched bars.* Journal of Materials Engineering and Performance, 2002. **11**(5): p. 571-576.

88. Gupte, K.A. and S. Banerjee, *Fracture of round bars loaded in mode III and a procedure for KIIIc determination.* Engineering Fracture Mechanics, 1984. **19**(5): p. 919-946.
89. Londe, N.V., T. Jayaraju, and P.R.S. Rao, *Use of round bar specimen in fracture toughness test of metallic materials.* International Journal of Engineering Science and Technology, 2010. **2**(9): p. 4130-4136.
90. Lukács, J., *Determination of Plane-Strain Fracture Toughness Using Cracked Round Bar Specimens and their Applicability for Reliability Assessment Calculations.* Procedia Engineering, 2011. **10**: p. 2526-2531.
91. Ule, B., V. Leskovsek, and B. Tuma, *Estimation of plain strain fracture toughness of AISI M2 steel from precracked round-bar specimens.* Engineering Fracture Mechanics, 2000. **65**(5): p. 559-572.
92. Wang, C., *Measurement of fracture toughness K1c by single small-scale cylindrical specimen with ring-shaped crack.* Engineering Fracture Mechanics, 1987. **28**(3): p. 241-250.
93. Wu, F.W., et al., *Fracture toughness for CNT specimens from numerically obtained critical CTOD values.* Theoretical and Applied Fracture Mechanics, 2009. **52**(1): p. 50-54.
94. Ibrahim, R.N., R. Rihan, and R.K.S. Raman, *Validity of a new fracture mechanics technique for the determination of the threshold stress intensity factor for stress corrosion cracking (KIscc) and crack growth rate of engineering materials.* Engineering Fracture Mechanics, 2008. **75**(6): p. 1623-1634.
95. Ibrahim, R.N. and A. Kotousov, *Eccentricity correction for the evaluation of fracture toughness from cylindrical notched test small specimens.* Engineering Fracture Mechanics, 1999. **64**(1): p. 49-58.
96. Ibrahim, R.N. and H.L. Stark, *Establishing K1c from eccentrically fatigue cracked small circumferentially grooved cylindrical specimens.* International Journal of Fracture, 1990. **44**(3): p. 179-188.
97. Baik, J.-M., J. Kameda, and O. Buck, *Small punch test evaluation of intergranular embrittlement of an alloy steel.* Scripta Metallurgica, 1983. **17**(12): p. 1443-1447.
98. Manahan, M.P., et al., *Miniaturized disk bend test technique developement and application.* ASTM STP 888, 1986: p. 17-49.
99. Harling, O.K., et al., *The use of small-scale specimens for testing irradiated material* ASTM STP 888, 1986: p. 50-65.
100. Lucas, G., *Review of small specimen test techniques for irradiation testing.* Metallurgical and Materials Transactions A, 1990. **21**(5): p. 1105-1119.
101. Hickey, J.J. and J.H. Bulloch, *Review of nondestructive techniques designed to evaluate elevated temperature toughness degradation.* Theoretical and Applied Fracture Mechanics, 1992. **18**(1): p. 1-13.
102. Husain, A., D.K. Sehgal, and R.K. Pandey, *Review of small punch test technique for evaluating mechanical behaviour of materials and in-service components using miniature specimen.* Journal of Structural Engineering, 2004. **31**(2): p. 91-100.
103. Proriol Serre, I., et al., *Mechanical behavior of coated T91 steel in contact with lead-bismuth liquid alloy at 300 °C.* Surface and Coatings Technology. **In Press, Corrected Proof**.

104. Jaekel, D.J., D.W. MacDonald, and S.M. Kurtz, *Characterization of PEEK biomaterials using the small punch test.* Journal of the Mechanical Behavior of Biomedical Materials, 2011. **In Press, Corrected Proof**.

105. Budzakoska, E., et al., *Predicting the J integral fracture toughness of Al 6061 using the small punch test.* Fatigue & Fracture of Engineering Materials and Structures, 2007. **30**(9): p. 796-807.

106. Mak, J., et al., *Small Punch Test of LC4/SiCp Metal Matrix Composites.* Advanced Materials Research, 2010. **123-125**: p. 439-442.

107. Mak, J., et al., *Small Punch Test of Advanced In-Situ Synthesized Ti Metal Matrix Composites.* Advanced Materials Research, 2008. **47-50**: p. 738-741.

108. Mak, J., et al., *Microstructural Analysis on Ti-6Al-4V and 10 Vol.% (TiB+TiC)/Ti-6Al-4V Metal Matrix Composites.* Advanced Materials Research, 2008. **32**: p. 53-56.

109. Mak, J., et al., *Microstructural Analysis on Ti-6Al-4V and 10 Vol.% (TiB+TiC)/Ti-6Al-4V Metal Matrix Composites.* Advanced Materials Research, 2008. **47-50**: p. 115-118.

110. Mak, J., et al., *Equal Channel Angular Extrusion of Zinc-Aluminium Metal Matrix Composites.* Key Engineering materials, 2007. **345-346**: p. 113-116.

111. Mak, J., et al., *Research on Titanium Metal Matrix Composites at the University of Technology, Sydney*, in *Materials Australia*. 2010, Materials Australia: Melbourne.

112. Hamilton, M.L. and F.H. Huang, *Use of the disk bend test to assess irradiation performance of structural alloys* ASTM STP 888, 1986: p. 5-16.

113. Klueh, R.L. and D.N. Braski, *Disk-bend ductility tests for irradiated materials.* ASTM STP 888, 1986: p. 66-62.

114. Baik, J.-M., J. Kameda, and O. Buck, *Development of the small punch tests for ductile-brittle transition temperature measurement of temper embrittled Ni-Cr steels.* ASTM STP 888, 1986: p. 92-111.

115. Eto, M., et al., *Developement of a miniaturized bulge test (small punch test) for post irradiation mechanical property evaluation.* ASTM STP 1204, 1993: p. 241-255.

116. Jitsukawa, S., et al., *Methods and devices for small specimen testing at the Japan Atomic Energy Research Institute.* ASTM STP 1204, 1993: p. 289-307.

117. Nunomura, S., et al., *Evaluation of tensile properties using a TEM disks sized specimen.* ASTM STP 1204, 1993: p. 256-266.

118. Sinclair, A.N., et al., *Assessment of fracture toughness by a punch test with minature specimens.* ASTM STP 1204, 1993: p. 162-179.

119. Suzuki, M., et al., *Estimation of Toughness by Degradation Microhardness and Small Punch Tests.* ASTM STP 1204, 1993: p. 217-227.

120. Foulds, J.R., et al., *Fracture and tensile properties of ASTM cross-comparison excercise A533B steel by small punch testing.* ASTM STP 1329, 1998: p. 557-574.

121. Geary, W. and J. Dutton, T., *The prediction of fracture toughness properties from 3mm diameter punch discs.* ASTM STP 1329, 1998: p. 588-601.

122. Fong, R.W.L. and C.R. Fraser, *Evaluation of ductility of zircaloy-2 materials using a small ellipsoidal-shaped punch.* ASTM STP 1329, 1998: p. 602-613.

123. Lee, W.K., et al., *The use of a small punch test procedure to determine mechanical properties.* ASTM STP 1329, 1998: p. 539-551.

124. Catherine, C.S., et al., *EPRI-CEA Finite Element Simulation Benchmark and Inverse Method for the Estimation of Elastic Plastic Behavior.* ASTM STP 1418, 2002: p. 350-371.
125. Wei, T., et al., *Surveillance of the fracture behavior of zircaloy-4 welds using the small punch test.* ASTM STP 1502 2009: p. 196-217.
126. Linse, T., et al., *Application of the small-punch test to irradiated reactor vessel steels in the brittle-ductile transition region.* ASTM STP 1502, 2009. **5**(4): p. 218-235.
127. Serrano, M., P. Fernández, and J. Lapeña, *Fracture toughness evaluation of Eurofer97 by testing small specimens.* ASTM STP 1502, 2009. **5**(4): p. 114-121.
128. *Recommended practice for the small punch (SP) testing of metallic materials* 1988, JAEIR-M. p. 88-172.
129. *Standard Test Method for Small Punch Testing of Ultra-High Molecular Weight Polyethylene Used in Surgical Impants*. 2008, American Society for Testing and Materials.
130. *Small Punch Test Method for Metallic Materials*. 2007, National Standards Authority of Ireland.
131. Tong, X., et al., *Study on Standardization of Small Punch Test(1)——General Requirements.* Pressure Vessel Technology, 2010. **27**(7): p. 37-46.
132. Sokolov, M., J.D. Landes, and G.E. Lucas, *Small specimen test techniques*. Vol. 4th. 2002, Philadelphia: ASTM International Committee E10 on Nuclear Technology and Applications.
133. Takahashi, H., et al., *Recommended practice for the small punch (SP) testing of metallic materials* in *JAEIR-M*. 1988. p. 88-172.
134. Mao, X. and J. Kameda, *Small-punch technique for measurement of material degradation of irradiated ferritic alloys.* Journal of Materials Science, 1991. **26**(9): p. 2436-2440.
135. Mao, X., M. Saito, and H. Takahashi, *Small punch test to predict ductile fracture toughness JIC and brittle fracture toughness KIC.* Scripta Metallurgica et Materialia, 1991. **25**(11): p. 2481-2485.
136. Mao, X., H. Takahashi, and T. Kodaira, *Estimation of mechanical properties of irradiated nuclear pressure vessel steel by use of subsized CT specimen and small punch specimen.* Scripta Metallurgica et Materialia, 1991. **25**(11): p. 2487-2490.
137. Mao, X. and H. Takahashi, *Development of a further-miniaturized specimen of 3 mm diameter for tem disk (ø 3 mm) small punch tests.* Journal of Nuclear Materials, 1987. **150**(1): p. 42-52.
138. Isselin, J., et al., *Assessment of the constitutive law by inverse methodology: Small punch test and hardness.* Journal of Nuclear Materials, 2006. **352**(1-3): p. 97-106.
139. Abendroth, M. and M. Kuna, *Identification of ductile damage and fracture parameters from the small punch test using neural networks.* Engineering Fracture Mechanics, 2006. **73**(6): p. 710-725.
140. Dobes, F. and K. Milicka, *On the Monkman-Grant relation for small punch test data.* Materials Science and Engineering: A, 2002. **336**(1-2): p. 245-248.
141. Bulloch, J.H., *Toughness losses in low alloy steels at high temperatures: an appraisal of certain factors concerning the small punch test.* International Journal of Pressure Vessels and Piping, 1998. **75**(11): p. 791-804.

142. Suzuki, M., et al., *Evaluation of toughness degradation by small punch (SP) tests for neutron-irradiated 2Cr-1Mo steel.* Journal of Nuclear Materials, 1991. **179-181**(Part 1): p. 441-444.
143. Fleury, E. and J.S. Ha, *Small punch tests to estimate the mechanical properties of steels for steam power plant: I. Mechanical strength.* International Journal of Pressure Vessels and Piping, 1998. **75**(9): p. 699-706.
144. Husain, A., D.K. Sehgal, and R.K. Pandey, *An inverse finite element procedure for the determination of constitutive tensile behavior of materials using miniature specimen.* Computational Materials Science, 2004. **31**(1-2): p. 84-92.
145. Shekhter, A., et al., *Towards the correlation of fracture toughness in an ex-service power generating rotor.* International Journal of Pressure Vessels and Piping, 2000. **77**(2-3): p. 113-116.
146. Ju, J.-B., J.-i. Jang, and D. Kwon, *Evaluation of fracture toughness by small-punch testing techniques using sharp notched specimens.* International Journal of Pressure Vessels and Piping, 2003. **80**(4): p. 221-228.
147. Tanaka, K., et al., *Evaluation on high temperature fracture toughness of CrMoV cast steel by small punch testing.* International Journal of Pressure Vessels and Piping, 2009. **86**(9): p. 643-648.
148. Foulds, J.R., et al., *Fracture toughness by small punch test.* Journal of Testing and Evaluation, 1995. **23**(1): p. 3-10.
149. Peñuelas, I., et al., *Inverse determination of the elastoplastic and damage parameters on small punch tests.* Fatigue & Fracture of Engineering Materials & Structures, 2009. **32**(11): p. 872-885.
150. Cuesta, I.I., J.M. Alegre, and R. Lacalle, *Determination of the Gurson–Tvergaard damage model parameters for simulating small punch tests.* Fatigue & Fracture of Engineering Materials & Structures, 2010. **33**(11): p. 703-713.
151. Eskner, M. and R. Sandström, *Mechanical Propertie Evaluation Using the Small Punch Test.* Journal of Testing and Evaluation, 2004. **32**(4): p. 1-8.
152. Isselin, J. and T. Shoji, *Yield Strength Evaluation by Small-Punch Test.* Journal of Testing and Evaluation, 2009. **37**(6): p. 1-7.
153. *Metallic materials - Tensile testing at ambient temperatures*. 2007, Standards Australia.
154. Bulloch, J.H., *A study concerning material fracture toughness and some small punch test data for low alloy steels.* Engineering Failure Analysis, 2004. **11**(4): p. 635-653.
155. Chakrabarty, J., *A theory of stretch forming over hemispherical punch heads.* International Journal of Mechanical Sciences, 1970. **12**(4): p. 315-325.
156. Young, W.C., R.J. Roarke, and R.G. Budynas, *Roark's formulas for stress and strain*. 7th ed. 2002, New York: McGraw-Hill.
157. Cicero, S., R. Lacalle, and F. Gutiérrez-Solana, *Application of Small Punch Techniques for the Determination of Gold Mechanical Properties.* Strain, 2009: p. no-no.
158. Xu, Y. and Z. Zhao, *A modified miniature disk test for determining material mechanical properties.* Journal of Testing and Evaluation, 1995. **23**(4): p. 300-306.
159. Cheon, J.S. and I.S. Kim, *Initial deformation during small punch testing.* Journal of Testing and Evaluation, 1996. **24**(4): p. 255-262.

160. Ruan, Y., P. Spätig, and M. Victoria, *Assessment of mechanical properties of the martensitic steel EUROFER97 by means of punch tests.* Journal of Nuclear Materials, 2002. **307-311**(Part 1): p. 236-239.
161. Finarelli, D., M. Roedig, and F. Carsughi, *Small punch tests on austenitic and martensitic steels irradiated in a spallation environment with 530 MeV protons.* Journal of Nuclear Materials, 2004. **328**(2-3): p. 146-150.
162. Cuesta, I.I. and J.M. Alegre, *Determination of the fracture toughness by applying a structural integrity approach to pre-cracked Small Punch Test specimens.* Engineering Fracture Mechanics, 2011. **78**(2): p. 289-300.
163. Takahashi, H., M.A. Khan, and S. Masahiko, *A single specimen determination of J1c for Different Alloys Steels.* Journal of Testing and Evaluation, 1980. **8**(2): p. 63-67.
164. Takahashi, H., M.A. Khan, and S. Masahiko, *A simple test method for the evaluation of tearing modulus.* Journal of Testing and Evaluation, 1981. **9**(1): p. 14-23.
165. Ju, J.-B. and D. Kwon, *Assessment of fracture characteristics from revised small punch test using pre-cracked specimen.* Metals and Materials, 1998. **4**(4): p. 742-746.
166. Ritchie, R.O., J.F. Knott, and J.R. Rice, *On the relationship between critical tensile stress and fracture toughness in mild steel.* Journal of the Mechanics and Physics of Solids, 1973. **21**(6): p. 395-410.
167. Ha, J.S. and E. Fleury, *Small punch tests to estimate the mechanical properties of steels for steam power plant: II. Fracture toughness.* International Journal of Pressure Vessels and Piping, 1998. **75**(9): p. 707-713.
168. Ritchie, R., W. Server, and R. Wullaert, *Critical fracture stress and fracture strain models for the prediction of lower and upper shelf toughness in nuclear pressure vessel steels.* Metallurgical and Materials Transactions A, 1979. **10**(10): p. 1557-1570.
169. Hutchinson, J.W., *Singular behaviour at the end of a tensile crack in a hardening material.* Journal of the Mechanics and Physics of Solids, 1968. **16**(1): p. 13-31.
170. Rice, J.R. and G.F. Rosengren, *Plane strain deformation near a crack tip in a power-law hardening material.* Journal of the Mechanics and Physics of Solids, 1968. **16**(1): p. 1-12.
171. Joo, Y.-H., et al., *The use small punch (bulge) tests to estimate fracture stress in the lower shelf regime.* Journal of Testing and Evaluation, 1992. **20**(5): p. 336-342.
172. Rice, J.R., *A path independant intergral and the approximate analysis of strain concentration by notches and cracks.* J. Appl. Mech., 1968. **35**: p. 379–386.
173. Zidan, A.A. and D.J. Brookfield, *A technique for the determination of post-yield material properties from the small punch test.* The Journal of Strain Analysis for Engineering Design 2003 **38** (4): p. 367-376
174. Cheon, J.-S. and C.-H. Joo, *Small punch test for determining a flow stress by using a hybrid inverse procedure.* Computational Materials Science, 2008. **43**(4): p. 744-751.
175. Shen, H. and C.J. Lissenden, *3D finite element analysis of particle-reinforced aluminum.* Materials Science and Engineering A, 2002. **338**(1-2): p. 271-281.
176. Chawla, N., V.V. Ganesh, and B. Wunsch, *Three-dimensional (3D) microstructure visualization and finite element modeling of the mechanical*

behavior of SiC particle reinforced aluminum composites. Scripta Materialia, 2004. **51**(2): p. 161-165.

177. Ayyar, A. and N. Chawla, *Microstructure-based modeling of crack growth in particle reinforced composites.* Composites Science and Technology, 2006. **66**(13): p. 1980-1994.
178. Wei, T., et al., *Assessment of the fracture toughness of 6061 aluminium by the small punch test and finite element analysis.* Materials Forum, 2006. **30**: p. 39-44.
179. Abendroth, M. and M. Kuna, eds. *Determination of deformation and failure properties of ductile materials by means of the small punch test and neural networks*. Computational Materials Science. Vol. 28. 2003. 633-644.
180. Gurson, A.L., *Continuum Theory of Ductile Rupture by Void Nucleation and Growth: Part I---Yield Criteria and Flow Rules for Porous Ductile Media.* Journal of Engineering Materials and Technology, 1977. **99**(1): p. 2-15.
181. Björklund, O., *Modelling of Failure*, in *Department of Management and Engineering*. 2008, Linköping University: Linköping.
182. Seibi, A. and S.M. Al-Alawi, *Prediction of fracture toughness using artificial neural networks (ANNs).* Engineering Fracture Mechanics, 1997. **56**(3): p. 311-319.
183. Partheepan, G., D.K. Sehgal, and R.K. Pandey, *Fracture toughness evaluation using miniature specimen test and neural network.* Computational Materials Science, 2008. **44**(2): p. 523-530.
184. Koker, R., N. Altinkok, and A. Demir, *Neural network based prediction of mechanical properties of particulate reinforced metal matrix composites using various training algorithms.* Materials & Design, 2007. **28**(2): p. 616-627.
185. *Standard Terminology Relating to Fatigue and Fracture Testing*. 2005, American Society for Testing and Materials.
186. Weidmann, E. and A. Guesnier (2007) *Metallographic preparation of aluminium and aluminium alloys*.
187. Taylor, B. and E. Weidmann (2002) *Metallographic preparation of titanium*.
188. Goldstein, J., et al., *Scanning Electron Microscopy and X-ray Microanalysis*. 3rd ed. 1981, New York: Plenum Press. 673.
189. Moran, K. and R. Wuhrer, *Quantitative Bulk and Trace Element X-Ray Mapping Using Multiple Detectors*. Microchimica Acta, 2006. **155**(1): p. 59-66.
190. Wuhrer, R., M. Lee, and W.Y. Yeung, *Interface Development in Sintering of Roll Bonded Metal Laminates*. Solid States Phenomena, 2006. **118**: p. 437-442.
191. Mak, J., et al., *Characterization of Advance Titanium Metal Matrix Composites through Quantitative X-Ray Mapping*, in *Proceedings of ACMM-20 & IUMAS-IV*. 2008, Australian Microscopy and Microanalysis Society Inc.: Perth, Australia. p. 427-428.
192. Moran, K. and R. Wuhrer, *X-Ray Mapping and Interpretation of Scatter Diagrams*. Microchimica Acta, 2006. **155**(1): p. 209-217.
193. Stuert, M., *The Drawing Office Handbook*. Third ed, ed. R.W.S. Mitchell. 1956, London: Sir Isaac Pitman & Sons LTD.
194. Egan, P., et al., *Small punch test: An approach to solve the inverse problem by deformation shape and finite element optimization.* Computational Materials Science, 2006. **In Press, Corrected Proof**.
195. Zhu, C.C., et al., *Finite Element Analysis of Small Punch Test for Ti Matrix Composites.* 机械工程材料, 2010. **34**(4): p. 87-91.

196. Heness, G., et al., *Developement of finite element micromodal for metal matrix composites.* Computational Materials Science, 1998. **13**: p. 259-269.
197. Sakai, E. and J. Sugita, *Composite mechanisms of polymer modified cement.* Cement and Concrete Research, 1995. **25**(1): p. 127-135.
198. Kamat, S.V. and J.P. Hirth, *Mixed mode I/II fracture toughness of 2034 aluminum alloys.* Acta Materialia, 1996. **44**(1): p. 201-208.
199. Kamat, S.V., N. Eswara Prasad, and G. Malakondaiah, *Comparison of mode I and mode II fracture toughness of an 8090 Al---Li alloy.* Materials Science and Engineering: A, 1991. **149**(1): p. L1-L3.
200. Heness, G.L., *Fracture and Fatigue of Particulate MMCs*, in *Department of Mechanical and Mechatronic Engineering*. 1996, University of Sydney: Sydney. p. 327.
201. Ma, Y.W. and K.B. Yoon, *Assessment of tensile strength using small punch test for transversely isotropic aluminum 2024 alloy produced by equal channel angular pressing.* Materials Science and Engineering: A, 2010. **527**(16-17): p. 3630-3638.
202. Wanjara, P., R.A.L. Drew, and S. Yue, *Application of small specimen testing technique for mechanical property assessment of discontinuously reinforced composites.* Materials Science & Technology, 2006. **22**(1): p. 61-71.
203. Wanjara, P., *Characterization of Ti-6%Al-4%V/TiC particulate reinforced metal matrix composites consolidated by sintering and thermomechanical processing*, in *Department of Mining and Metallurgical Engineering*. 1999, McGill University: Montreal.
204. Bulloch, J.H., *A review of the ESB small punch test data on various plant components with special emphasis on fractographic details.* Engineering Failure Analysis, 2002. **9**(5): p. 511-534.
205. Mao, X., H. Takahashi, and T. Kodaira, *Supersmall punch test to estimate fracture toughness JIc and its application to radiation embrittlement of 2.25Cr-1Mo steel.* Materials Science and Engineering: A, 1992. **150**(2): p. 231-236.
206. Callaghan, M.D., et al., *An Analysis of Deformation and Fracture Behaviour of Zircaloy-4 Alloy Using Small Punch Test.* Materials Science Forum, 2005. **475-479**: p. 1415 -1420
207. Chi, S.-H., J.-H. Hong, and I.-S. Kim, *Evaluation of irradiation effects of 16 MeV proton-irradiated 12Cr---1MoV steel by small punch(SP) tests.* Scripta Metallurgica et Materialia, 1994. **30**(12): p. 1521-1525.
208. Lucas, G.E., et al., *Shear punch tests for mechanical property measurements in TEM disc-sized specimens.* Journal of Nuclear Materials, 1984. **122**(1-3): p. 429-434.
209. Karthik, V., et al., *Tensile-shear correlations obtained from shear punch test technique using a modified experimental approach.* Journal of Nuclear Materials, 2009. **393**(3): p. 425-432.
210. Kameda, J. and O. Buck, *Evaluation of the ductile-to-brittle transition temperature shift due to temper embrittlement and neutron irradiation by means of a small-punch test.* Materials Science and Engineering: A, 1986. **83**(1): p. 29-38.
211. Misawa, T., et al., *Small punch tests for evaluating ductile-brittle transition behavior of irradiated ferritic steels.* Journal of Nuclear Materials, 1987. **150**(2): p. 194-202.

212. Vorlicek, V., L.F. Exworthy, and P.E.J. Flewitt, *Evaluation of a miniaturized disc test for establishing the mechanical properties of low-alloy ferritic steels.* Journal of Materials Science, 1995. **30**(11): p. 2936-2943.

213. Börger, A., P. Supancic, and R. Danzer, *The ball on three balls test for strength testing of brittle discs: stress distribution in the disc.* Journal of the European Ceramic Society, 2002. **22**(9-10): p. 1425-1436.

214. Börger, A., P. Supancic, and R. Danzer, *The ball on three balls test for strength testing of brittle discs: Part II: analysis of possible errors in the strength determination.* Journal of the European Ceramic Society, 2004. **24**(10-11): p. 2917-2928.

215. Westergaard, H.M., *Stresses in concrete pavements computed by theoretical analysis.* Public Roads, 1926. **7**(2): p. 25-35.

216. Godfrey, D.J., *Fabrication, formulation, mechanical properties, and oxidation of sintered Si3N4 ceramics using disc specimens.* Materials Science and Technology, 1985. **1**(0267-0836, 0267-0836): p. 510-510-515.

217. Shetty, D.K., et al., *A Biaxial-Flexure Test for Evaluating Ceramic Strengths.* Journal of the american ceramic society, 1983. **66**(1): p. 36-42.

218. Lucas, G.E., *The development of small specimen mechanical test techniques.* Journal of Nuclear Materials, 1983. **117**: p. 327-339.

219. Toloczko, M.B., M.L. Hamilton, and G.E. Lucas, *Ductility correlations between shear punch and uniaxial tensile test data.* Journal of Nuclear Materials, 2000. **283-287**(Part 2): p. 987-991.

220. Hankin, G.L., et al., *Validation of the shear punch-tensile correlation technique using irradiated materials.* Journal of Nuclear Materials, 1998. **258-263**(Part 2): p. 1651-1656.

221. Guduru, R.K., et al., *Evaluation of mechanical properties using shear-punch testing.* Materials Science and Engineering A, 2005. **395**(1-2): p. 307-314.

222. Guan, K., et al., *Assessment of toughness in long term service CrMo low alloy steel by fracture toughness and small punch test.* Nuclear Engineering and Design, 2011. **In Press, Corrected Proof**.

223. Wang, G.Z., J.H. Chen, and G.H. Liu, *On the characteristic distance and minimum fracture toughness for cleavage fracture in a C-Mn steel.* International Journal of Fracture, 2002. **118**(1): p. 57-76.

224. Chen, J.H., et al., *Advances in the mechanism of cleavage fracture of low alloy steel at low temperature. Part II: Fracture model.* International Journal of Fracture, 1997. **83**(2): p. 121-138.

APPENDIX I

7A04-T6

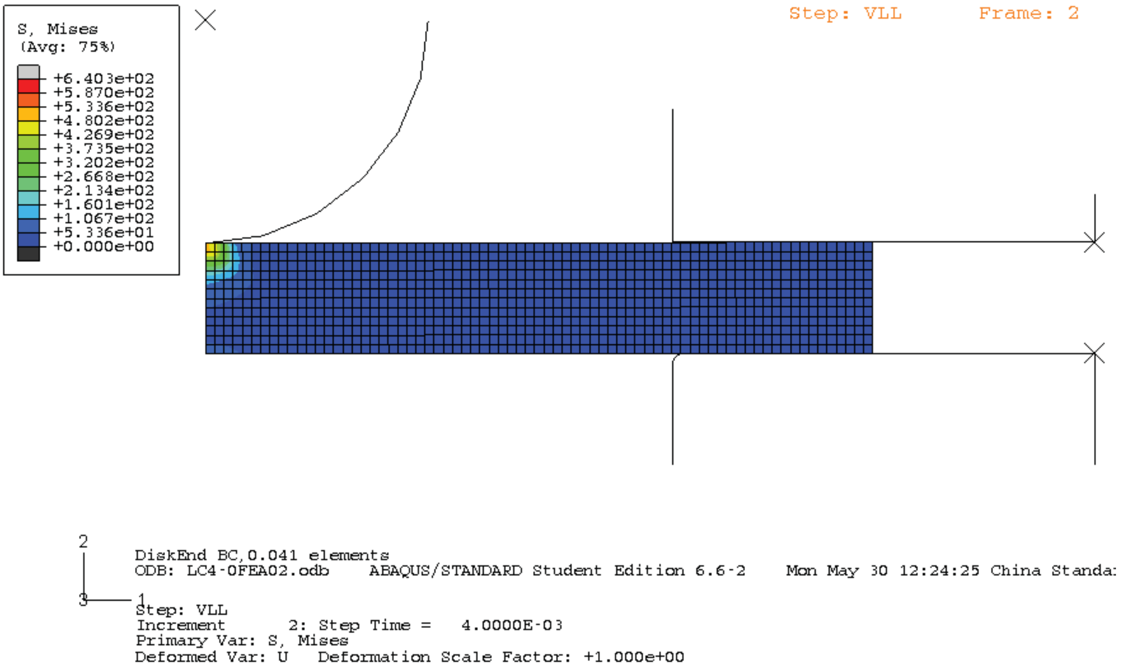

```
DiskEnd BC,0.041 elements
ODB: LC4-0FEA02.odb     ABAQUS/STANDARD Student Edition 6.6-2     Mon May 30 12:24:25 China Standa
Step: VLL
Increment      2: Step Time =     4.0000E-03
Primary Var: S, Mises
Deformed Var: U   Deformation Scale Factor: +1.000e+00
```

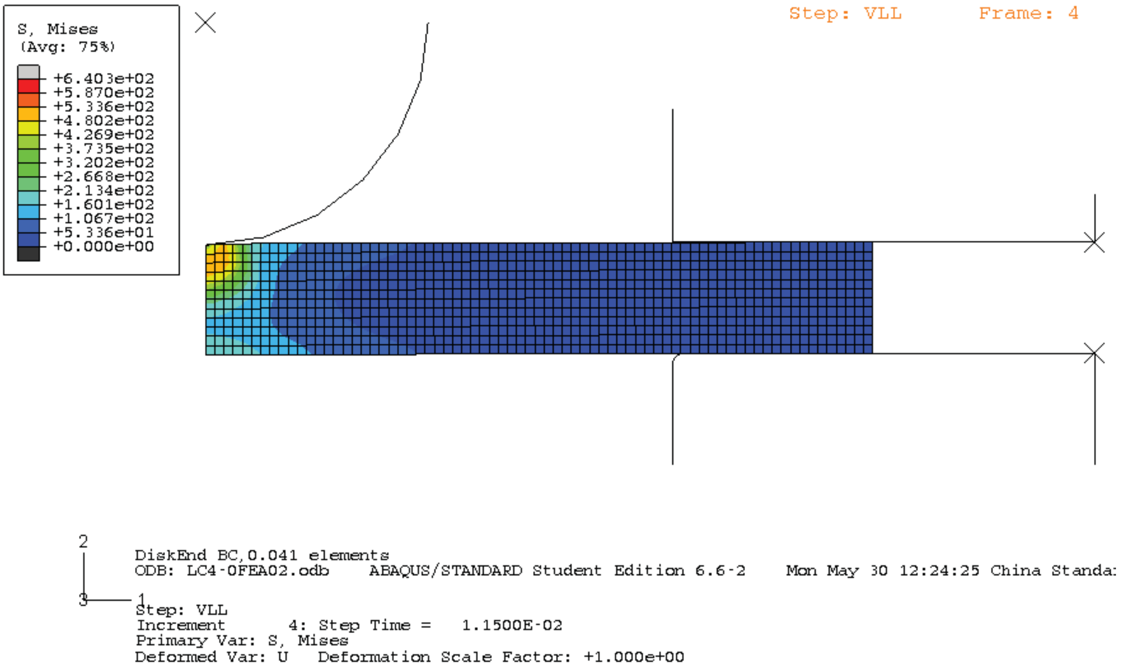

```
DiskEnd BC,0.041 elements
ODB: LC4-0FEA02.odb     ABAQUS/STANDARD Student Edition 6.6-2     Mon May 30 12:24:25 China Standa
Step: VLL
Increment      4: Step Time =     1.1500E-02
Primary Var: S, Mises
Deformed Var: U   Deformation Scale Factor: +1.000e+00
```

7A04-T6

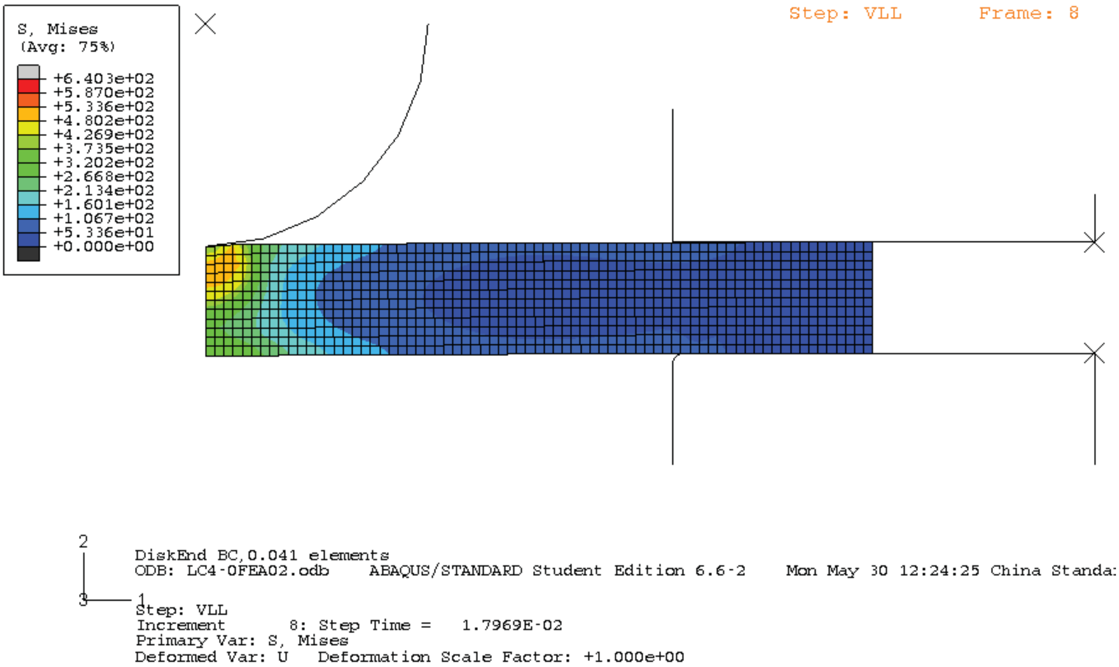

```
DiskEnd BC,0.041 elements
ODB: LC4-0FEA02.odb    ABAQUS/STANDARD Student Edition 6.6-2    Mon May 30 12:24:25 China Standa
Step: VLL
Increment      8: Step Time =    1.7969E-02
Primary Var: S, Mises
Deformed Var: U   Deformation Scale Factor: +1.000e+00
```

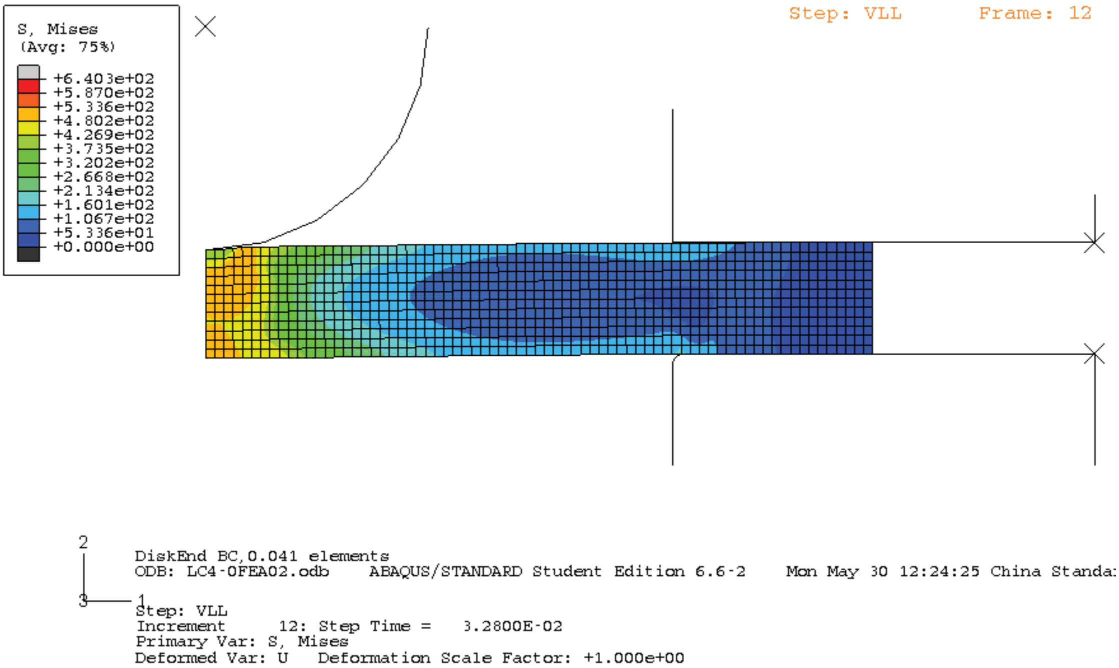

```
DiskEnd BC,0.041 elements
ODB: LC4-0FEA02.odb    ABAQUS/STANDARD Student Edition 6.6-2    Mon May 30 12:24:25 China Standa
Step: VLL
Increment     12: Step Time =    3.2800E-02
Primary Var: S, Mises
Deformed Var: U   Deformation Scale Factor: +1.000e+00
```

7A04-T6

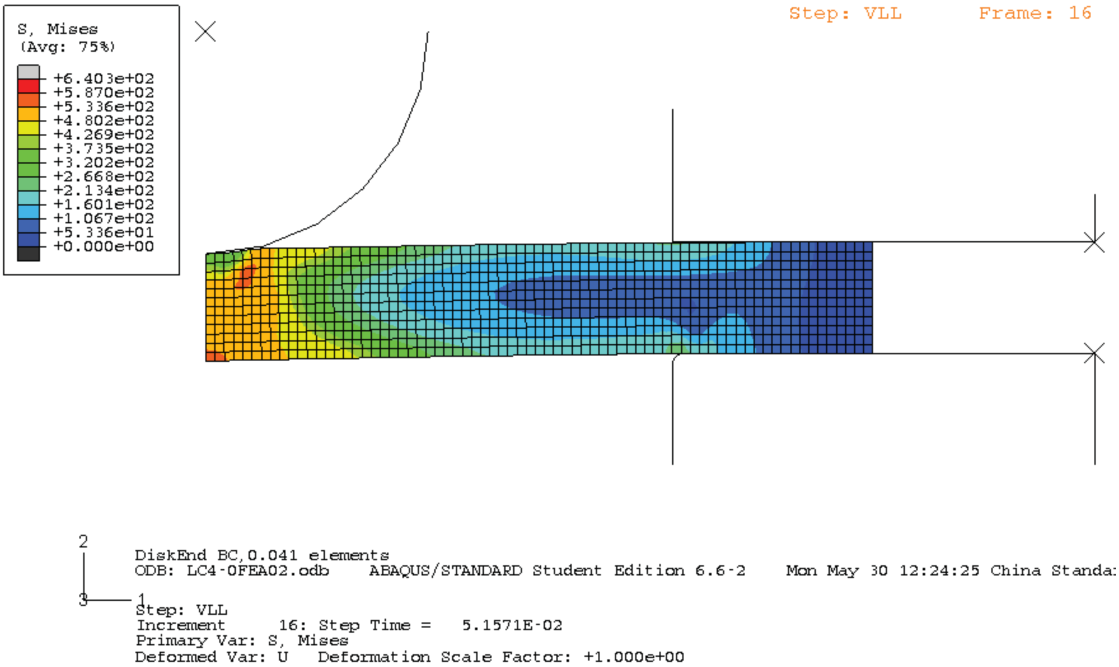

```
DiskEnd BC,0.041 elements
ODB: LC4-0FEA02.odb    ABAQUS/STANDARD Student Edition 6.6-2    Mon May 30 12:24:25 China Standa:

Step: VLL
Increment     16: Step Time =    5.1571E-02
Primary Var: S, Mises
Deformed Var: U   Deformation Scale Factor: +1.000e+00
```

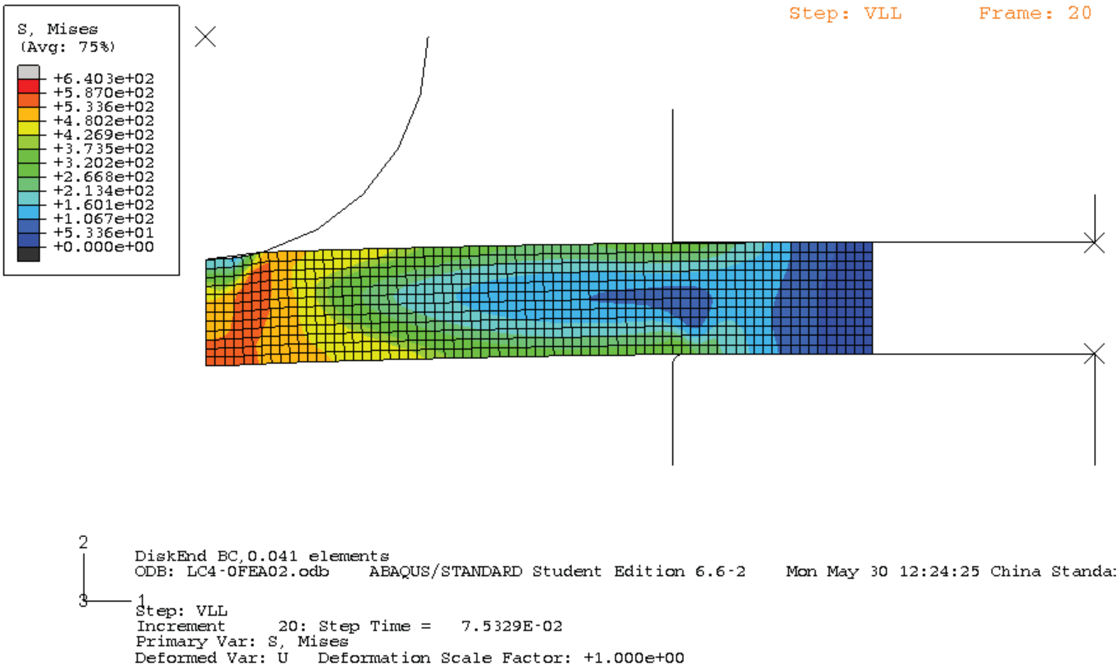

```
DiskEnd BC,0.041 elements
ODB: LC4-0FEA02.odb    ABAQUS/STANDARD Student Edition 6.6-2    Mon May 30 12:24:25 China Standa:

Step: VLL
Increment     20: Step Time =    7.5329E-02
Primary Var: S, Mises
Deformed Var: U   Deformation Scale Factor: +1.000e+00
```

7A04-T6

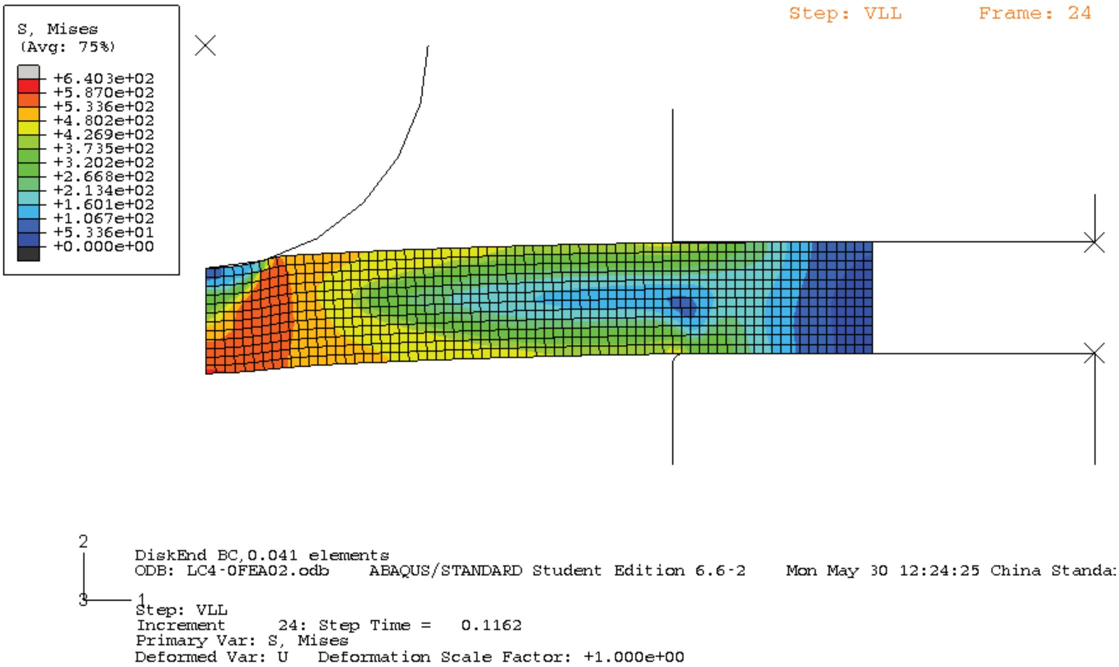

```
DiskEnd BC,0.041 elements
ODB: LC4-0FEA02.odb    ABAQUS/STANDARD Student Edition 6.6-2    Mon May 30 12:24:25 China Standa
Step: VLL
Increment     24: Step Time =    0.1162
Primary Var: S, Mises
Deformed Var: U   Deformation Scale Factor: +1.000e+00
```

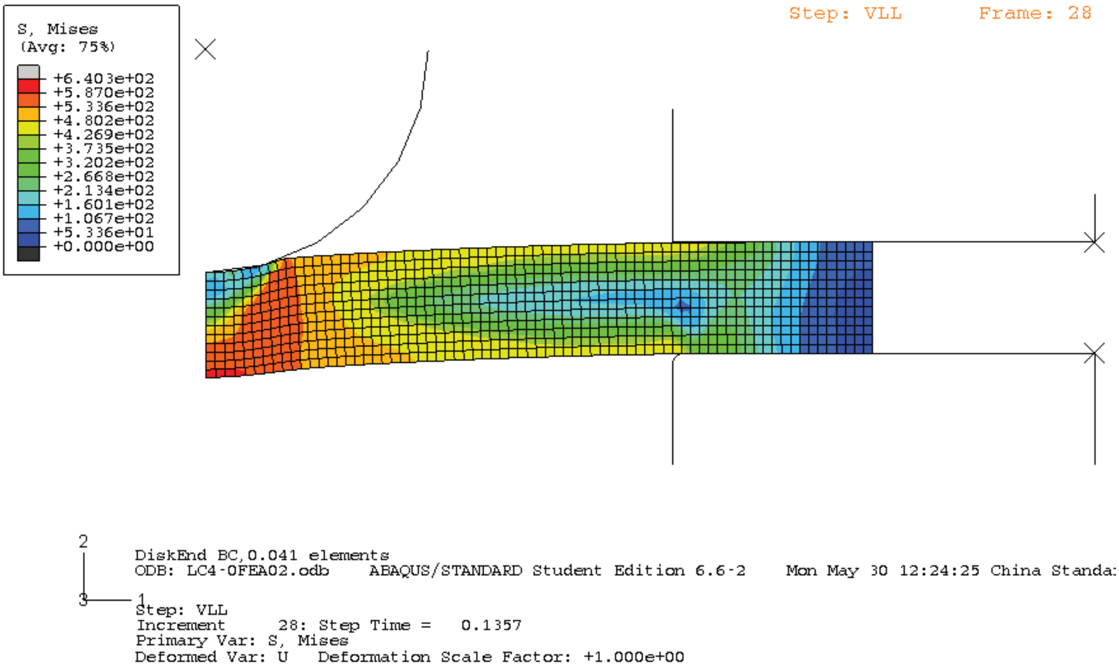

```
DiskEnd BC,0.041 elements
ODB: LC4-0FEA02.odb    ABAQUS/STANDARD Student Edition 6.6-2    Mon May 30 12:24:25 China Standa
Step: VLL
Increment     28: Step Time =    0.1357
Primary Var: S, Mises
Deformed Var: U   Deformation Scale Factor: +1.000e+00
```

7A04-T6/SiC/7.5p

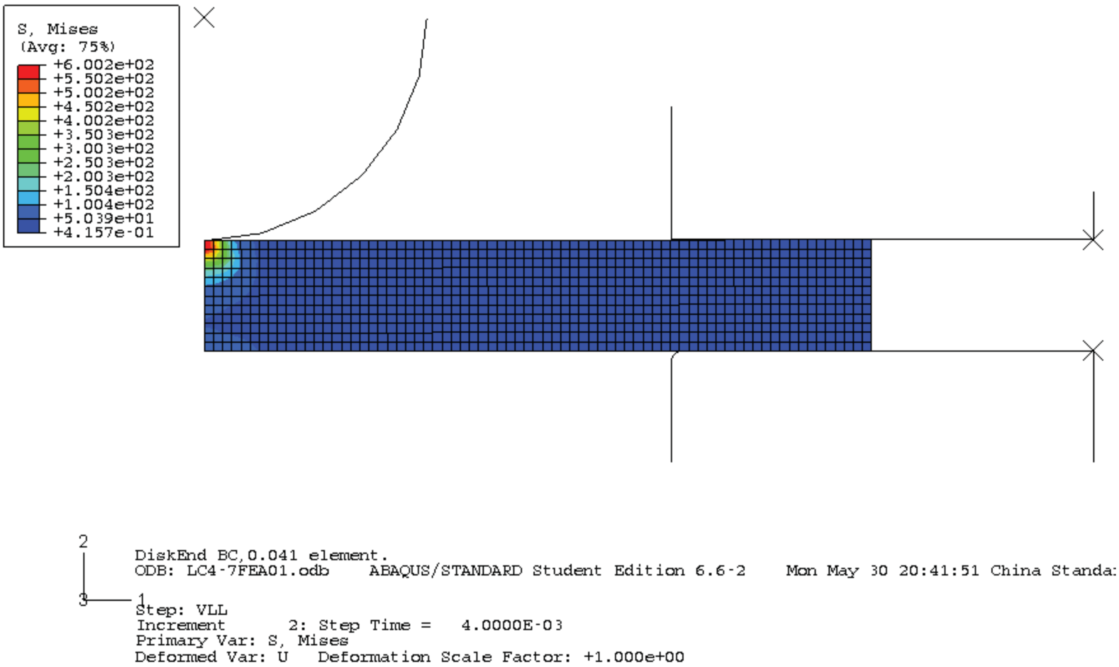

```
DiskEnd BC,0.041 element.
ODB: LC4-7FEA01.odb     ABAQUS/STANDARD Student Edition 6.6-2     Mon May 30 20:41:51 China Standa
Step: VLL
Increment       2: Step Time =    4.0000E-03
Primary Var: S, Mises
Deformed Var: U   Deformation Scale Factor: +1.000e+00
```

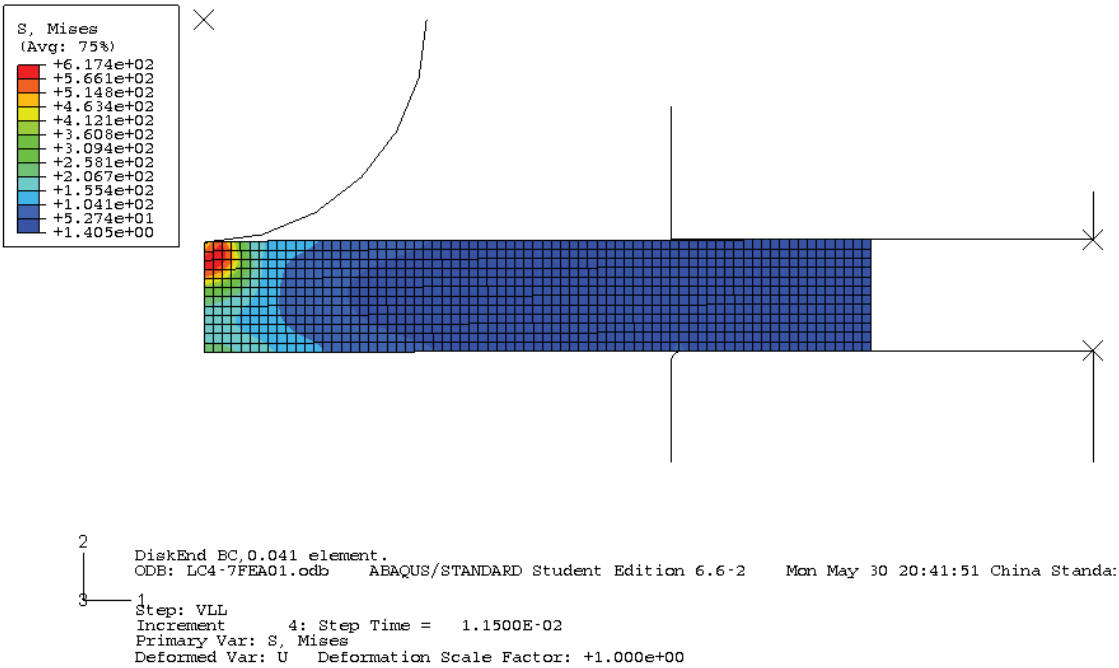

```
DiskEnd BC,0.041 element.
ODB: LC4-7FEA01.odb     ABAQUS/STANDARD Student Edition 6.6-2     Mon May 30 20:41:51 China Standa
Step: VLL
Increment       4: Step Time =    1.1500E-02
Primary Var: S, Mises
Deformed Var: U   Deformation Scale Factor: +1.000e+00
```

7A04-T6/SiC/7.5p

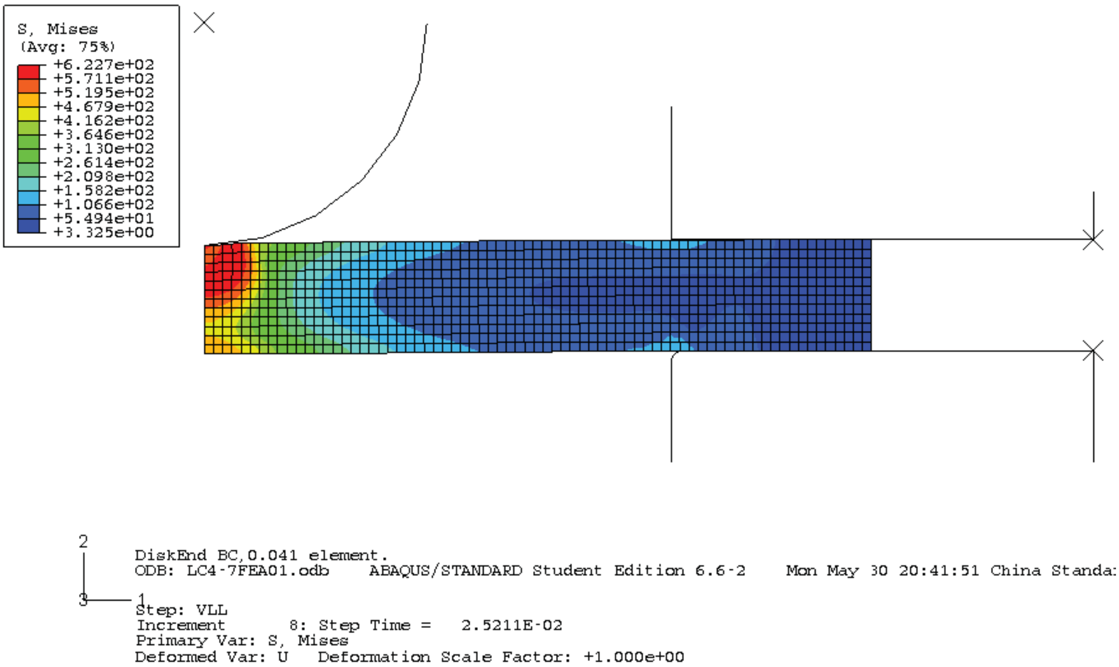

```
DiskEnd BC,0.041 element.
ODB: LC4-7FEA01.odb     ABAQUS/STANDARD Student Edition 6.6-2     Mon May 30 20:41:51 China Standa
Step: VLL
Increment       8: Step Time =    2.5211E-02
Primary Var: S, Mises
Deformed Var: U   Deformation Scale Factor: +1.000e+00
```

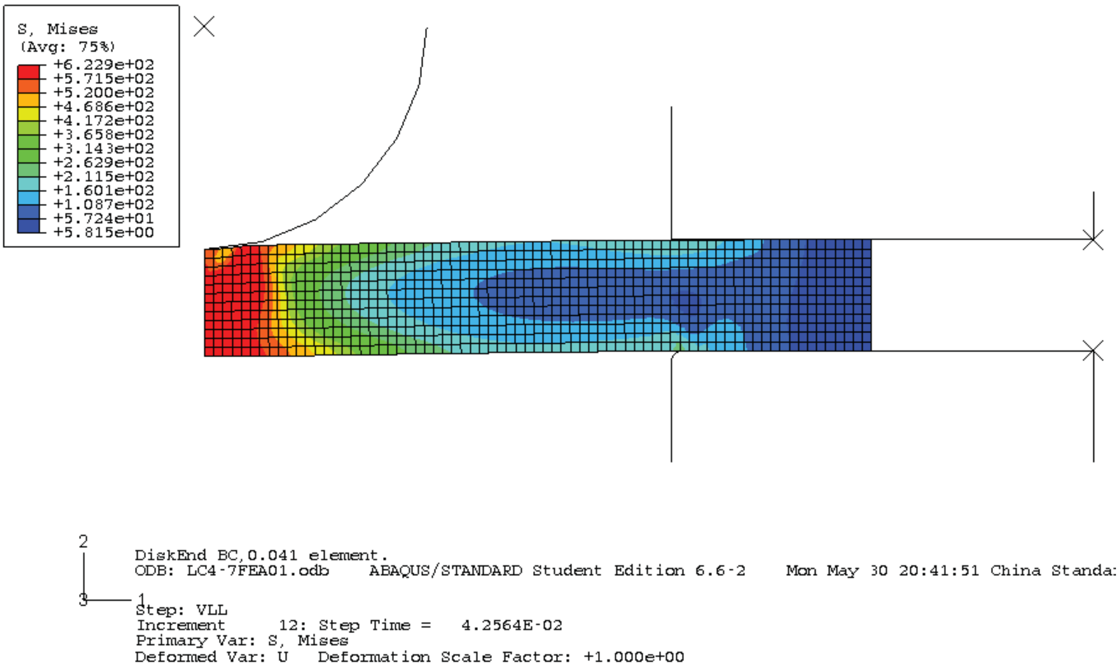

```
DiskEnd BC,0.041 element.
ODB: LC4-7FEA01.odb     ABAQUS/STANDARD Student Edition 6.6-2     Mon May 30 20:41:51 China Standa
Step: VLL
Increment      12: Step Time =    4.2564E-02
Primary Var: S, Mises
Deformed Var: U   Deformation Scale Factor: +1.000e+00
```

7A04-T6/SiC/7.5p

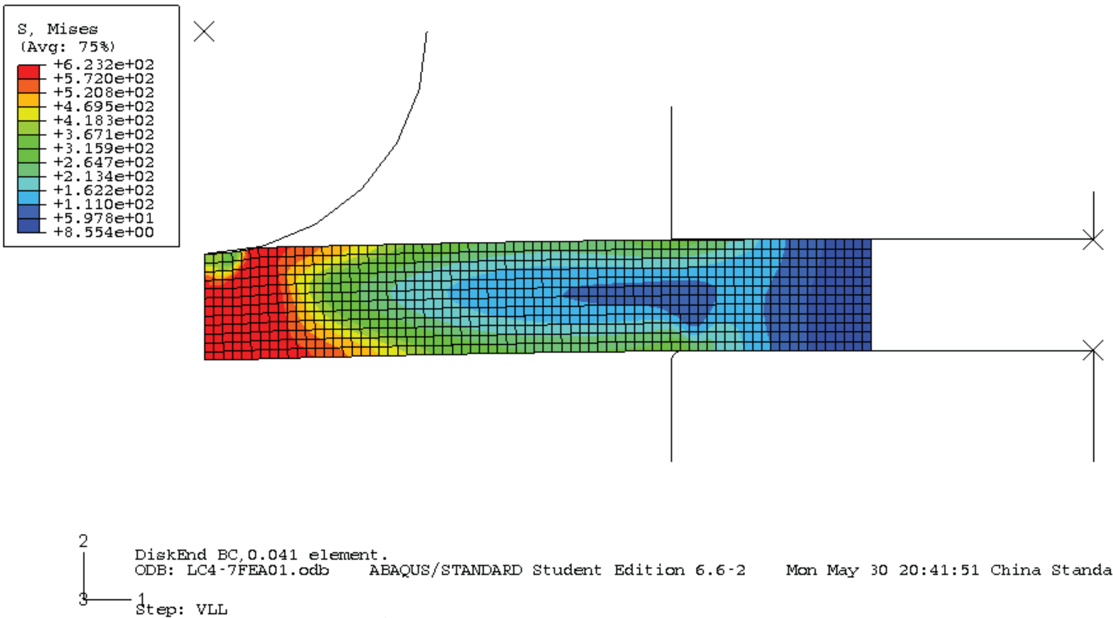

```
DiskEnd BC,0.041 element.
ODB: LC4-7FEA01.odb    ABAQUS/STANDARD Student Edition 6.6-2    Mon May 30 20:41:51 China Standa

Step: VLL
Increment     16: Step Time =    6.4526E-02
Primary Var: S, Mises
Deformed Var: U   Deformation Scale Factor: +1.000e+00
```

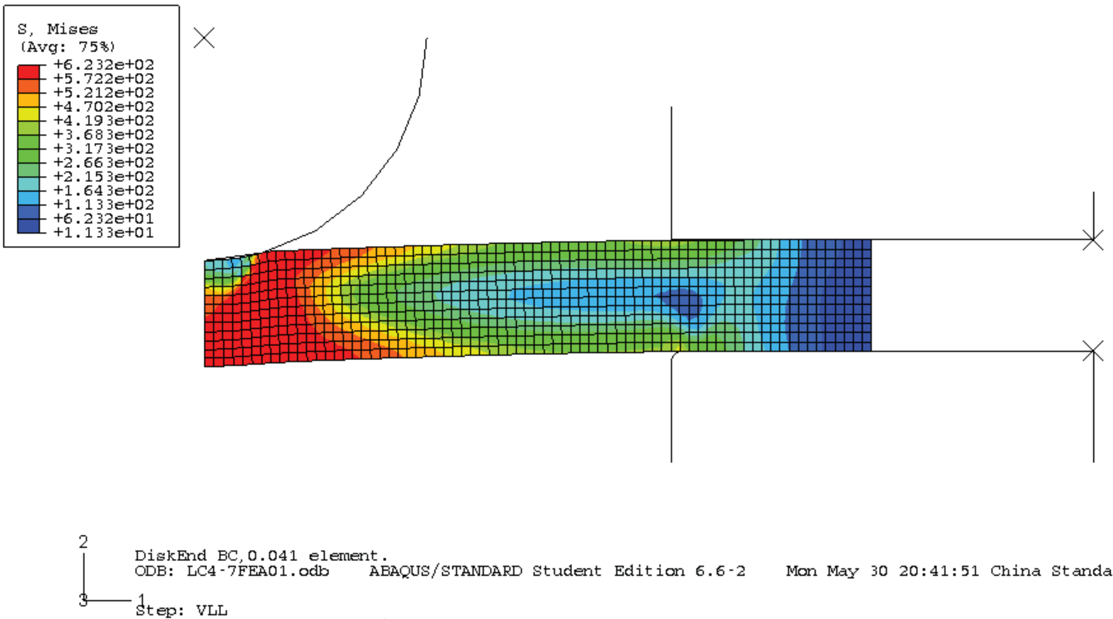

```
DiskEnd BC,0.041 element.
ODB: LC4-7FEA01.odb    ABAQUS/STANDARD Student Edition 6.6-2    Mon May 30 20:41:51 China Standa

Step: VLL
Increment     20: Step Time =    9.2322E-02
Primary Var: S, Mises
Deformed Var: U   Deformation Scale Factor: +1.000e+00
```

7A04-T6/SiC/7.5p

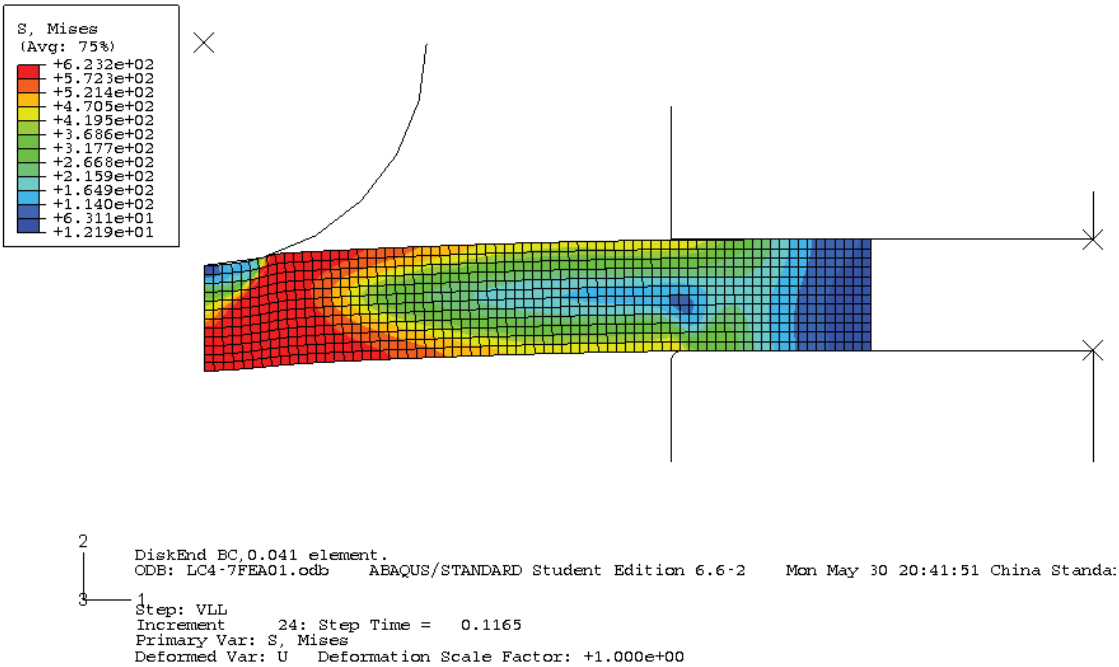

```
DiskEnd BC,0.041 element.
ODB: LC4-7FEA01.odb    ABAQUS/STANDARD Student Edition 6.6-2    Mon May 30 20:41:51 China Standa

Step: VLL
Increment     24: Step Time =    0.1165
Primary Var: S, Mises
Deformed Var: U   Deformation Scale Factor: +1.000e+00
```

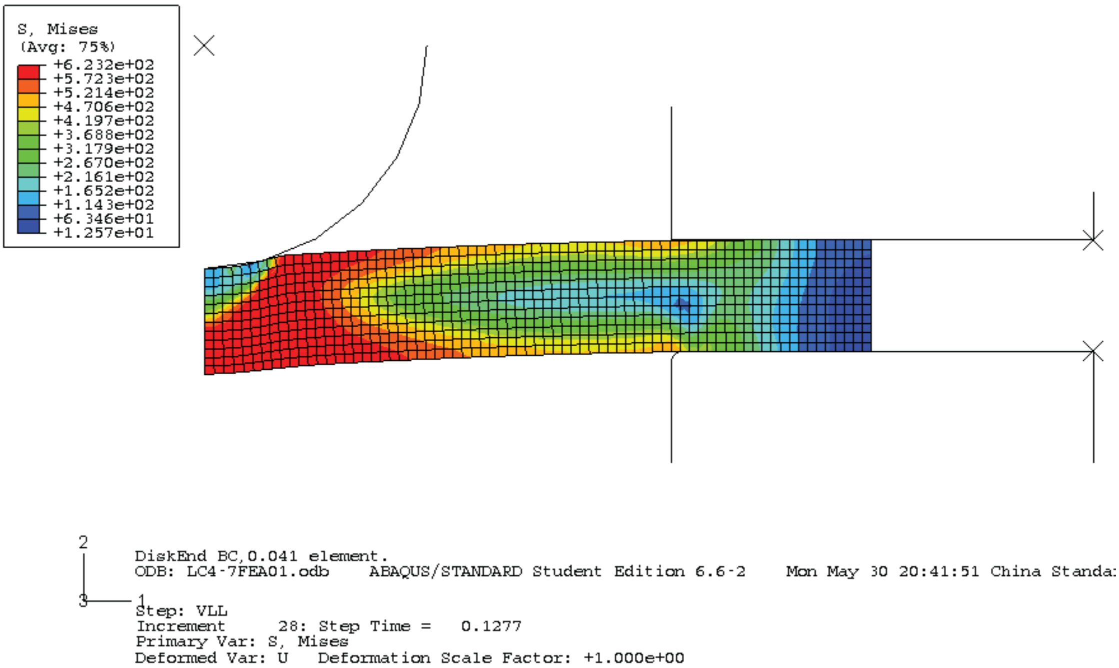

```
DiskEnd BC,0.041 element.
ODB: LC4-7FEA01.odb    ABAQUS/STANDARD Student Edition 6.6-2    Mon May 30 20:41:51 China Standa

Step: VLL
Increment     28: Step Time =    0.1277
Primary Var: S, Mises
Deformed Var: U   Deformation Scale Factor: +1.000e+00
```

7A04/SiC/10p

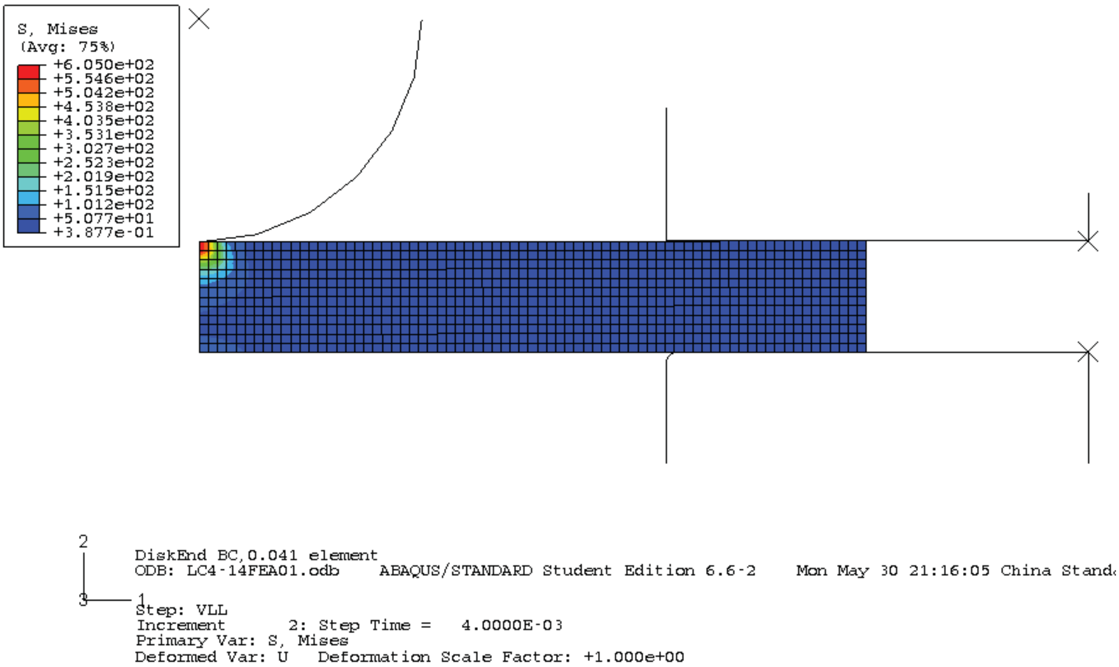

```
DiskEnd BC,0.041 element
ODB: LC4-14FEA01.odb    ABAQUS/STANDARD Student Edition 6.6-2    Mon May 30 21:16:05 China Stand
Step: VLL
Increment      2: Step Time =    4.0000E-03
Primary Var: S, Mises
Deformed Var: U   Deformation Scale Factor: +1.000e+00
```

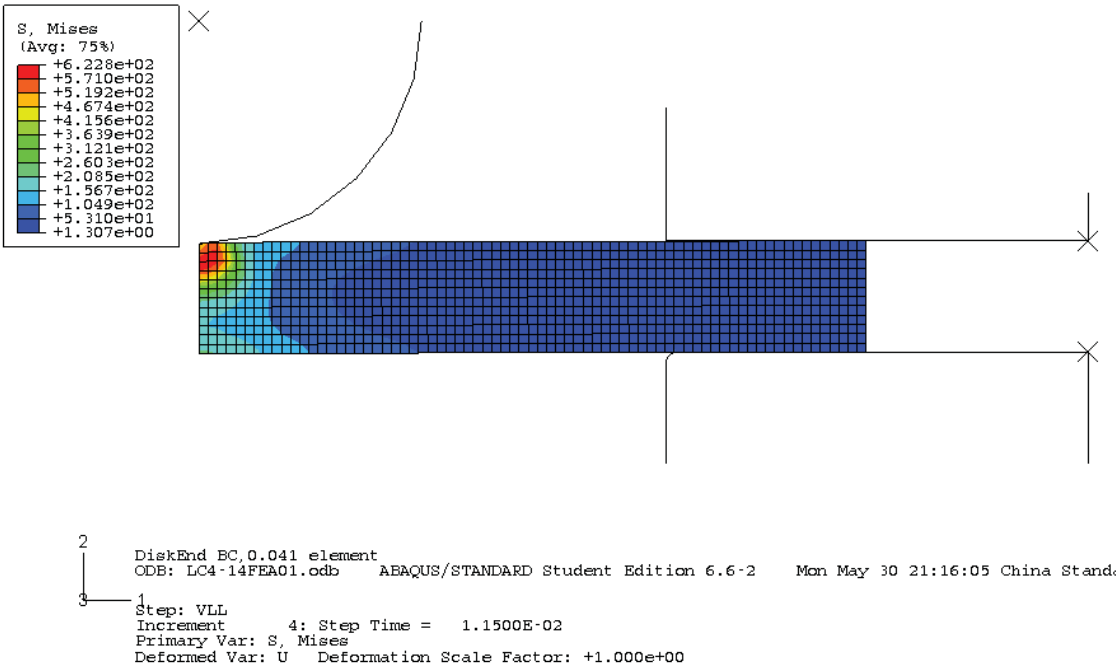

```
DiskEnd BC,0.041 element
ODB: LC4-14FEA01.odb    ABAQUS/STANDARD Student Edition 6.6-2    Mon May 30 21:16:05 China Stand
Step: VLL
Increment      4: Step Time =    1.1500E-02
Primary Var: S, Mises
Deformed Var: U   Deformation Scale Factor: +1.000e+00
```

7A04/SiC/10p

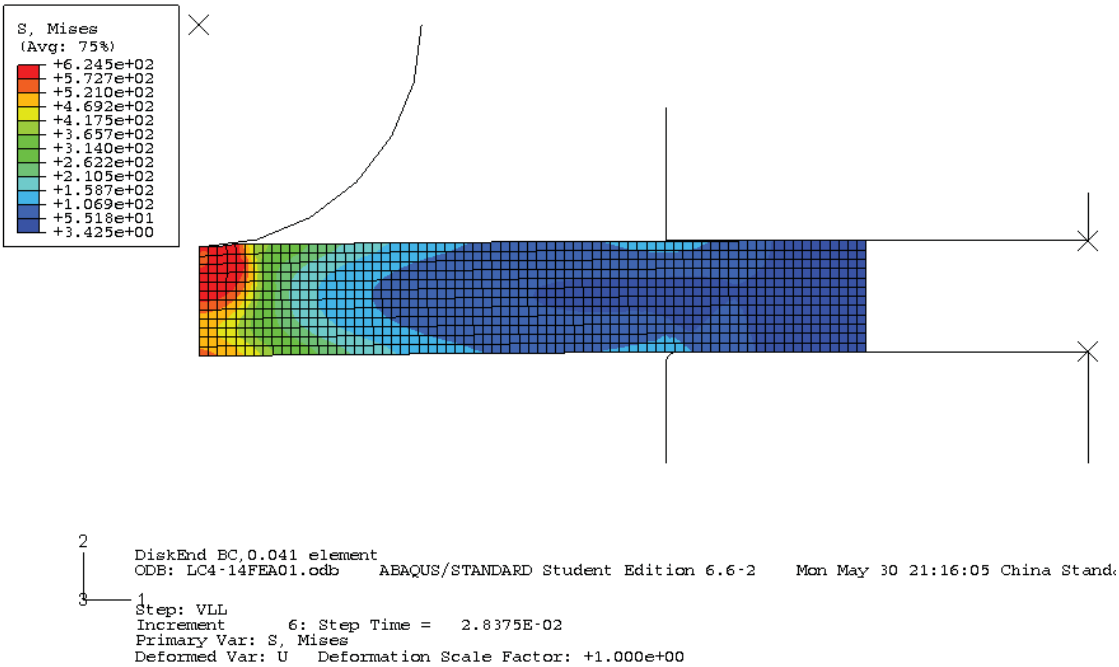

```
DiskEnd BC,0.041 element
ODB: LC4-14FEA01.odb    ABAQUS/STANDARD Student Edition 6.6-2    Mon May 30 21:16:05 China Stand
Step: VLL
Increment      6: Step Time =    2.8375E-02
Primary Var: S, Mises
Deformed Var: U   Deformation Scale Factor: +1.000e+00
```

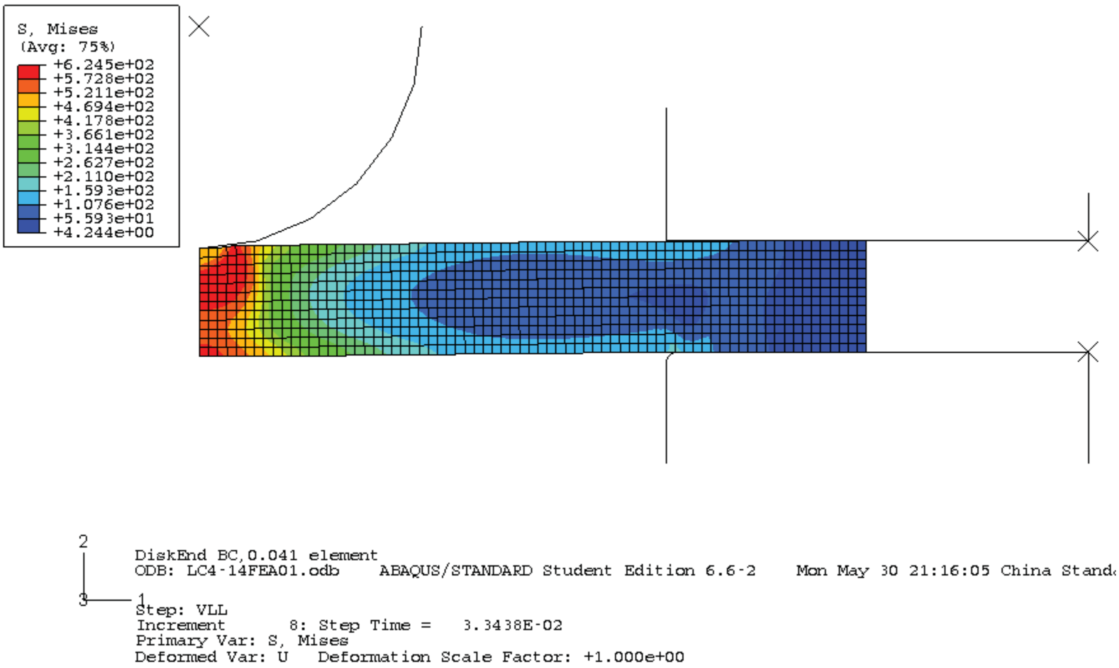

```
DiskEnd BC,0.041 element
ODB: LC4-14FEA01.odb    ABAQUS/STANDARD Student Edition 6.6-2    Mon May 30 21:16:05 China Stand
Step: VLL
Increment      8: Step Time =    3.3438E-02
Primary Var: S, Mises
Deformed Var: U   Deformation Scale Factor: +1.000e+00
```

7A04/SiC/10p

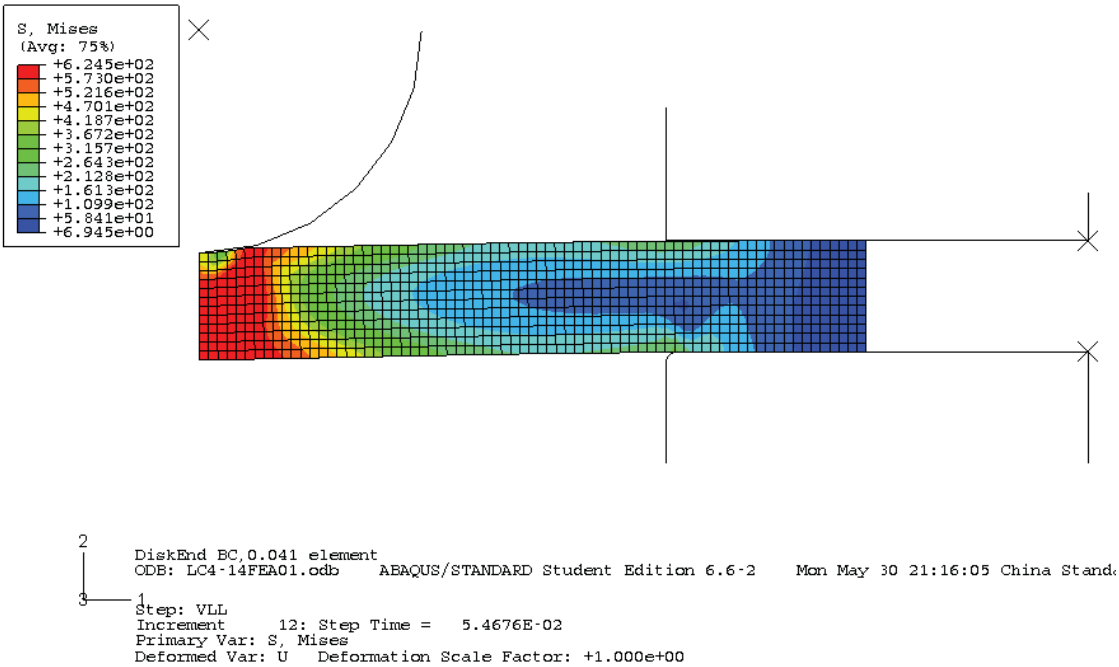

```
DiskEnd BC,0.041 element
ODB: LC4-14FEA01.odb    ABAQUS/STANDARD Student Edition 6.6-2    Mon May 30 21:16:05 China Stand
Step: VLL
Increment     12: Step Time =    5.4676E-02
Primary Var: S, Mises
Deformed Var: U   Deformation Scale Factor: +1.000e+00
```

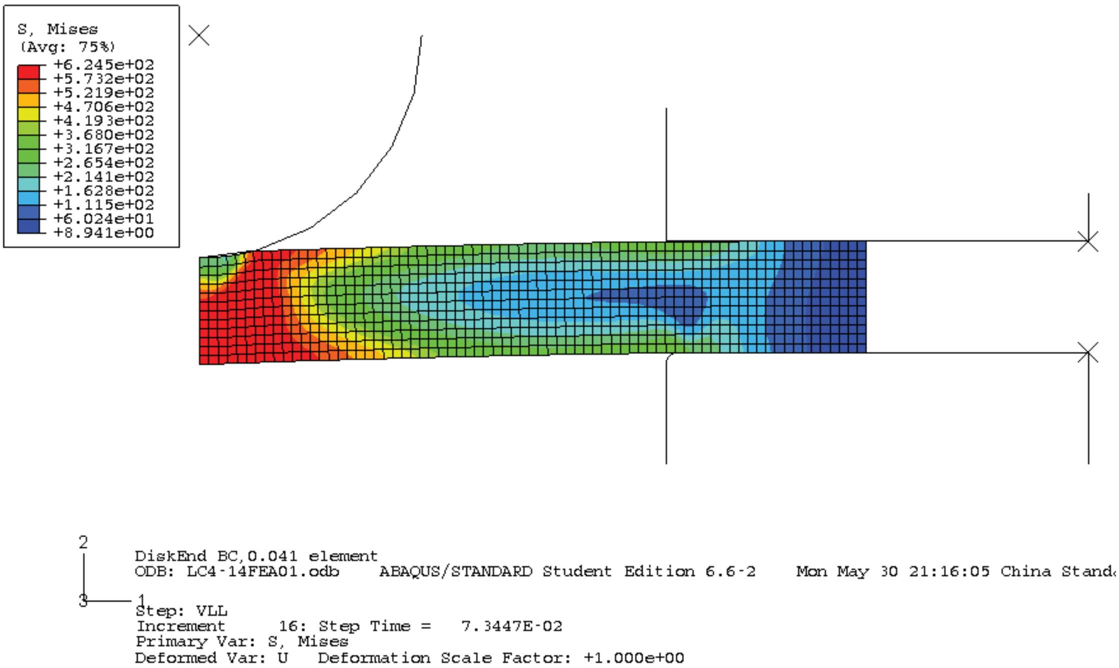

```
DiskEnd BC,0.041 element
ODB: LC4-14FEA01.odb    ABAQUS/STANDARD Student Edition 6.6-2    Mon May 30 21:16:05 China Stand
Step: VLL
Increment     16: Step Time =    7.3447E-02
Primary Var: S, Mises
Deformed Var: U   Deformation Scale Factor: +1.000e+00
```

7A04/SiC/10p

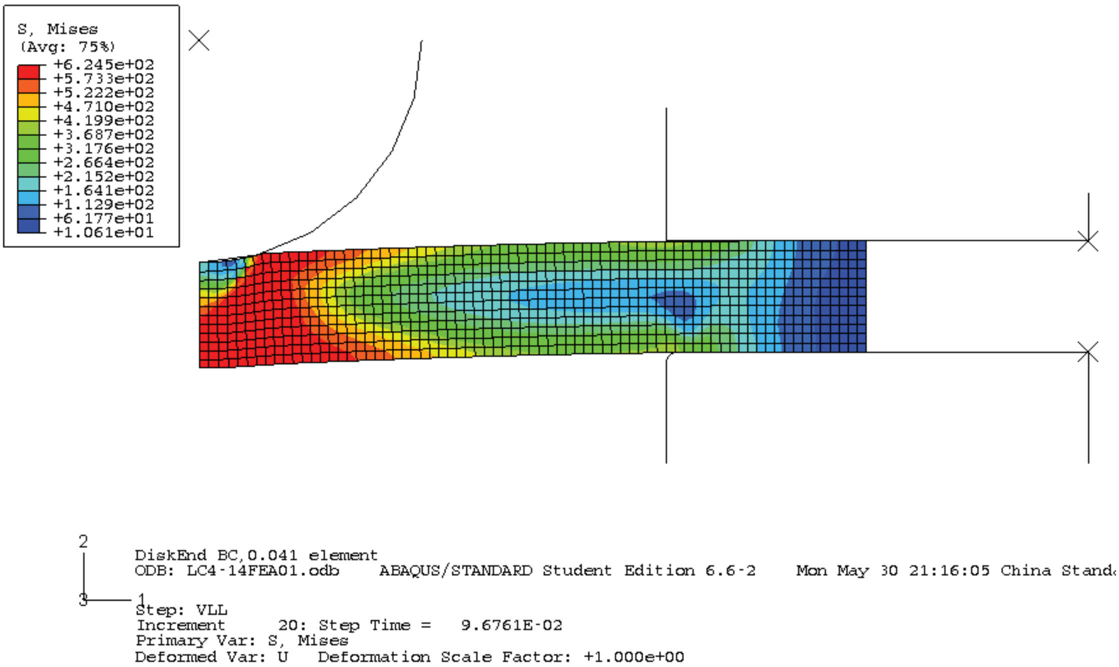

```
DiskEnd BC,0.041 element
ODB: LC4-14FEA01.odb    ABAQUS/STANDARD Student Edition 6.6-2    Mon May 30 21:16:05 China Stand
Step: VLL
Increment     20: Step Time =    9.6761E-02
Primary Var: S, Mises
Deformed Var: U   Deformation Scale Factor: +1.000e+00
```

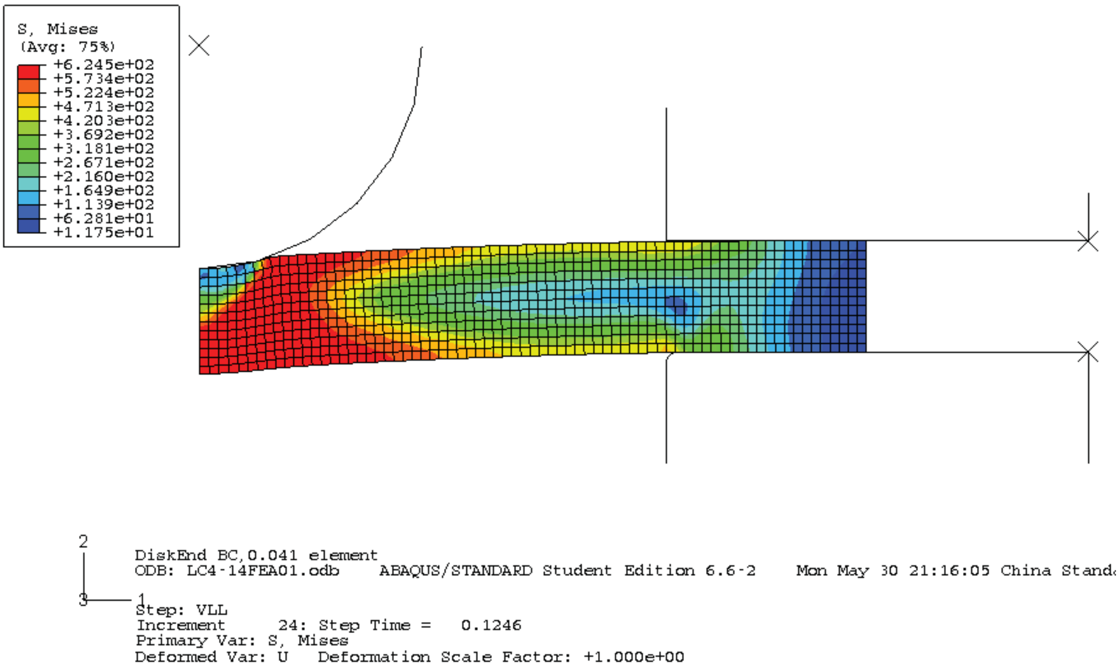

```
DiskEnd BC,0.041 element
ODB: LC4-14FEA01.odb    ABAQUS/STANDARD Student Edition 6.6-2    Mon May 30 21:16:05 China Stand
Step: VLL
Increment     24: Step Time =    0.1246
Primary Var: S, Mises
Deformed Var: U   Deformation Scale Factor: +1.000e+00
```

TC4

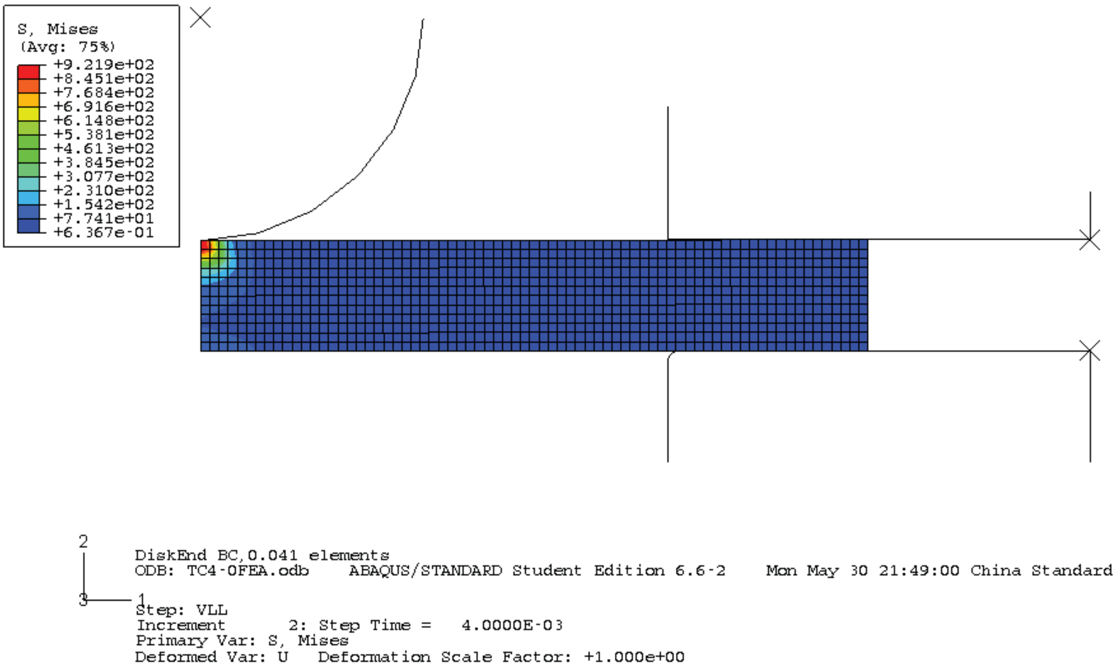

```
DiskEnd BC,0.041 elements
ODB: TC4-0FEA.odb    ABAQUS/STANDARD Student Edition 6.6-2     Mon May 30 21:49:00 China Standard

Step: VLL
Increment      2: Step Time =    4.0000E-03
Primary Var: S, Mises
Deformed Var: U   Deformation Scale Factor: +1.000e+00
```

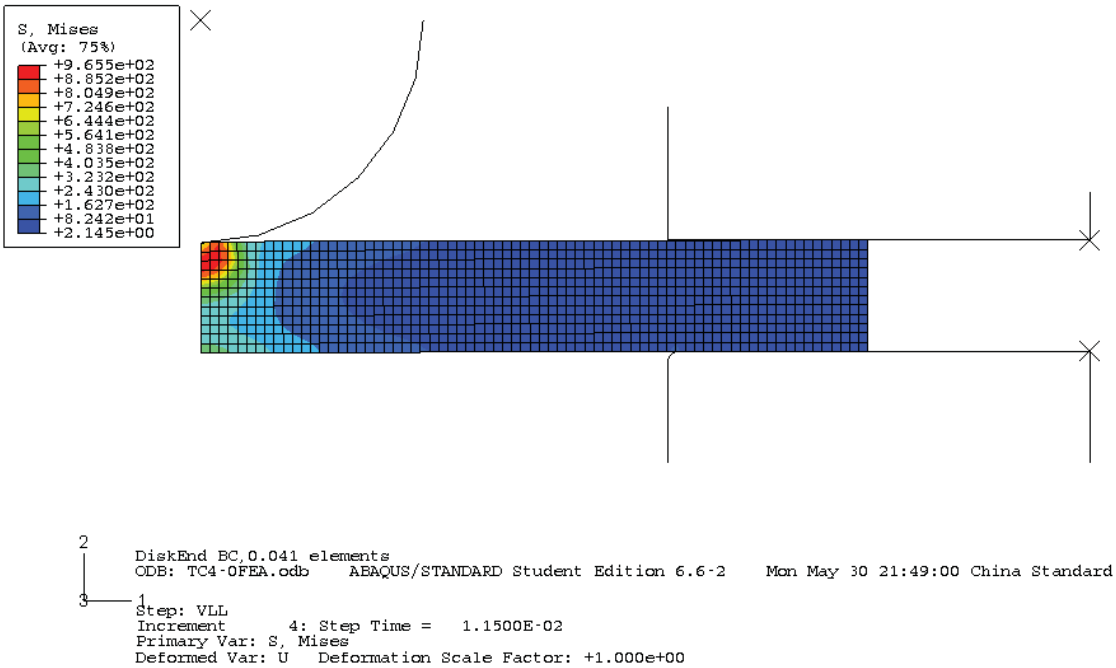

```
DiskEnd BC,0.041 elements
ODB: TC4-0FEA.odb    ABAQUS/STANDARD Student Edition 6.6-2     Mon May 30 21:49:00 China Standard

Step: VLL
Increment      4: Step Time =    1.1500E-02
Primary Var: S, Mises
Deformed Var: U   Deformation Scale Factor: +1.000e+00
```

TC4

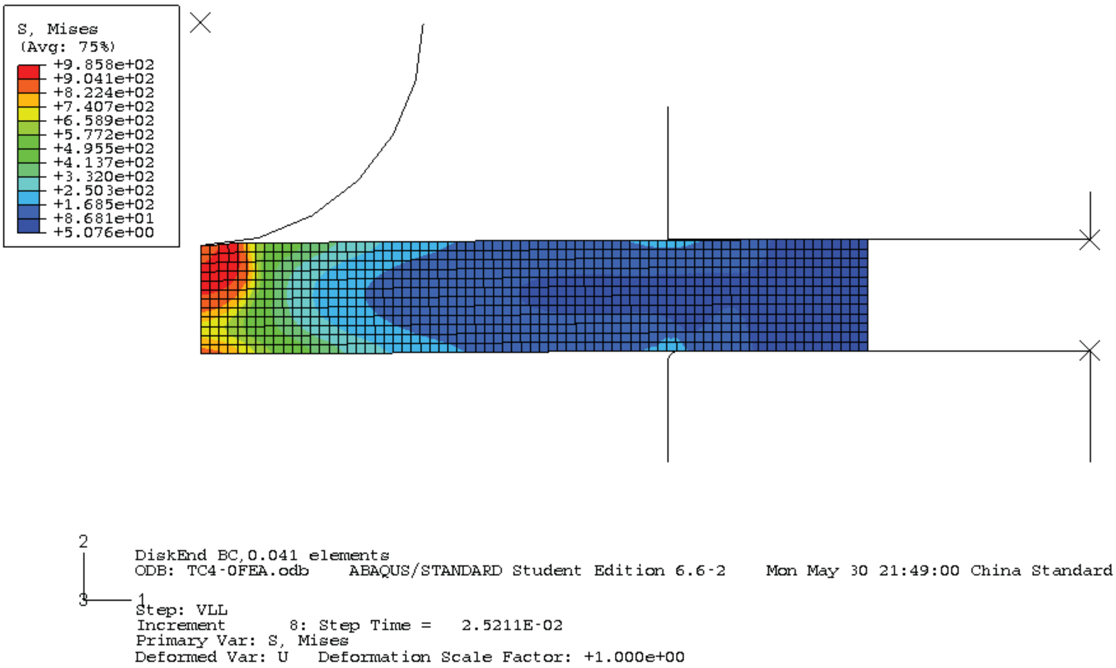

```
DiskEnd BC,0.041 elements
ODB: TC4-0FEA.odb    ABAQUS/STANDARD Student Edition 6.6-2    Mon May 30 21:49:00 China Standard

Step: VLL
Increment      8: Step Time =    2.5211E-02
Primary Var: S, Mises
Deformed Var: U   Deformation Scale Factor: +1.000e+00
```

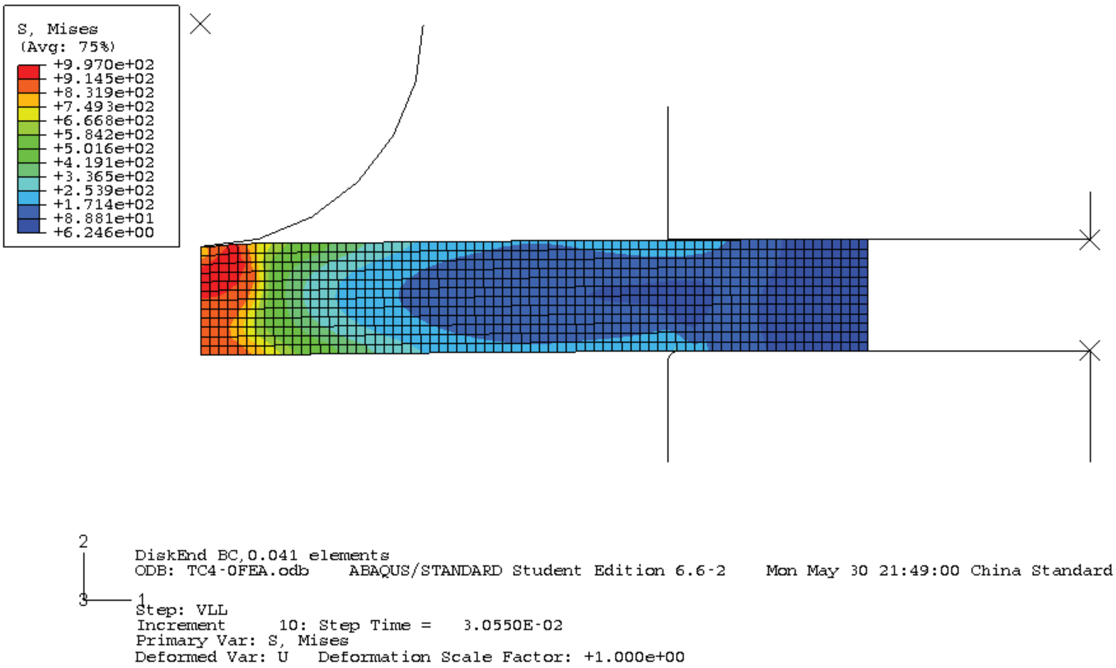

```
DiskEnd BC,0.041 elements
ODB: TC4-0FEA.odb    ABAQUS/STANDARD Student Edition 6.6-2    Mon May 30 21:49:00 China Standard

Step: VLL
Increment     10: Step Time =    3.0550E-02
Primary Var: S, Mises
Deformed Var: U   Deformation Scale Factor: +1.000e+00
```

TC4

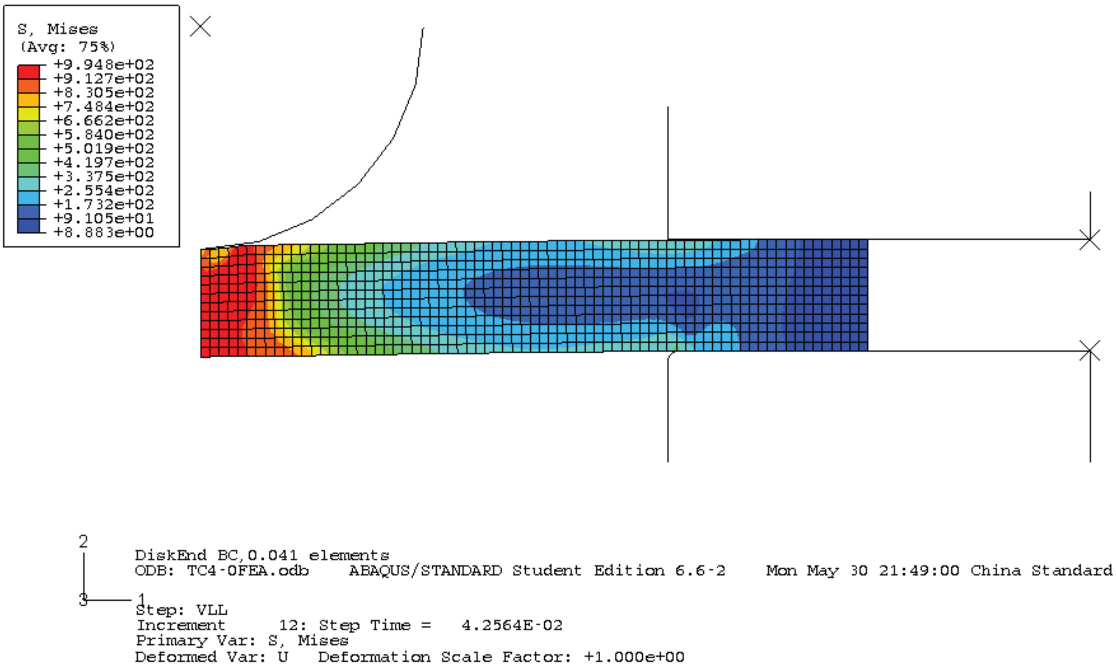

```
DiskEnd BC,0.041 elements
ODB: TC4-0FEA.odb     ABAQUS/STANDARD Student Edition 6.6-2     Mon May 30 21:49:00 China Standard

Step: VLL
Increment      12: Step Time =     4.2564E-02
Primary Var: S, Mises
Deformed Var: U    Deformation Scale Factor: +1.000e+00
```

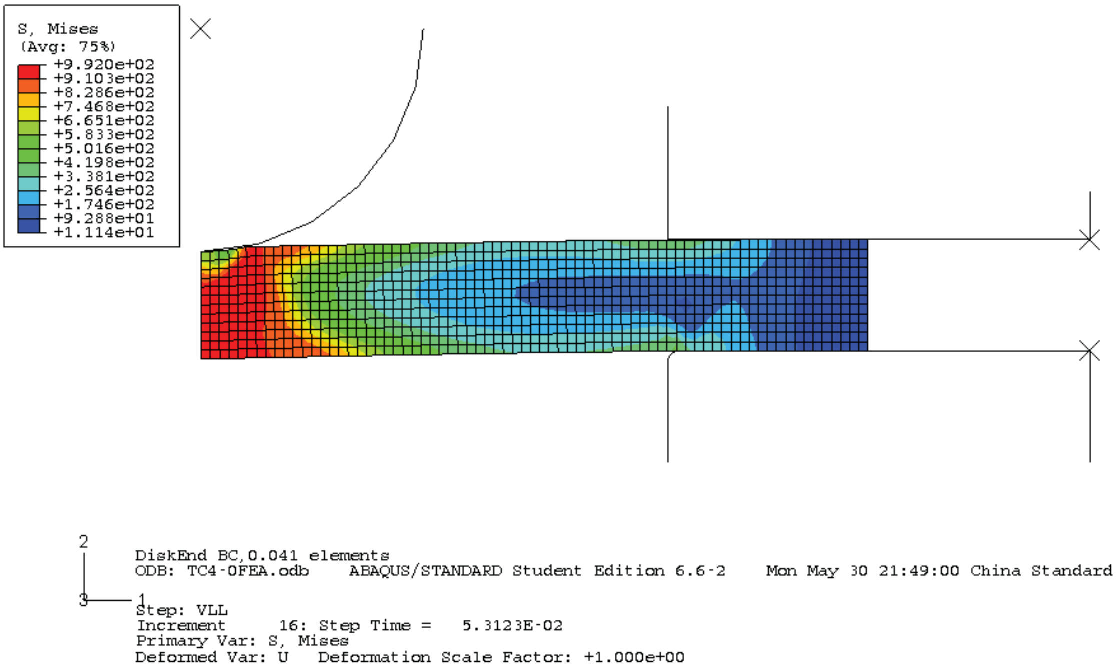

```
DiskEnd BC,0.041 elements
ODB: TC4-0FEA.odb     ABAQUS/STANDARD Student Edition 6.6-2     Mon May 30 21:49:00 China Standard

Step: VLL
Increment      16: Step Time =     5.3123E-02
Primary Var: S, Mises
Deformed Var: U    Deformation Scale Factor: +1.000e+00
```

TC4

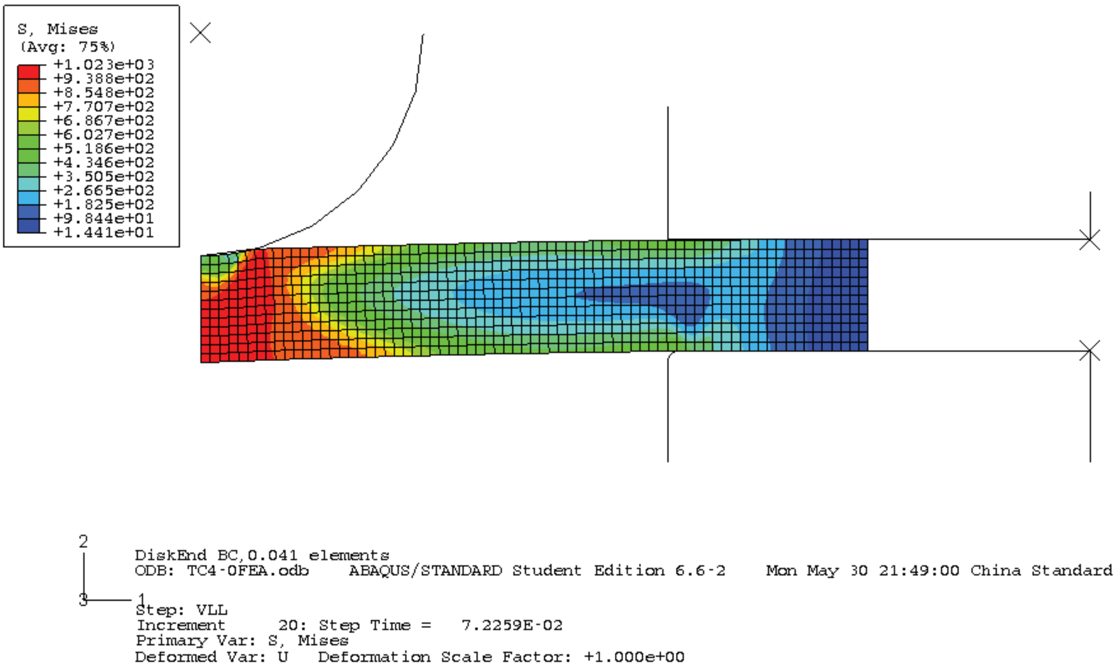

```
DiskEnd BC,0.041 elements
ODB: TC4-0FEA.odb    ABAQUS/STANDARD Student Edition 6.6-2    Mon May 30 21:49:00 China Standard

Step: VLL
Increment     20: Step Time =    7.2259E-02
Primary Var: S, Mises
Deformed Var: U   Deformation Scale Factor: +1.000e+00
```

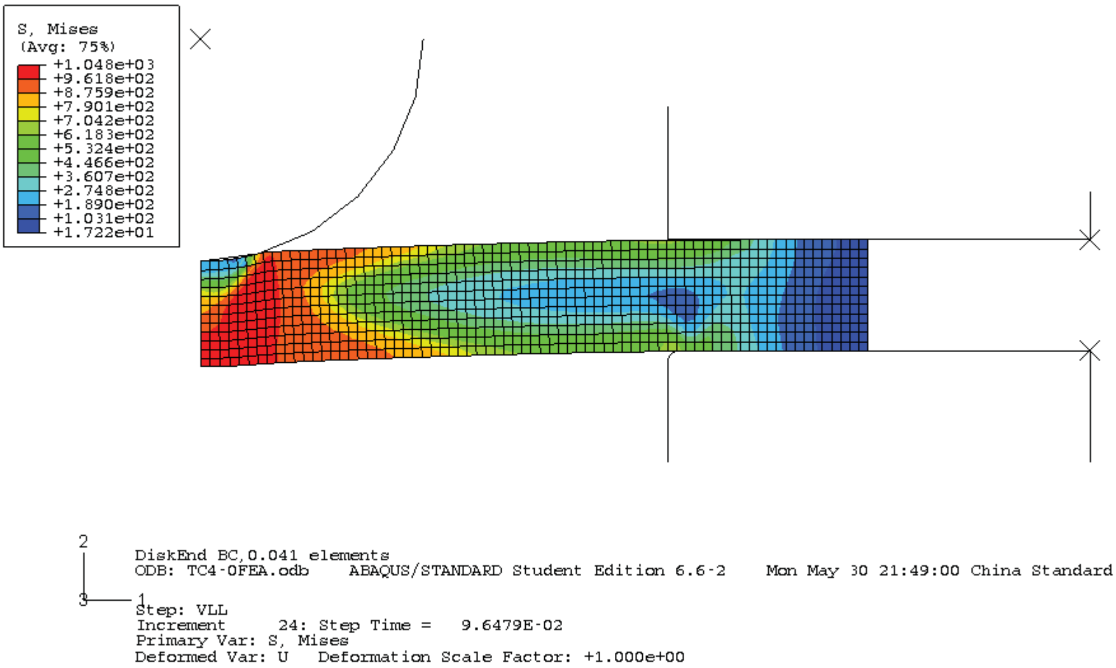

```
DiskEnd BC,0.041 elements
ODB: TC4-0FEA.odb    ABAQUS/STANDARD Student Edition 6.6-2    Mon May 30 21:49:00 China Standard

Step: VLL
Increment     24: Step Time =    9.6479E-02
Primary Var: S, Mises
Deformed Var: U   Deformation Scale Factor: +1.000e+00
```

TC4/TiB, TiC/2.5w, 2.5p

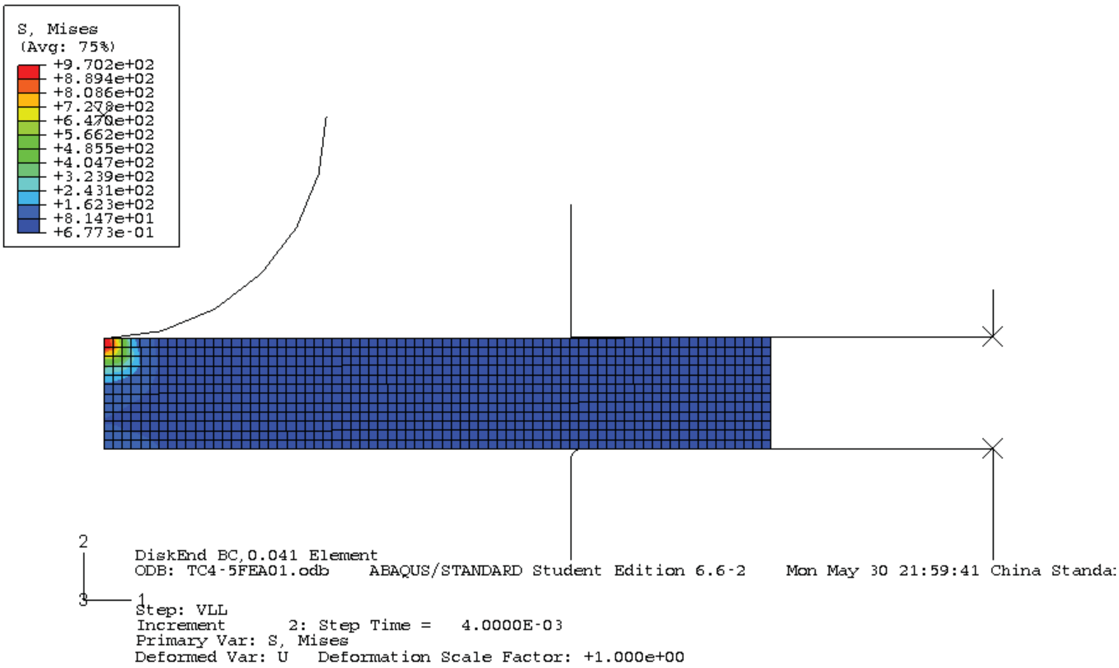

```
DiskEnd BC,0.041 Element
ODB: TC4-5FEA01.odb    ABAQUS/STANDARD Student Edition 6.6-2    Mon May 30 21:59:41 China Standa:

Step: VLL
Increment      2: Step Time =    4.0000E-03
Primary Var: S, Mises
Deformed Var: U   Deformation Scale Factor: +1.000e+00
```

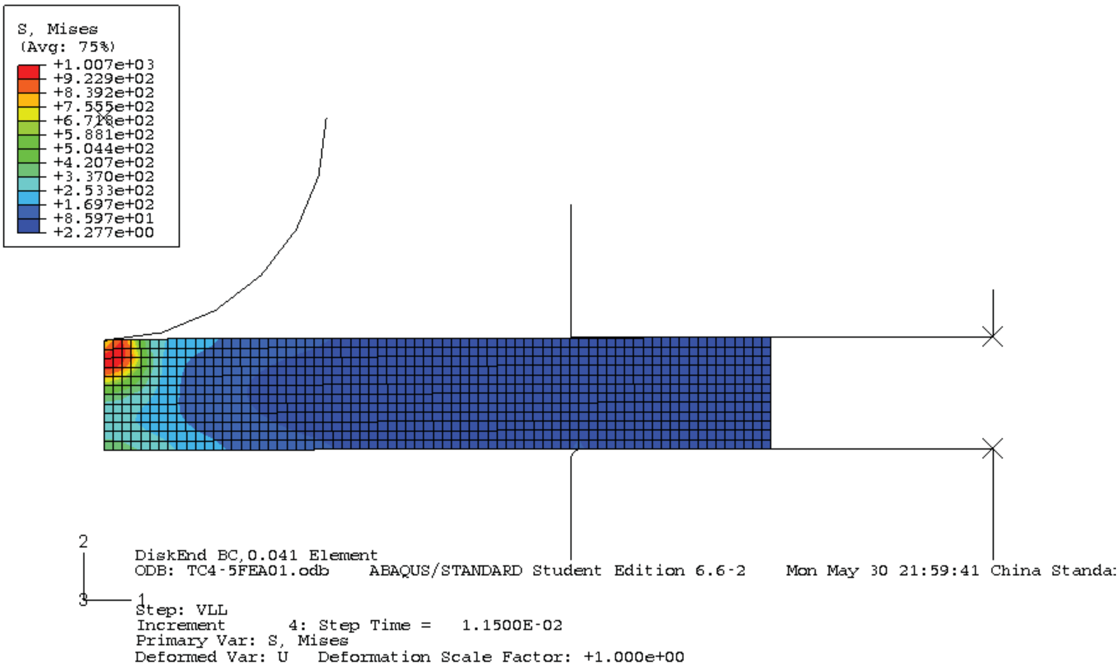

```
DiskEnd BC,0.041 Element
ODB: TC4-5FEA01.odb    ABAQUS/STANDARD Student Edition 6.6-2    Mon May 30 21:59:41 China Standa:

Step: VLL
Increment      4: Step Time =    1.1500E-02
Primary Var: S, Mises
Deformed Var: U   Deformation Scale Factor: +1.000e+00
```

TC4/TiB, TiC/2.5w, 2.5p

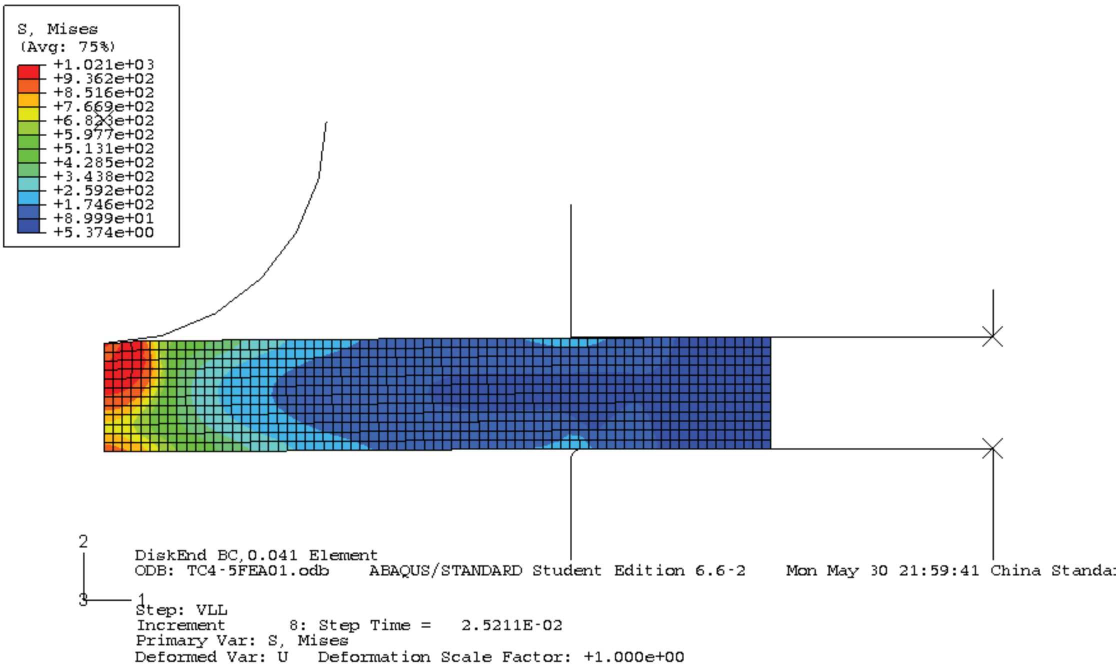

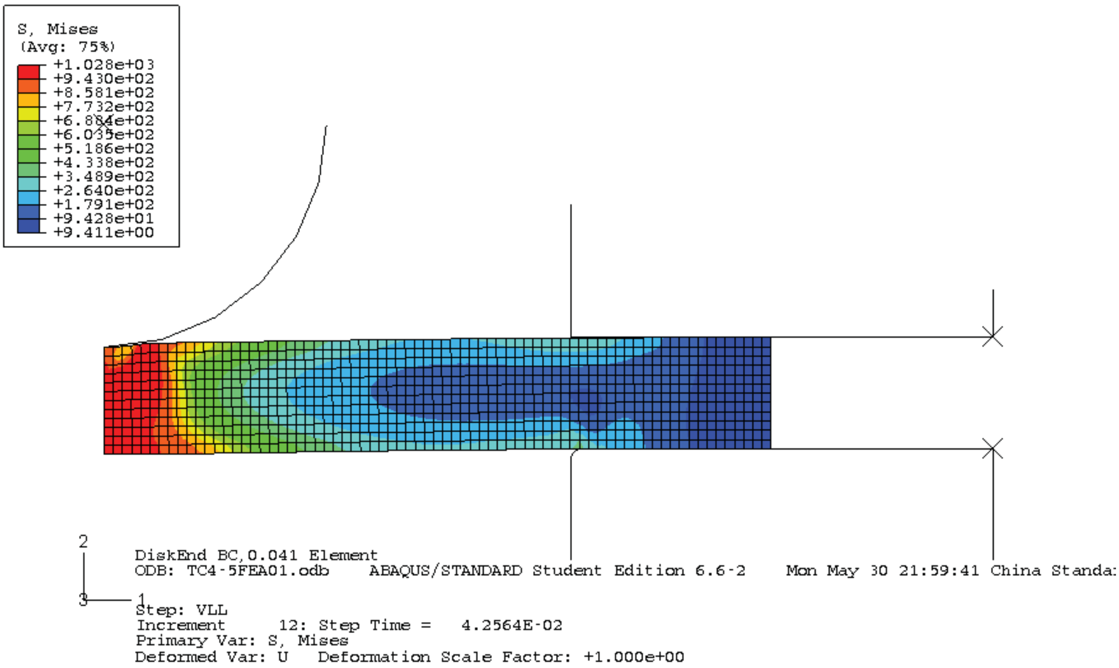

TC4/TiB, TiC/2.5w, 2.5p

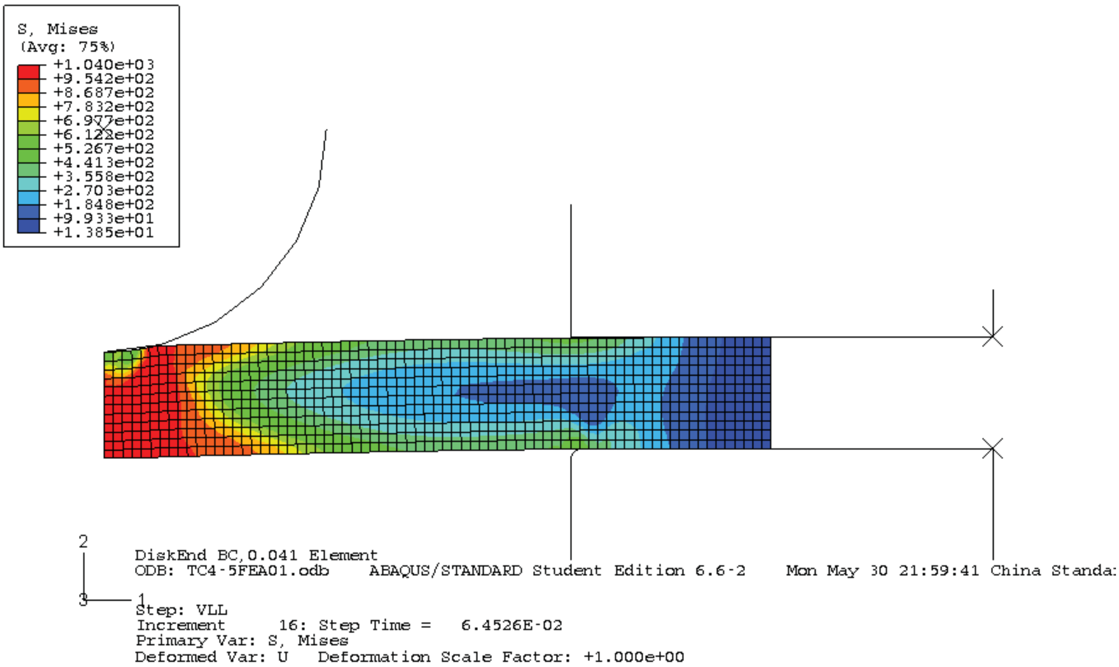

```
DiskEnd BC,0.041 Element
ODB: TC4-5FEA01.odb     ABAQUS/STANDARD Student Edition 6.6-2     Mon May 30 21:59:41 China Standa:

Step: VLL
Increment      16: Step Time =    6.4526E-02
Primary Var: S, Mises
Deformed Var: U   Deformation Scale Factor: +1.000e+00
```

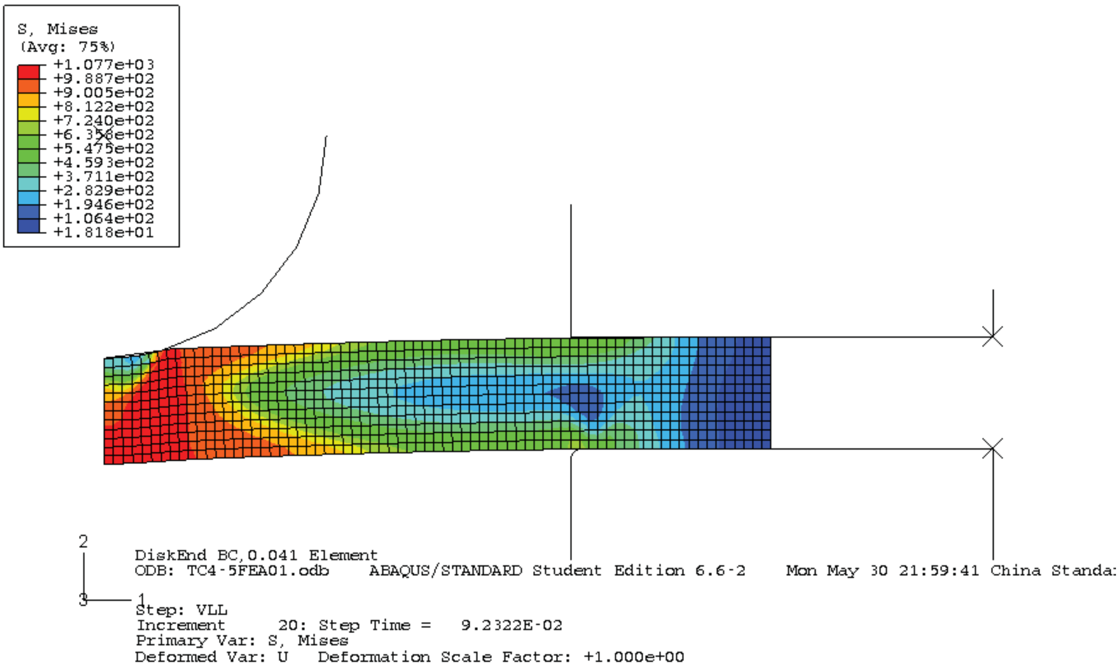

```
DiskEnd BC,0.041 Element
ODB: TC4-5FEA01.odb     ABAQUS/STANDARD Student Edition 6.6-2     Mon May 30 21:59:41 China Standa:

Step: VLL
Increment      20: Step Time =    9.2322E-02
Primary Var: S, Mises
Deformed Var: U   Deformation Scale Factor: +1.000e+00
```

TC4/TiB, TiC/2.5w, 2.5p

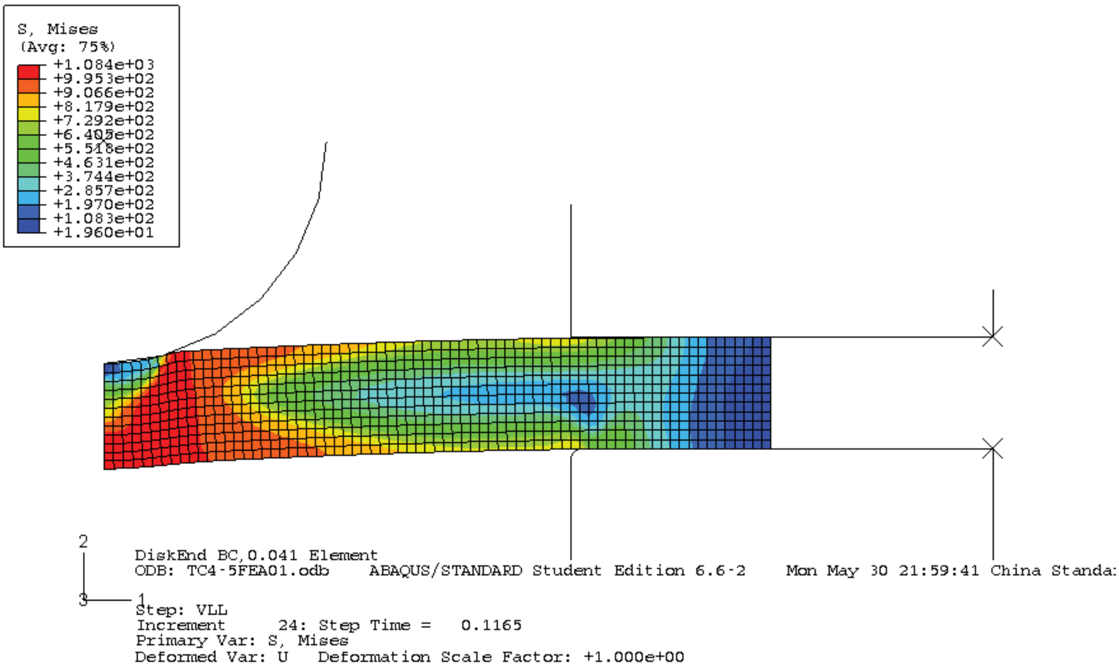

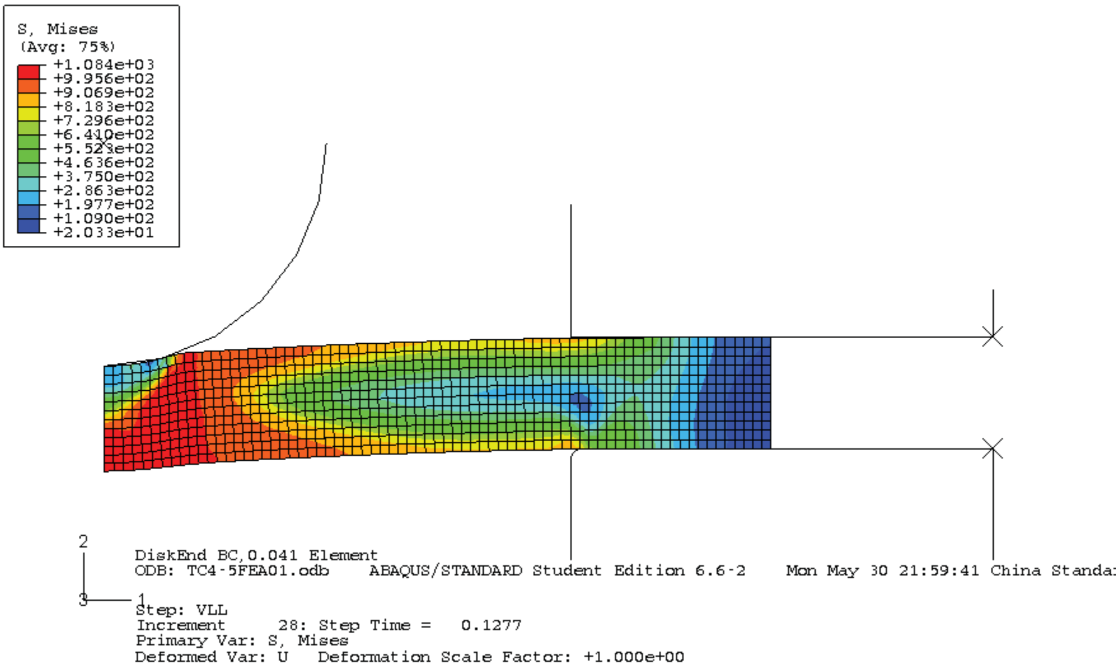

TC4/TiB, TiC/5w, 5p

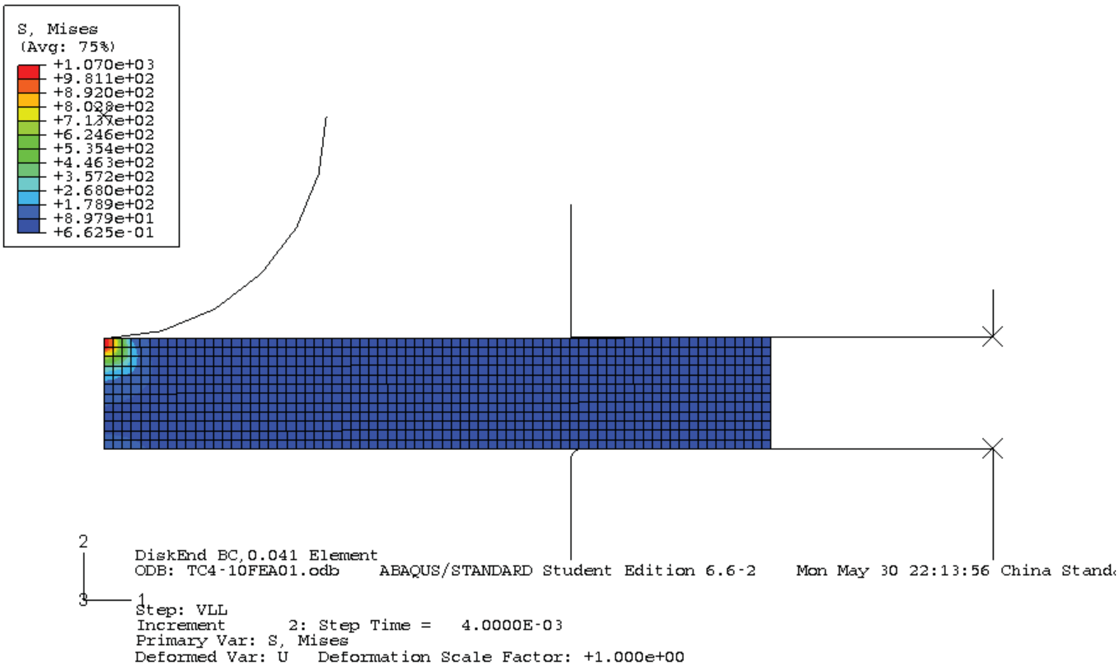

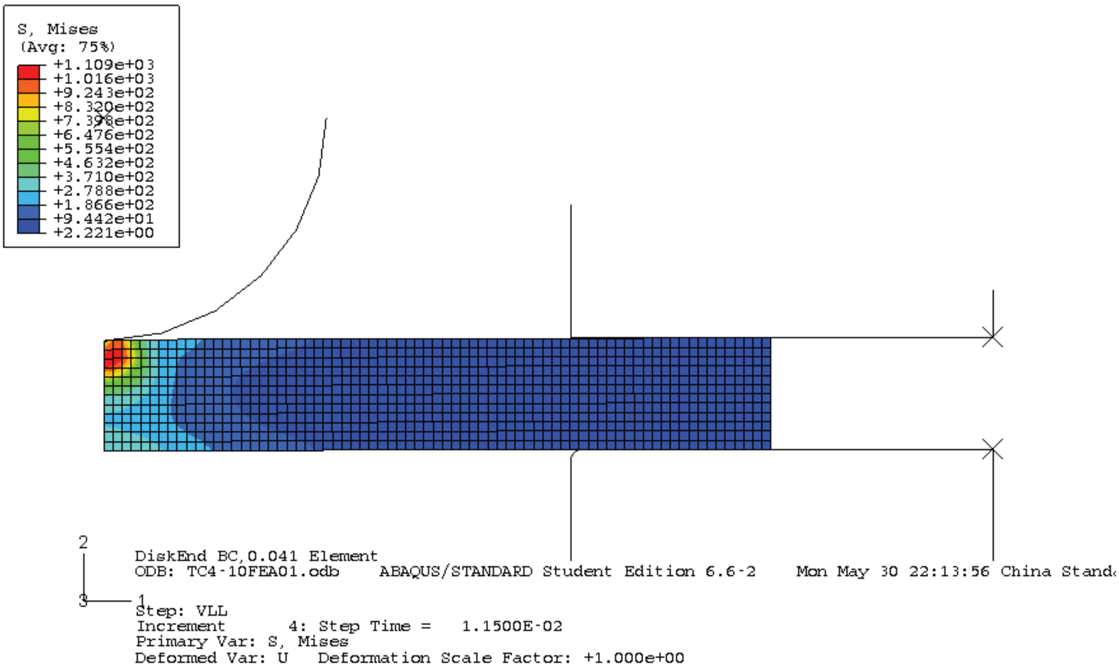

TC4/TiB, TiC/5w, 5p

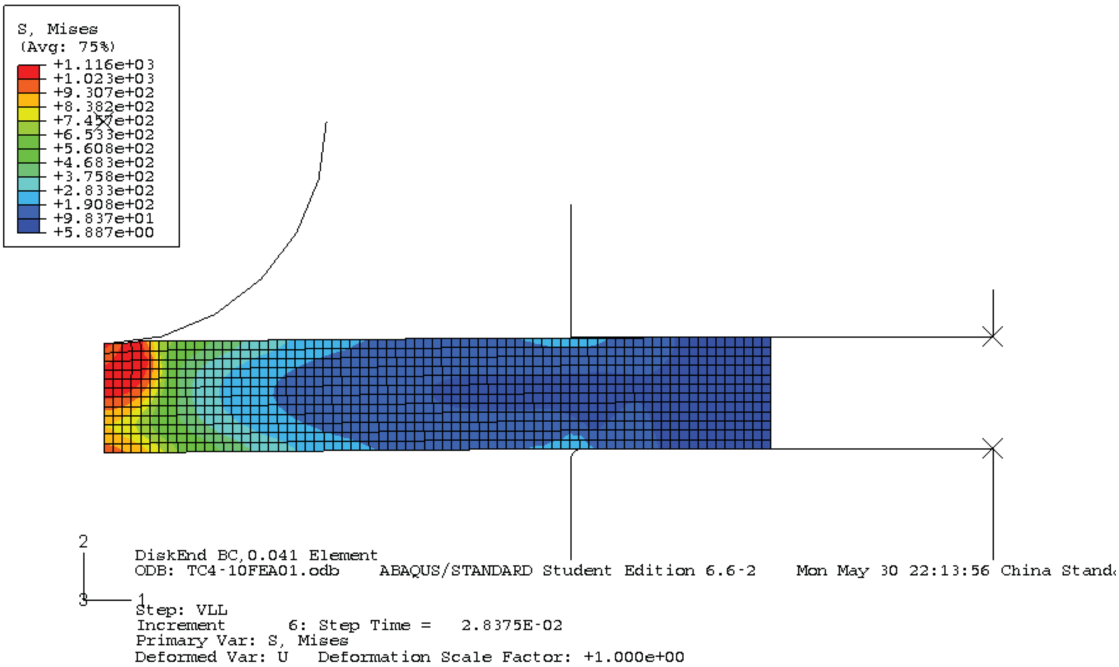

```
DiskEnd BC,0.041 Element
ODB: TC4-10FEA01.odb    ABAQUS/STANDARD Student Edition 6.6-2    Mon May 30 22:13:56 China Stand

Step: VLL
Increment      6: Step Time =    2.8375E-02
Primary Var: S, Mises
Deformed Var: U   Deformation Scale Factor: +1.000e+00
```

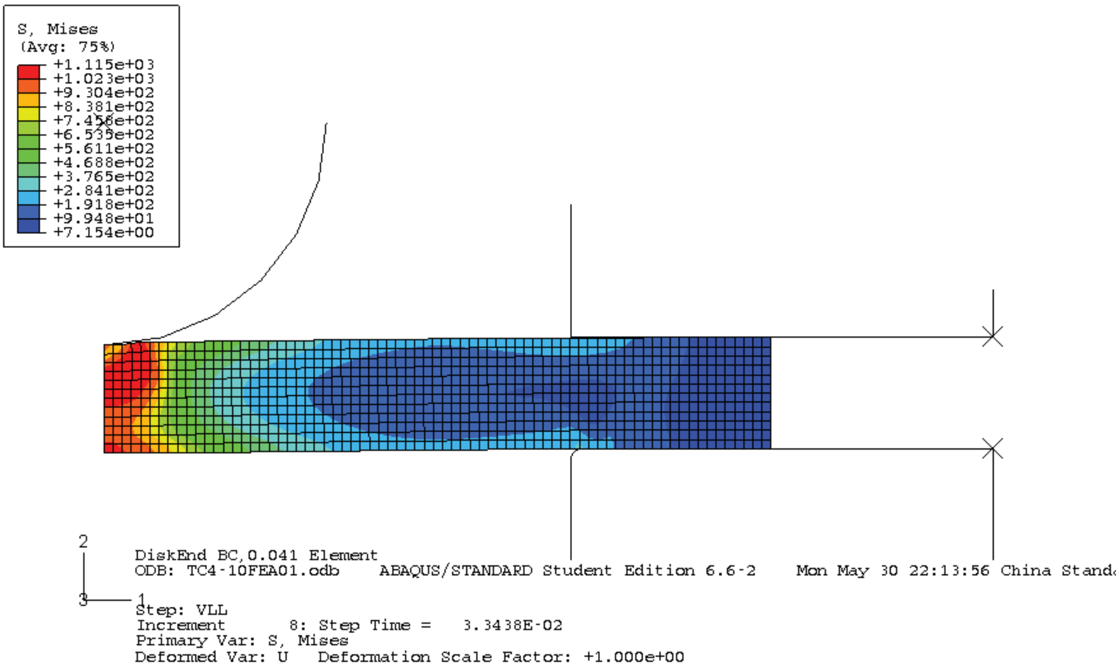

```
DiskEnd BC,0.041 Element
ODB: TC4-10FEA01.odb    ABAQUS/STANDARD Student Edition 6.6-2    Mon May 30 22:13:56 China Stand

Step: VLL
Increment      8: Step Time =    3.3438E-02
Primary Var: S, Mises
Deformed Var: U   Deformation Scale Factor: +1.000e+00
```

TC4/TiB, TiC/5w, 5p

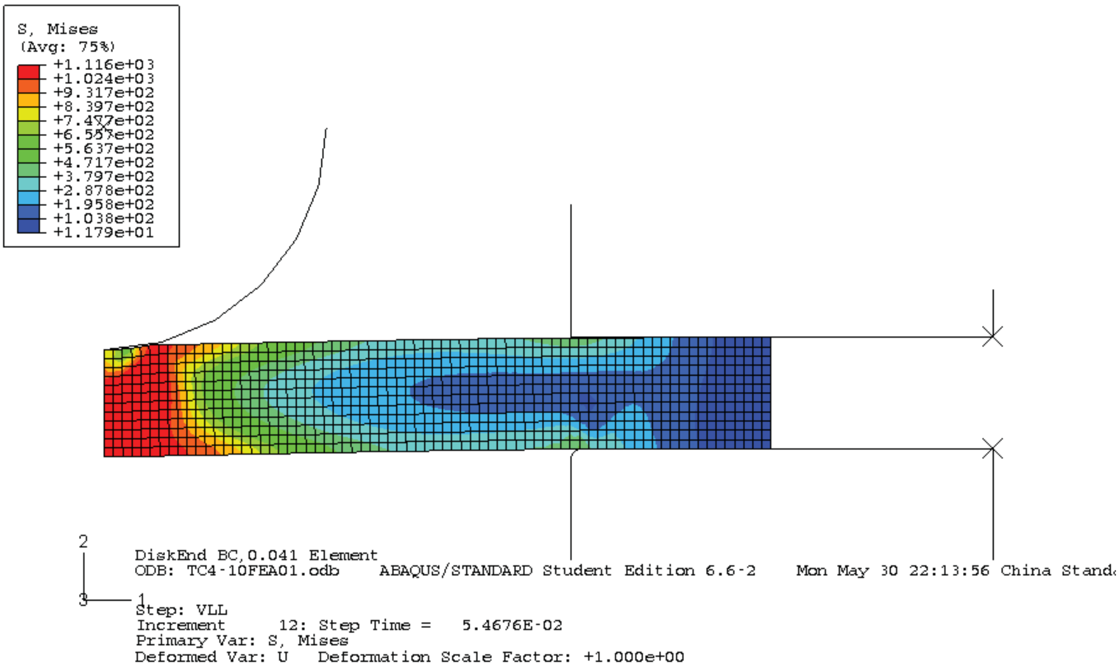

```
DiskEnd BC,0.041 Element
ODB: TC4-10FEA01.odb    ABAQUS/STANDARD Student Edition 6.6-2    Mon May 30 22:13:56 China Stand

Step: VLL
Increment     12: Step Time =    5.4676E-02
Primary Var: S, Mises
Deformed Var: U   Deformation Scale Factor: +1.000e+00
```

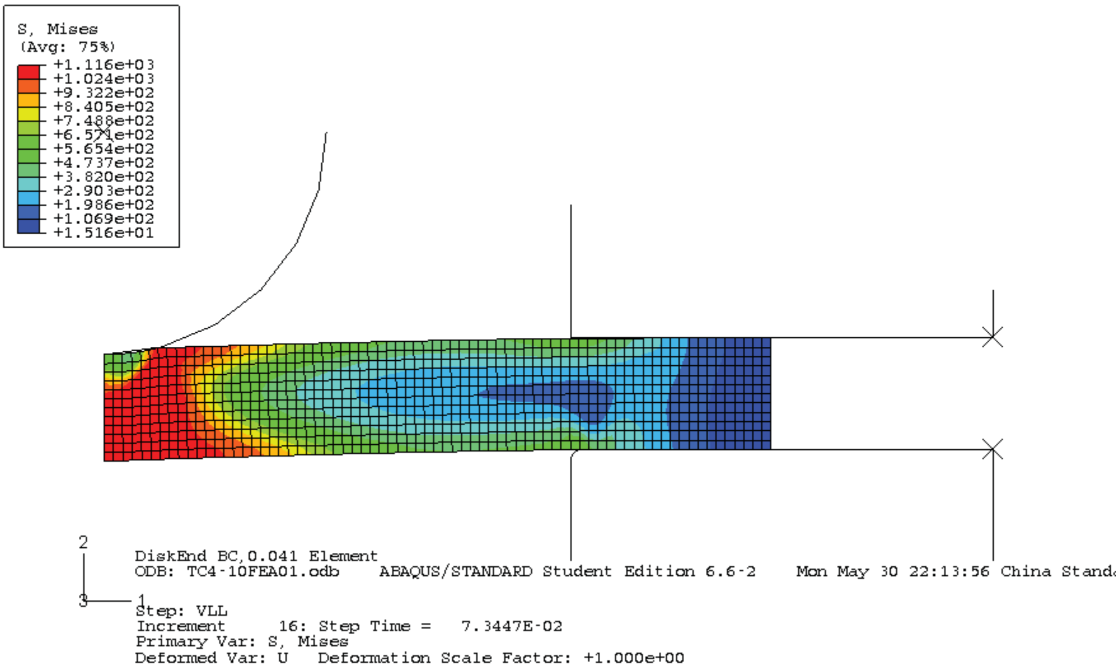

```
DiskEnd BC,0.041 Element
ODB: TC4-10FEA01.odb    ABAQUS/STANDARD Student Edition 6.6-2    Mon May 30 22:13:56 China Stand

Step: VLL
Increment     16: Step Time =    7.3447E-02
Primary Var: S, Mises
Deformed Var: U   Deformation Scale Factor: +1.000e+00
```

TC4/TiB, TiC/5w, 5p